Description of quasiparticle decay by continuous unitary transformations

Dissertation

zur Erlangung des Grades eines
Doktors der Naturwissenschaften

der Fakultät Physik
der Technischen Universität Dortmund

vorgelegt von

Tim Fischer

aus Dortmund

April, 2012

Abstract

In sufficiently dimerized quantum antiferromagnets the elementary excitations are given by gapped spin $S = 1$ triplon quasiparticles. Although these triplons are protected by a gap at low energies they may decay spontaneously at higher energies where the one-triplon dispersion merges with the two-triplon continuum.

First, we illustrate and characterize such a spontaneous decay in low-dimensional quantum antiferromagnets on the basis of a simple one-dimensional bosonic model. The decay implies the breakdown of the quasiparticle picture. No quantitative description by a Lorentzian resonance is possible. In particular, three qualitatively different scenarios are identified depending on the one-triplon dispersion and the two-triplon interaction.

To describe unstable quasiparticles in more complex models we introduced an adapted generator for continuous unitary transformations. Its general properties are derived and discussed.

Next, we investigate asymmetric antiferromagnetic and asymmetric ferro-antiferromagnetic spin $S = 1/2$ Heisenberg ladders, which allow for spontaneous triplon decay, to illustrate this approach. Results for the low-energy spectra and the dynamical structure factors for these systems are presented. We show that quasiparticle decay is more pronounced in the case of ferro-antiferromagnetic ladders than in solely antiferromagnetic ladders.

Finally, we use continuous unitary transformations and high temperature series expansions to determine a quantitative model for the compound IPA-$CuCl_3$ based on data of inelastic neutron scattering and measurements of the magnetic susceptibility. Our calculations reveal IPA-$CuCl_3$ as system of coupled asymmetric spin $S = 1/2$ Heisenberg ladders with the four magnetic couplings $J_1 \approx -2.3$ meV, $J_2 \approx 1.2$ meV, $J_3 \approx 2.9$ meV and $J_4 \approx -0.3$ meV.

Based on this microscopic model for IPA-$CuCl_3$ the adapted continuous unitary transformation is used to describe the quasiparticle decay in IPA-$CuCl_3$. The results agree very well with the experimental data. In addition the magnetic field dependence of the lowest modes in the condensed phase as well as the temperature dependence of the gap without magnetic field corroborate our microscopic model.

Kurze Zusammenfassung

In hinreichend stark dimerisierten Quanten-Antiferromagneten sind die elementaren Anregungen durch Spin $S = 1$ Quasiteilchen gegeben, die eine Anregungslücke besitzen und Triplonen genannt werden. Obwohl diese Triplonen bei niedrigen Energien durch die Anregungslücke geschützt sind, können sie bei höheren Energien, bei denen ihre Dispersion mit dem Kontinuum mischt, spontan zerfallen.

Zunächst beschreiben und charakterisieren wir diesen, in niedrigdimensionalen Quanten-Antiferromagneten auftretenden, spontanen Zerfall anhand eines einfachen eindimensionalen bosonischen Modells. Der Zerfall lässt sich nur unzureichend durch das übliche Quasiteilchenkonzept beschreiben, da keine quantitative Beschreibung der zerfallenden Anregungen in Form einer Lorentzkurve möglich ist. Insbesondere sind je nach Form der Dispersion der Triplonen und der Stärke der Wechselwirkung zwischen je zwei Triplonen drei unterschiedliche Zerfallsszenarien möglich.

Um zerfallende Quasiteilchen in komplexeren Modellen zu beschreiben, werden kontinuierliche unitäre Transformationen verwendet, welche durch einen speziell angepassten Generator gegeben sind. Die allgemeinen Eigenschaften dieser angepassten kontinuierlichen unitären Transformation werden hergeleitet und diskutiert.

Danach wird dieser Zugang anhand von asymmetrischen antiferromagentischen und asymmetrischen ferro-antiferromagnetischen Spin $S = 1/2$ Heisenberg Leitern illustriert. Resultate für die Niederenergiespektren und die dynamischen Strukturfaktoren werden präsentiert. Wir zeigen, dass der Zerfall von Quasiteilchen im Falle der ferro-antiferromagnetischen Leiter ausgeprägter ist als im Falle der rein antiferromagnetischen Leiter.

Zuletzt verwenden wir kontinuierliche unitäre Transformationen und Hochtemperatur-Reihenentwicklungen um auf Grundlage von Daten aus inelastischer Neutronstreuung und Messungen der magnetischen Suszeptibilität ein quantitatives Modell für die Verbindung IPA-$CuCl_3$ zu bestimmen. Unsere Rechnungen zeigen, dass IPA-$CuCl_3$ durch ein System von gekoppelten asymmetrischen Spin $S = 1/2$ Heisenberg Leitern beschrieben werden kann, wobei die vier magnetischen Kopplungen gegeben sind durch $J_1 \approx -2.3$ meV, $J_2 \approx 1.2$ meV, $J_3 \approx 2.9$ meV und $J_4 \approx -0.3$ meV.

Ausgehend von diesem mikroskopischen Modell für IPA-$CuCl_3$ wird mittels

angepasster kontinuierlicher unitärer Transformationen der Quasiteilchenzerfall in IPA-$CuCl_3$ beschrieben. Die erzielten Ergebnisse stimmen sehr gut mit den experimentellen Befunden überein. Zusätzlich gestützt wird unser mikroskopisches Modell durch die Abhängigkeit dessen tiefliegender Anregungsmoden innerhalb der kondensierten Phase im magnetischen Feld, sowie durch die Temperaturabhängigkeit der Anregungslücke ohne magnetisches Feld.

Contents

Acronyms

AASHL asymmetric antiferromagnetic spin $S = 1/2$ Heisenberg ladder

AFASHL asymmetric ferro-antiferromagnetic spin $S = 1/2$ Heisenberg ladder

BEC Bose-Einstein condensation

CUT continuous unitary transformation

epCUT enhanced perturbative continuous unitary transformation

deepCUT directly evaluated enhanced perturbative continuous unitary transformation

gCUT graph theory based continuous unitary transformation

HTSE high temperature series expansion

HWHM half-width at half-maximum

INS inelastic neutron scattering

IPA-$CuCl_3$ isopropylammonium trichlorocuprate(II) $(CH_3)_2CHNH_3CuCl_3$

pCUT perturbative continuous unitary transformation

PHCC piperazinium hexachlorodicuprate

ROD residual off-diagonality

sCUT self-similar continuous unitary transformation

SQPD spontaneous quasiparticle decay

Chapter 1

Introduction

A standard approach to calculate electric properties of condensed matter is to treat the electrons as independent particles in a periodic potential induced by the underlying lattice [Ashcroft & Mermin(1976), Czycholl(2004)]. Within this approach interactions between the electrons are completely neglected or at most considered statically within density functional theory. Naturally, phenomena caused by correlations of the electrons due to their interactions can not or only insufficiently be described in this fashion.

Particularly the discovery of high-temperature superconductivity in cuprates by Bednorz and Müller in 1986 [Bednorz & Müller(1986)] illustrates which fascinating and surprising phenomena can be caused by strong correlations and raised the interest in strongly correlated systems. The example of high-temperature superconductivity also shows how challenging theoretical descriptions of systems with strong correlations are. Although Zhang and Rice [Zhang & Rice(1988)] derived an effective model Hamiltonian to describe the high-temperature superconductivity in cuprates already two years after its discovery the exact mechanisms behind this superconductivity is in our days, more than 25 years later, still a subject of ongoing research.

Besides superconductivity also the magnetic properties of insulators, typically described by spin models, can be defined by correlated localized electrons. Especially in low-dimensional quantum spin systems built up by spins with a small spin quantum number S quantum fluctuations are important. Therefore, low-dimensional quantum spin systems display various fascinating properties. Examples are, the spin-Peierls transition [Peierls(1955), Bray *et al.*(1975), Hase *et al.*(1993)], the appearance of a Haldane gap for integer spins [Haldane(1983), Renard *et al.*(1987)], the previously mentioned high-temperature superconductivity upon doping [Bednorz & Müller(1986)], and the Bose-Einstein condensation (BEC) in spin-dimer systems [Affleck(1991), Shiramura *et al.*(1997), Giamarchi & Tsvelik(1999), Garlea *et al.*(2007), Mills(2007)]. The latter one is characterized by a phase transition from a non-magnetic phase to a long range antiferromagnetically ordered gapless phase at some critical magnetic field H_{c_1}. A candidate for such a BEC studied in

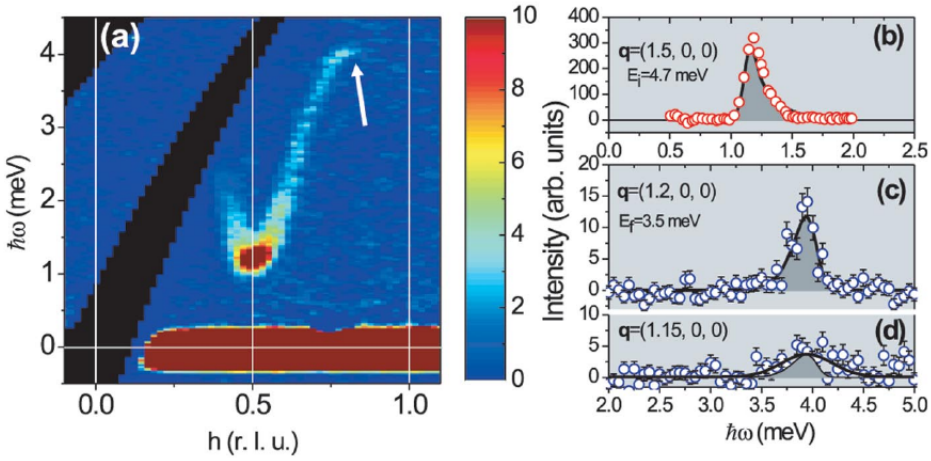

Figure 1.1: Time-of-flight **(a)** and 3-axis **(b)**, **(c)**, **(d)** inelastic neutron data measured in IPA-$CuCl_3$ at T = 1.5K. (Figure and caption are taken from reference [Masuda *et al.*(2006)]).

detail is $TlCuCl_3$ [Nikuni *et al.*(2000), Matsumoto *et al.*(2002), Rüegg *et al.*(2003)]. Unfortunately recent research suggests that the high field spectrum remains gapped [Sirker *et al.*(2005), Johannsen *et al.*(2005)] in contrast to what is expected from a phase where a continuous symmetry is broken. Another promising candidate for a BEC in a spin-dimer system is the quasi one-dimensional compound isopropylammonium trichlorocuprate(II) $(CH_3)_2CHNH_3CuCl_3$, abbreviated by IPA-$CuCl_3$, where inelastic neutron scattering (INS) data indeed imply an almost exact realization of a BEC [Garlea *et al.*(2007), Zheludev *et al.*(2007)].

Beside BEC IPA-$CuCl_3$ shows one further fascinating phenomenom recently observed in low-dimensional antiferromagnets, namely the decay of their elementary excitations [Masuda *et al.*(2006)], see figure 1.1. Although the elementary excitations are protected by a finite gap at low energies they decay at higher energies. Such a quasiparticle breakdown was measured for the first time in the two-dimensional quantum spin $S = 1/2$ system piperazinium hexachlorodicuprate (PHCC) [Stone *et al.*(2006)], see figure 1.2.

The situation is very similar to the quasiparticle decay occurring in superfluid helium II (^{4}He). To describe the superfluidity of helium II Landau postulated a dispersion relation of bosonic elementary excitations which consists of a phonon and a roton part [Landau(1941b), Landau(1941a), Landau(1947), Landau *et al.*(1980)]. Feynman and Cohen showed that the dispersion relation suggested by Landau can be obtained qualitatively by using an appropriate trial wave function [Feynman(1954), Feynman & Cohen(1956)] and they also suggested that the spectrum can be determined by INS [Cohen & Feynman(1957)]. Shortly afterwards, the energy spectrum of helium II was indeed measured by INS [Palevsky *et al.*(1957)] and confirmed Landau's ideas. Two years later Pitaevskii predicted that these quasiparticles can be-

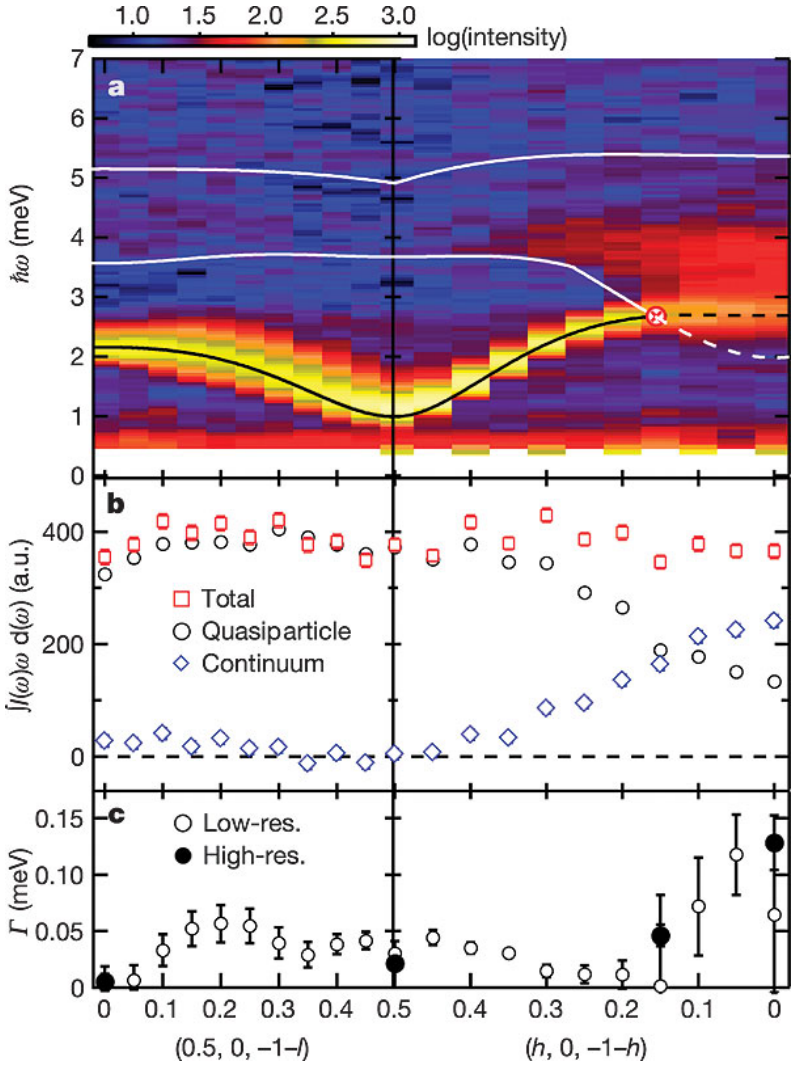

Figure 1.2: Magnetic excitation spectrum at $T = 1.4$K in PHCC. Panel **a**, background-corrected intensity along the $(1/2, 0, -1-l)$ and $(h, 0, -1-h)$ directions. A $\delta\hbar\omega = 0.25$meV running average was applied to each constant wave vector scan, retaining the actual point density of the acquired data. Black line, previously determined single-magnon dispersion [Stone *et al.*(2001)]. White lines, bounds of two-magnon continuum calculated from this dispersion. Red circle with cross, the point where the single-particle dispersion relation intersects the lower bound of the two-particle continuum. Panel **b**, first frequency moment of measured scattering intensity integrated over different energy ranges. Red squares (total), $0.8 \leq \hbar\omega \leq 5.5$meV; black circles (quasiparticle), $0.8 \leq \hbar\omega \leq 3$meV; blue diamonds (continuum), $3 \leq \hbar\omega \leq 5.5$meV. Panel **c**, resolution-corrected HWHM of the lower energy peak throughout the range of wave vector transfer for high resolution (solid points) and low resolution (open points) data. Error bars illustrate systematic error corresponding to 10% uncertainty in the neutron beam collimation used for resolution correction. (Figure and caption are taken from reference [Stone *et al.*(2006)])

come unstable if certain decay channels exist [Pitaevskii(1959), Landau *et al.*(1980)]. The quasiparticles do not survive beyond a certain threshold in momentum space where decay into two rotons is possible. Their spectrum terminates at this threshold. This prediction was confirmed later by INS measurements on superfluid helium II [Smith *et al.*(1977), Fåk & Bossy(1998)].

In PHCC [Stone *et al.*(2006)] and IPA-$CuCl_3$ [Masuda *et al.*(2006)] as well a threshold momentum was observed beyond which the quasiparticle merges with the two-quasiparticle continuum and ceases to exist as well-defined excitation, see figure 1.2 and figure 1.1.

Theoretical descriptions of quasiparticle decay in quantum magnets were given in 2006 by Kolezhuk and Sachdev using Fermi's golden rule to calculate the decay rate [Kolezhuk & Sachdev(2006)] and by Zhitomirsky who used diagrammatic techniques to describe the decay [Zhitomirsky(2006)], cf. chapter 2. Both papers show that elementary excitations in gapped spin systems become unstable if they merge with the two-particle continuum. Spin systems in one and higher dimensions are analyzed to explain the observations in IPA-$CuCl_3$ and in PHCC. For the special case of an asymmetric rung-dimerized spin ladder, Bibikov [Bibikov(2007)] confirmed these results by investigating the bare one- and two-triplon sector by a Bethe ansatz.

Theoretical considerations also predict quasiparticle decay in spin systems on a triangular lattice [Zheng *et al.*(2006a), Zheng *et al.*(2006b), Chernyshev & Zhitomirsky(2009)] and on square lattices in a strong magnetic field [Zhitomirsky & Chernyshev(1999), Syljuåsen(2008), Syromyatnikov(2009), Lüscher & Läuchli(2009), Mourigal *et al.*(2010)], where the elementary excitations are gapless magnons. In the latter case the instability of the one-magnon excitation could be confirmed experimentally in the spin $S = 5/2$ compound $Ba_2MnGe_2O_7$ [Masuda *et al.*(2010)].

Actually, physical systems of unstable quasiparticles are much more common than systems of completely stable quasiparticles. For instance, the quasiparticles occurring in the famous so-called Fermi liquid theory, developed by Landau in the late 1950s for interacting fermionic systems [Landau(1956), Landau(1958), Landau *et al.*(1980)], always have a finite lifetime except at the Fermi energy. All these examples of quasiparticles with finite lifetime show that for a theoretical description and the understanding of many systems in condensed matter physics it is an indispensable task to develop methods that are able to describe systems with unstable quasiparticles.

In the present thesis we introduce and investigate adaptations of the method of continuous unitary transformations (CUTs) to describe systems with quasiparticle decay. The method of CUTs was introduced by Wegner [Wegner(1994)] and independently by Głazek and Wilson [Głazek & Wilson(1993), Głazek & Wilson(1994)] in 1994. Instead of applying a unitary transformation induced by a constant generator to simplify

a given Hamiltonian the CUT performs the unitary transformation in a continuous fashion where the transformation is induced by an infinitesimal generator. Thereby the transformation can adjust itself permanently during its application. To deal with quasiparticles with finite lifetime we modify a generator suggested by KNETTER and UHRIG [Uhrig & Normand(1998), Knetter & Uhrig(2000)]. In its original form this generator creates quasiparticle number conserving effective Hamiltonians. Therefore, the one-particle states are separated from all other states which makes the direct description of quasiparticle decay impossible.

Besides a detailed general discussion of modified generators we illustrate the concept by explicit calculations for asymmetric spin $S = 1/2$ HEISENBERG ladders and for the quasi one-dimensional compound isopropylammonium trichlorocuprate(II) $(CH_3)_2CHNH_3CuCl_3$.

1.1 Thesis Overview

In the following chapter 2 spontaneous quasiparticle decay (SQPD) in gapped one-dimensional quantum systems is discussed on the basis of a toy model. The aim of this chapter is to give a pedagogical introduction to the physics of SQPD independent of all technical details of CUTs and to characterize different decay scenarios depending on the one-particle dispersion and two-particle interactions. We also elaborate differences to the decay occurring in a standard FERMI liquid.

In chapter 3 the concept of CUTs is introduced. Especially, we focus on a new adapted generator introduced to treat SQPD by CUTs. Subsequently, the self-similar realization of CUTs in real-space is described which is used in all following chapters.

In chapter 4 the low energy spectrum of the asymmetric antiferromagnetic spin $S = 1/2$ HEISENBERG ladder (AASHL) is investigated by self-similar continuous unitary transformations (sCUTs). We use this model to illustrate our general considerations of chapter 3 concerning CUTs in systems with unstable quasiparticles. Additionally, results for the dynamical structure factor for the AASHL obtained by sCUTs are presented. This quantity can be experimentally determined by INS.

In chapter 5 results for the dynamical structure factor of the asymmetric ferro-antiferromagnetic spin $S = 1/2$ HEISENBERG ladder (AFASHL) obtained by sCUTs are presented. We show that in this model the SQPD is much more pronounced than in the AASHL due to the larger mobility of the excitations.

In chapter 6 a microscopic model for IPA-$CuCl_3$ is determined by using CUTs and high temperature series expansions (HTSEs). Starting from the derived model we calculate the dynamical structure factor of IPA-$CuCl_3$ by CUTs designed for SQPD. Additionally, we calculate the magnetic field dependence as well as the temperature dependence of the lowest energy modes.

Chapter 2

Introduction to spontaneous quasiparticle decay

In this chapter an introduction to the physics of spontaneous quasiparticle decay (SQPD) in gapped one-dimensional quantum spin systems is given. The word "spontaneous" emphasizes that the decay occurs at zero temperature ($T = 0$) and is *not* caused by thermal fluctuations as discussed, e.g., in references [James *et al.*(2008), Essler & Konik(2008)]. Following Zhitomirsky's general arguments [Zhitomirsky(2006)] the scenario of SQPD is illustrated on a simple one-dimensional bosonic model where in first order all important quantities can be calculated analytically. We want to emphasize that despite its simplicity the model is closely related to the asymmetric spin $S = 1/2$ Heisenberg ladder (cf. chapter 4 and chapter 5) and therefore helps to quantitatively understand the SQPD in this system.

Generically the ground state $|0\rangle$ is given by a spin $S = 0$ singlet and the elementary excitations are given by a triplet of spin $S = 1$ quasiparticles, also called triplons [Schmidt & Uhrig(2003)]. A spin gap Δ separates the singlet energy from the triplet energies and without any intrinsic anisotropies and without an external magnetic field the energy levels of the quasiparticles are threefold degenerate. Qualitatively such a situation can be described in one dimension by the Hamiltonian

$$H_0 = \sum_{\alpha} \sum_{r=0}^{\mathcal{N}-1} \left[t^\dagger_{\alpha,r} t_{\alpha,r} + \frac{\tau}{4} \left(t^\dagger_{\alpha,r} t_{\alpha,r+1} + t^\dagger_{\alpha,r+1} t_{\alpha,r} \right) \right] \tag{2.1}$$

with bosonic operators[1] $t^\dagger_{\alpha,r}$ and $t_{\alpha,r}$ creating and destroying a quasiparticle on site r with a polarization $\alpha \in \{x, y, z\}$. The hopping amplitude is given by $\tau > 0$ and we assume periodic boundary conditions $\left(t^\dagger_{\alpha,\mathcal{N}} = t^\dagger_{\alpha,0} \right)$.

[1] Actually, triplons are represented by hard-core bosons, cf. chapter 4

The Hamiltonian H_0 can easily be diagonalized by a Fourier transformation

$$t^\dagger_{\alpha,r} := \frac{1}{\sqrt{\mathcal{N}}} \sum_Q \mathrm{e}^{\mathrm{i}Qr}\, b^\dagger_{\alpha,Q} \tag{2.2a}$$

$$t_{\alpha,r} := \frac{1}{\sqrt{\mathcal{N}}} \sum_Q \mathrm{e}^{-\mathrm{i}Qr}\, b_{\alpha,Q} \tag{2.2b}$$

with bosonic operators $b^\dagger_{\alpha,r}$ and $b_{\alpha,r}$. The sum $\sum_Q$ runs over all $Q_n = \frac{2\pi n}{\mathcal{N}}$ with $n = 0,\ldots,\mathcal{N}-1$. Then the Hamiltonian H_0 is given by

$$H_0 = \sum_\alpha \sum_Q \omega_1(Q)\, b^\dagger_{\alpha,Q} b_{\alpha,Q} \tag{2.3}$$

with the one-particle dispersion

$$\omega_1(Q) = 1 + \frac{\tau}{2}\cos(Q)\,. \tag{2.4}$$

To ensure the existence of a gap the hopping amplitude τ must be smaller than two ($\tau < 2$). We also demand that $\tau > 0$ so that the minimum of the gap Δ is located at the momentum $Q = \pi$.

Besides the one-particle energy spectrum $\omega_1(Q)$ it is also possible to calculate the energy spectrum of states consisting of two particles. The two-particle continuum is defined by

$$\omega_2(Q,q) := \omega_1\left(Q/2+q\right) + \omega_1\left(Q/2-q\right) \tag{2.5a}$$

$$= 2 + \tau\cos\left(Q/2\right)\cos\left(q\right) \tag{2.5b}$$

with total momentum Q and relative momentum q. It is completely determined by one-particle properties, namely the one-particle dispersion $\omega_1(Q)$. The upper edge of the two-particle continuum is given by $\max_{q\in[-\pi,\pi]}\omega_2(Q,q) = 2 + \tau\cos\left(Q/2\right)$ and the lower edge by $\min_{q\in[-\pi,\pi]}\omega_2(Q,q) = 2 - \tau\cos\left(Q/2\right)$. For total momentum $Q = -\pi$ and $Q = \pi$ respectively the upper edge and the lower edge have the same value, so that at this particular momentum no real continuum exists. This is due to the simplicity of the model which only considers nearest neighbor hopping. Figure 2.1 shows the one-particle dispersion $\omega_1(Q)$ and the two-particle continuum $\omega_2(Q,q)$ for $\tau = 1.0$.

From

$$\frac{\partial\omega_2(Q,q)}{\partial q} = v_1\left(Q/2+q\right) - v_1\left(Q/2-q\right) \tag{2.6}$$

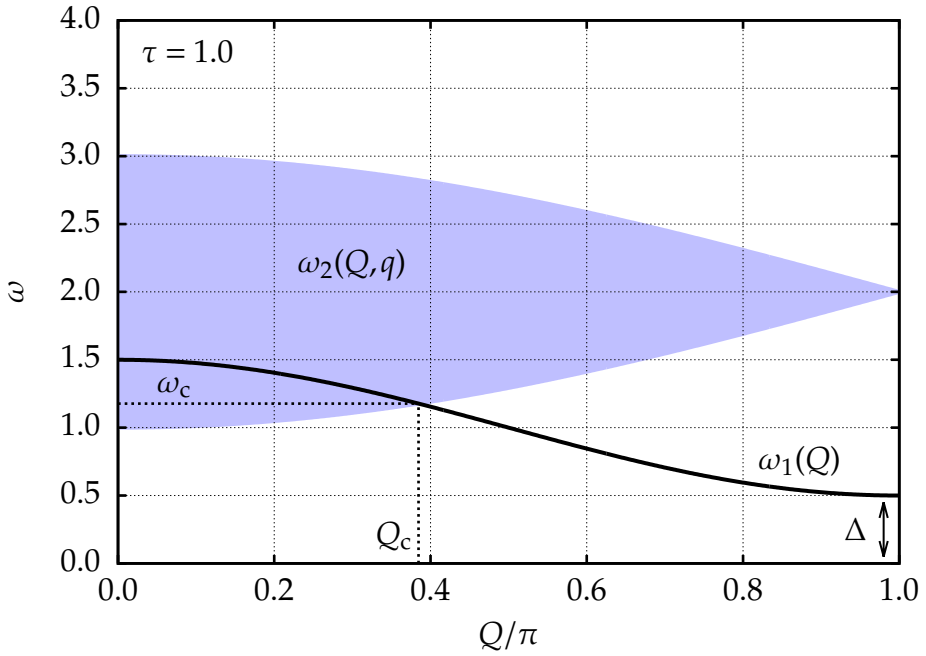

Figure 2.1: One-particle dispersion $\omega_1(Q)$ and two-particle continuum $\omega_2(Q,q)$ for $\tau = 1.0$. For momenta Q smaller than the decay threshold momentum Q_c spontaneous quasiparticle decay is possible.

with the spin group velocity

$$v_1(Q) := \frac{\partial \omega_1(Q)}{\partial Q} \tag{2.7a}$$

$$= -\frac{\tau}{2}\sin(Q)\,. \tag{2.7b}$$

follows that at the edges of the continuum, where $\omega_2(Q,q)$ becomes extremal with respect to q, the two quasiparticles have the same velocity because $\frac{\partial \omega_2(Q,q)}{\partial q} = 0$.

To allow SQPD one important prerequisite of the energy spectrum is that the one-particle dispersion merges with the two particle continuum, e.g. the equation

$$\omega_1(Q) = \omega_2(Q,q) \tag{2.8}$$

can be satisfied. The intersection point of the one-particle dispersion and the lower edge of the two-particle continuum defines the decay threshold momentum Q_c, so that the equation

$$\omega_c := \omega_1(Q_c) = \min_{q\in[-\pi,\pi]} \omega_2(Q_c,q) \tag{2.9}$$

holds, cf. figure 2.1. In the present model the decay threshold momentum Q_c is given

by

$$Q_c = 2\arccos\left(\frac{-\tau + \sqrt{3\tau^2 + 4\tau}}{2\tau}\right). \tag{2.10}$$

The second important ingredient to make SQPD possible is the existence of a decay vertex so that decay of the one-particle mode into the continuum is possible. In Heisenberg spin systems the decay term typically has the form (cf. chapter 4 and chapter 5)

$$H_1 = \frac{\lambda\tau}{4} \sum_{\alpha,\beta,\gamma} \sum_{r=0}^{N-1} \mathrm{i}\, \varepsilon_{\alpha\beta\gamma}\, t^\dagger_{\alpha,r} t^\dagger_{\beta,r+1} \left(t_{\gamma,r} + t_{\gamma,r+1}\right) + \text{H.c.}\,. \tag{2.11}$$

The antisymmetric tensor $\varepsilon_{\alpha\beta\gamma}$ assures that one quasiparticle decays in an antisymmetric two-quasiparticle state. Thus the total spin is conserved during the decay process so that the two created spin $S = 1$ quasiparticles form a $S = 1$ state.

Fourier transformation (2.2) of (2.11) leads to

$$H_1 = \frac{1}{2\sqrt{N}} \sum_{\alpha,\beta,\gamma} \sum_{Q,q} \varepsilon_{\alpha\beta\gamma}\, \Gamma_1(Q,q)\, b^\dagger_{\alpha,Q/2+q} b^\dagger_{\beta,Q/2-q} b_{\gamma,Q} + \text{H.c.} \tag{2.12}$$

with

$$\Gamma_1(Q,q) = \lambda\tau \sin(q) \cos(Q/2)\,. \tag{2.13}$$

Note, that $\Gamma_1(Q,q) = -\Gamma_1(Q,-q)$. This property is a consequence of conserving the total spin during the decay process and the associated appearance of the antisymmetric tensor $\varepsilon_{\alpha\beta\gamma}$.

To describe SQPD we calculate the effect of the decay processes on the self-energy $\Sigma(Q,\omega)$. Considering the second-order contribution of the decay processes (2.12) to the

self-energy $\Sigma(Q,\omega)$ yields

$$\Sigma(Q,\omega) = \quad (2.14a)$$

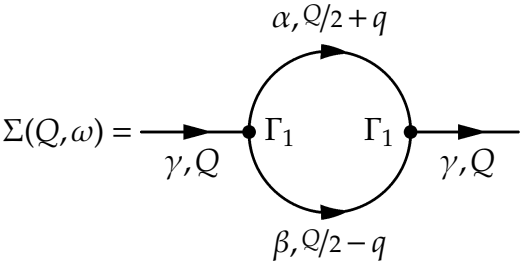

$$= \lim_{\delta\to 0^+} \frac{1}{2\pi} \int_{-\pi}^{\pi} \frac{\Gamma_1^2(Q,q)}{\omega - \omega_2(Q,q) + \mathrm{i}\delta}\,\mathrm{d}q\,. \quad (2.14b)$$

The imaginary part of the self-energy $\Sigma(Q,\omega)$ is given by

$$\mathrm{Im}\,\Sigma(Q,\omega) = -\frac{(\lambda\tau)^2}{2}\cos^2(Q/2)\int_{-\pi}^{\pi}\sin^2(q)\delta(\omega-\omega_2(Q,q))\,\mathrm{d}q \quad (2.15a)$$

$$= \begin{cases} -\lambda^2\left[(\tau\cos(Q/2))^2 - (\omega-2)^2\right]^{1/2} & \text{if } |\omega-2| \le \tau\cos(Q/2) \\ 0 & \text{if } |\omega-2| > \tau\cos(Q/2) \end{cases} \quad (2.15b)$$

and the real part of the self-energy $\Sigma(Q,\omega)$ calculated by Kramers-Kronig relation results in

$$\mathrm{Re}\,\Sigma(Q,\omega) = \frac{1}{\pi}\fint_{-\infty}^{\infty}\frac{\mathrm{Im}\,\Sigma(Q,x)}{x-\omega}\,\mathrm{d}x \quad (2.16a)$$

$$= \frac{1}{\pi}\fint_{2-\tau\cos(Q/2)}^{2+\tau\cos(Q/2)}\frac{\mathrm{Im}\,\Sigma(Q,x)}{x-\omega}\,\mathrm{d}x \quad (2.16b)$$

$$= \begin{cases} \lambda^2(\omega-2) & \text{if } |\omega-2| \le \tau\cos(Q/2) \\ \lambda^2(\omega-2)\left(1-\left[1-\left(\frac{\tau\cos(Q/2)}{\omega-2}\right)^2\right]^{1/2}\right) & \text{if } |\omega-2| > \tau\cos(Q/2) \end{cases}. \quad (2.16c)$$

The integral occurring in equation (2.16) can be found in reference [Bronstein *et al.*(2001)]. Figure 2.2 illustrates the self-energy $\Sigma(Q,\omega)$ for $\tau = 1.0$ and $\lambda = 1.0$.

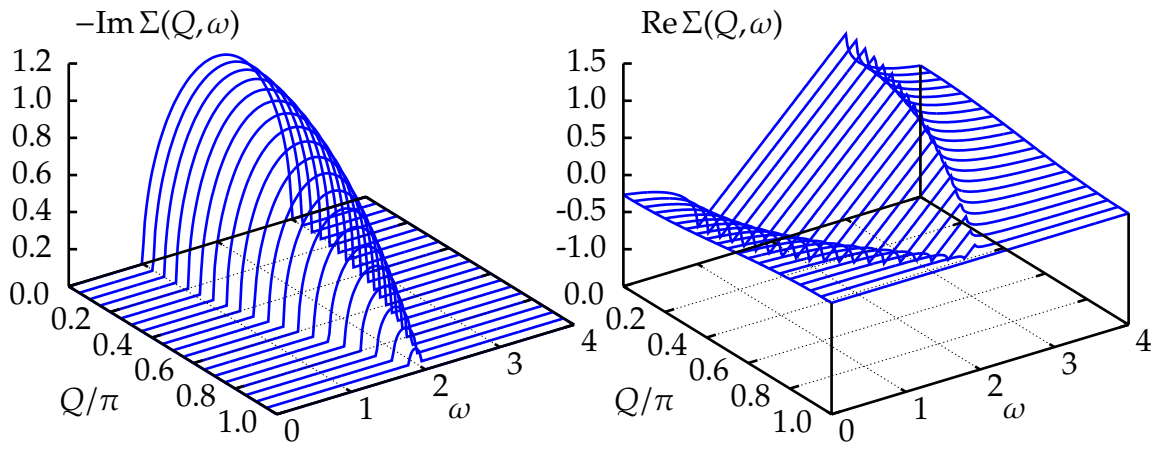

Figure 2.2: Real and imaginary part of the self-energy $\Sigma(Q,\omega)$ for $\tau = 1.0$ and $\lambda = 1.0$.

2.1 Stable region

We follow the analysis of Zhitomirsky [Zhitomirsky(2006)] and start our discussion in the stable region of the single quasiparticle, where spontaneous decay is forbidden. Defining the renormalized one-particle dispersion $\omega_{1,\mathrm{r}}(Q)$ implicitly by the poles of the complete one-particle Green function $\mathcal{G}(Q,\omega)$, given by Dyson's equation, leads to

$$\mathcal{G}^{-1}(Q,\omega) = \omega - \omega_1(Q) - \Sigma(Q,\omega) = 0\,. \tag{2.17}$$

Squaring equation (2.17) and solving the resulting quadratic equation yields the two solutions[2]

$$\begin{aligned}\omega_{+/-}(Q) = &\frac{1}{1-2\lambda^2}\Bigg(1-3\lambda^2-\frac{\tau}{2}+\frac{\lambda^2\tau}{2}+\Big[\tau-\lambda^2\tau\Big]\cos^2(Q/2)\\ &\pm\lambda^2\left[\left(1+\frac{\tau}{2}\right)^2-2\Big(\tau+\tau^2-\lambda^2\tau^2\Big)\cos^2(Q/2)+\tau^2\cos^4(Q/2)\right]^{1/2}\Bigg)\,.\end{aligned} \tag{2.18}$$

This result holds independently whether one is considering the region where spontaneous quasiparticle decay is allowed or the region where decay is forbidden. Note, that $\omega_{+/-}(Q)$ are the solutions of the quadratic equation. They are not necessarily solutions of equation (2.17).

In the generic case, the solutions $\omega_{+/-}(Q)$ become complex for $Q < Q_0$, where Q_0 is given by the root of the radicand

$$0 = \left(1+\frac{\tau}{2}\right)^2-2\Big(\tau+\tau^2-\lambda^2\tau^2\Big)\cos^2(Q/2)+\tau^2\cos^4(Q/2)\,. \tag{2.19}$$

[2]Note, that for $\lambda^2 = 1/2$ the solutions diverge. For the description of SQPD the interval $\lambda^2 < 1/2$ is relevant. For completeness we now and then discuss values $\lambda^2 > 1/2$, too.

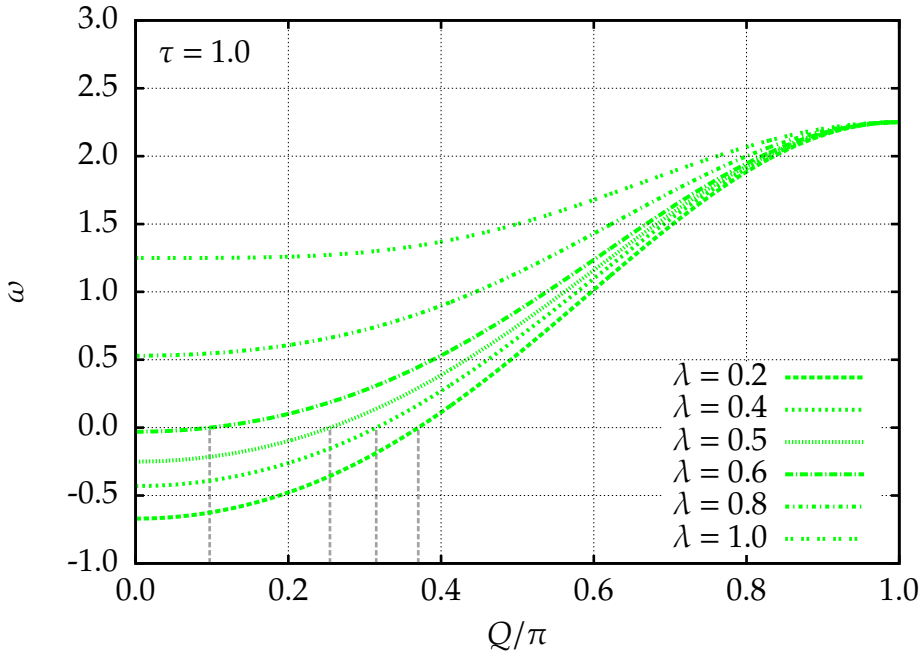

Figure 2.3: Radicand of the square root in $\omega_{+/-}(Q)$ for $\tau = 1.0$. The radicand is negative in the region $Q < Q_0$ for $\lambda = 0.2, 0.4, 0.5, 0.6$. The dotted grey lines indicate the respective Q_0.

Figure 2.3 shows the right hand side of (2.19) for $\tau = 1.0$ and various values of λ. For $\lambda = 0.2, 0.4, 0.5, 0.6$ and $Q < Q_0$ the function (2.19) is negative and therefore the two solutions $\omega_{+/-}(Q)$ become complex. Thus we restrict our analysis to the case $Q \geq Q_0$. For $\lambda = 0.8, 1.0$ no root appears and the two solutions $\omega_{+/-}(Q)$ stay real for all momenta Q.

As mentioned before, $\omega_{+/-}(Q)$ are solutions of the quadratic equation obtained by squaring equation (2.17). For $\tau = 1.0$ and $\lambda = 0.5$ these solutions are depicted in figure 2.4a. Both solutions satisfy $\omega_{+/-}(Q) - 2 \leq \tau \cos(Q/2)$ so that the self-energy $\Sigma\left(Q, \omega_{+/-}(Q)\right)$ has no imaginary part for $Q \geq Q_0$. To check whether the solutions $\omega_{+/-}(Q)$ solve equation (2.17) or not we calculate $\omega_{+/-}(Q) - \omega_1(Q) - \Sigma\left(Q, \omega_{+/-}(Q)\right)$. The results are shown in figure 2.4b. Obviously, only $\omega_+(Q)$ satisfies equation (2.17) for $Q \geq Q_{c,r}$ where $Q_{c,r}$ is defined by

$$\omega_+(Q_{c,r}) = \min_{q \in [-\pi, \pi]} \omega_2(Q_{c,r}, q) \tag{2.20}$$

and explicitly given by

$$Q_{c,r} = 2 \arccos\left(\frac{\lambda^2 - 1}{2} + \frac{1}{2\tau} \left[\left(\lambda^4 - 2\lambda^2 + 3 \right) \tau^2 + 4\tau \right]^{1/2} \right) . \tag{2.21}$$

Therefore, we define the renormalized one-particle dispersion $\omega_{1,r}(Q)$ outside the two-

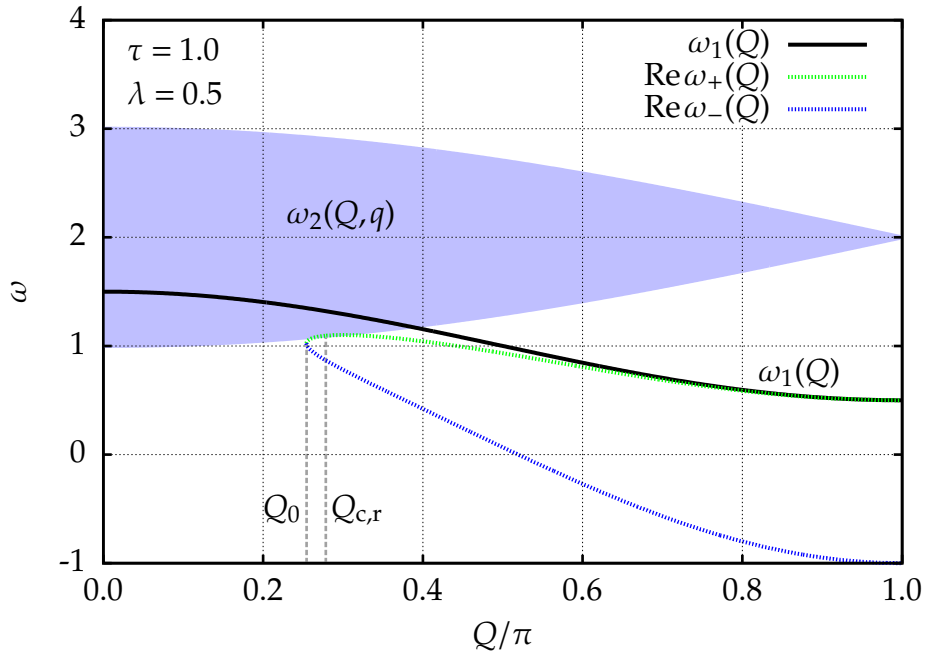

(a) Solutions $\omega_{+/-}(Q)$ for $\tau = 1.0$ and $\lambda = 0.5$. Only $\omega_+(Q)$ for $Q \geq Q_{c,r}$ satisfies equation (2.17).

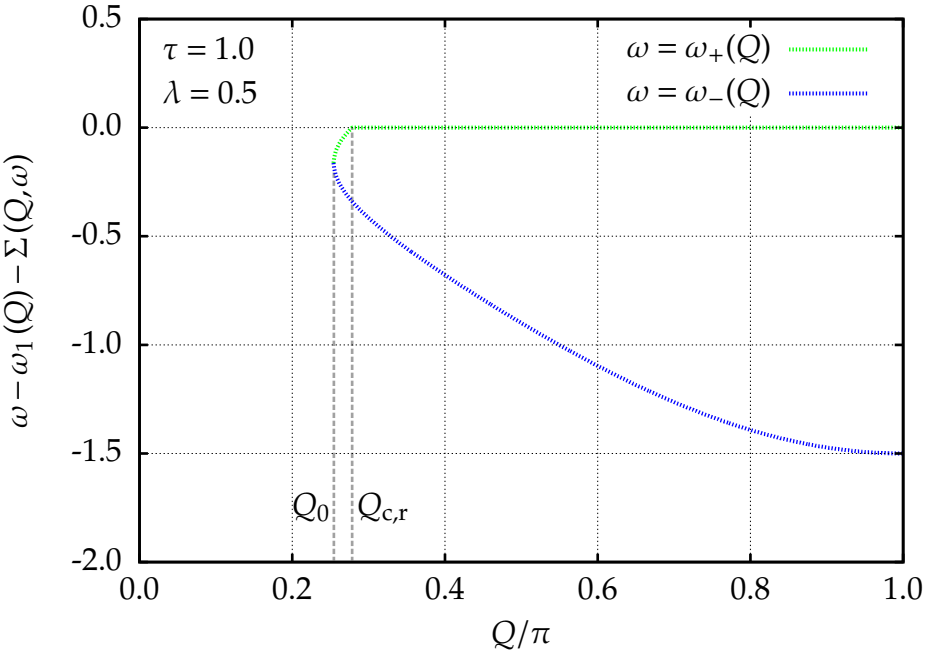

(b) Results for $\omega_{+/-}(Q) - \omega_1(Q) - \Sigma\left(Q, \omega_{+/-}(Q)\right)$ for $\tau = 1.0$ and $\lambda = 0.5$. Only $\omega_+(Q)$ for $Q \geq Q_{c,r}$ satisfies equation (2.17).

Figure 2.4: Results for $\tau = 1.0$ and $\lambda = 0.5$.

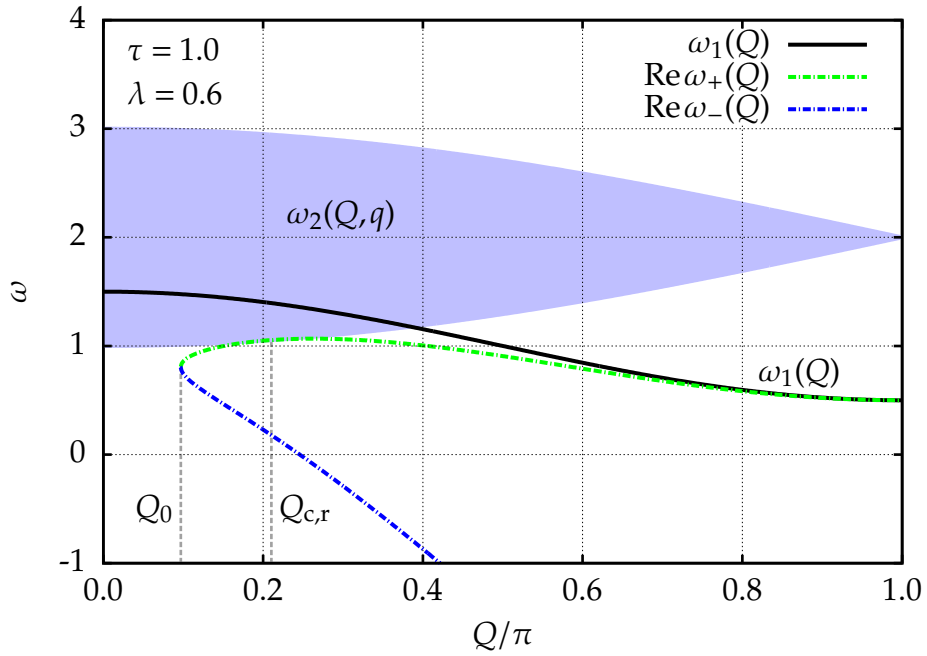

(a) Solutions $\omega_{+/-}(Q)$ for $\tau = 1.0$ and $\lambda = 0.6$. Only $\omega_+(Q)$ for $Q \geq Q_{c,r}$ satisfies equation (2.17).

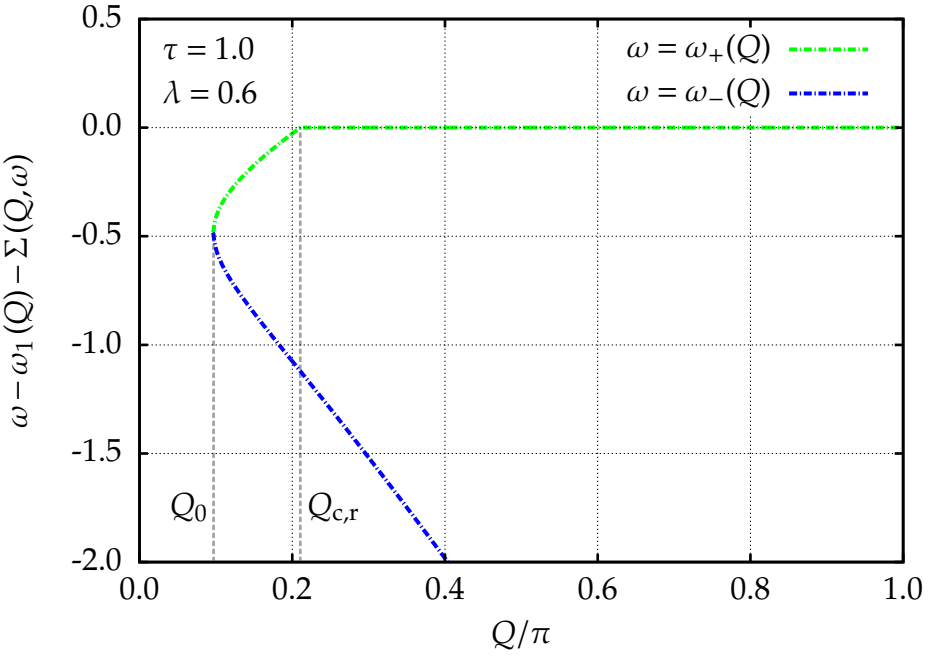

(b) Results for $\omega_{+/-}(Q) - \omega_1(Q) - \Sigma\left(Q, \omega_{+/-}(Q)\right)$ for $\tau = 1.0$ and $\lambda = 0.6$. Only $\omega_+(Q)$ for $Q \geq Q_{c,r}$ satisfies equation (2.17).

Figure 2.5: Results for $\tau = 1.0$ and $\lambda = 0.6$.

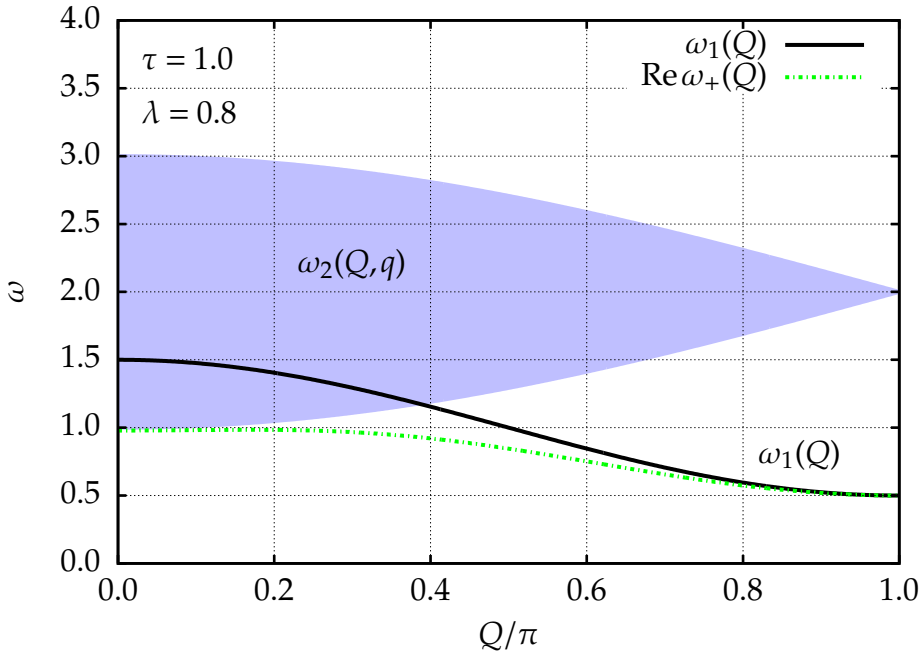

Figure 2.6: Solution $\omega_+(Q)$ for $\tau = 1.0$ and $\lambda = 0.8$.

particle continuum by

$$\omega_{1,\mathrm{r}}(Q) := \omega_+(Q) \quad \text{for} \quad Q \geq Q_{\mathrm{c,r}} \,. \tag{2.22}$$

Interestingly, no solution of equation (2.17) exists between Q_0 and $Q_{\mathrm{c,r}}$.

In figure 2.5a and figure 2.5b the same quantities as before are depicted for $\tau = 1.0$ and $\lambda = 0.6$. Qualitatively nothing changes to the case with $\lambda = 0.5$. The higher value of λ only shifts both momenta Q_0 and $Q_{\mathrm{c,r}}$ to lower values and pushes them apart at the same time, so that the interval, where no solution of equation (2.17) exists, grows.

For $\tau = 1.0$ and $\lambda = 0.8$ the situation changes qualitatively as shown in figure 2.6. The solution $\omega_+(Q)$ satisfies equation (2.17) for all momenta Q.

The next quantity we want to discuss is the spin velocity

$$v_{1,\mathrm{r}}(Q) := \frac{\partial \omega_{1,\mathrm{r}}(Q)}{\partial Q} \quad \text{for} \quad Q \geq Q_0 \tag{2.23a}$$

$$= \frac{\partial \omega_+(Q)}{\partial Q} \quad \text{for} \quad Q \geq Q_0 \tag{2.23b}$$

of the renormalized quasiparticle. Particularly, the behavior of $v_{1,\mathrm{r}}(Q)$ at the momentum $Q_{\mathrm{c,r}}$ where the renormalized one-particle dispersion $\omega_{1,\mathrm{r}}(Q)$ merges with the two-particle continuum $\omega_2(Q,q)$ is of interest. In figure 2.7 the difference of the spin velocity of the renormalized quasiparticle $v_{1,\mathrm{r}}(Q)$ and the velocity of the lower edge of the

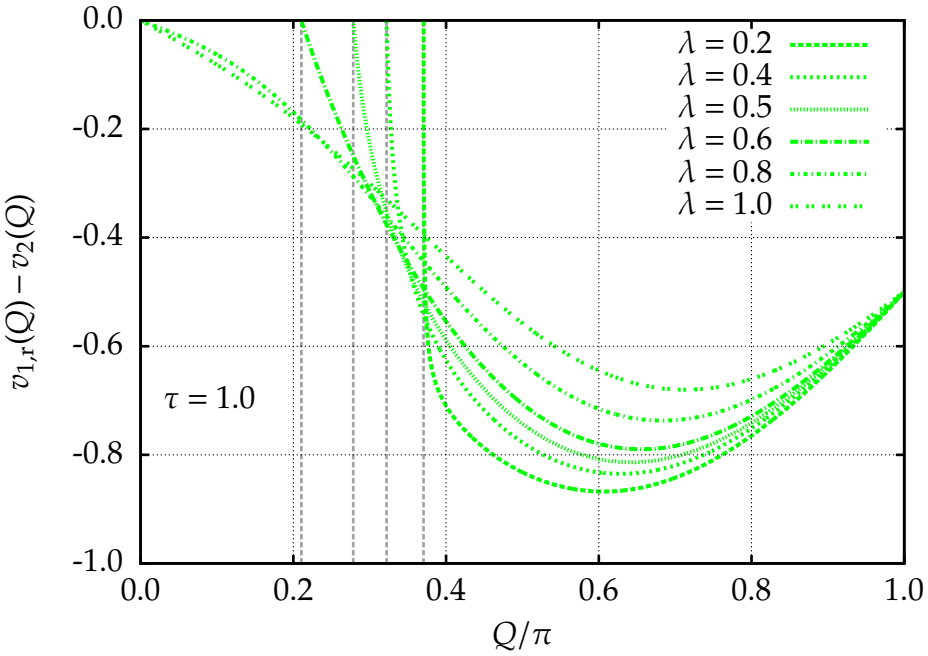

Figure 2.7: Difference of the spin velocity of the renormalized quasiparticle $v_{1,r}(Q)$ and the velocity of the lower edge of the continuum $v_2(Q)$ for $\tau = 1.0$ and various values λ. Since this difference vanishes at $Q_{c,r}$, for $\lambda = 0.2, 0.4, 0.5, 0.6$ the renormalized one-particle branch approaches tangentially the boundary of the two-particle continuum. Dotted grey lines indicate the respective $Q_{c,r}$.

continuum

$$v_2(Q) := \frac{\partial}{\partial Q}\left(\min_{q\in[-\pi,\pi]} \omega_2(Q,q)\right) \tag{2.24a}$$

$$= \frac{\tau}{2}\sin(Q/2) \tag{2.24b}$$

is depicted for $\tau = 1.0$ and different values λ. For $\lambda = 0.2, 0.4, 0.5, 0.6$ the difference vanishes at $Q_{c,r}$. Hence the renormalized one-particle branch approaches tangentially the boundary of the two-particle continuum.

Finally, we want to discuss the quasiparticle weight $Z(Q)$ with

$$Z^{-1}(Q) := \left.\frac{\partial G^{-1}(Q,\omega)}{\partial \omega}\right|_{\omega=\omega_{1,r}(Q)}. \tag{2.25}$$

Figure 2.8 shows the quasiparticle weight $Z(Q)$ for $\tau = 1.0$ and various values λ. For $\lambda = 0.2, 0.4, 0.5, 0.6$ the weight $Z(Q)$ is continuously suppressed and vanishes at $Q_{c,r}$, while for $\lambda = 0.8, 1.0$, where no $Q_{c,r}$ exists, the weight shrinks for smaller Q but never vanishes.

All results of this section quantitatively coincide with the results of Zhitomirsky [Zhitomirsky(2006)] who showed by a linearization around $Q_{c,r}$ that close to $Q_{c,r}$ the

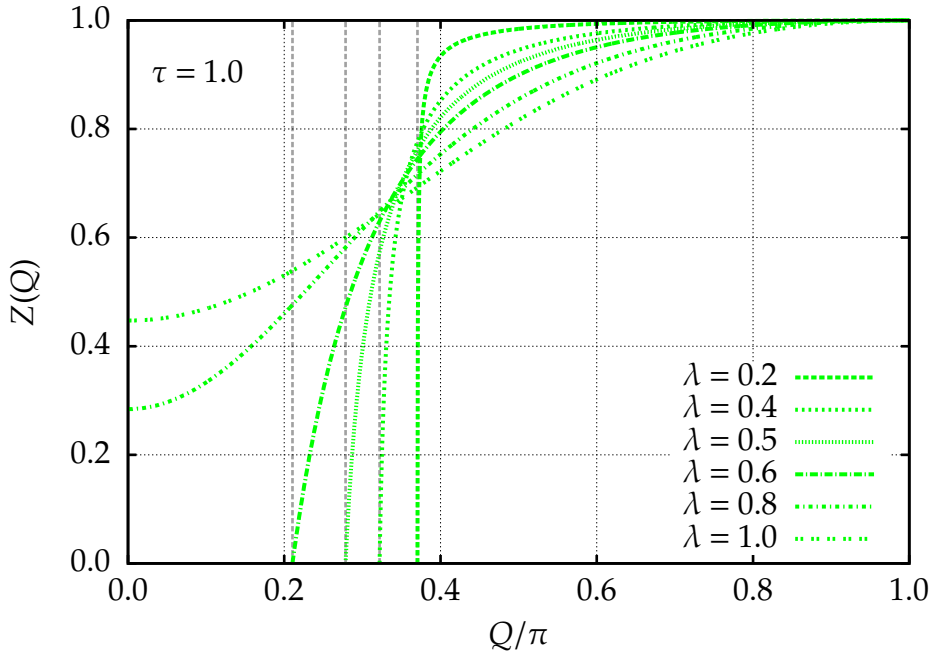

Figure 2.8: Quasiparticle weight $Z(Q)$ for $\tau = 1.0$ and variant values λ. For $\lambda = 0.2$, 0.4, 0.5, 0.6 the weight $Z(Q)$ is continuously suppressed and vanishes at $Q_{c,r}$. Dotted grey lines indicate the respective $Q_{c,r}$.

quasiparticle weight Z is continuously suppressed and vanishes completely at $Q_{c,r}$, where the one-particle branch merges with the two-particle continuum. In addition, Zhitomirsky [Zhitomirsky(2006)] stated that the one-particle branch terminates at the continuum boundary. This corresponds to the fact that typically a region ($Q_0 < Q < Q_{c,r}$) exists where no solution of equation (2.17) can be found. This can be interpreted as quasiparticle breakdown. Nevertheless, the question, what happens inside the continuum, remains. It could be possible that the spectral density $\rho(Q,\omega)$ has still a marked peak inside the continuum which vanishes gradually. In this case one would rather speak of a decay than a breakdown. Therefore, in the next section 2.2 we discuss results for the spectral density $\rho(Q,\omega)$.

2.2 Unstable region

Inelastic neutron scattering INS experiments typically measure the dynamical structure factor $S^{\alpha\beta}(Q,\omega)$ (cf. chapter F). For the discussed model (cf. equation (2.1) and equation (2.11)) the dynamical structure factor $S^{\alpha\beta}(Q,\omega)$ corresponds to the spectral density $\rho(Q,\omega)$ which we now discuss in detail.

In the region where decay is possible, the self-energy is complex and the spectral

density $\rho(Q,\omega)$ is given by

$$\rho(Q,\omega) = -\frac{1}{\pi}\operatorname{Im}\mathcal{G}(Q,\omega) \tag{2.26a}$$

$$= -\frac{1}{\pi}\frac{\operatorname{Im}\Sigma(Q,\omega)}{\big(\omega-\omega_1(Q)-\operatorname{Re}\Sigma(Q,\omega)\big)^2+\big(\operatorname{Im}\Sigma(Q,\omega)\big)^2}\,. \tag{2.26b}$$

Referring to a Lorentz distribution one can define the energy of the quasiparticle by

$$\omega-\omega_1(Q)-\operatorname{Re}\Sigma(Q,\omega)=0 \tag{2.27}$$

and interpret the imaginary part of the self-energy $\operatorname{Im}\Sigma(Q,\omega)$ as the inverse lifetime of the quasiparticle. It roughly determines the width of the quasiparticle resonance.

Solving equation (2.27) for $|\omega-2| \leq |\tau\cos(Q/2)|$ yields

$$\omega_{1,\mathrm{r}}(Q) = \frac{1-2\lambda^2+\frac{\tau}{2}\cos(Q)}{1-\lambda^2}\,. \tag{2.28}$$

Therefore, the renormalized one-particle dispersion for the total Brillouin zone is given by

$$\omega_{1,\mathrm{r}}(Q) = \begin{cases} \frac{1-2\lambda^2+\frac{\tau}{2}\cos(Q)}{1-\lambda^2} & \text{if } Q < Q_{\mathrm{c,r}} \\ \omega_+(Q) & \text{if } Q \geq Q_{\mathrm{c,r}} \end{cases}\,. \tag{2.29}$$

Note that both definitions meet continuously at $Q_{\mathrm{c,r}}$.

In figure 2.9 the renormalized one-particle dispersion $\omega_{1,\mathrm{r}}(Q)$ for $\tau = 1$ and various values λ is presented. Of course, for $\lambda = 0.0$ no renormalization takes place so that equation $\omega_{1,\mathrm{r}}(Q) = \omega_1(Q)$ holds. For $\lambda = 0.8$ and $\lambda = 1.0$ the renormalized one-particle dispersion lies below the two-particle continuum $\omega_2(Q,q)$. In contrast to equation (2.17) a solution of equation (2.27) exists for all momenta Q. If one only considers the real part of the self-energy $\operatorname{Re}\Sigma(Q,\omega)$ to define the position of the quasiparticle, the position of the quasiparticle is well-defined for the whole Brillouin zone. There is no reason to assume a breakdown of the quasiparticle picture on the basis of equation (2.27).

Previously, it was shown that the one-particle branch in the stable region $Q \geq Q_{\mathrm{c,r}}$ approaches tangentially the boundary of the two-particle continuum (cf. figure 2.7). Figure 2.10 depicts the angle φ under which the one-particle dispersion $\omega_{1,\mathrm{r}}(Q)$ (2.28) inside the continuum $Q < Q_{\mathrm{c,r}}$ touches the lower edge of the two-particle continuum as a function of the parameters λ and τ. Formally, the angle φ is defined by

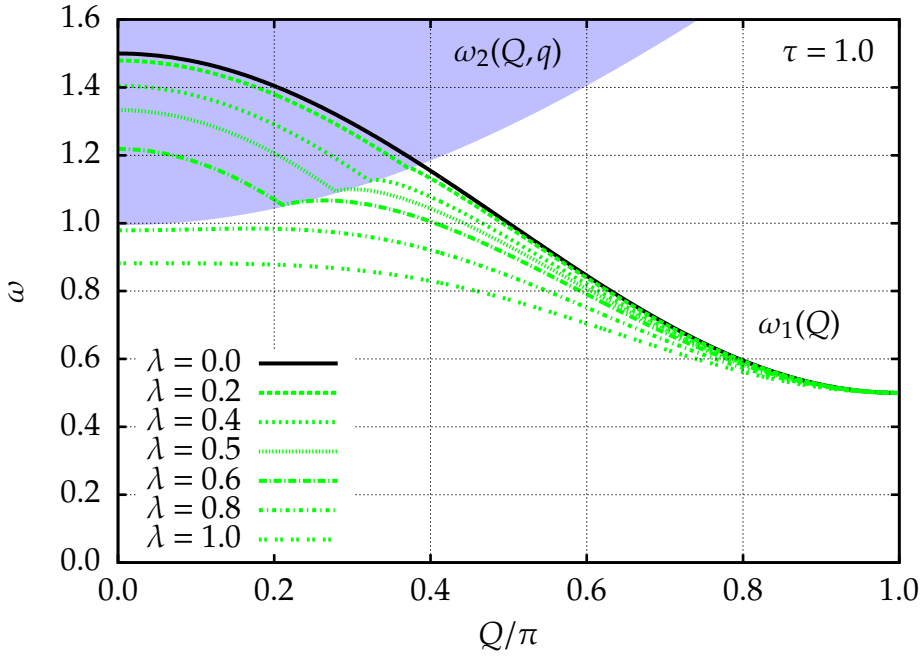

Figure 2.9: Renormalized one-particle dispersion $\omega_{1,\mathrm{r}}(Q)$ for $\tau = 1.0$ and various values λ. For $\lambda = 0.0$ no renormalization takes place.

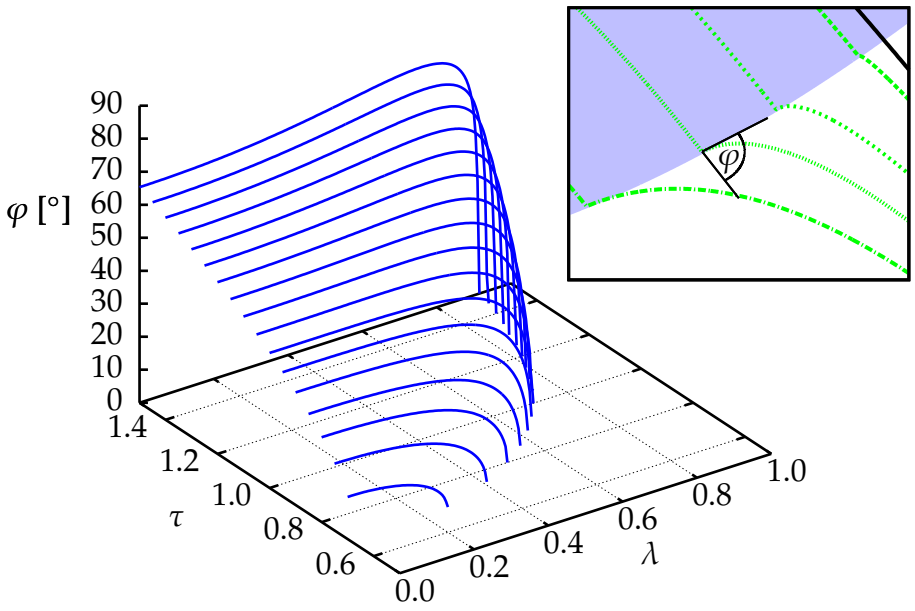

Figure 2.10: Angle φ under which the one-particle dispersion $\omega_{1,\mathrm{r}}(Q)$ (2.28) inside the continuum $Q < Q_{\mathrm{c,r}}$ touches the lower edge of the two-particle continuum as a function of the parameters λ and τ. For the definition of φ see inset and equation (2.30a).

$$\varphi := \arctan\left(v_2(Q_{c,r})\right) - \arctan\left(\lim_{Q\to Q_{c,r}^-}\left[\frac{\omega_{1,r}(Q)-\omega_{1,r}(Q_{c,r})}{Q-Q_{c,r}}\right]\right) \tag{2.30a}$$

$$= \arctan\left(\lim_{Q\to Q_{c,r}^+}\left[\frac{\omega_{1,r}(Q)-\omega_{1,r}(Q_{c,r})}{Q-Q_{c,r}}\right]\right) - \arctan\left(\lim_{Q\to Q_{c,r}^-}\left[\frac{\omega_{1,r}(Q)-\omega_{1,r}(Q_{c,r})}{Q-Q_{c,r}}\right]\right) \tag{2.30b}$$

and depends on the values of λ and τ as shown in figure 2.10. The situation is different from the situation outside the two-particle continuum, where the one-particle dispersion merges wiht the two-particle continuum for all values λ under the same angle zero.

Figure 2.11a, figure 2.11b and figure 2.11c depict the spectral density $\rho(Q,\omega)$ for $\tau = 1.0$ and $\lambda = 0.2$, 0.5 and 0.6. As expected, the spectral density becomes broader for larger λ. Nevertheless, a distinct correlation between the maximum of the spectral density $\rho(Q,\omega)$ and the energy of the quasiparticle defined by equation (2.27) exists and even for $\lambda = 0.6$ an obvious peak in the spectral density $\rho(Q,\omega)$ near $Q_{c,r}$ is present.

In the prototype model for the quasiparticle concept, the standard Fermi liquid in two or three dimensions [Landau(1956), Landau(1958), Landau *et al.*(1980)] , the decay of the quasiparticles is typically characterized by their width relative to their excitation energy [Nozières & Pines(1999), Uhrig(2005)]. The width behaves like $(\epsilon(\mathbf{Q})-\epsilon_F)^2$ with the dispersion relation $\epsilon(\mathbf{Q})$ and the Fermi energy ϵ_F. Thus the width relative to the excitation energy $|\epsilon(\mathbf{Q})-\epsilon_F|$ is proportional to

$$\frac{(\epsilon(\mathbf{Q})-\epsilon_F)^2}{|\epsilon(\mathbf{Q})-\epsilon_F|} = |\epsilon(\mathbf{Q})-\epsilon_F| \,. \tag{2.31}$$

This quantity vanishes if the energy $\epsilon(\mathbf{Q})$ approaches the Fermi energy ϵ_F. Therefore, close to the Fermi surface the quasiparticle width decreases faster than their excitation energy. In this sense quasiparticles are well-defined.

Analogously , we want to discuss the ratio between the width or inverse lifetime of the renormalized quasiparticle

$$\gamma(Q) := -\operatorname{Im}\Sigma\left(Q,\omega_{1,r}(Q)\right) \quad \text{for} \quad Q \le Q_{c,r} \tag{2.32}$$

depicted in figure 2.12 and the distance of the renormalized quasiparticle to the lower edge of the two-particle continuum

$$\delta(Q) := \omega_{1,r}(Q) - \min_{q\in[-\pi,\pi]}\omega_2(Q,q) \quad \text{for} \quad Q \le Q_{c,r} \,. \tag{2.33}$$

A short calculation yields

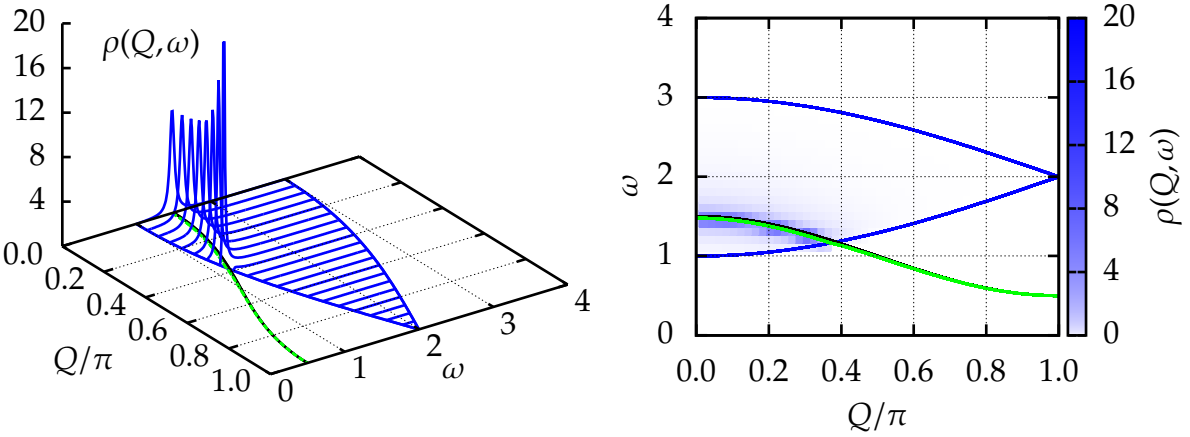

(a) $\lambda = 0.2$

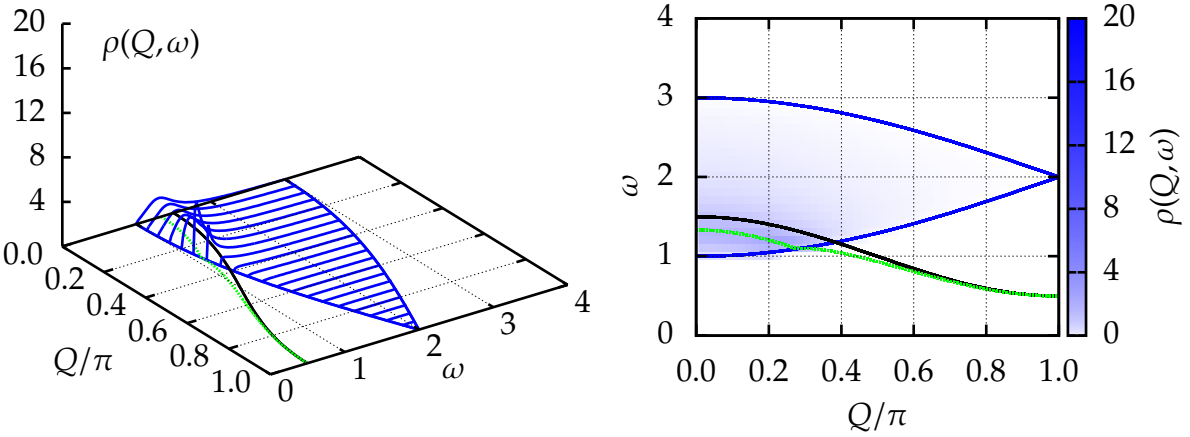

(b) $\lambda = 0.5$

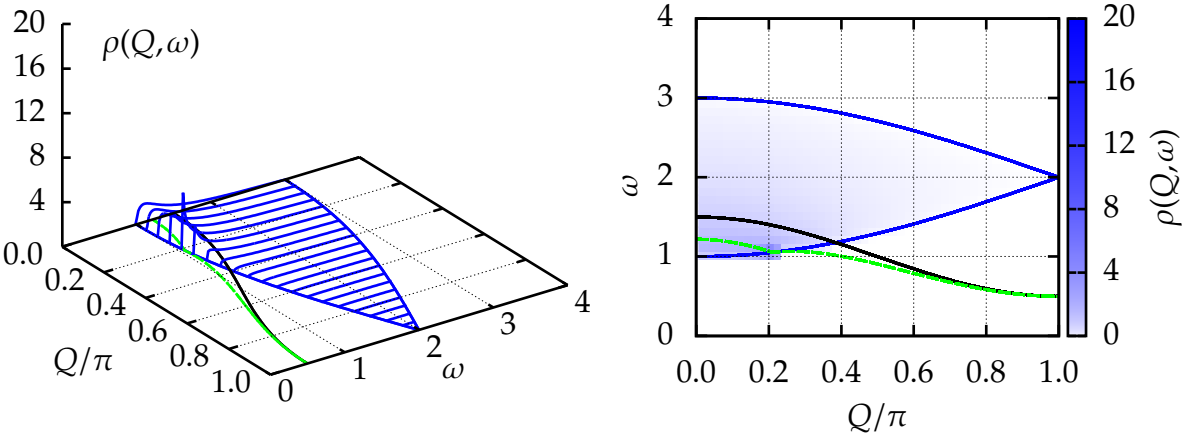

(c) $\lambda = 0.6$

Figure 2.11: Spectral density $\rho(Q,\omega)$ for $\tau = 1.0$ and various values λ. Black lines indicate $\omega_1(Q)$. Green lines indicate the renormalized one-particle dispersions $\omega_{1,r}(Q)$.

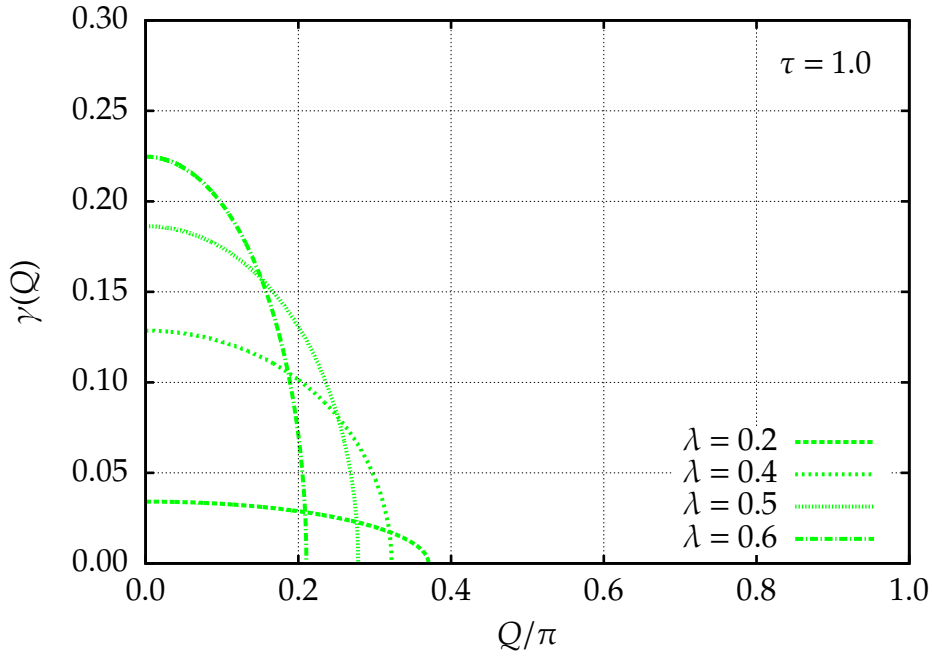

Figure 2.12: Quasiparticle width $\gamma(Q)$ for $\tau = 1.0$ and different values λ.

$$\frac{\gamma(Q)}{\delta(Q)} = \lambda^2 \frac{\sqrt{\tau\cos(Q/2) - \left(\omega_{1,\mathrm{r}}(Q) - 2\right)}}{\sqrt{\tau\cos(Q/2) + \left(\omega_{1,\mathrm{r}}(Q) - 2\right)}} \quad \text{for} \quad Q \leq Q_{\mathrm{c,r}} \,. \tag{2.34}$$

Since the numerator of equation (2.34) stays finite for $Q \to Q_{\mathrm{c,r}}$ while the denominator goes to zero the ratio $\gamma(Q)/\delta(Q)$ diverges for $Q \to Q_{\mathrm{c,r}}$ as depicted in figure 2.13. Therefore, near the merging momentum $Q_{\mathrm{c,r}}$ the width of the excitations is *always* arbitrarily large compared to the distance to the lower edge of the continuum. According to that the ratio $\gamma(Q)/\delta(Q)$ behaves completely opposite compared to the case of a Fermi liquid where the quasiparticles become more and more well-defined if they approach the Fermi surface. This motivates the naming "*quasiparticle breakdown*" instead of "*quasiparticle decay*".

For $\lambda = 0.5$ and $\lambda = 0.6$ the width $\gamma(Q)$ is greater than the distance to the lower edge of the two-particle continuum $\delta(Q)$ even down to $Q = 0$, cf. figure 2.13, so one could state that no well-defined quasiparticles exist inside the continuum.

A further difference to the quasiparticle concept in a Fermi liquid becomes apparent if one tries to calculate the quasiparticle weight $Z(Q)$ of the decaying excitation. Using the definition of the quasiparticle weight $Z(Q)$ commonly used in a Fermi liquid leads to

$$Z(Q) = \frac{1}{1 - \frac{\partial}{\partial\omega}\mathrm{Re}\,\Sigma(Q,\omega)\Big|_{\omega=\omega_{1,\mathrm{r}}(Q)}} \tag{2.35a}$$

$$= \frac{1}{1-\lambda^2} > 1 \quad \text{for} \quad Q \leq Q_{\mathrm{c,r}} \,. \tag{2.35b}$$

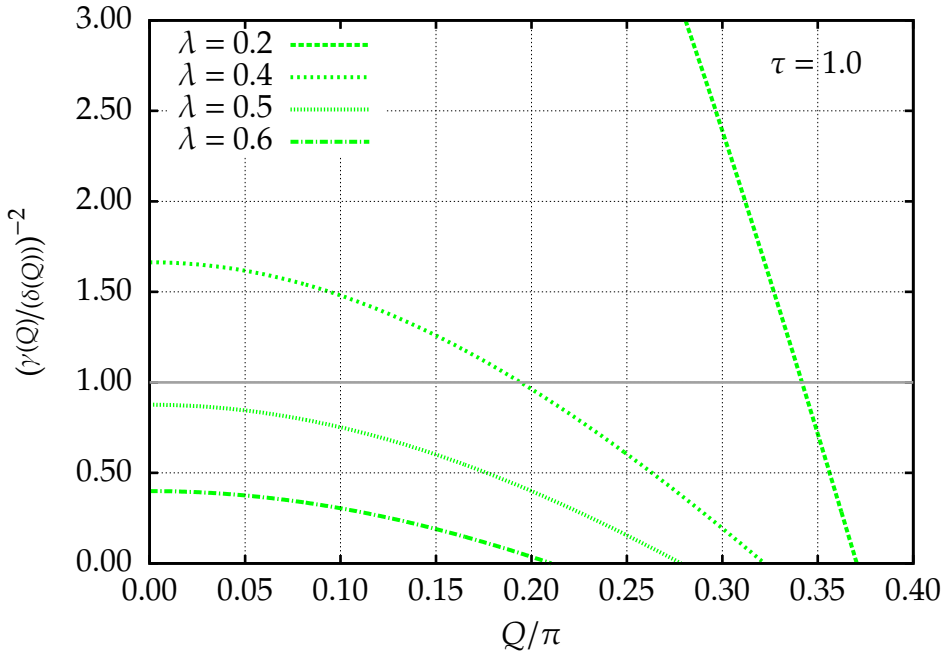

Figure 2.13: Ratio $(\gamma(Q)/(\delta(Q)))^{-2}$ for $Q \leq Q_{c,r}$ for $\tau = 1.0$ and different values λ. Near the merging momentum $Q_{c,r}$ the width of the excitations $\gamma(Q)$ becomes arbitrarily large compared to the distance of the quasiparticle to the lower edge of the continuum $\delta(Q)$. Thus a quasiparticle breakdown occurs. For $\lambda = 0.5$ and $\lambda = 0.6$ the ratio $(\gamma(Q)/(\delta(Q)))^{-2}$ is smaller than one down to $Q = 0$.

Thus, for all interactions λ the quasiparticle weight inside the continuum is greater than one, which clarifies that the quasiparticle weight is ill-defined for the system under study.

2.3 Influence of interaction terms

In dimerized spin systems two-particle interactions of the structure

$$H_2 = \mu\tau \sum_{\alpha\neq\beta} \sum_{r=0}^{N-1} \left(t^\dagger_{\alpha,r} t_{\beta,r} t^\dagger_{\beta,r+1} t_{\alpha,r+1} - t^\dagger_{\alpha,r} t_{\beta,r} t^\dagger_{\alpha,r+1} t_{\beta,r+1} \right) \tag{2.36}$$

occur, cf. appendix C. The influence of these interactions on the SQPD is discussed in this section where we restrict ourselves to the case $\mu > 0$, which leads to threefold degenerate $S = 1$ bound states.

On the diagrammatic level the two-particle interactions H_2 can be considered by calculating the scattering function given by the Bethe–Salpeter equation [Fetter & Walecka(1971)]. Here were use a Lanczos tridiagonalization, see appendix

A, in the spin $S = 1$, $m = 0$ subspace spanned by the states

$$\left|Q\right\rangle_{m=0}^{S=1} = \frac{1}{\sqrt{N}} \sum_r \mathrm{e}^{\mathrm{i}Qr}\, t_{z,r}^\dagger |0\rangle \tag{2.37a}$$

$$\left|Q,d\right\rangle_{m=0}^{S=1} = \frac{\mathrm{i}}{\sqrt{2N}} \sum_r \mathrm{e}^{\mathrm{i}Q\left(r+\frac{d}{2}\right)} \left(t_{x,r}^\dagger t_{y,r+d}^\dagger - t_{y,r}^\dagger t_{x,r+d}^\dagger\right) |0\rangle \tag{2.37b}$$

with $d > 0$ to include the two-particle interactions H_2[3]. This leads to the one-particle Green function $G(Q,\omega)$ represented by a continued fraction

$$\mathcal{G}(Q,\omega) = \cfrac{1}{\omega - a_0(Q) - \cfrac{b_1^2(Q)}{\omega - a_1(Q) - \cfrac{b_2^2(Q)}{\cdots}}} \tag{2.38}$$

with

$$a_0(Q) = \omega_1(Q) = 1 + \frac{\tau}{2}\cos(Q) \tag{2.39a}$$

$$a_1(Q) = 2 - \mu\tau \tag{2.39b}$$

$$a_n(Q) = 2 \quad \text{for} \quad n \geq 2 \tag{2.39c}$$

and

$$b_1^2(Q) = \frac{(\lambda\tau)^2}{2}\cos^2(Q/2) \tag{2.40a}$$

$$b_n^2(Q) = \frac{\tau^2}{4}\cos^2(Q/2) \quad \text{for} \quad n \geq 2 \tag{2.40b}$$

where the coefficients $a_n(Q)$ and $b_n(Q)$ are calculated by repeated application of $H = H_0 + H_1 + H_2$ on the initial state $\left|Q\right\rangle_{m=0}^{S=1}$, cf. appendix A. Since for $n \geq 2$ all coefficients $a_n(Q)$ and $b_n(Q)$ are identical the continued fraction can easily be terminated. Using the square root terminator (A.4) leads to the self-energy

$$\Sigma(Q,\omega) = \frac{b_1^2(Q)}{\omega - a_1(Q) - \Lambda(Q,\omega)} \tag{2.41}$$

[3]This Lanczos tridiagonalization yields the same results as the diagrammatic approach without self-consistency.

with

$$\Lambda(Q,\omega) = \begin{cases} \frac{(\omega-2)}{2} - \frac{\mathrm{i}}{2}\left[(\tau\cos(Q/2))^2 - (\omega-2)^2\right]^{1/2} & \text{if } |\omega-2| \leq \tau\cos(Q/2) \\ \frac{(\omega-2)}{2}\left(1-\left[1-\left(\frac{\tau\cos(Q/2)}{\omega-2}\right)^2\right]^{1/2}\right) & \text{if } |\omega-2| > \tau\cos(Q/2) \end{cases} . \tag{2.42}$$

Such a Lanczos algorithm we also use in the next section 2.4 to discuss the effects of next-nearest-neighbor hopping and in chapter 4, chapter 5 and chapter 6 to analyze effective models generated by continuous unitary transformations (CUTs).

Before we consider SQPD induced by a finite λ we discuss the case $\lambda = 0$. For $\lambda = 0$ one can start the Lanczos tridiagonalization with the two-particle initial state $\left|Q,1\right\rangle_{m=0}^{S=1}$ to calculate the dispersion $\omega_{\text{bound}}(Q)$ of the bare $S = 1$ two-particle bound state. Its dispersion $\omega_{\text{bound}}(Q)$ is implicitly given by

$$\omega - a_1(Q) - \Lambda(Q,w) = 0 \quad \text{if} \quad \omega < 2 - \tau\cos(Q/2) \tag{2.43}$$

which leads to

$$\omega_{\text{bound}}(Q) = 2 - \mu\tau - \frac{\tau}{4\mu}\cos^2(Q/2) \quad \text{if} \quad \omega_{\text{bound}}(Q) < 2 - \tau\cos(Q/2) \ . \tag{2.44}$$

This bound state exists for momenta $Q > 2\arccos(2\mu) =: Q_{\text{bound,c}}$. Thus for $\mu \geq 1/2$ it exists for all Q. The one-particle dispersion $\omega_1(Q)$ and the dispersion of the bound state $\omega_{\text{bound}}(Q)$ cross each other if $Q_{\text{bound,c}} < Q_{\text{c}}$. Thus for $\mu > \mu_{\text{c}}$ with

$$\mu_{\text{c}} = \frac{\sqrt{3\tau^2+4\tau}-\tau}{4\tau} \tag{2.45}$$

the one-particle dispersion $\omega_1(Q)$ and the dispersion of the bound state $\omega_{\text{bound}}(Q)$ meet below the two-particle continuum $\omega_2(Q,q)$, cf. equation (2.10). All in all the two-particle interaction H_2 (2.36) with $\mu > 0$ and $\lambda = 0$ leads to three different scenarios: (i) For small values of μ, i.e., $0 \leq \mu < \mu_{\text{c}}$ a bound state exists which merges with the two-particle continuum before it crosses the one-particle dispersion. (ii) In the region $\mu_{\text{c}} \leq \mu < 1/2$ the bound state crosses the one-particle dispersion before it merges with the two-particle continuum. (iii) Finally for $\mu \geq 1/2$ the $S = 1$ bound state exists for all momenta Q[4].

In figure 2.14 for each scenario one example is depicted. For $\mu = 0.2$ the bound state merges with the continuum before it crosses the one-particle dispersion. For $\mu = 0.45$ the bound state crosses the one-particle dispersion and merges with the two-particle continuum at smaller momenta Q. Finally, for $\mu = 0.6$ the bound state exists for all

[4]For $\mu > \frac{\tau+2}{2\tau}$ the bound state lies below the one-particle dispersion for all momenta Q. Thus at least for these high values of μ the model becomes erroneous.

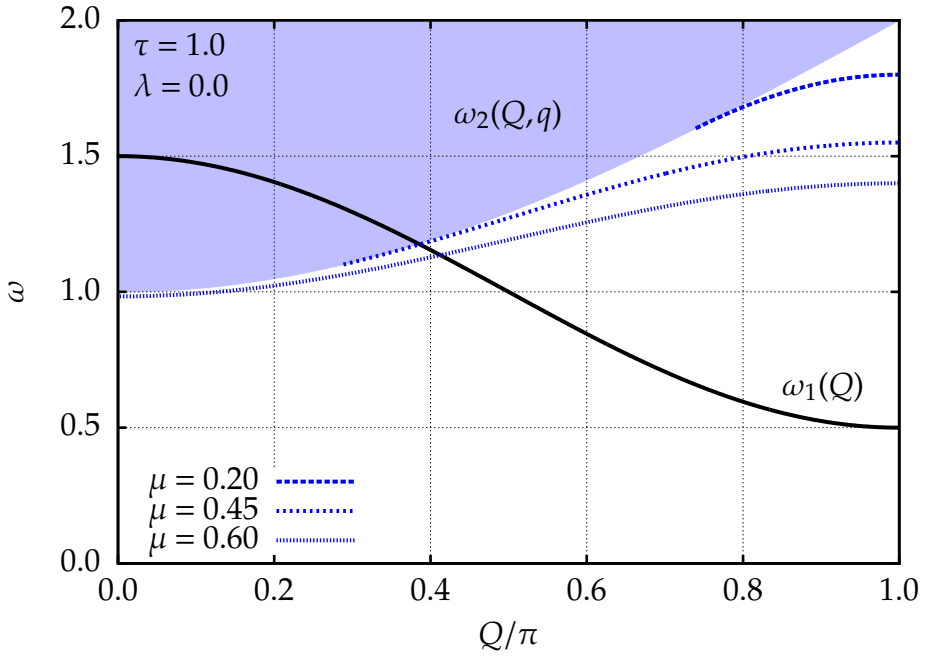

Figure 2.14: Dispersion $\omega_{\text{bound}}(Q)$ of the bare ($\lambda = 0$) two-particle bound states for $\tau = 1$ and various values μ. Bound state exists for momenta $Q > Q_{\text{bound,c}} = 2\arccos(2\mu)$.

momenta Q.

In the following we discuss the one- and two-particle spectrum for $\tau = 1.0$, $\lambda = 0.2$ and values $\mu = 0.2, 0.45, 0.6$. A finite value of λ renormalizes the one-particle dispersion and the dispersion of the two-particle bound state. Additionally, it makes SQPD possible.

Below the two-particle continuum ($\omega < 2 - \tau\cos(Q/2)$) the renormalized one-particle dispersion $\omega_{1,\text{r}}(Q)$ and the renormalized dispersion of the two-particle bound state $\omega_{\text{bound,r}}(Q)$ are given implicitly by the roots of

$$G^{-1}(Q,\omega) = \omega - \omega_1(Q) - \Sigma(Q,\omega) = 0\,. \tag{2.46}$$

From equations (2.39), (2.40), (2.41) and (2.42) follows that the solutions of equation (2.46) are given by roots of a cubic function. Note, that the roots of the cubic function are not necessarily solutions of equation (2.46). In figure 2.15 the renormalized one-particle dispersion $\omega_{1,\text{r}}(Q)$ (green lines) and the renormalized dispersion of the two-particle bound state $\omega_{\text{bound,r}}(Q)$ (blue lines) are depicted for $\tau = 1.0$, $\lambda = 0.2$ and $\mu = 0.2, 0.45, 0.6$.

Inside the two-particle continuum ($|\omega - 2| \leq \tau\cos(Q/2)$) we define the energy of the quasiparticles by

$$\omega - \omega_1(Q) - \text{Re}\,\Sigma(Q,\omega) = 0\,. \tag{2.47}$$

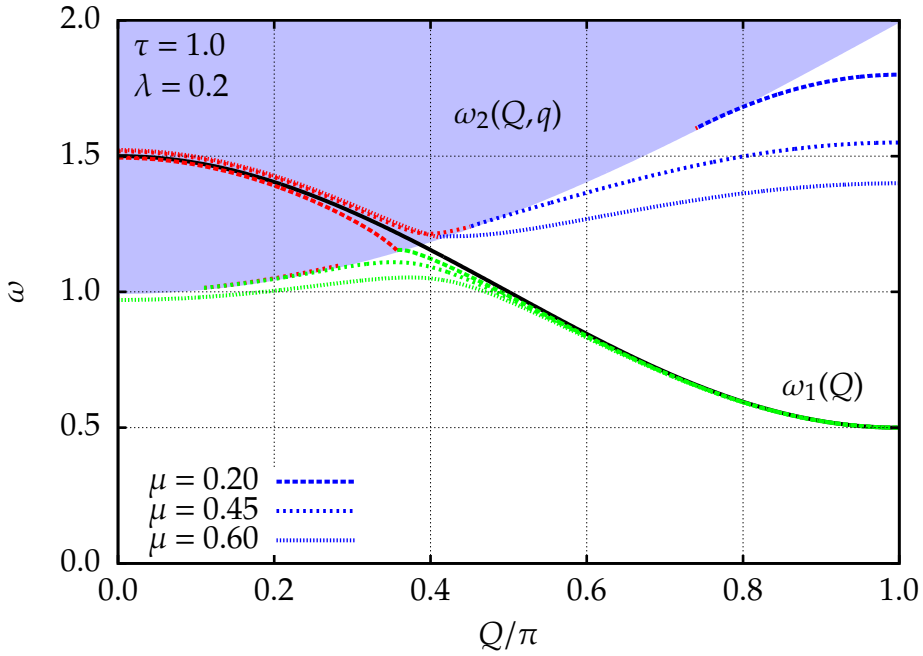

Figure 2.15: Renormalized one-particle dispersion $\omega_{1,\mathrm{r}}(Q)$ and the renormalized dispersion of the two-particle bound state $\omega_{\mathrm{bound,r}}(Q)$ for $\tau = 1.0$, $\lambda = 0.2$ and various values μ.

The solutions of this equation are depicted in figure 2.15 by red lines for $\tau = 1.0$, $\lambda = 0.2$ and $\mu = 0.2,\ 0.45,\ 0.6$.

For $\mu = 0.2$ nothing out of the ordinary occurs. The point where the bound state merges with the continuum is slightly shifted from $Q_{\mathrm{bound,c}} \approx 0.7380\pi$ to $Q_{\mathrm{bound,c,r}} \approx 0.7425\pi$. Within this interval $[Q_{\mathrm{bound,c}}, Q_{\mathrm{bound,c,r}}]$ a solution of equation (2.47) exists for $|\omega - 2| \leq \tau \cos(Q/2)$. The one-particle dispersion changes slightly as well and starts to decay once it merges with the two-particle continuum analogous to the case $\mu = 0.0$.

For $\mu = 0.45$ the bare ($\lambda = 0$) two-particle bound state crosses the one-particle dispersion $\omega_1(Q)$. This has a significant effect. Now the decaying quasiparticle (red line close to $\omega_1(Q)$) is continued by the renormalized two-particle bound state for $Q > Q_{\mathrm{bound,c,r}} \approx 0.4510\pi$. The renormalized one-particle dispersion $\omega_{1,\mathrm{r}}(Q)$ (green line) merges with the continuum at $Q = Q_{\mathrm{c,r}} \approx 0.1097\pi$ and ceases to exist at this momentum. There is *no* solution of equation (2.47) between $Q = 0$ and $Q_{\mathrm{c,r}}$ inside the continuum. Interestingly, a solution of equation (2.47) exists between $Q_{\mathrm{c,r}}$ and $Q_{\mathrm{bound,c}}$ just above the lower edge of the two-particle continuum. The finite value of $\lambda = 0.2$ leads to level repulsion between the one-particle dispersion and the two-particle bound state. These two states avoid any crossing.

For $\mu = 0.6$ the bare two-particle bound state exists for all momenta Q. This leads to a stable renormalized one-particle dispersion for all momenta Q, cf. figure 2.15. Again the decaying particle inside the continuum is continued by the renormalized two-particle bound state. They meet at $Q = Q_{\mathrm{bound,c,r}} \approx 0.4111$.

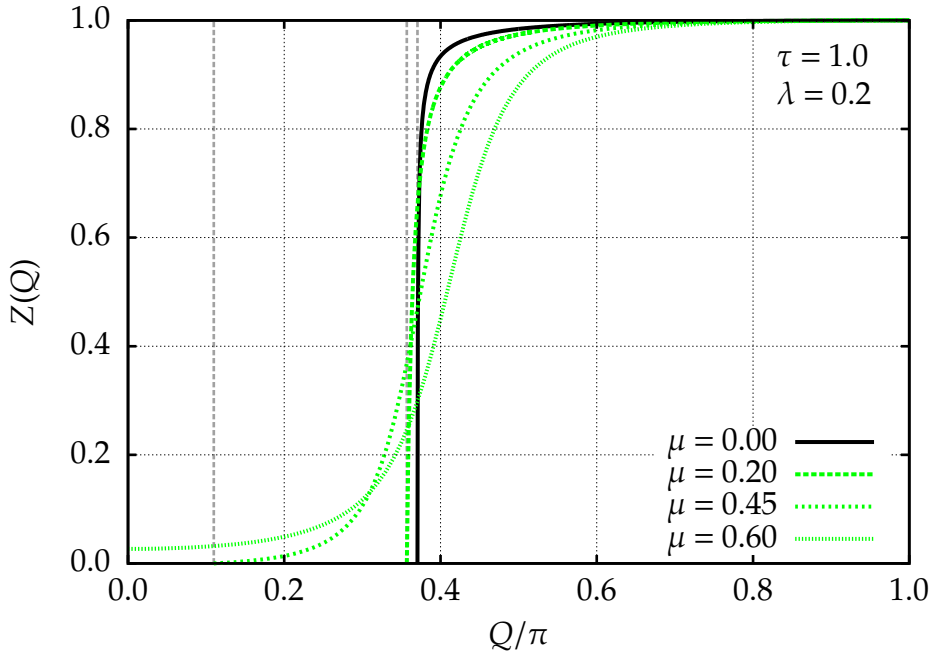

Figure 2.16: Quasiparticle weight $Z(Q)$ for $\tau = 1.0$, $\lambda = 0.2$ and variant values μ. For $\mu = 0.2, 0.45$ the weight $Z(Q)$ is continuously suppressed and vanishes at $Q_{c,r}$. Dotted grey lines indicate the respective $Q_{c,r}$.

In figure 2.16 the quasiparticle weight $Z(Q)$ (2.25) below the two-particle continuum is depicted for $\tau = 1.0$, $\lambda = 0.2$ and $\mu = 0.2, 0.45, 0.6$. For $\mu = 0.2, 0.45$ the weight $Z(Q)$ is continuously suppressed and vanishes at $Q_{c,r}$. In the case $\mu = 0.6$ the weight $Z(Q)$ stays finite for all momenta Q although it shrinks for smaller momenta Q. It is remarkable that for $\mu = 0.45$ the weight $Z(Q)$ of the renormalized one-particle dispersion decreases significantly for $Q \lessapprox Q_{c,\text{bound},r} \approx 0.4510\pi$ where the two-particle bound state passes over to the decaying excitation inside the continuum. Thus, although the particle described by the renormalized one-particle dispersion $\omega_{1,r}(Q)$ (green line) has infinite lifetime down to $Q_{c,r} \approx 0.1097\pi$ the main part of the spectral weight is allocated in the continuum for $Q \lessapprox 0.35\pi$.

Figure 2.17 shows the weight $Z_{\text{bound}}(Q)$ of the bound state given by

$$Z^{-1}_{\text{bound}}(Q) := \left.\frac{\partial G^{-1}(Q,\omega)}{\partial \omega}\right|_{\omega=\omega_{\text{bound},r}(Q)} \tag{2.48}$$

for $\tau = 1.0$, $\lambda = 0.2$ and $\mu = 0.2, 0.45, 0.6$. For all values μ the weight $Z_{\text{bound}}(Q)$ vanishes at $Q_{\text{bound},c,r}$ and at $Q = \pi$.

Next, we want to discuss the influence of the two-particle interaction on the imaginary part of the self-energy $\operatorname{Im}\Sigma(Q,\omega)$ and on the spectral density $\rho(Q,\omega)$.

In figure 2.18 the imaginary part of the self-energy $\operatorname{Im}\Sigma(Q,\omega)$ (left panels) and the spectral density $\rho(Q,\omega)$ (right panels) for $\tau = 1.0$, $\lambda = 0.2$ and $\mu = 0.2, 0.45, 0.6$ are

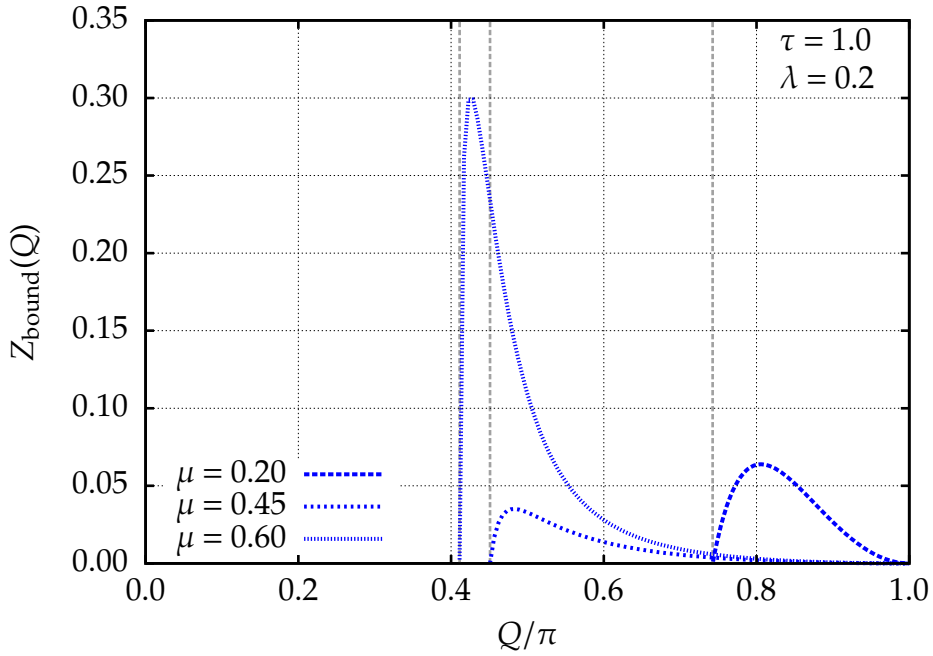

Figure 2.17: Weight $Z_{\mathrm{bound}}(Q)$ of the bound states for $\tau = 1.0$, $\lambda = 0.2$ and variant values μ. For all μ the weight $Z_{\mathrm{bound}}(Q)$ is continuously suppressed and vanishes at $Q_{\mathrm{bound,c,r}}$. Dotted grey lines indicate the respective $Q_{\mathrm{bound,c,r}}$. The data for $\mu = 0.2$ is multiplied by a factor of 100.

depicted. The left panels show the bare one-particle dispersion $\omega_1(Q)$ (black line) and the bare two-particle bound state (blue line below the continuum) as well. In the right panels the renormalized dispersions are depicted, cf. figure 2.15.

Inside the two-particle continuum ($|\omega - 2| \leq \tau \cos(Q/2)$) the imaginary part of the self-energy is given by

$$\mathrm{Im}\,\Sigma(Q,\omega) = -\lambda^2 \frac{\frac{1}{4}\sqrt{(\tau\cos(Q/2))^2 - (\omega-2)^2}}{\left[\left(\frac{\omega-2}{2}\right) + \tau\mu\right]^2 + \frac{1}{4}\left[(\tau\cos(Q/2))^2 - (\omega-2)^2\right]}\,. \tag{2.49}$$

At the edges of the continuum this quantity stays finite unless $2\mu = \pm\cos(Q/2)$. For $2\mu = \cos(Q/2)$ the bare bound state enters the continuum and the imaginary part of the self-energy $\mathrm{Im}\,\Sigma(Q,\omega)$ diverges like $\left[(\tau\cos(Q/2))^2 - (\omega-2)^2\right]^{-1/2}$. Generically, a positive value of μ shifts weight in the imaginary part of the self-energy $\mathrm{Im}\,\Sigma(Q,\omega)$ to lower energies ω.

For $\mu = 0.2$ and $\mu = 0.45$ these two effects of the two-particle interaction on the imaginary part of the self-energy $\mathrm{Im}\,\Sigma(Q,\omega)$ are clearly visible, see left panel of figure 2.18a and left panel of figure 2.18b. For both values of μ more weight is accumulated in the lower part than in the upper part. Also the one over square root behavior in the vicinity of the point where the two-particle bound state merges with the one-particle

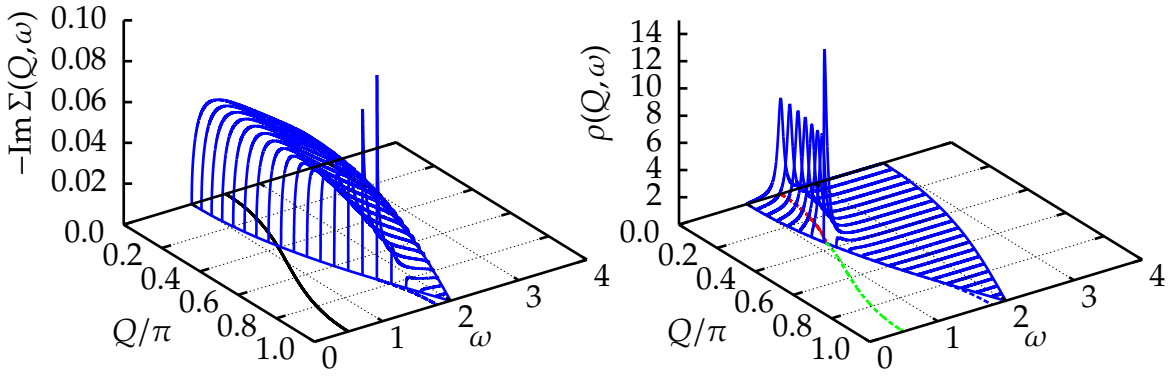

(a) $\tau = 1.0$, $\lambda = 0.2$, $\mu = 0.2$

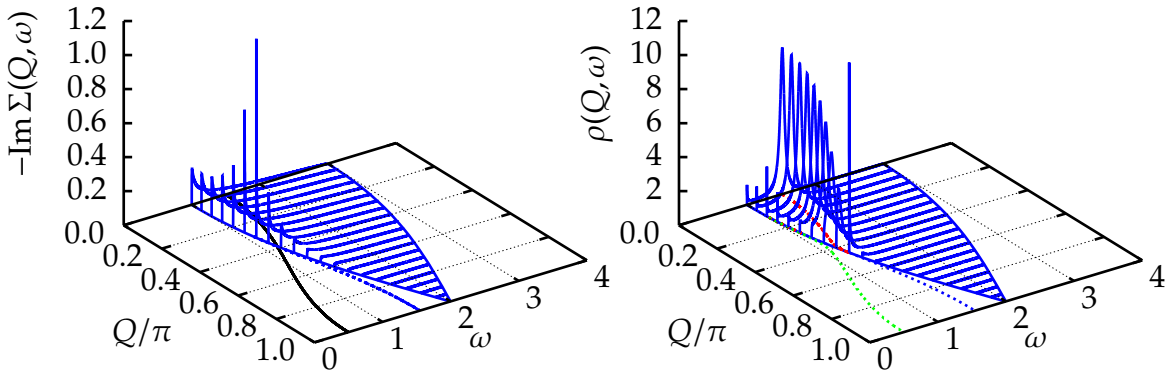

(b) $\tau = 1.0$, $\lambda = 0.2$, $\mu = 0.45$

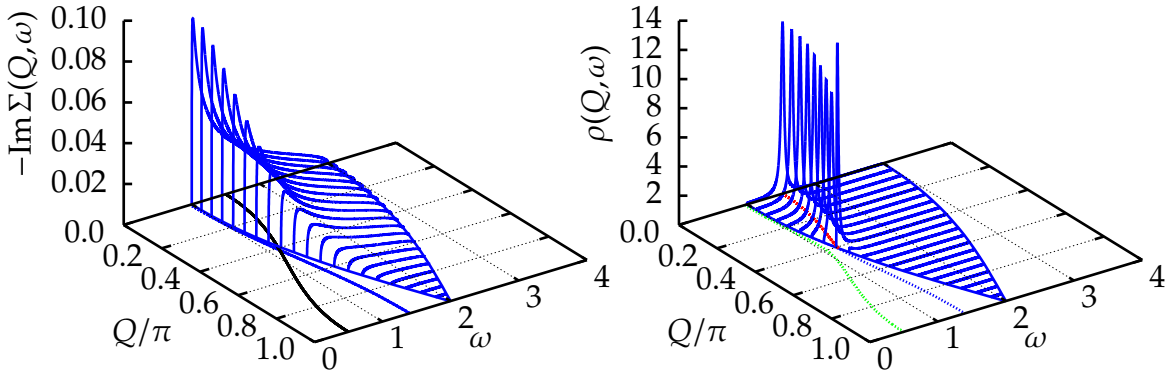

(c) $\tau = 1.0$, $\lambda = 0.2$, $\mu = 0.6$

Figure 2.18: Imaginary part of the self-energy $\mathrm{Im}\,\Sigma(Q,\omega)$ and the spectral density $\rho(Q,\omega)$ for $\tau = 1.0$, $\lambda = 0.2$ and various values μ. Black lines occurring in the left panels indicate the one-particle dispersion $\omega_1(Q)$. Blue lines below the two-particle continuum occurring in the left panels indicate the bare two-particle bound state $\omega_{\mathrm{bound}}(Q)$. Additional lines occurring in the right panels indicate the renormalized dispersions, cf. figure 2.15.

dispersion can be observed. For $\mu = 0.6$ the bare two-particle bound state exists for all momenta Q, so it never merges with the two-particle continuum. Thus the imaginary part of the self-energy $\mathrm{Im}\,\Sigma(Q,\omega)$ stays finite for all momenta Q. Nevertheless, the two-particle interaction shifts weight to lower energies ω, cf. left panel of figure 2.18c.

Inside the continuum peaks occur in the spectral density $\rho(Q,\omega)$ for all three values of μ whose positions are given by the solutions of equation (2.47) (red lines). In addition, for $\mu = 0.45$ small peaks very close to the lower edge of the continuum are present for momenta $Q \lessapprox 0.3\pi$ caused by the renormalized one-particle dispersion (green line), cf. right panel of figure 2.18b. For $\mu = 0.6$ these small peaks are not present, see right panel of figure 2.18c. Note, that the stable excitation below the continuum (green line) has a small spectral weight, cf. figure 2.16.

Finally, we discuss the width of the the excitation inside the continuum given by the red curves close to the bare one-particle dispersion $\omega_1(Q)$, cf. figure 2.15 and figure 2.18. In figure 2.19 the quasiparticle width $\gamma(Q)$ for $\tau = 1.0$, $\lambda = 0.2$ and various values μ is depicted. A finite value of μ considerably changes the width of the the quasipar-

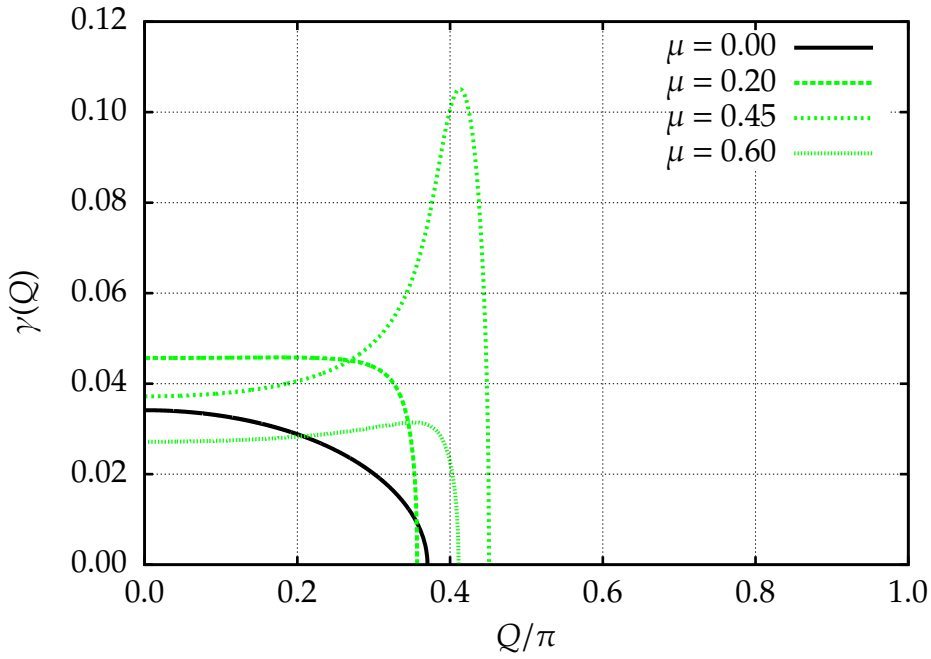

Figure 2.19: Width $\gamma(Q)$ for $\tau = 1.0$, $\lambda = 0.2$ and various values μ.

ticle inside the continuum. Especially, for $\mu = 0.45$ the width of the quasiparticle is markedly enhanced close to the point where the two-particle bound state merges with the two-particle continuum. Nevertheless, the width vanishes when the quasiparticle approaches the lower edge of the continuum.

Instead of a two-particle interaction also a next-nearest-neighbor hopping can effect the kind of decay. This is discussed in the next section.

2.4 Influence of next-nearest-neighbor hopping

In this section the influence of next-nearest-neighbor hopping is discussed. Thus, we consider the Hamiltonian

$$H = H_0^{\mathrm{NNN}} + H_1 \tag{2.50a}$$

with

$$H_0^{\mathrm{NNN}} = \sum_{\alpha} \sum_{r=0}^{\mathcal{N}-1} \left[t_{\alpha,r}^\dagger t_{\alpha,r} + \frac{\tau_1}{4} \left(t_{\alpha,r}^\dagger t_{\alpha,r+1} + t_{\alpha,r+1}^\dagger t_{\alpha,r} \right) + \frac{\tau_2}{4} \left(t_{\alpha,r}^\dagger t_{\alpha,r+2} + t_{\alpha,r+2}^\dagger t_{\alpha,r} \right) \right] \tag{2.50b}$$

$$H_1 = \frac{\lambda\tau_1}{4} \sum_{\alpha,\beta,\gamma} \sum_{r=0}^{\mathcal{N}-1} \mathrm{i}\, \varepsilon_{\alpha\beta\gamma}\, t_{\alpha,r}^\dagger t_{\beta,r+1}^\dagger \left(t_{\gamma,r} + t_{\gamma,r+1} \right) + \mathrm{H.c.}\,. \tag{2.50c}$$

For the bare one-particle dispersion $\omega_1(Q)$ follows

$$\omega_1(Q) = 1 + \frac{\tau_1}{2} \cos(Q) + \frac{\tau_2}{2} \cos(2Q) \tag{2.51}$$

leading to the two-particle continuum

$$\omega_2(Q,q) := \omega_1\left(Q/2 + q\right) + \omega_1\left(Q/2 - q\right) \tag{2.52a}$$

$$= 2 + \tau_1 \cos\left(Q/2\right) \cos\left(q\right) + \tau_2 \cos\left(Q\right) \cos\left(2q\right)\,. \tag{2.52b}$$

Unfortunately, it is no longer possible to derive a closed formula for the self-energy $\Sigma(Q,\omega)$. However, the imaginary part of the self-energy is still given by

$$\mathrm{Im}\,\Sigma(Q,\omega) = -\frac{(\lambda\tau_1)^2}{2} \cos^2\left(Q/2\right) \int_{-\pi}^{\pi} \sin^2(q)\, \delta\left(\omega - \omega_2(Q,q)\right) \mathrm{d}q\,, \tag{2.53}$$

cf. equation (2.15a).

For $\tau_2 = 0$ the extrema of the two-particle continuum for a fixed total momentum Q are always at $q = 0$ and $q = \pm\pi$. For these momenta the $\sin^2(q)$ appearing in the integrand of the imaginary part of the self-energy is zero, cf. equation (2.53). As a result, the imaginary part of the self-energy $\mathrm{Im}\,\Sigma(Q,\omega)$ stays finite. *No* singularities occur.

For a finite τ_2 the extrema of the two-particle continuum are determined by

$$\tau_1 \cos\left(Q/2\right) \sin\left(q\right) + 2\tau_2 \cos\left(Q\right) \sin\left(2q\right) = 0\,. \tag{2.54}$$

As for $\tau_2 = 0$, $q = 0$ and $q = \pm\pi$ are possible solutions. But for

$$\left(\frac{\tau_2}{\tau_1}\right)^2 > \frac{1}{16} \cdot \frac{\cos^2(Q/2)}{(2\cos^2(Q/2)-1)^2} \tag{2.55}$$

equation (2.54) is also fulfilled by

$$q_\pm = \pi \mp \tilde{q}_\pm \tag{2.56}$$

with

$$\tilde{q}_\pm = \arctan\left(\pm \frac{\sqrt{64(\tau_2/\tau_1)^2\cos^4(Q/2) - 64(\tau_2/\tau_1)^2\cos^2(Q/2) + 16(\tau_2/\tau_1)^2 - \cos^2(Q/2)}}{\cos(Q/2)}\right). \tag{2.57}$$

for $\tau_2/\tau_1 > 0$ and by $\tilde{q}_\pm$ for $\tau_2/\tau_1 < 0$. At these additional solutions the $\sin^2(q)$ appearing in the integrand of the imaginary part of the self-energy is *not* zero. This leads to singularities in the imaginary part of the self-energy $\mathrm{Im}\,\Sigma(Q,\omega)$ (2.53).

In the following we illustrate the effects caused by next-nearest-neighbor hopping for $\tau_1 = 1.0$, $\lambda = 0.2$ and various values τ_2.

As in the previous section 2.3 we use a Lanczos tridiagonalization in the spin $S = 1$, $m = 0$ subspace (2.37) to calculate the one-particle Green function $\mathcal{G}(Q,\omega)$. We determine numerically the coefficients $a_n(Q)$ and $b_{n+1}(Q)$ for $n < 1400$ in the subspace (2.37) with $d < 4000$. Thus, for fixed momentum Q we obtain a representation of the Green function $\mathcal{G}(Q,\omega)$ given by a finite continued fraction. This finite continued fraction has poles at the zeros of the denominator leading to a collection of δ-peaks. To obtain a continuous density $\rho(Q,\omega)$ we introduce a small broadening via $\omega \to \omega + \mathrm{i}\delta$ with a small real number δ. Unfortunately, this broadening smears out all sharp features like band edges or van Hove singularities. To avoid such a loss of resolution one can use an appropriate termination [Viswanath & Müller(1994)]. We terminate the finite continued fraction for $n < 1400$ by using the square root terminator, cf. appendix A. To approximate the limits $a_\infty(Q)$ and $b_\infty(Q)$ we calculate the arithmetic mean of $a_n(Q)$ and $b_n(Q)$ for $n \in [1400, 1490]$. In the following, results for the spectral density $\rho(Q,\omega)$ and for the imaginary part of the self-energy $\mathrm{Im}\,\Sigma(Q,\omega)$ obtained by a small broadening ($\delta = 0.05$) as well as by a termination with the square root terminator are presented.

We start our discussion of the influence of next-nearest-neighbor hopping by considering positive interactions $\tau_2 > 0$. In figure 2.20 the one-particle dispersion $\omega_1(Q)$, the two-particle continuum $\omega_2(Q,q)$, the imaginary part of the self-energy $\mathrm{Im}\,\Sigma(Q,\omega)$ and the spectral density $\rho(Q,\omega)$ for $\tau_1 = 1.0$, $\tau_2 = 0.2$ and $\lambda = 0.2$ are depicted. The bare

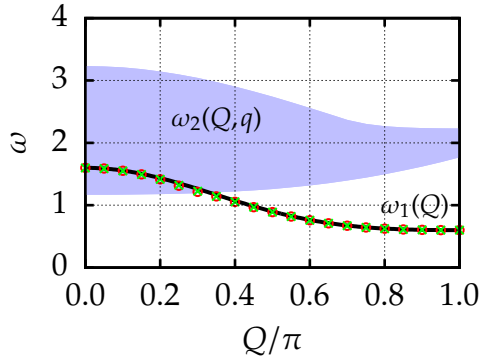

(a) Bare (black line) and renormalized (green crosses, red circles) one-particle dispersion for $\tau_1 = 1.0$, $\tau_2 = 0.2$ and $\lambda = 0.2$.

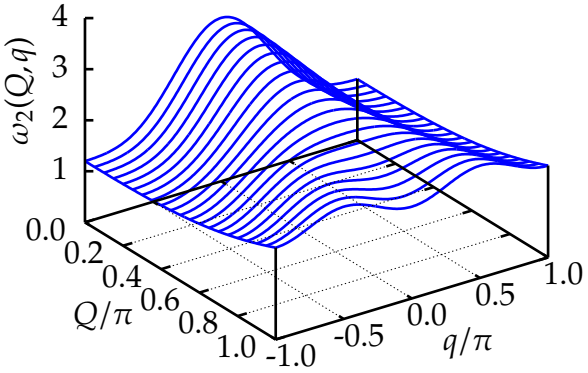

(b) Two-particle continuum $\omega_2(Q,q)$ for $\tau_1 = 1.0$, $\tau_2 = 0.2$ and $\lambda = 0.2$.

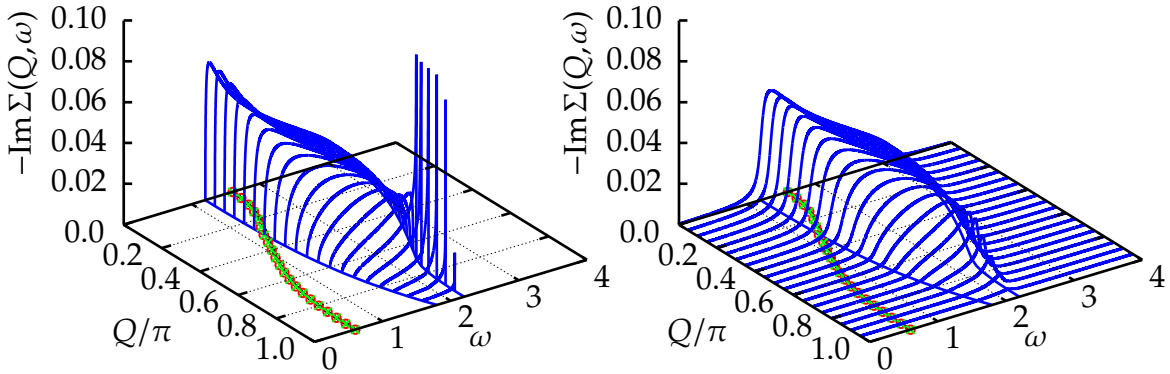

(c) Imaginary part of the self-energy $\mathrm{Im}\,\Sigma(Q,\omega)$ for $\tau_1 = 1.0$, $\tau_2 = 0.2$ and $\lambda = 0.2$. Left panel: Results obtained by a square root terminator. Right panel: Results obtained by a small broadening ($\delta = 0.05$).

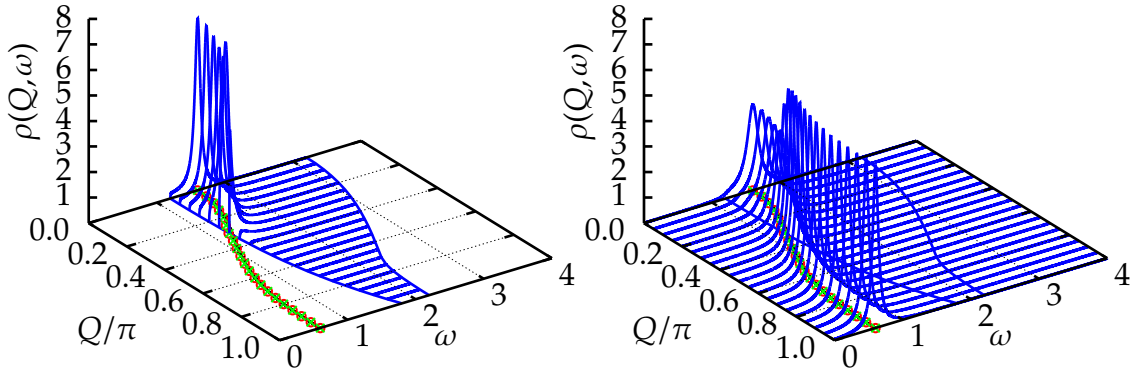

(d) Spectral density $\rho(Q,\omega)$ for $\tau_1 = 1.0$, $\tau_2 = 0.2$ and $\lambda = 0.2$. Left panel: Results obtained by a square root terminator. Right panel: Results obtained by a small broadening ($\delta = 0.05$).

Figure 2.20: One-particle dispersion, two-particle continuum, imaginary part of the self-energy and one-particle spectral density for $\tau_1 = 1.0$, $\tau_2 = 0.2$, $\lambda = 0.2$. The green crosses depict the renormalized one-particle dispersion determined by the smallest root of equation (2.58) where a small broadening ($\delta = 0.05$) is used. Red circles represent the renormalized one-particle dispersion resulting from the use of the square root terminator.

one-particle dispersion $\omega_1(Q)$ is represented by a black line. The green crosses depict the renormalized one-particle dispersion determined by the smallest root of

$$\omega - \omega_1(Q) - \operatorname{Re}\Sigma(Q,\omega) = 0\,, \tag{2.58}$$

where a small broadening ($\delta = 0.05$) is used to determine $\operatorname{Re}\Sigma(Q,\omega)$. The red circles represent the renormalized one-particle dispersion defined by the smallest root of equation (2.58), too. But instead of a small broadening the square root terminator is used to determine the real part of the self-energy $\operatorname{Re}\Sigma(Q,\omega)$. For $\tau_1 = 1.0$, $\tau_2 = 0.2$, $\lambda = 0.2$ the green crosses and the red circles lay on top of each other, see figure 2.20a.

From equation (2.55) follows that for finite $\tau_2/\tau_1 > 0$ and momenta $Q \approx \pi$ the two-particle continuum $\omega_2(Q,q)$ exhibits additional extrema at $q_\pm$ (2.56). For $\tau_2 = 0.2$ the two-particle continuum has maxima at $q_\pm$ for $Q \approx \pi$, see figure 2.20b. These maxima yield to singularities in the imaginary part of the self-energy at the upper edge of the two-particle continuum, cf. left panel of figure 2.20c. A broadening ($\delta = 0.05$) smears out these singularities, see right panel of figure 2.20c. Since the imaginary part of the self-energy has no singularities in the region of the Brillouin zone where the one-particle dispersion merges with the two-particle continuum the decay of the quasiparticle is qualitatively the same as in the case without next-nearest-neighbor hopping ($\tau_2 = 0.0$). Thus, the spectral density $\rho(Q,\omega)$ for $\tau = 0.2$ and for $\tau = 0.0$ have qualitatively the same structure, cf. figure 2.11 and the left panel of figure 2.20d. Below the two-particle continuum the quasiparticles are stable. According to this, the quasiparticles are represented by δ-peaks. The position of these δ-peaks are represented by the red circles. A slight broadening transforms the δ-peaks to Lorentzian functions. This can be observed in the right panel of figure 2.20d where the spectral density $\rho(Q,\omega)$ is depicted for a broadening of $\delta = 0.05$.

From equation (2.55) follows that singularities in the imaginary part of the self-energy $\operatorname{Im}\Sigma(Q,\omega)$ around $Q \approx 0.0$ can only occur for $|\tau_2/\tau_1| > 1/4$. Thus, in figure 2.21 the same quantities as in figure 2.20 are depicted for $\tau_1 = 1.0$, $\tau_2 = 0.4 > 1/4$ and $\lambda = 0.2$. For $\tau_2 = 0.4$ the two-particle continuum $\omega_2(Q,q)$ has minima at $q_\pm$ (2.56) around $Q \approx 0.0$, cf. figure 2.21b. Due to these minima the imaginary part of the self-energy $\operatorname{Im}\Sigma(Q,\omega)$ exhibits singularities at the lower edge of the continuum, see left panel of figure 2.21c, and stable excitations exist below the two-particle continuum for *all* momenta Q. The dispersion of these stable excitations is depicted by the red circles, see figure 2.21a. From the right panel of figure 2.21d one can conclude that the weight of the stable excitations is small, once the bare one-particle dispersion $\omega_1(Q)$ has merged with the two-particle continuum. Thus a small broadening annihilates the roots of equation (2.58) which describe these excitations. As a consequence, the green crosses lie inside the two-particle continuum. Most of the weight of $\rho(Q,\omega)$ is located at the decaying

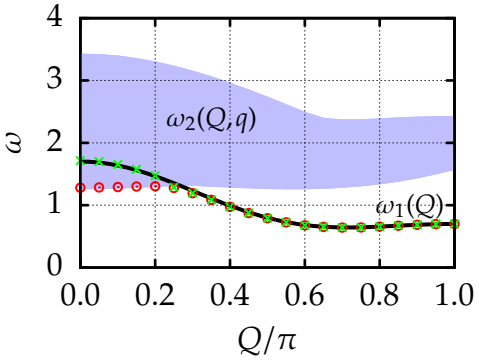

(a) Bare (black line) and renormalized (green crosses, red circles) one-particle dispersion for $\tau_1 = 1.0$, $\tau_2 = 0.4$ and $\lambda = 0.2$.

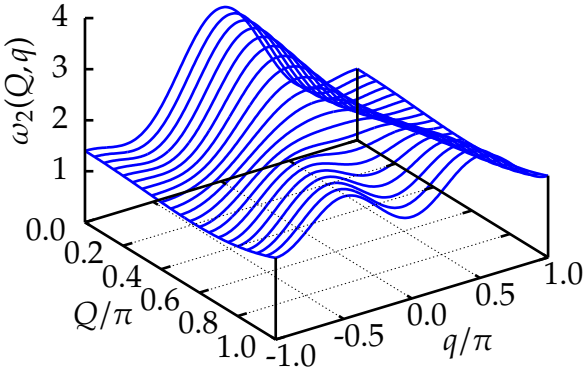

(b) Two-particle continuum $\omega_2(Q,q)$ for $\tau_1 = 1.0$, $\tau_2 = 0.4$ and $\lambda = 0.2$.

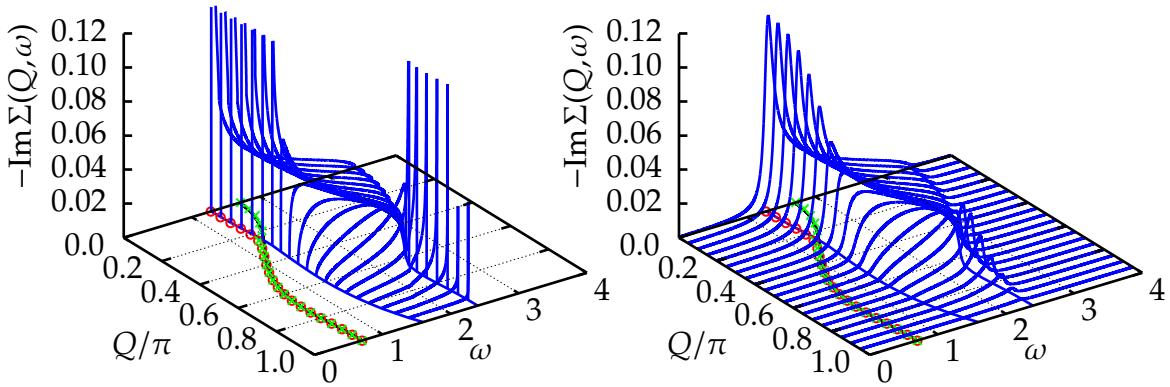

(c) Imaginary part of the self-energy $\mathrm{Im}\,\Sigma(Q,\omega)$ for $\tau_1 = 1.0$, $\tau_2 = 0.4$ and $\lambda = 0.2$. Left panel: Results obtained by a square root terminator. Right panel: Results obtained by a small broadening ($\delta = 0.05$).

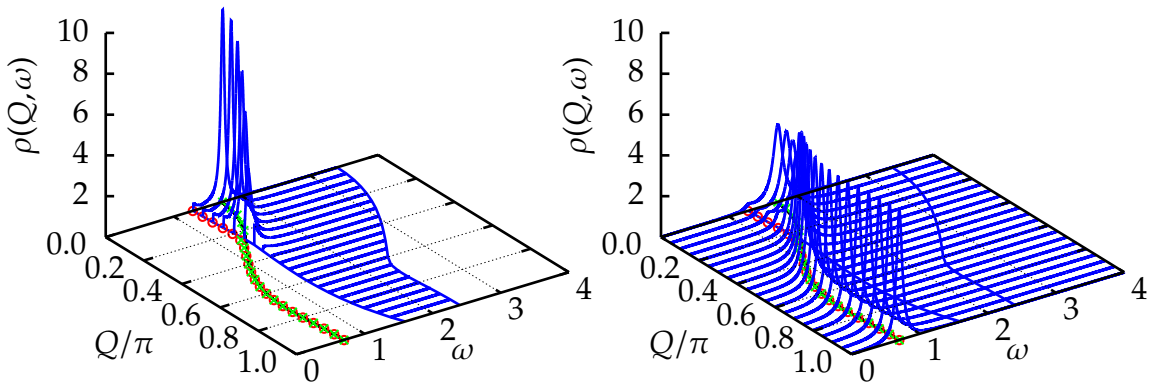

(d) Spectral density $\rho(Q,\omega)$ for $\tau_1 = 1.0$, $\tau_2 = 0.4$ and $\lambda = 0.2$. Left panel: Results obtained by a square root terminator. Right panel: Results obtained by a small broadening ($\delta = 0.05$).

Figure 2.21: One-particle dispersion, two-particle continuum, imaginary part of the self-energy and one-particle spectral density for $\tau_1 = 1.0$, $\tau_2 = 0.4$, $\lambda = 0.2$. The green crosses depict the renormalized one-particle dispersion determined by the smallest root of equation (2.58) where a small broadening ($\delta = 0.05$) is used. Red circles represent the renormalized one-particle dispersion resulting from the use of the square root terminator.

excitations inside the two-particle continuum indicated by the green crosses.

Note, that for $\tau_2 > 1/4$ the minimum of the dispersion $\omega_1(Q)$ is no longer at $Q = \pi$, see figure 2.21a.

For the sake of completeness, figure 2.22 and figure 2.23 depict the one-particle dispersion, the two-particle continuum, the imaginary part of the self-energy and the one-particle spectral density for $\tau_1 = 1.0$, $\lambda = 0.2$ and negative values $\tau_2 = -0.2,\ -0.4$. The negative sign of τ_2 transforms minima at $q_\pm$ for $\tau_2/\tau_1 > 0$ to maxima at $\tilde{q}_\pm$ for $\tau_2/\tau_1 < 0$, and maxima at $q_\pm$ for $\tau_2/\tau_1 > 0$ to minima at $\tilde{q}_\pm$ for $\tau_2/\tau_1 < 0$. Hence, for $\tau_2 = -0.2,\ -0.4$ the two-particle continuum $\omega_2(Q,q)$ has minima at $\tilde{q}_\pm$ for total momenta Q around π, cf. figure 2.22b and figure 2.23b. In addition, for $\tau_2 = -0.4$ maxima appear in the two-particle continuum $\omega_2(Q,q)$ at $\tilde{q}_\pm$ for total momenta Q close to $Q = 0$. Replacing a minimum by a maximum shifts a singularity occurring in $\operatorname{Im}\Sigma(Q,\omega)$ at the lower edge of the two-particle continuum to the upper edge of the continuum. Analogously, replacing a maximum by a minimum shifts a singularity occurring in $\operatorname{Im}\Sigma(Q,\omega)$ at the upper edge of the two-particle continuum to the lower edge of the continuum, cf. figure 2.22c and figure 2.23c. As a consequence, for $\tau_2 < 0$ the imaginary part of the self-energy $\operatorname{Im}\Sigma(Q,\omega)$ has no singularities at the lower edge of the two-particle continuum in the region of the Brillouin zone where the one-particle branch merges with the continuum. Thus, even for $\tau_2 = -0.4$ no stable excitation exists below the two-particle continuum for all momenta Q. Only positive interactions $\tau_2 > \tau_1/4 > 0$ yield stable excitations within the whole Brillouin zone.

Finally, we discuss the influence of next-nearest-neighbor interactions on the width $Z(Q)$ of the quasiparticles. To define the positions of the quasiparticles we choose the green crosses depicted in figures 2.20–2.23. Thus for $\tau_1 = 1.0$, $\tau_2 = 0.4$, $\lambda = 0.2$ and small total momenta Q we ignore the stable excitations below the continuum due to their negligible spectral weights. To calculate the width $\gamma(Q)$ we use the square root terminated continued fraction representation of the self-energy $\Sigma(Q,\omega)$.

Figure 2.24 shows the width $\gamma(Q)$ for $\tau_1 = 1.0$, $\lambda = 0.2$ and various τ_2. In addition to the previously discussed interactions $\tau_2 = \pm 0.2,\ \pm 0.4$ results for $\tau_2 = \pm 0.6$ are depicted as well. For $\tau_2 = 0.6$ stable excitations exist in the whole Brillouin zone. But their spectral weight is negligible for small total momenta Q so that the maxima of the spectral density $\rho(Q,\omega)$ are inside the continuum. As for $\tau_2 = 0.4$ we use these maxima of the spectral density $\rho(Q,\omega)$ to define the quasiparticle dispersion.

Interestingly, it seems that for $\tau_2 = 0.4$ and $\tau_2 = 0.6$ the width $\gamma(Q)$ is discontinuous at the lower edge of the continuum while for all other considered values of τ_2 the width vanishes at the boundary of the continuum , see figure 2.24.

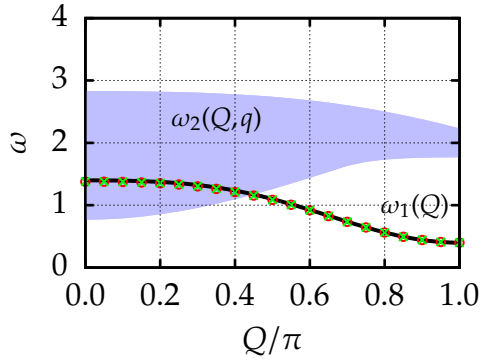

(a) Bare (black line) and renormalized (green crosses, red circles) one-particle dispersion for $\tau_1 = 1.0$, $\tau_2 = -0.2$ and $\lambda = 0.2$.

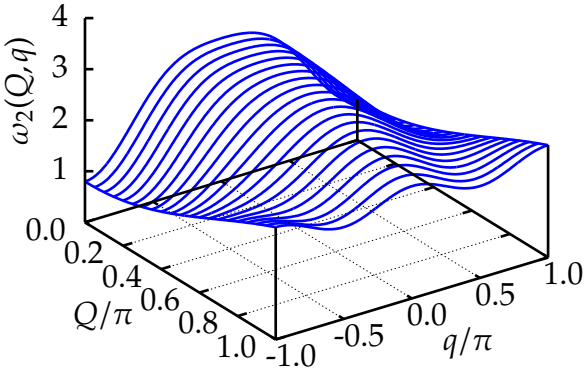

(b) Two-particle continuum $\omega_2(Q,q)$ for $\tau_1 = 1.0$, $\tau_2 = -0.2$ and $\lambda = 0.2$.

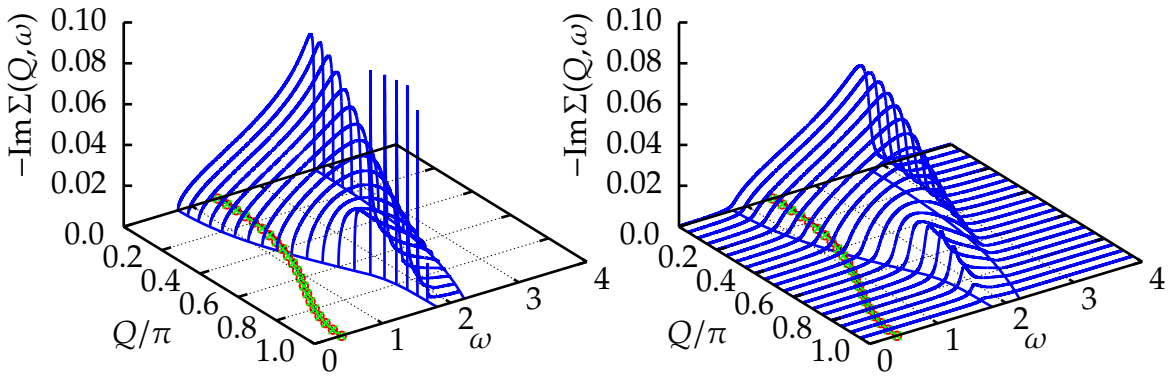

(c) Imaginary part of the self-energy $\mathrm{Im}\,\Sigma(Q,\omega)$ for $\tau_1 = 1.0$, $\tau_2 = -0.2$ and $\lambda = 0.2$. Left panel: Results obtained by a square root terminator. Right panel: Results obtained by a small broadening ($\delta = 0.05$).

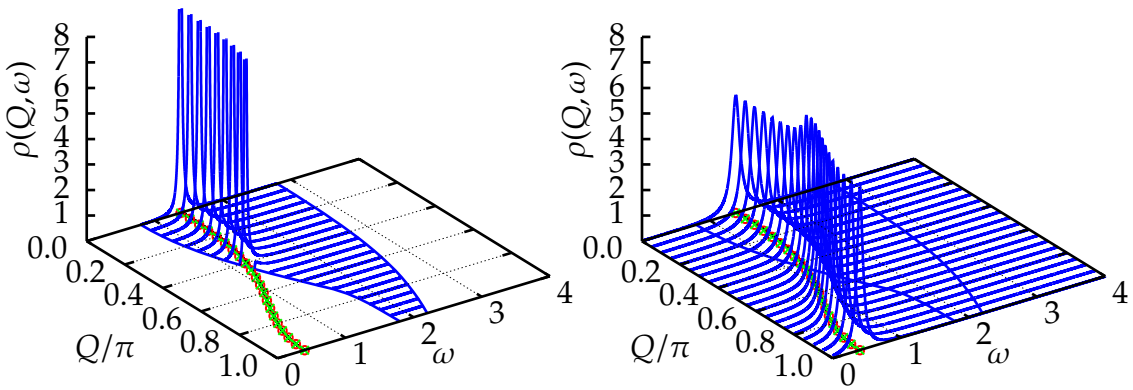

(d) Spectral density $\rho(Q,\omega)$ for $\tau_1 = 1.0$, $\tau_2 = -0.2$ and $\lambda = 0.2$. Left panel: Results obtained by a square root terminator. Right panel: Results obtained by a small broadening ($\delta = 0.05$).

Figure 2.22: One-particle dispersion, two-particle continuum, imaginary part of the self-energy and one-particle spectral density for $\tau_1 = 1.0$, $\tau_2 = -0.2$, $\lambda = 0.2$. The green crosses depict the renormalized one-particle dispersion determined by the smallest root of equation (2.58) where a small broadening ($\delta = 0.05$) is used. Red circles represent the renormalized one-particle dispersion resulting from the use of the square root terminator.

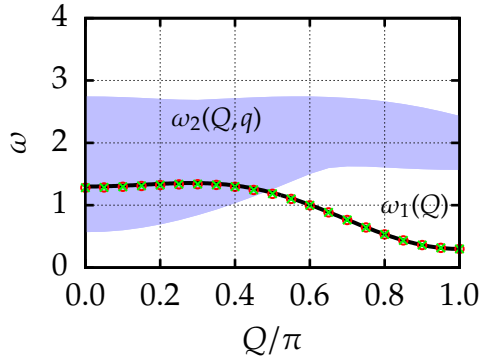

(a) Bare (black line) and renormalized (green crosses, red circles) one-particle dispersion for $\tau_1 = 1.0$, $\tau_2 = -0.4$ and $\lambda = 0.2$.

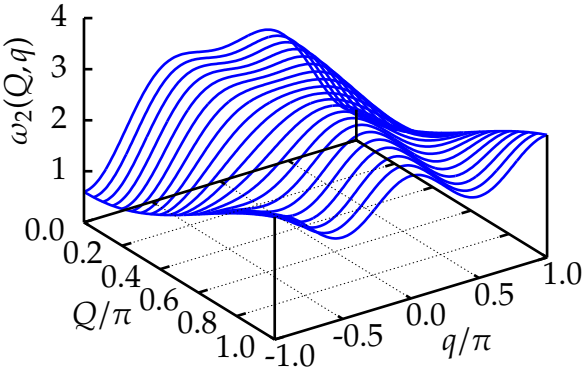

(b) Two-particle continuum $\omega_2(Q,q)$ for $\tau_1 = 1.0$, $\tau_2 = -0.4$ and $\lambda = 0.2$.

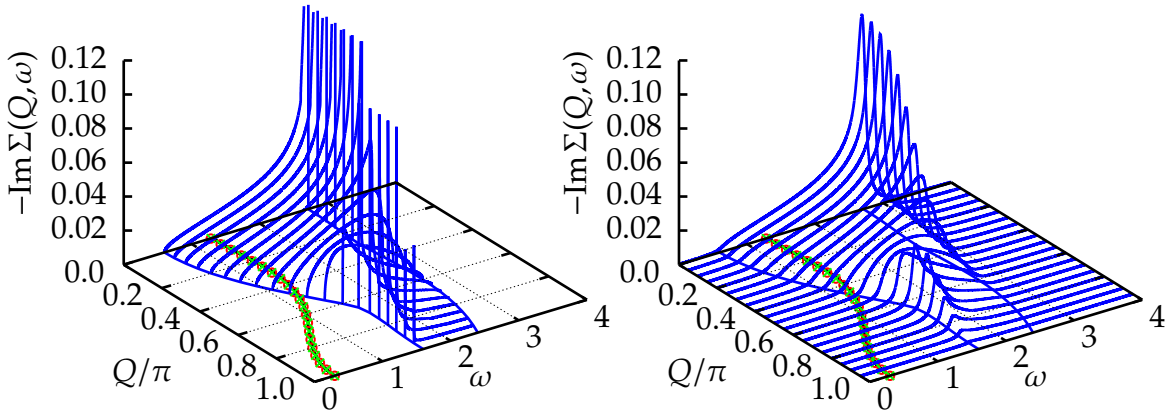

(c) Imaginary part of the self-energy $\mathrm{Im}\,\Sigma(Q,\omega)$ for $\tau_1 = 1.0$, $\tau_2 = -0.4$ and $\lambda = 0.2$. Left panel: Results obtained by a square root terminator. Right panel: Results obtained by a small broadening ($\delta = 0.05$).

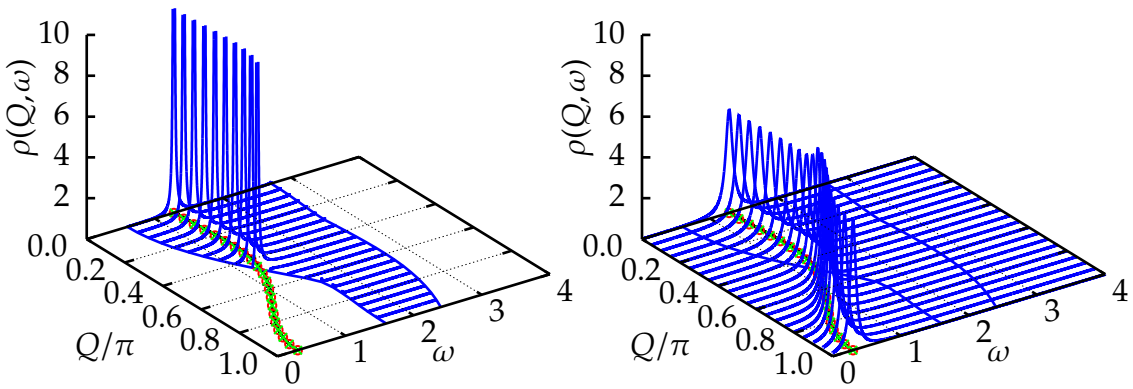

(d) Spectral density $\rho(Q,\omega)$ for $\tau_1 = 1.0$, $\tau_2 = -0.4$ and $\lambda = 0.2$. Left panel: Results obtained by a square root terminator. Right panel: Results obtained by a small broadening ($\delta = 0.05$).

Figure 2.23: One-particle dispersion, two-particle continuum, imaginary part of the self-energy and one-particle spectral density for $\tau_1 = 1.0$, $\tau_2 = -0.4$, $\lambda = 0.2$. The green crosses depict the renormalized one-particle dispersion determined by the smallest root of equation (2.58) where a small broadening ($\delta = 0.05$) is used. Red circles represent the renormalized one-particle dispersion resulting from the use of the square root terminator.

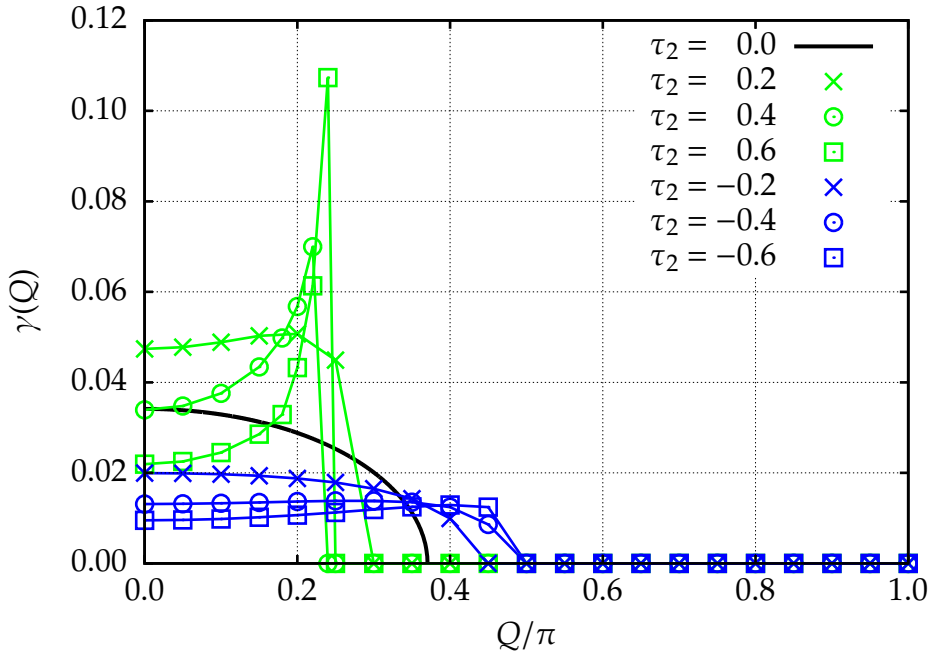

Figure 2.24: Width $\gamma(Q)$ for $\tau_1 = 1.0$, $\lambda = 0.2$ and various τ_2.

2.5 Chapter summary

In this chapter an introduction to spontaneous quasiparticle decay (SQPD) in gapped one-dimensional quantum spin systems has been given. For this purpose a bosonic toy model has been discussed where the one-particle dispersion merges with the two-particle continuum.

We have calculated the self-energy $\Sigma(Q,\omega)$ to describe the renormalization of the one-particle dispersion caused by decay processes.

Within this approach outside the continuum, where the quasiparticles have infinite lifetime, the quasiparticle weight continuously decreases when the dispersion approaches the two-particle continuum and vanishes completely at the merging point. At the merging point the lower edge of the two-particle continuum and the renormalized one-particle dispersion have the same velocities, so that the renormalized one-particle branch approaches the boundary of the two-particle continuum tangentially.

Inside the continuum the quasiparticles show SQPD characterized by a finite lifetime. In contrast to the decay in a Fermi liquid where the width of the excitations near to the Fermi surface decreases faster than the distance to the Fermi surface, in the model discussed the width of the excitations near to the merging point becomes arbitrarily large compared to the distance to the lower edge of the two-particle continuum. In this sense a breakdown of the quasiparticle picture occurs. Additionally, the usual definition of the quasiparticle weight can not be used.

Furthermore, we discussed the influence of two-particle interactions and next-

nearest-neighbor hopping on the SQPD.

If the two-particle interaction is large enough to produce a bound state in the region of the Brillouin zone where the SQPD occurs a new decay scenario emerges. Level repulsion occurs and the bound state is continued inside the continuum by a particle with finite lifetime. Simultaneously, the one-particle branch is pushed below the continuum and stays stable in the region where the bound state starts to decay. Thereby most of the spectral weight of the one-particle spectral density is allocated inside the continuum. Whether the one-particle branch is stable in the whole Brillouin zone or merges with the continuum at a small momentum and ceases to exist depends on the strength of the two-particle interaction.

For a sufficiently large positive next-nearest-neighbor hopping a stable excitation throughout the whole Brillouin zone occurs as well. But again, for small momenta most of the spectral weight is allocated at an excitation with finite lifetime inside the continuum.

All in all, we have found three different decay scenarios: (i) The stable one-particle branch below the continuum is continued inside the continuum by a quasiparticle branch with a finite lifetime and non-Fermi-liquid behavior. (ii) A two-particle bound state below the continuum is continued inside the continuum by a quasiparticle branch with a finite lifetime. Simultaneously, the one-particle branch is pushed below the continuum due to level repulsion and stays stable in the region where the bound state starts to decay. (iii) Next-neighbor-hopping causes additional minima inside the two-particle continuum whereby stable excitations within the whole Brillouin zone are produced. Nevertheless, for small momenta most of the spectral weight is gathered around an excitation with finite width inside the continuum.

Chapter 3

Continuous unitary transformations

"Hilbert space is a big place!" Carlton M. Caves

In this chapter the general concept of continuous unitary transformations (CUTs), also referred to as flow equation method or double-bracket flow, is described in detail. The method was introduced in 1994 by Wegner [Wegner(1994)] and independently by Głazek and Wilson [Głazek & Wilson(1993), Głazek & Wilson(1994)].

Since then, CUTs were applied to a wide range of problems in condensed matter physics, including electron-phonon coupling [Lenz & Wegner(1996), Ragwitz & Wegner(1999)], dissipative quantum systems [Kehrein & Mielke(1997), Kehrein & Mielke(1998)], the Hubbard model [Stein(1997), Reischl *et al.*(2004), Hamerla *et al.*(2010), Yang *et al.*(2010), Yang & Schmidt(2011)], the Anderson impurity model [Kehrein & Mielke(1994), Kehrein & Mielke(1996b)], the spin-boson model [Kehrein *et al.*(1995), Kehrein & Mielke(1996a)], spin systems [Knetter *et al.*(2003a), Schmidt & Uhrig(2006)], and the toric code model in a magnetic field [Vidal *et al.*(2009)]. A detailed description of the method and its applications is given in the book "*The Flow Equation Approach to Many-Particle Systems*" by Kehrein [Kehrein(2006)].

Various approaches based on CUTs were developed in the last years. Besides the approach Wegner used in his original work [Wegner(1994)], which we will denote by self-similar continuous unitary transformation (sCUT), the perturbative realization of CUT [Uhrig & Normand(1998), Knetter & Uhrig(2000)], usually denoted as perturbative continuous unitary transformation (pCUT), has become a powerful tool to perform high-order perturbation theory. Also a combination of pCUT and sCUT referred to as enhanced perturbative continuous unitary transformation (epCUT) is an issue of ongoing research [Krull(2011)]. A very recently developed approach called graph theory based continuous unitary transformation (gCUT) combines graph theory and CUTs [Yang & Schmidt(2011)].

In the following section 3.1 we give an introduction to the concept of CUTs. We

introduce the flow equation (3.3) which is the key element of all CUTs. The outcome of this equation depends on the particular choice of a generator which is the issue of section 3.2. We give a brief overview over the original choice of a generator by WEGNER (cf. section 3.2.1) and discuss in detail a class of generators where the coefficients of the Hamiltonian appear in the generator in linear order. Hamiltonians given explicitly by a matrix as well as Hamiltonians formulated in second quantization are considered (cf. section 3.2.2 and section 3.2.3). In particular, we discuss a generator capable to describe systems with unstable quasiparticles in an efficient way.

In section 3.3 differences and similarities of some generators are indicated and illustrated on systems with finite dimension. We also prove that a certain class of generators transform subspaces of the HILBERT space entirely equally, see section 3.3.4.

Section 3.4 is dedicated to the concept of sCUTs in real space for systems in the thermodynamic limit as used in chapter 4, 5, and 6. The usage of translational symmetry is explained explicitly (cf. section 3.4.2) and a truncation scheme is introduced to deal with the infinite dimension of the system (cf. section 3.4.3).

Finally, some remarks about the implementation on a computer are given (cf. section 3.5).

3.1 General concept of continuous unitary transformations

A central issue of theoretical quantum mechanics is the diagonalization of a self-adjoint Hamiltonian H. Particularly, in the field of condensed matter physics, where non-relativistic point-like particles interact only via COULOMB interactions, the so-called "*theory of everything*" is well-known. This means that it is possible to write down the Hamiltonian H which should describe *all* properties of the system under study [Czycholl(2004), Schmidt(2008)].

Theoretically, a diagonalization of a normal operator and in particular of a self-adjoint operator is always possible. According to that a unitary operator U exists which changes the basis in a way that $U^\dagger H U$ is diagonal. But unfortunately, the actual diagonalization of the full Hamiltonian H, although possible in theory, is usually an impossible task due to the huge number of degrees of freedom. Therefore, often a reductive approach is used. One tries to identify the relevant degrees of freedom and to write down an effective model which hopefully describes the partial aspect of interest sufficiently well and is easier to solve than the initial problem. Typically, the derivation of such an effective model is a highly nontrivial and challenging task.

In a certain way the main aims of condensed matter physics are therefore contrary to those of high energy physics where the low-energy effective theory, the so called

"*standard model of particle physics*", is well established but the "*theory of everything*" is unknown.

A famous example in the field of correlated electrons for the derivation of an effective model is the reduction of the half-filled HUBBARD model [1] to the antiferromagnetic spin $S = 1/2$ HEISENBERG model in the limit of strongly interacting electrons [Anderson(1959), Harris & Lange(1967), Takahashi(1977), Reischl *et al.*(2004), Hamerla *et al.*(2010)].

The method of CUTs offers a general approach to diagonalize matrices and operators or at least to achieve a form closer to diagonality and to derive effective models in a systematic way.

3.1.1 The flow equation

Normally, the Hamiltonian H is transformed by a finite number of unitary transformations U_n

$$H_{\text{eff}} = U^\dagger H U \tag{3.1a}$$

with

$$U := U_1 U_2 \cdots U_N \,. \tag{3.1b}$$

In the following we always denote the transformed Hamiltonian $U^\dagger H U$ by H_{eff}. If U is a unitary transformation, H_{eff} is entirely equivalent to H. The eigenvalues e_n of H_{eff} are the same as for the initial Hamiltonian H and if $v_{n,\text{eff}}$ is an eigenvector of H_{eff} then $U v_{n,\text{eff}}$ is an eigenvector of H. In this case the subscript "eff" as an abbreviation for effective is misleading. But in actual calculations we usually have to perform some approximations due to the complexity of the problems (cf. section 3.4.3). Typically this slightly destroys the unitarity of the transformation and we only achieve an effective description of the initial problem. For that reason we use the subscript "eff".

In 1994 WEGNER [Wegner(1994)] and independently GŁAZEK and WILSON [Głazek & Wilson(1993), Głazek & Wilson(1994)] generalized equation (3.1) by replacing the finite number of unitary transformations $U := \prod_{n=1}^{N} U_n$ by infinitely many, thus a continuous unitary transformation (CUT). The idea is to introduce a continuous auxiliary variable ℓ and to define an ℓ-dependent Hamiltonian

$$H(\ell) := U^\dagger(\ell) H U(\ell) \,. \tag{3.2}$$

[1] The HUBBARD model itself is a effective model.

Then the Hamiltonian $H(\ell)$ transforms according to the flow equation

$$\frac{\partial H(\ell)}{\partial \ell} = [G(\ell), H(\ell)] \tag{3.3a}$$

with the initial condition

$$H(0) = H \tag{3.3b}$$

and an antihermitian generator $G(\ell)$ defined by

$$G(\ell) := -U^\dagger(\ell)\frac{\partial U(\ell)}{\partial \ell} \,. \tag{3.4}$$

The antihermiticity of the generator $G(\ell)$ ensures that the transformation (3.3) of $H(\ell)$ is unitary. So for all values ℓ the transformed Hamiltonian $H(\ell)$ is unitarily equivalent to the initial Hamiltonian H. Usually, we consider the limit $\ell \to \infty$ and denote $H(\infty)$ as the effective Hamiltonian

$$H_{\text{eff}} := \lim_{\ell\to\infty} H(\ell) \,. \tag{3.5}$$

Multiplying equation (3.4) from the left by $U(\ell)$ yields a differential equation for the unitary transformation $U(\ell)$

$$\frac{\partial U(\ell)}{\partial \ell} = -U(\ell)G(\ell) \tag{3.6a}$$

with the initial condition

$$U(0) = \mathbb{1} \,. \tag{3.6b}$$

This differential equation can formally be solved by

$$U(\ell) = \mathcal{L}\exp\left(-\int_0^\ell G(\ell')\,\mathrm{d}\ell'\right) \tag{3.7}$$

where $\mathcal{L}$ denotes the ℓ- ordering operator which orders the following expressions from left to right in increasing order of ℓ. Due to this ordering a simple choice of a generator $G(\ell)$ may produce a very complicated unitary transformation $U(\ell)$.

Certainly, the final structure of the effective Hamiltonian H_{eff} depends on the form of the chosen generator $G(\ell)$. So the crucial point is to choose a generator $G(\ell)$ that leads to a simplification of the initial Hamiltonian. Another important issue is whether the ensuing flow equation (3.3) is practically tractable. Nevertheless, the continuous

representation of the unitary transformation (3.3) offers some considerable advantages in comparison to the finite representation (3.1). Firstly, the CUT can adjust itself during the diagonalization depending on the current form of the Hamiltonian whereby a simple choice of a generator $G(\ell)$ can produce an elaborated unitary transformation $U(\ell)$. Secondly, the flow equation (3.3) can be used to determine the asymptotic structure of the Hamiltonian. By inspecting the right hand side of the flow equation (3.3) one recognizes that the transformation only stops if the generator $G(\ell)$ commutes with the Hamiltonian $H(\ell)$

$$[G(\ell), H(\ell)] = 0 \,. \tag{3.8}$$

Therefore, if the flow equations converge to a fixed point the structure of the effective Hamiltonian H_{eff} can be easily predicted by the structure of the generator $G(\ell)$. Examples are given in section 3.2 where various generators are introduced and discussed.

3.1.2 Transformation of observables

For a comparison of theoretical calculations with experimental data observables must be considered as well. For example, in inelastic neutron scattering (INS) measurements the cross section is proportional to the dynamical structure factor $S^{\alpha\beta}(\mathbf{Q}, \omega)$ which involves matrix elements of spin operators (cf. section F).

In the same way as for the Hamiltonian H the technique of CUTs can be used to transform an observable O. The flow equation for an observable is given by

$$\frac{\partial O(\ell)}{\partial \ell} = [G(\ell), O(\ell)] \tag{3.9a}$$

with the initial condition

$$O(0) = O \,. \tag{3.9b}$$

Typically, the structure of the observable $O(\ell)$ will become more and more complicated during the flow (cf. section 3.4.3 and chapter E).

3.2 Generators

3.2.1 Wegner's generator

In his first work about CUTs [Wegner(1994)] Wegner split the Hamiltonian H into a diagonal part H_d and a non-diagonal part H_nd

$$H = H_\mathrm{d} + H_\mathrm{nd} \tag{3.10}$$

and defined the generator $G_\mathrm{W}(\ell)$ by

$$G_\mathrm{W}(\ell) := [H_\mathrm{d}(\ell), H(\ell)] = [H_\mathrm{d}(\ell), H_\mathrm{nd}(\ell)] \ . \tag{3.11}$$

The definition of $H_\mathrm{d}(\ell)$ is arbitrary. One is free to choose which part of the Hamiltonian H is called diagonal implying which part is called non-diagonal depending on the problem under study [Wegner(2006)].

If one considers a Hamiltonian $H(\ell)$ given by a $(N+1)\times(N+1)$ matrix[2]

$$H(\ell) = \begin{pmatrix} e_0(\ell) & h_{0,1}(\ell) & h_{0,2}(\ell) & \dots & h_{0,N}(\ell) \\ h_{1,0}(\ell) & e_1(\ell) & h_{1,2}(\ell) & \dots & h_{1,N}(\ell) \\ h_{2,0}(\ell) & h_{2,1}(\ell) & e_2(\ell) & \dots & h_{2,N}(\ell) \\ \vdots & \vdots & \vdots & \ddots & \vdots \\ h_{N,0}(\ell) & h_{N,1}(\ell) & h_{N,2}(\ell) & \dots & e_N(\ell) \end{pmatrix} \tag{3.12}$$

and defines the diagonal part as

$$H(\ell) = \begin{pmatrix} e_0(\ell) & 0 & 0 & \dots & 0 \\ 0 & e_1(\ell) & 0 & \dots & 0 \\ 0 & 0 & e_2(\ell) & \dots & 0 \\ \vdots & \vdots & \vdots & \ddots & \vdots \\ 0 & 0 & 0 & \dots & e_N(\ell) \end{pmatrix} . \tag{3.13}$$

The sum over all squared non-diagonal elements is a monotonically decreasing function for the generator $G_\mathrm{W}(\ell)$ since its derivative is given by [Wegner(1994)]

$$\frac{\partial}{\partial \ell} \sum_{\substack{n,m=0 \\ n\neq m}}^{N} \left|h_{n,m}(\ell)\right|^2 = -2 \sum_{n,m=0}^{N} (e_n(\ell) - e_m(\ell))^2 \left|h_{n,m}(\ell)\right|^2 \ . \tag{3.14}$$

Therefore, the flow equation (3.3) has to converge in the limit $\ell \to \infty$ and the Hamil-

[2] We denote matrix elements of the Hamiltonian $H(\ell)$ by $\langle n|H(\ell)|m\rangle = h_{n,m}(\ell)$. For diagonal elements we use besides $h_{n,n}(\ell)$ also $e_n(\ell)$. Matrix elements of a generator $G(\ell)$ are denoted by $\langle n|G(\ell)|m\rangle = g_{n,m}(\ell)$.

tonian $H(\ell)$ becomes more and more diagonal during the flow. From equation (3.14) follows for $\ell \to \infty$

$$\lim_{\ell\to\infty} (e_n(\ell) - e_m(\ell))^2 \left|h_{n,m}(\ell)\right|^2 = 0 \quad \forall n,m \; . \tag{3.15}$$

Thus Wegner's generator $G_W(\ell)$ diagonalizes the Hamiltonian $H(\ell)$ up to degenerate subspaces[3] (cf. section 3.3.1). This property also applies for infinite matrices [Dusuel & Uhrig(2004)].

3.2.2 Generators for matrices

Mielke's generator

For band-diagonal Hamiltonian matrices, i.e.,

$$h_{n,m}(0) = 0 \quad \text{for} \quad |n-m| > N_0 \; , \tag{3.16}$$

Mielke proposed another generator $G_M(\ell)$. His choice conserves the initial band structure during the flow [Mielke(1998)], which is not the case for Wegner's generator. Mielke achieved the conservation of the banded structure by introducing a sign function depending on the difference between the row index n and the column index m of the considered matrix element

$$g_{n,m}(\ell) = \operatorname{sgn}(n-m)\, h_{n,m}(\ell) \; . \tag{3.17}$$

From this choice follows that the flow of a diagonal element $e_n(\ell)$ is given by

$$\frac{\partial e_n(\ell)}{\partial \ell} = 2 \sum_{\substack{m=0 \\ m\neq n}}^{N} \operatorname{sgn}(n-m) \left|h_{n,m}(\ell)\right|^2 \; . \tag{3.18}$$

Therefore, the sum of the first $r+1$ diagonal element is a monotonically decreasing function [Mielke(1998)]

$$\frac{\partial}{\partial \ell} \sum_{n=0}^{r} e_n(\ell) = -2 \sum_{n=0}^{r} \sum_{m=r+1}^{N} \left|h_{n,m}(\ell)\right|^2 \leq 0 \; . \tag{3.19}$$

[3] Note, here we mean by degenerate $e_n(\ell) = e_m(\ell)$ and do *not* refer to the eigenvalues of $H(\ell)$.

For finite systems and systems which are bounded from below the sum $\sum_{n=0}^{r} e_n(\ell)$ has a lower limit. Then, since r is arbitrary, from equation (3.19) follows

$$\lim_{\ell\to\infty} \left|h_{n,m}(\ell)\right|^2 = 0 \quad \forall n,m:\ n \neq m\ . \tag{3.20}$$

Thus the effective Hamiltonian H_{eff} is diagonal even if the spectrum is degenerate.

Another important property of Mielke's generator is the asymptotic behavior of the non-diagonal elements $h_{n,m}(\ell)$ with $n \neq m$ and the implied ordering of the diagonal elements $e_n(\ell)$. The flow of a non-diagonal element is given by

$$\begin{aligned}\frac{\partial h_{n,m}(\ell)}{\partial \ell} = &-\operatorname{sgn}(n-m)\Big(e_n(\ell)-e_m(\ell)\Big)\, h_{n,m}(\ell) \\ &+ \sum_{\substack{k=0\\ k\neq m,n}}^{N} \Big(\operatorname{sgn}(n-k)+\operatorname{sgn}(m-k)\Big)\, h_{n,k}(\ell)h_{k,m}(\ell)\ .\end{aligned} \tag{3.21}$$

Since the non-diagonal elements $h_{n,m}(\ell)$ vanish for $\ell \to \infty$ the second term in equation (3.21), quadratic in the non-diagonal elements, can be neglected for large enough values of ℓ. Therefore, if $h_{n,m}(\ell)$ tends to zero, one must have

$$\operatorname{sgn}(n-m)\,(e_n(\ell)-e_m(\ell)) > 0 \tag{3.22}$$

for sufficiently large values ℓ. Thus the generator proposed by Mielke orders the diagonal matrix elements $e_n(\ell)$ in ascending order and the non-diagonal matrix elements $h_{n,m}(\ell)$ decrease exponentially for large values ℓ. Note that the exponential decay of the non-diagonal elements holds only asymptotically. For smaller values of ℓ the non-diagonal matrix elements $h_{n,m}(\ell)$ can even increase, see for example reference [Dusuel & Uhrig(2004)]. Also the sum over all squared non-diagonal elements $\sum_{\substack{n,m=0\\ n\neq m}}^{N} \left|h_{n,m}(\ell)\right|^2$ can increase during the flow in contrast to Wegner's version, see equation (3.14). Thus during the flow the Hamiltonian $H(\ell)$ can be even less diagonal that at $\ell = 0$.

The generator of Dawson *et al.*

Dawson *et al.*[Dawson *et al.*(2008)] used variational calculations to derive generators optimized for ground state properties of Hamiltonians represented by matrices. In section 3.2.3 we present a generalization for Hamiltonians formulated in second quantization, see reference [Fischer *et al.*(2010)] as well. The idea is to minimize $\frac{\partial e_0(\ell)}{\partial \ell} = \frac{\partial \langle 0|H(\ell)|0\rangle}{\partial \ell}$ with $|0\rangle = (1,0,\ldots,0)^T$ under the constraint of a bounded $G(\ell)$ so that the quantity $e_0(\ell)$

decreases as fast as possible[4]. This leads to the variation

$$\delta\Big\{ \langle 0|\,[G(\ell),H(\ell)]\,|0\rangle + \mu\,\|G(\ell)\|_{\mathrm{H}}^2 \Big\} = 0 \tag{3.23}$$

with the Lagrange multiplier $\mu > 0$ and $\|.\|$ denoting the HILBERT-SCHMIDT norm. For the matrix elements one obtains the expression

$$\delta\Bigg\{ \sum_{n=0}^{N} \Big(g_{0,n}(\ell) h_{n,0}(\ell) - h_{0,n}(\ell) g_{n,0}(\ell) \Big) + \mu \sum_{n,m=0}^{N} \underbrace{g_{n,m}^*(\ell)}_{-g_{m,n}(\ell)} g_{n,m}(\ell) \Bigg\} = 0\,. \tag{3.24}$$

The variation implies

$$\delta_{0,n} h_{m,0}(\ell) - h_{0,n}(\ell)\delta_{m,0} - 2\mu g_{m,n}(\ell) = 0 \tag{3.25}$$

and hence

$$g_{n,m}(\ell) = \frac{1}{2\mu}\left(h_{n,0}(\ell)\delta_{0,m} - \delta_{n,0} h_{0,m}(\ell) \right)\,. \tag{3.26}$$

In the following, we set $\mu = 1/2$ and denote this generator by $G_{\mathrm{DEO}}(\ell)$ explicitly given by

$$G_{\mathrm{DEO}}(\ell) = \begin{pmatrix} 0 & -h_{0,1}(\ell) & -h_{0,2}(\ell) & \dots & -h_{0,N}(\ell) \\ h_{1,0}(\ell) & 0 & 0 & \dots & 0 \\ h_{2,0}(\ell) & 0 & 0 & \dots & 0 \\ \vdots & \vdots & \vdots & \ddots & \vdots \\ h_{N,0}(\ell) & 0 & 0 & \dots & 0 \end{pmatrix}. \tag{3.27}$$

It has the property that only matrix elements involving the state $|0\rangle$ are different from zero.

Choosing the generator $G_{\mathrm{DEO}}(\ell)$ leads to

$$\frac{\partial e_0(\ell)}{\partial \ell} = -2 \sum_{n=1}^{N} \left| h_{0,n} \right|^2 \leq 0 \tag{3.28}$$

for the flow of the matrix element $e_0(\ell)$. Therefore, the matrix element $e_0(\ell)$ is a monotonically decreasing function and it follows

$$\lim_{\ell\to\infty} \left| h_{0,n}(\ell) \right|^2 = 0 \quad \forall n:\ n > 0 \tag{3.29}$$

[4]To correspond with our approach in second quantization (see section 3.2.3) we use the vacuum state $|0\rangle$ as the starting vector for the minimization. In principle, one can use an arbitrary starting vector.

so that in the limit $\ell \to \infty$ the matrix element $e_0(\ell)$ is an eigenvalue of the Hamiltonian $H(\ell)$. In section 3.3.4 we prove that the transformation of the matrix element $e_0(\ell)$ is the same as in the case of Mielke's generator $G_{\mathrm{M}}(\ell)$. Therefore, for $\ell \to \infty$ the matrix element $e_0(\ell)$ yields the ground state energy if $e_0(\ell)$ is linked to the ground state by matrix elements.

3.2.3 Generators in second quantization

In this section generalizations of the generator $G_{\mathrm{M}}(\ell)$ (3.17) and the generator $G_{\mathrm{DEO}}(\ell)$ (3.27) for models formulated in second quantization are discussed. We also generalize the variational derivation of generators by Dawson *et al.* [Dawson *et al.*(2008)]. The ordering properties of the introduced generators and their implications for the description of quasiparticles with finite lifetime are another important issue of this section.

The generator by Knetter and Uhrig

Knetter and Uhrig [Uhrig & Normand(1998), Knetter & Uhrig(2000)] suggested a generator that allows us to create (quasi)particle number conserving effective many-body Hamiltonians. As in the case of Mielke's generator their choice of a generator is also based on the idea of using a sign function. In contrast to Mielke's choice they used the difference of the particle number as the argument of the sign function. This generator can be regarded as a generalization of Mielke's generator for Hamiltonians formulated in second quantization. In the following, we denote this generator creating (quasi)particle number conserving effective Hamiltonians by $G_{\mathrm{pc}}(\ell)$. An analogous generator was also used by Stein [Stein(1997), Stein(1998)] for models where the use of the sign function was not necessary.

Generally, a Hamiltonian in second quantization can be written as

$$H(\ell) = \sum_{i,j=0}^{N} H_j^i(\ell) \tag{3.30}$$

where $H_j^i(\ell)$ stands for the sum over all normal ordered terms that annihilate j and create i (quasi)particles. For instance, $H_0^0(\ell)$ is proportional to the identity and describes the vacuum energy during the flow. By the expression "term", we refer to both, the operators and the corresponding prefactor. The whole ℓ-dependence of the Hamiltonian is carried by the prefactor (cf. equation (3.52) and equation (3.53)). Note that for infinitely large systems the maximum number of involved (quasi)particles N might be infinite, but this does not need to be the case.

According to the form of the Hamiltonian (3.30) the generator $G_{\mathrm{pc}}(\ell)$ is given by

$$G_{\mathrm{pc}}(\ell) = \sum_{i,j=0}^{N} \mathrm{sgn}(i-j) H^i_j(\ell) \; . \tag{3.31}$$

This means that terms in $H(\ell)$ which contain more creation operators than annihilation operators are taken over to $G_{\mathrm{pc}}(\ell)$ with the same sign. Terms with more annihilation operators than creation operators are included in $G_{\mathrm{pc}}(\ell)$ with a negative sign. Terms leaving the number of particles unchanged do not occur in $G_{\mathrm{pc}}(\ell)$.

To discuss properties of the flow and the resulting effective model obtained by using the generator $G_{\mathrm{pc}}(\ell)$ we use an eigenbasis $\{|n\rangle\}$ of the operator Q counting the (quasi)particle number

$$Q|n\rangle = q_n |n\rangle \; . \tag{3.32}$$

As before, we denote the matrix elements of the Hamiltonian $H(\ell)$ by $h_{n,m}(\ell) = \langle n|H(\ell)|m\rangle$. The matrix elements of the generator $G_{\mathrm{pc}}(\ell)$ are given by

$$\begin{aligned} g_{n,m}(\ell) &= \langle n|G(\ell)|m\rangle \\ &= \mathrm{sgn}\,(q_n - q_m)\, h_{n,m}(\ell) \end{aligned} \tag{3.33}$$

For this generator the flow equation (3.3) yields

$$\begin{aligned} \frac{\partial h_{n,m}(\ell)}{\partial \ell} = &-\mathrm{sgn}\,(q_n - q_m)\Big(h_{n,n}(\ell) - h_{m,m}(\ell)\Big)\, h_{n,m}(\ell) \\ &+ \sum_{k\neq n,m} \Big(\mathrm{sgn}(q_n - q_k) + \mathrm{sgn}(q_m - q_k)\Big)\, h_{n,k}(\ell) h_{k,m}(\ell) \; . \end{aligned} \tag{3.34}$$

Without loss of generality, we assume the eigenstates of the counting operator Q ordered so that $q_n \geq q_m$ for $n > m$. Then the derivative of the sum over the first $r+1$ diagonal elements of the Hamiltonian

$$\frac{\partial}{\partial \ell} \sum_{n=0}^{r} h_{n,n}(\ell) = 2 \sum_{n=0}^{r} \sum_{k>r} \mathrm{sgn}(q_n - q_k) \left|h_{n,k}(\ell)\right|^2 \leq 0 \tag{3.35}$$

is a monotonically decreasing function since $q_n \leq q_k$. For physically reasonable systems the spectrum of the Hamiltonian $H(\ell)$ is bounded from below. Thus the sum $\sum_{n=0}^{r} h_{n,n}(\ell)$ has to converge for $\ell \to \infty$ which also implies that

$$\lim_{\ell\to\infty} \mathrm{sgn}(q_n - q_k) \left|h_{n,k}(\ell)\right|^2 = 0 \quad \forall n,k: \; n \neq k \; . \tag{3.36}$$

Since r is arbitrary, all matrix elements $h_{n,k}(\ell)$ which couple to subspaces with a different particle number ($q_n \neq q_k$) have to vanish in the limit $\ell \to \infty$. Hence the effective Hamiltonian is block-diagonal and conserves the particle number, i.e.,

$$[Q, H_{\text{eff}}] = 0 \,. \tag{3.37}$$

This is the most significant property of the flow induced by $G_{\text{pc}}(\ell)$. It allows us to consider all sectors with a different particle number separately. For example, the ground state of the effective Hamiltonian H_{eff} is given by the (quasi)particle vacuum and diagonalization of the one-particle sector yields the one-particle energies.

Next, we discuss the asymptotic behavior of the flow equations induced by the generator $G_{\text{pc}}(\ell)$. We show that the generator $G_{\text{pc}}(\ell)$ sorts the eigenvalues e_n in ascending order of the particle number q_n of the corresponding eigenvectors such that $e_n \geq e_m$ holds, if $q_n > q_m$ [Mielke(1998), Heidbrink & Uhrig(2002), Fischer *et al.*(2010)]. Particularly, this implies that the vacuum state $|0\rangle$ of the effective Hamiltonian represents the ground state of the system.

In an eigenbasis of the operator Q the generator $G_{\text{pc}}(\ell)$ can also be written as

$$\mathbf{g}_{i,j}(\ell) = \operatorname{sgn}(q_i - q_j)\mathbf{h}_{i,j}(\ell) \,, \tag{3.38}$$

where $\mathbf{g}_{i,j}(\ell)$ and $\mathbf{h}_{i,j}(\ell)$ stand not only for a single matrix element but for the whole submatrix of the Hamiltonian $H(\ell)$ that connects the eigenspace belonging to the eigenvalue q_j with the eigenspace belonging to the eigenvalue q_i. Therefore $\mathbf{h}_{i,j}(\ell)$ is given by a matrix with the dimension $d_i \times d_j$, where d_i is the dimension of the eigenspace belonging to q_i. In general, the eigenspace for a given number of (quasi)particles q_i has a large dimension d_i, which is infinite for infinite systems, but for the purpose of the present derivation we stick to finite dimensional Hilbert spaces.

Using the form (3.38) the flow equation (3.3) yields the matrix equation

$$\begin{aligned}\frac{\partial \mathbf{h}_{i,j}(\ell)}{\partial \ell} = &-\operatorname{sgn}\big(q_i - q_j\big)\big(\mathbf{h}_{i,i}(\ell)\mathbf{h}_{i,j}(\ell) - \mathbf{h}_{i,j}(\ell)\mathbf{h}_{j,j}(\ell)\big) \\ &+ \sum_{k\neq i,j}\big(\operatorname{sgn}(q_i - q_k) + \operatorname{sgn}(q_j - q_k)\big)\mathbf{h}_{i,k}(\ell)\mathbf{h}_{k,j}(\ell) \,.\end{aligned} \tag{3.39}$$

Since the effective model will be block diagonal, all off-diagonal submatrices $\mathbf{h}_{i,j}(\ell)$ with $i \neq j$ have to vanish for $\ell \to \infty$. Hence, for large ℓ, equation (3.39) is dominated by the first term on the right hand side where the off-diagonal matrices only appear linearly. So, for large ℓ, the asymptotic behavior of (3.39) is given by

$$\frac{\partial \mathbf{h}_{i,j}(\ell)}{\partial \ell} = -\operatorname{sgn}\big(q_i - q_j\big)\big(\mathbf{h}_{i,i}\mathbf{h}_{i,j}(\ell) - \mathbf{h}_{i,j}(\ell)\mathbf{h}_{j,j}\big) + O(\mathbf{h}_{i,j}^2(\ell)) \,. \tag{3.40}$$

Note that to this order $\frac{\partial \mathbf{h}_{i,j}(\ell)}{\partial \ell} = 0 \ \forall i$, so that we can neglect the ℓ-dependence of $\mathbf{h}_{i,i}(\ell)$ and $\mathbf{h}_{j,j}(\ell)$. Without loss of generality we assume in the following that $q_i > q_j$. Then (3.40) yields

$$\frac{\partial \mathbf{h}_{i,j}(\ell)}{\partial \ell} = -\Big(\mathbf{h}_{i,i}\mathbf{h}_{i,j}(\ell) - \mathbf{h}_{i,j}(\ell)\mathbf{h}_{j,j}\Big) + O(\mathbf{h}_{i,j}^2(\ell)) \ . \tag{3.41}$$

The matrix $\mathbf{h}_{i,i}$ and the matrix $\mathbf{h}_{j,j}$ are Hermitian. Thus unitary transformations $\mathbf{u}_i$ and $\mathbf{u}_j$ exist that diagonalize $\mathbf{h}_{i,i}$ and $\mathbf{h}_{j,j}$, respectively. We will denote these diagonal matrices by $\mathbf{d}_i = \mathbf{u}_i^\dagger \mathbf{h}_{i,i}\mathbf{u}_i$ and $\mathbf{d}_j = \mathbf{u}_j^\dagger \mathbf{h}_{j,j}\mathbf{u}_j$. Multiplying (3.41) from left by $\mathbf{u}_i^\dagger$ and from right by $\mathbf{u}_j^\dagger$, one obtains

$$\frac{\partial \tilde{\mathbf{h}}_{i,j}(\ell)}{\partial \ell} = -\Big(\mathbf{d}_i\tilde{\mathbf{h}}_{i,j}(\ell) - \tilde{\mathbf{h}}_{i,j}(\ell)\mathbf{d}_j\Big) + O(\tilde{\mathbf{h}}_{i,j}^2(\ell)) \ , \tag{3.42}$$

where $\tilde{\mathbf{h}}_{i,j}(\ell) := \mathbf{u}_i^\dagger \mathbf{h}_{i,j}(\ell)\mathbf{u}_j$. According to (3.42) the matrix elements $\left(\tilde{\mathbf{h}}_{i,j}(\ell)\right)_{n,m}$ satisfy

$$\begin{aligned} \frac{\partial \left(\tilde{\mathbf{h}}_{i,j}(\ell)\right)_{n,m}}{\partial l} &= -\sum_k (\mathbf{d}_i)_{n,k}\left(\tilde{\mathbf{h}}_{i,j}(\ell)\right)_{k,m} + \sum_k \left(\tilde{\mathbf{h}}_{i,j}(\ell)\right)_{n,k}\left(\mathbf{d}_j\right)_{k,m} \\ &= -\Big((\mathbf{d}_i)_{n,n} - \left(\mathbf{d}_j\right)_{m,m}\Big)\left(\tilde{\mathbf{h}}_{i,j}(\ell)\right)_{n,m} \end{aligned} \tag{3.43}$$

in linear order in the non-diagonal matrices. Since $\mathbf{h}_{i,j}(\ell)$ vanishes for $\ell \to \infty$, $\tilde{\mathbf{h}}_{i,j}(\ell)$ must vanish as well. Therefore, for large ℓ the inequality

$$\left(\mathbf{d}_i\right)_{n,n} - \left(\mathbf{d}_j\right)_{m,m} > 0 \tag{3.44}$$

must be fulfilled[5] for all n, m for which the matrix elements $\left(\tilde{\mathbf{h}}_{i,j}(\ell)\right)_{n,m}$ are nonzero. This implies that all eigenvalues of $\mathbf{d}_i$ must be larger than the eigenvalues of $\mathbf{d}_j$. Thus, the eigenvalues are sorted in ascending order of the particle number of the corresponding eigenvectors, as asserted above.

In summary, for the generator $G_{\text{pc}}(\ell)$ the flow equation (3.3) displays the following properties:

(a) If the spectrum of $H(\ell)$ is bounded from below, the flow equation converges [Mielke(1998), Knetter & Uhrig(2000)]. This is the generic situation for physical systems. The mathematical derivation requires the Hilbert space of the system to be finite dimensional.

(b) The effective Hamiltonian H_{eff} will be block-diagonal in the sense that it conserves the (quasi)particle number [Knetter & Uhrig(2000)]. Therefore, the effec-

[5] For $\ell = \infty$ $(\mathbf{d}_i)_{n,n} - \left(\mathbf{d}_j\right)_{m,m} = 0$ is also possible.

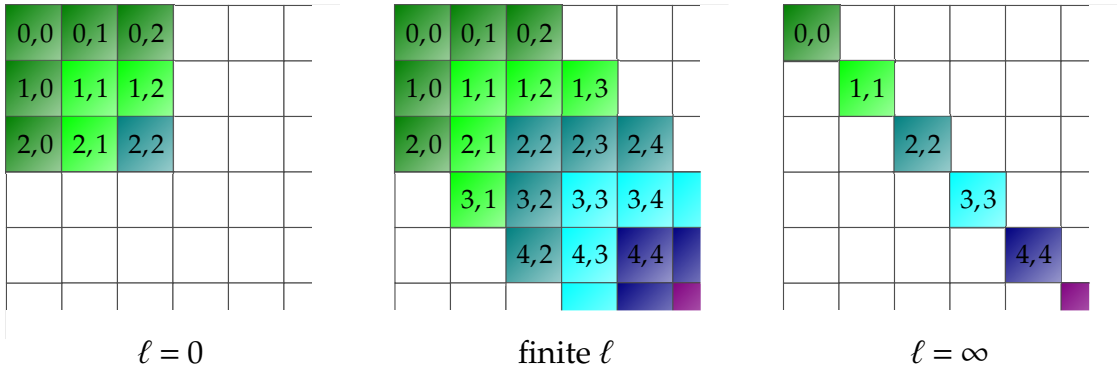

Figure 3.1: Schematical representation of the structure of the Hamiltonian $H(\ell)$ during the flow for the generator $G_{\mathrm{pc}}(\ell)$. A colored block described by the pair i, j stands for the part $H^i_j(\ell)$ of the Hamiltonian. Only those blocks are colored where at least one term of $H^i_j(\ell)$ has a non-vanishing coefficient. We assume an initial Hamiltonian that creates or annihilates at most two particles. For finite ℓ the generator $G_{\mathrm{pc}}(\ell)$ conserves the block band-diagonality of the initial Hamiltonian. For $\ell = \infty$ the Hamiltonian conserves the (quasi)particle number.

tive Hamiltonian commutes with the operator Q which counts the number of (quasi)particles

$$[Q, H_{\mathrm{eff}}] = 0 \,. \tag{3.45}$$

Thus it is of the form

$$H_{\mathrm{eff}} = \lim_{\ell\to\infty} \sum_{i=0}^{N} H^i_i(\ell) \,. \tag{3.46}$$

This property allows us to analyze subspaces with different (quasi)particle numbers separately.

(c) If the initial Hamiltonian $H(0)$ has a block band-diagonal structure (i.e. $H^i_j(0) = 0$ for $|i-j| > N_0$), this block band-diagonal structure will be conserved during the flow [Mielke(1998), Knetter & Uhrig(2000)].

(d) The generator $G_{\mathrm{pc}}(\ell)$ will sort the eigenvalues in ascending order of the particle number of the corresponding eigenvectors [Mielke(1998), Heidbrink & Uhrig(2002), Fischer *et al.*(2010)] if the eigenvectors are linked by a matrix element of the Hamiltonian.

Items (b) and (c) are schematically illustrated in figure 3.1.

Despite all the favorable properties of the generator $G_{\mathrm{pc}}(\ell)$, it is not advantageous in every situation. Particularly, the last point is both a blessing and a curse. On the one hand, it ensures that the ground state is represented by the vacuum state of the

effective model. Additionally, it produces the appropriate (quasi)particle picture in systems where the elementary excitations have an infinite lifetime. On the other hand, the described ordering of the eigenstates does not reflect the situation in many physical systems, e.g., systems with unstable (quasi)particles. This is schematically illustrated in figure 3.2.

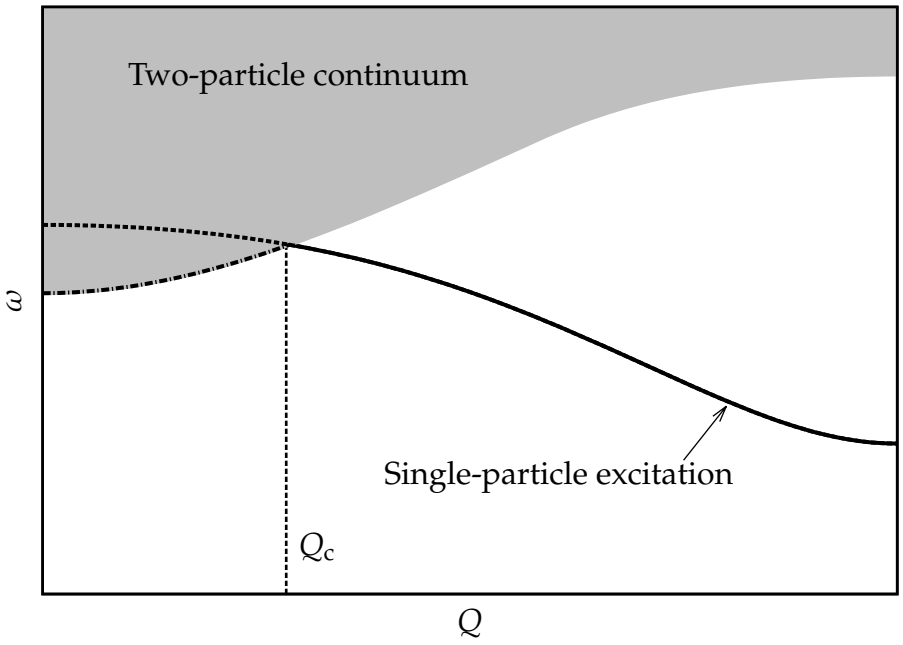

Figure 3.2: States with two excitations lying energetically below the single-particle dispersion for momentum $Q < Q_c$. If in addition the Hamiltonian contains matrix elements that connect the one-particle space with the two-particle space, the (quasi)particles will become unstable for $Q < Q_c$ (dashed line), cf. chapter 2. The generator $G_{\mathrm{pc}}(\ell)$ leads to a dispersion relation consisting of the solid and the dashed-dotted lines. Instead, the solid line and the dotted line appear to be physically more reasonable.

The generator $G_{\mathrm{pc}}(\ell)$ interprets the energetically lowest states above the ground state as the elementary excitations. In principle, it is possible to define the elementary excitations of the system in this way. But this definition can be misleading in the sense that states with very low or zero spectral weight are regarded as the elementary excitations of the system. Without spectral weight we consider such states to be meaningless in terms of elementary excitations which serve as building blocks of all other excitations. Therefore, one usually defines the states with the largest spectral weight above the ground state as the elementary excitations of the system. Moreover, previous calculations [Reischl *et al.*(2004), Reischl(2006)] strongly suggest that the rearrangement of the Hilbert space causes convergence problems in practice, because all practical calculations comprise approximations. In the perturbative approach of CUT [Knetter & Uhrig(2000), Knetter *et al.*(2003b)] (pCUT) these problems become

perceivable in the extrapolations [Schmidt & Uhrig(2005), Dusuel *et al.*(2010)], which can become meaningless and unreliable.

The second property, $[Q, H_{\text{eff}}] = 0$, of the effective Hamiltonian generated by $G_{\text{pc}}(\ell)$ makes the description of unstable (quasi)particles difficult. By construction, the generator $G_{\text{pc}}(\ell)$ produces an effective Hamiltonian H_{eff} where the elementary excitations exhibit an infinite lifetime. The information of the decay is stored in the unitary transformation and therefore an additional transformation of observables is indispensable to describe the (quasi)particle decay. This approach was first used by Kehrein and Mielke to describe dissipative quantum systems [Kehrein & Mielke(1997), Kehrein & Mielke(1998)].

In the following, we present a generator which does not eliminate the decay processes. Therefore, it is possible to study the (quasi)particle decay more easily and more directly. The transformation of the observable is still necessary for quantitative results, but the essential aspect, i.e., the finite lifetime, is obvious without this transformation.

Generator for the ground state

To tackle the problems of (quasi)particle decay within the framework of CUTs mentioned in the previous section, we introduce the adapted generator

$$G_{\text{gs}}(\ell) = \sum_{i>0}^{N} \left(H_0^i(\ell) - H_i^0(\ell) \right) \tag{3.47}$$

relying on the form of the Hamiltonian (3.30). We included only those terms in the generator $G_{\text{gs}}(\ell)$ which either contain only creation operators or only annihilation operators. The terms that contain only creation operators are included as they appear in $H(\ell)$. The terms that contain only annihilation operators are included with a negative sign relative to their sign in $H(\ell)$.

Again, the flow equation (3.3) converges if the spectrum is bounded from below. This follows directly from introducing a basis $\{|n\rangle\}$, including the vacuum state $|0\rangle$, and examining

$$\frac{\partial h_{0,0}(\ell)}{\partial \ell} = -2 \sum_{n \neq 0} \left| h_{0,n}(\ell) \right|^2 \tag{3.48}$$

with $h_{n,m}(\ell) := \langle n | H(\ell) | m \rangle$. Note that $h_{n,m}(\ell)$ describes an explicit matrix element in contrast to the previously appearing quantity $H_j^i(\ell)$ which stands for a sum over terms in second quantization. According to equation (3.48) $h_{0,0}(\ell)$ is a monotonically decreasing function of ℓ. Therefore, if the spectrum is bounded from below, its derivative must vanish in the limit $\ell \to \infty$. This also implies that

$$\lim_{\ell \to \infty} h_{0,n}(\ell) = \lim_{\ell \to \infty} \overline{h}_{n,0}(\ell) = 0 \,, \tag{3.49}$$

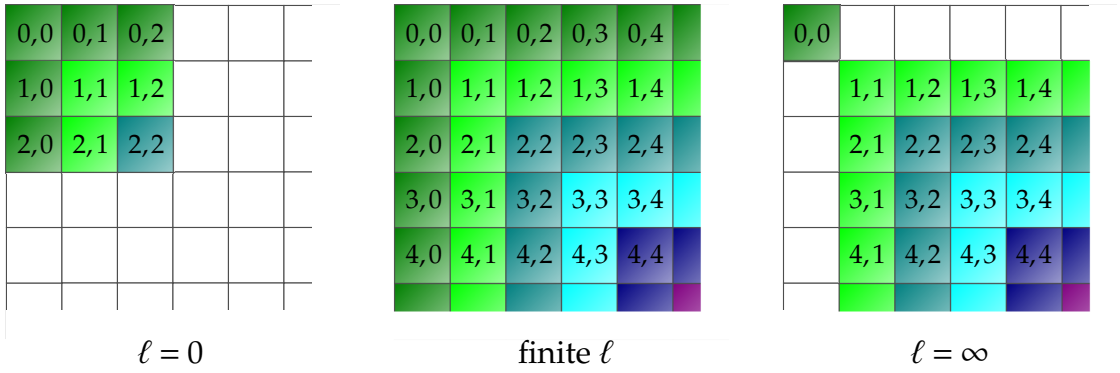

Figure 3.3: Schematical representation of the structure of the Hamiltonian $H(\ell)$ during the flow for the generator $G_{\text{gs}}(\ell)$. A colored block described by the pair i, j stands for the part $H^i_j(\ell)$ of the Hamiltonian. Only those blocks are colored where at least one term of $H^i_j(\ell)$ has a non-vanishing coefficient. We assume an initial Hamiltonian that creates or annihilates at most two particles. For finite ℓ the block band-diagonality of the initial Hamiltonian is not conserved. For $\ell = \infty$ only the $H^0_0(\ell)$ part is separated. The information about decay is still stored in the effective Hamiltonian H_{eff} in the parts $H^i_1(\ell)$ and $H^1_i(\ell)$.

i.e., all matrix elements connected to the vacuum state vanish in the limit $\ell \to \infty$. In contrast to the generator $G_{\text{pc}}(\ell)$ this generator destroys a block band-diagonal structure of the initial Hamiltonian $H(0)$. It solely separates the vacuum state from all other states. Hence the effective Hamiltonian is more difficult to analyze. The evolution of the Hamiltonian $H(\ell)$ during the flow using the generator $G_{\text{gs}}(\ell)$ is depicted in Fig. 3.3.

The generator $G_{\text{gs}}(\ell)$ (3.47) can be regarded as a generalization of the generator $G_{\text{DEO}}(\ell)$ (3.27) for Hamiltonians formulated in second quantization. Consequently, the question arises if it is possible to adapt the variational derivation of the generator $G_{\text{DEO}}(\ell)$ to the generator $G_{\text{gs}}(\ell)$ formulated in second quantization. This can be achieved by modifying the applied scalar product as we show next.

We consider a system formulated in second quantization. Each operator acting on the HILBERT space can be represented by a sum over terms consisting of a product of creation and annihilation operators and a prefactor. We call the product of creation and annihilation operators a monomial. Thus a term consists of a monomial and a prefactor.

To obtain a unique representation of each monomial we first assume them to be normal ordered. Second, a certain ordering within all creation (annihilation) operators is implied. The creation and annihilation operators are denoted by $e^\dagger_{i_k}$ and e_{i_k}, where i_k contains all quantum numbers describing the considered operator, for instance its position and spin. Note that such an expansion of a general operator is unique since all possible (ordered) monomials are linearly independent. They can be distinguished

from one another by appropriate matrix elements.

Next we define the scalar product $\langle M_1, M_2 \rangle$ of two monomials M_1 and M_2 by

$$\langle M_1, M_2 \rangle := \begin{cases} 1 & \text{for} \quad M_1 = M_2 \\ 0 & \text{for} \quad M_1 \neq M_2 \end{cases} . \tag{3.50}$$

Since any operator on the total HILBERT space can be expanded in monomials, equation (3.50) in combination with the usual bilinearity of scalar products defines a valid scalar product. The scalar product (3.50) defines different monomials as pairwise orthogonal. So the set of all possible monomials are an orthonormal basis of the super HILBERT space of operators.

The scalar product (3.50) implies the norm of an operator A as $\|A\|^2 := \langle A, A \rangle$. We again minimize $\langle 0|[G, H(\ell)]|0\rangle$, but with the constraint $\|G(\ell)\|^2 = \text{const}$. Thus we calculate the variation

$$\delta \Big\{ \langle 0|[G(\ell), H(\ell)]|0\rangle + \mu \|G(\ell)\|^2 \Big\} = 0. \tag{3.51}$$

The operators $H(\ell)$ and $G(\ell)$ are expanded in second quantization

$$H(\ell) = \sum_{\mathbf{i},\mathbf{j}} h^{\mathbf{i}}_{\mathbf{j}}(\ell) M^{\mathbf{i}}_{\mathbf{j}} \tag{3.52a}$$

and

$$G(\ell) = \sum_{\mathbf{i},\mathbf{j}} g^{\mathbf{i}}_{\mathbf{j}}(\ell) M^{\mathbf{i}}_{\mathbf{j}} \tag{3.52b}$$

with the ℓ-dependent prefactors $\left\{h^{\mathbf{i}}_{\mathbf{j}}(\ell)\right\}$ and $\left\{g^{\mathbf{i}}_{\mathbf{j}}(\ell)\right\}$. Here the bold indices $\mathbf{i}$ and $\mathbf{j}$ are sets of indices, e.g. $\mathbf{i} = \left\{i_1, \ldots, i_{N_\mathbf{i}}\right\}$. Upper indices stand for creation operators and lower indices for annihilation operators. So $M^{\mathbf{i}}_{\mathbf{j}}$ is short hand for the monomial

$$M^{\mathbf{i}}_{\mathbf{j}} = e^\dagger_{i_1} \cdots e^\dagger_{i_{N_\mathbf{i}}} e_{j_1} \cdots e_{j_{N_\mathbf{j}}} . \tag{3.53}$$

The sums $\sum_{\mathbf{i},\mathbf{j}}$ in (3.52a) and (3.52b) run over all possible ordered sets $\mathbf{i}$ and $\mathbf{j}$ so that a unique expansion in monomials $M^{\mathbf{i}}_{\mathbf{j}}$ is achieved.

Based on (3.52a) and (3.52b) the right hand side of equation (3.51) to be varied has

two additive contributions. The first one reads

$$\langle 0|\,[G(\ell),H(\ell)]\,|0\rangle = \langle 0|\,G(\ell)H(\ell) - H(\ell)G(\ell)\,|0\rangle \tag{3.54a}$$

$$= \sum_{\mathbf{i}} \left(g_{\mathbf{i}}^{\emptyset}(\ell) h_{\emptyset}^{\mathbf{i}}(\ell) - h_{\mathbf{i}}^{\emptyset}(\ell) g_{\emptyset}^{\mathbf{i}}(\ell) \right) , \tag{3.54b}$$

where the empty set $\emptyset$ stands for the lack of nontrivial operators, in particular, a prefactor $g_{\mathbf{i}}^{\emptyset}(\ell)$ belongs to a term which only contains annihilation operators. We exploit the fact that only creation operators yield non-vanishing results if applied to $|0\rangle$. Conversely, only annihilation operators yield non-vanishing bra states if placed right to $\langle 0|$.

The second contribution reads

$$\mu\left(\|G(\ell)\|^2\right) = \mu\left(\sum_{\mathbf{i},\mathbf{j}} \left| g_{\mathbf{j}}^{\mathbf{i}}(\ell) \right|^2 \right) . \tag{3.55}$$

Making the variation with respect to $g_{\mathbf{j}}^{\mathbf{i}}(\ell)$ vanish leads to

$$g_{\mathbf{j}}^{\mathbf{i}}(\ell) = \frac{1}{2\mu} \left(h_{\emptyset}^{\mathbf{i}}(\ell) \delta_{\emptyset,\mathbf{j}} - \delta_{\mathbf{i},\emptyset} h_{\mathbf{j}}^{\emptyset}(\ell) \right) . \tag{3.56}$$

This generator solely contains monomials, which are only composed of creation operators or only of annihilation operators. If we set $\mu = 1/2$ we obtain exactly the generator $G_{\mathrm{gs}}(\ell)$ we conjectured in equation (3.47). Note that the above derivation holds for all kinds of operators in second quantization, including bosons, hard-core bosons, fermions and hard-core fermions[6]. This terminates the general derivation of $G_{\mathrm{gs}}(\ell)$ and its properties.

In the following, we only consider the case where the generator $G_{\mathrm{gs}}(\ell)$ separates only the vacuum state $|0\rangle$ from all other states. But we want to mention that it is also possible to generalize the generator $G_{\mathrm{gs}}(\ell)$ to the case where the vacuum state $|0\rangle$ is replaced by a statistical operator, which defines a certain subspace, for example a reference ensemble. In this case the generator $G_{\mathrm{gs}}(\ell)$ induces an effective model on the reference subspace, which is separated from all other states. A well-known example is the derivation of the Heisenberg model or the $t-J$ model from the Hubbard model. This generalization works very much in the same way as it was done for the generator $G_{\mathrm{pc}}(\ell)$ before [Reischl *et al.*(2004), Reischl(2006), Lorscheid(2007)] and has already been used successfully to derive $t-J$ models for finite doping [Hamerla(2009), Hamerla *et al.*(2010)].

[6] Fermions of the *same kind* have a hard-core property anyway. If different kinds of fermions exist but only *one* fermion can occupy a certain site the fermions are called hard-core fermions. For example, a dimerized $t-J$ model can be formulated by a combination of hard-core bosons and hard-core fermions [Duffe(2010)].

Other similar generators

Beside the two choices $G_{\mathrm{pc}}(\ell)$ in (3.31) and $G_{\mathrm{gs}}(\ell)$ in (3.47) for a generator, there also exist other similar possibilities. For example, one can also include all terms to the generator which are connected to the one-particle subspace and define

$$G_{\mathrm{gs,1p}}(\ell) = \sum_{i>0}^{N} \left(H_0^i(\ell) - H_i^0(\ell) \right) + \sum_{i>1}^{N} \left(H_1^i(\ell) - H_i^1(\ell) \right). \tag{3.57}$$

Analogous to the cases of the generators $G_{\mathrm{pc}}(\ell)$ and $G_{\mathrm{gs}}(\ell)$ convergence of the flow equation (3.3) can be proven for a bounded spectrum by examining

$$\frac{\partial}{\partial \ell} \left(h_{0,0}(\ell) + \sum_{\substack{n \\ qn=1}} h_{n,n}(\ell) \right) = -2 \sum_{n \neq 0} \left| h_{0,n}(\ell) \right|^2 - 2 \sum_{\substack{r \\ qr=1}} \sum_{\substack{n \\ qn>1}} \left| h_{r,n}(\ell) \right|^2 . \tag{3.58}$$

Since this generator also separates the one-particle subspace from all subspaces with two and more particles (cf. equation (3.58)), it is not an ideal choice to describe (quasi)particle decay. It suffers from the same caveats as $G_{\mathrm{pc}}(\ell)$. But this generator can be the optimal choice if the (quasi)particles have an infinite lifetime, while the higher particle subspaces are overlapping in energy (cf. figure 3.4). In figure 3.5 the

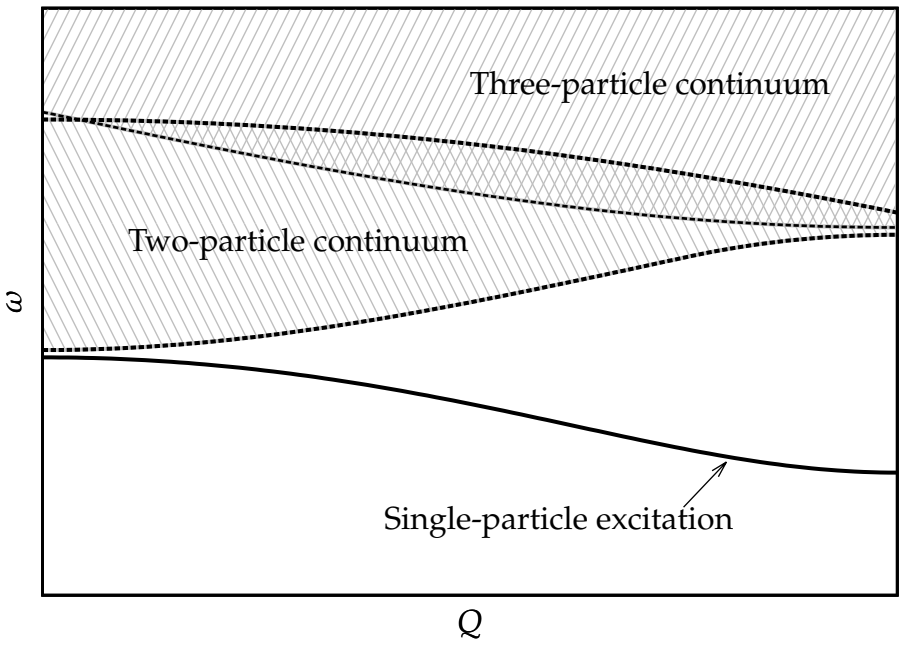

Figure 3.4: Overlap of the two- and three-particle continua.

structure of the corresponding Hamiltonian $H(\ell)$ during the flow is schematically illustrated. Nevertheless, it can be useful to use a generator which separates the $H_1^1(\ell)$ part (e.g. $G_{\mathrm{pc}}(\ell)$ or $G_{\mathrm{gs,1p}}(\ell)$) even if the (quasi)particles are unstable. In figure 3.2 a situa-

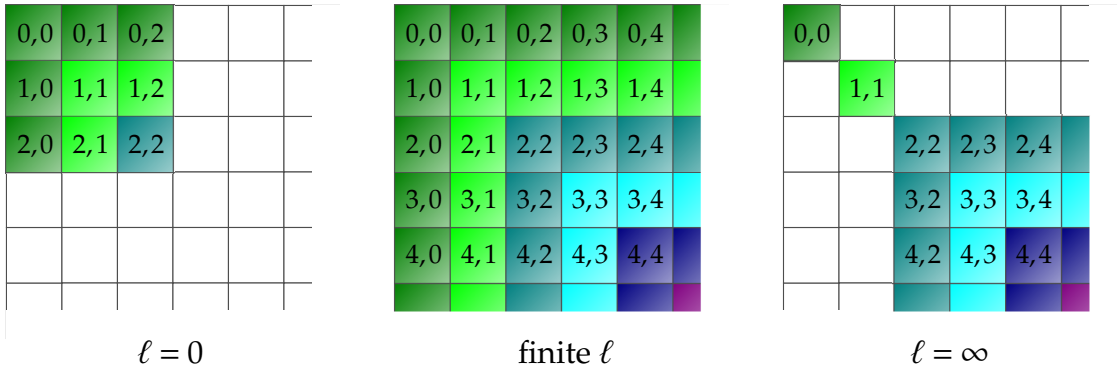

Figure 3.5: Schematical representation of the structure of the Hamiltonian $H(\ell)$ during the flow for the generator $G_{\mathrm{gs,1p}}(\ell)$. A colored block described by the pair i, j stands for the part $H^i_j(\ell)$ of the Hamiltonian. Only those blocks are colored where at least one term of $H^i_j(\ell)$ has a non-vanishing coefficient. We assume an initial Hamiltonian that creates or annihilates at most two particles. For finite ℓ the block band-diagonality of the initial Hamiltonian is not conserved. For $\ell = \infty$ the $H^0_0(\ell)$ part and the $H^1_1(\ell)$ are separated.

tion is depicted where the (quasi)particles are only unstable in a certain region ($Q < Q_c$) of the Brillouin zone. If in the actual calculation no convergence problems occurs, separating the $H^1_1(\ell)$ part will typically allow to calculate the dispersion relation quite easily in the region of stable quasiparticles ($Q > Q_c$). This can be used to test results obtained by the generator $G_{\mathrm{gs}}(\ell)$ and a following analysis of the generated effective model (cf. chapter D).

Generally, one can consider the generator

$$G_{\mathrm{gs,1p,\ldots,Mp}}(\ell) = \sum_{j=0}^{M} \sum_{i>j}^{N} \left(H^i_j(\ell) - H^j_i(\ell) \right) . \tag{3.59}$$

The effective Hamiltonian H_{eff} derived by this generator conserves the (quasi)particle number within each subspace with M or less (quasi)particles. For an initial Hamiltonian $H(0)$ at $\ell = 0$ given by

$$H(0) = \sum_{i,j=0}^{N_0} H^i_j(0) \tag{3.60}$$

the generator $G_{\mathrm{gs,1p,\ldots,Mp}}(\ell)$ is equal to the generator $G_{\mathrm{pc}}(\ell)$ for $M = N_0 \leq N$, since the generator $G_{\mathrm{pc}}(\ell)$ conserves a block band-diagonal structure.

Likewise, it might be reasonable to investigate generators which eliminate all elements connecting the one-particle space with the three-particle space (i.e. $H^3_1(\ell)$ and $H^1_3(\ell)$) but keeps elements connecting the one-particle space with the two-particle space (i.e. $H^2_1(\ell)$ and $H^1_2(\ell)$). If the three-particle space is energetically well separated from

the one-particle space no reordering should occur. Additionally, the structure of the effective Hamiltonian H_{eff} will be simpler than in the case of the generator $G_{\text{gs}}(\ell)$.

To achieve robust convergence of the flow and to generate an effective model as simple as possible also adaptations within a certain block H^i_j can be useful [Duffe & Uhrig(2011), Duffe(2010)].

In this thesis we will mainly restrict ourself to an investigation of the three generators $G_{\text{pc}}(\ell)$, $G_{\text{gs}}(\ell)$ and $G_{\text{gs,1p}}(\ell)$.

3.3 Differences and similarities of various generators

3.3.1 Example: Toy model of one hard-core boson

To illustrate some properties of Wegner's generator $G_{\text{W}}(\ell)$ and Mielke's generator $G_{\text{M}}(\ell)$ and, in particular, to illustrate the differences between them we discuss a two-level system given by one hard-core boson. In the spin $S = 1/2$ representation this two-level system is discussed in reference [Dusuel & Uhrig(2004), Reischl(2006)]. We consider the Hamiltonian

$$H(\ell) := h^{\emptyset}_{\emptyset}(\ell)\ \mathbb{1} + h^{\{1\}}_{\emptyset}(\ell)(b_1^\dagger + b_1) + h^{\{1\}}_{\{1\}}(\ell)\ b_1^\dagger b_1 \tag{3.61a}$$

$$= \begin{pmatrix} h^{\emptyset}_{\emptyset}(\ell) & h^{\{1\}}_{\emptyset}(\ell) \\ h^{\{1\}}_{\emptyset}(\ell) & h^{\emptyset}_{\emptyset}(\ell) + h^{\{1\}}_{\{1\}}(\ell) \end{pmatrix} \tag{3.61b}$$

$$= \begin{pmatrix} e_0(\ell) & h_{0,1}(\ell) \\ h_{0,1}(\ell) & e_1(\ell) \end{pmatrix} \tag{3.61c}$$

with the hard-core boson b_1 represented by

$$b_1 = \begin{pmatrix} 0 & 1 \\ 0 & 0 \end{pmatrix} \tag{3.62}$$

and obeying the commutation relation

$$\left[b_1, {b_1}^\dagger\right] = \mathbb{1} - 2\, b_1^\dagger b_1\ . \tag{3.63}$$

For simplicity, we assume all coefficients $h^{\text{i}}_{\text{j}}(\ell)$ to be real. Note, that due to the hermiticity of the Hamiltonian $h^{\emptyset}_{\{1\}}(\ell) = h^{\{1\}}_{\emptyset}(\ell)$ holds so we only have to consider $h^{\{1\}}_{\emptyset}(\ell)$.

For Wegner's generator $G_{\mathrm{W}}(\ell)$ the flow equation (3.3) yields

$$\frac{\partial h_{\emptyset}^{\emptyset}(\ell)}{\partial \ell} = -2\, h_{\{1\}}^{\{1\}}(\ell) \left(h_{\emptyset}^{\{1\}}(\ell)\right)^2 \tag{3.64a}$$

$$\frac{\partial h_{\{1\}}^{\{1\}}(\ell)}{\partial \ell} = 4\, h_{\{1\}}^{\{1\}}(\ell) \left(h_{\emptyset}^{\{1\}}(\ell)\right)^2 \tag{3.64b}$$

$$\frac{h_{\emptyset}^{\{1\}}(\ell)}{\partial \ell} = -\left(h_{\{1\}}^{\{1\}}(\ell)\right)^2 h_{\emptyset}^{\{1\}}(\ell)\,. \tag{3.64c}$$

Since all right sides of the flow equations (3.64) are proportional to $h_{\{1\}}^{\{1\}}(\ell)\, h_{\emptyset}^{\{1\}}(\ell)$ the flow stops if $h_{\{1\}}^{\{1\}}(\ell)$ *or* $h_{\emptyset}^{\{1\}}(\ell)$ are equal zero. Therefore, if $h_{\{1\}}^{\{1\}}(\ell) = 0$ (e.g. $e_0(\ell) = e_1(\ell)$) and $h_{\emptyset}^{\{1\}}(\ell) \neq 0$ the effective Hamiltonian H_{eff} will not be diagonal, cf. section 3.2.1. From equation (3.64c) follows that the off-diagonal element $h_{\emptyset}^{\{1\}}(\ell)$ always decreases monotonically.

For Mielke's generator $G_{\mathrm{M}}(\ell)$ the flow equation (3.3) reads

$$\frac{\partial h_{\emptyset}^{\emptyset}(\ell)}{\partial \ell} = -2 \left(h_{\emptyset}^{\{1\}}(\ell)\right)^2 \tag{3.65a}$$

$$\frac{\partial h_{\{1\}}^{\{1\}}(\ell)}{\partial \ell} = 4 \left(h_{\emptyset}^{\{1\}}(\ell)\right)^2 \tag{3.65b}$$

$$\frac{h_{\emptyset}^{\{1\}}(\ell)}{\partial \ell} = -h_{\emptyset}^{\{1\}}(\ell)\, h_{\{1\}}^{\{1\}}(\ell)\,. \tag{3.65c}$$

In that case a fixed point of the flow equation (3.3) is only given for $h_{\emptyset}^{\{1\}}(\ell) = 0$. Therefore, diagonality of the effective Hamiltonian $H(\ell)$ is achieved in any case, although the off-diagonal coefficient $h_{\emptyset}^{\{1\}}(\ell)$ might increase temporarily during the flow.

To illustrate differences in the ordering of eigenvalues depending on the chosen generator the evolution of the matrix elements $h_{n,m}(\ell)$ in the flow for Wegner's generator $G_{\mathrm{W}}(\ell)$ and Mielke's generator $G_{\mathrm{M}}(\ell)$ is depicted in figure 3.6 for two different sets of initial values.

In panel 3.6a the off-diagonal matrix element $h_{0,1}(\ell)$ decreases monotonically for both generators and the eigenvalues $\lim_{\ell\to\infty} e_n(\ell)$ are sorted in the same way.

This behavior changes for the set of initial values considered in panel 3.6b. In the case of Mielke's generator $G_{\mathrm{M}}(\ell)$ the off-diagonal matrix element $h_{0,1}(\ell)$ increases at first since the coefficient $h_{\{1\}}^{\{1\}}(\ell) = e_1(\ell) - e_0(\ell)$ in equation (3.65c) is negative at the beginning of the flow. The matrix element $h_{0,1}(\ell)$ increases as long as $e_0(\ell) > e_1(\ell)$. For $e_0(\ell) = e_1(\ell)$ the matrix element $h_{0,1}(\ell)$ has a maximum and for $e_0(\ell) < e_1(\ell)$ the matrix element $h_{0,1}(\ell)$ decreases exponentially. Therefore, the generator $G_{\mathrm{M}}(\ell)$ orders the eigenvalues $\lim_{\ell\to\infty} e_n(\ell)$. In contrast, for Wegner's generator $G_{\mathrm{W}}(\ell)$ no sorting of eigenvalues $\lim_{\ell\to\infty} e_n(\ell)$ occurs and the off-diagonal matrix element $h_{0,1}(\ell)$ decreases

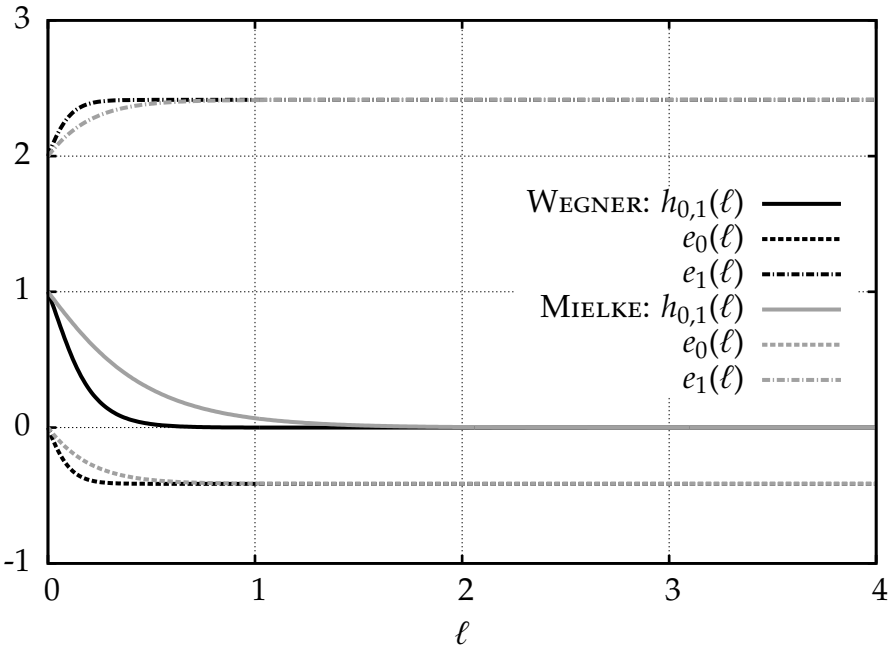

(a) Evolution of the matrix elements $h_{n,m}(\ell)$ for initial values $e_0(0) = 0$, $h_{0,1}(0) = 1$ and $e_1(0) = 2$.

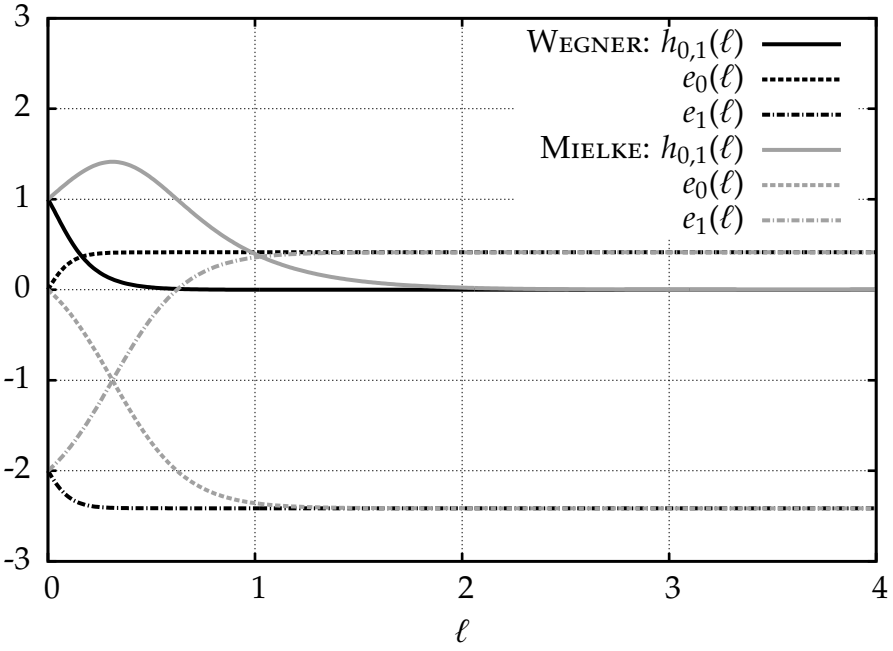

(b) Evolution of the matrix elements $h_{n,m}(\ell)$ for initial values $e_0(0) = 0$, $h_{0,1}(0) = 1$ and $e_1(0) = -2$.

Figure 3.6: Evolution of the matrix elements $h_{n,m}(\ell)$ of the toy model (3.61) in the flow for WEGNER's generator $G_W(\ell)$ and MIELKE's generator $G_M(\ell)$ for two different sets of initial values. Panel (b) shows sorting of eigenvalues $e_n(\ell)$ for MIELKE's generator $G_M(\ell)$. In the case of WEGNER's generator $G_W(\ell)$ no sorting occurs.

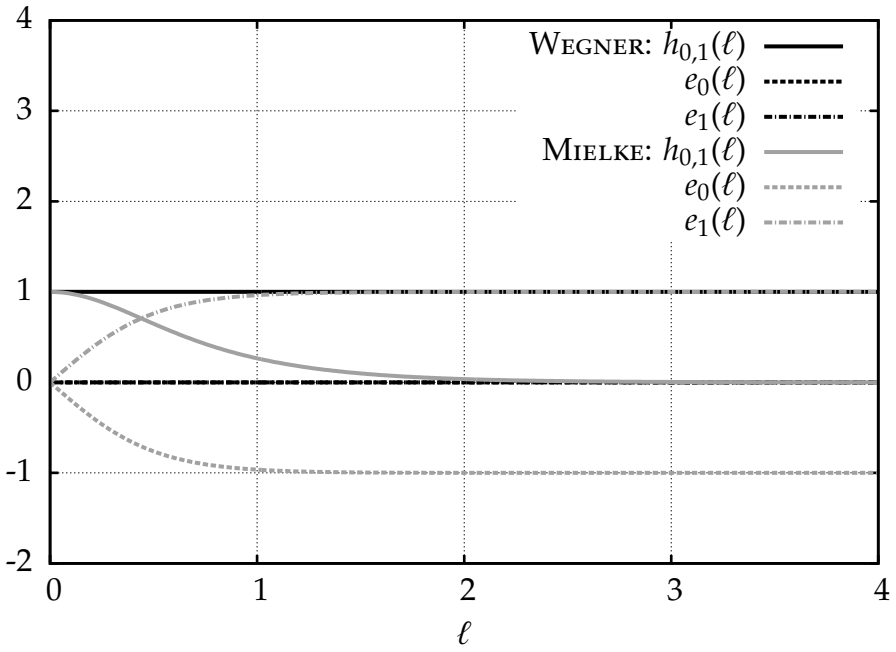

Figure 3.7: Evolution of the matrix elements $h_{n,m}(\ell)$ of the toy model (3.61) in the flow for Wegner's generator $G_{\mathrm{W}}(\ell)$ and Mielke's generator $G_{\mathrm{M}}(\ell)$ for initial values $e_0(0) = e_1(0) = 0$ and $h_{0,1}(0) = 1$. Wegner's generator $G_{\mathrm{W}}(\ell)$ stays stationary for all values ℓ.

monotonically during the whole flow.

This example illustrates that an increasing off-diagonal matrix element indicates rearrangement of the eigenvalues in the case of Mielke's generator $G_{\mathrm{M}}(\ell)$. It also shows that Wegner's generator $G_{\mathrm{W}}(\ell)$ does not sort the eigenvalues and therefore not necessarily need to yield a reasonable effective low-energy model.

Figure 3.7 illustrates that for degenerate diagonal matrix elements $e_0(\ell) = e_1(\ell)$ the flow for Wegner's generator $G_{\mathrm{W}}(\ell)$ stays stationary for all values ℓ. Thus Wegner's generator $G_{\mathrm{W}}(\ell)$ does not diagonalize the Hamiltonian (3.61). In contrast, Mielke's generator $G_{\mathrm{M}}(\ell)$ leads to a diagonal Hamiltonian for $\ell \to \infty$.

For the considered two-level system (3.61) no difference exists between the generators $G_{\mathrm{DEO}}(\ell)$, $G_{\mathrm{pc}}(\ell)$, $G_{\mathrm{gs}}(\ell)$ and Mielke's generator $G_{\mathrm{M}}(\ell)$. To discuss some differences one has to consider at least two particles. Therefore, in the next section 3.3.2 a toy model consisting of two hard-core bosons is discussed briefly.

3.3.2 Example: Toy model of two hard-core bosons

We consider the Hamiltonian

$$H(\ell) = H_0^0(\ell) + H_1^1(\ell) + H_2^2(\ell) + H_0^1(\ell) + H_1^0(\ell) + H_1^2(\ell) + H_2^1(\ell) + H_0^2(\ell) + H_2^0(\ell) \tag{3.66a}$$

with

$$H_0^0(\ell) = h_\emptyset^\emptyset(\ell)\ \mathbb{1} \tag{3.66b}$$
$$H_1^1(\ell) = h_{\{1\}}^{\{1\}}(\ell)\ b_1^\dagger b_1 + h_{\{2\}}^{\{2\}}(\ell)\ b_2^\dagger b_2 + h_{\{1\}}^{\{2\}}(\ell)\left(b_1^\dagger b_2 + b_2^\dagger b_1\right) \tag{3.66c}$$
$$H_2^2(\ell) = h_{\{1,2\}}^{\{1,2\}}(\ell)\ b_1^\dagger b_1 b_2^\dagger b_2 \tag{3.66d}$$
$$H_0^1(\ell) = h_\emptyset^{\{1\}}(\ell)\ b_1^\dagger + h_\emptyset^{\{2\}}(\ell)\ b_2^\dagger \tag{3.66e}$$
$$H_1^0(\ell) = \left(H_0^1(\ell)\right)^\dagger \tag{3.66f}$$
$$H_1^2(\ell) = h_{\{1\}}^{\{1,2\}}(\ell)\ b_1^\dagger b_1 b_2^\dagger + h_{\{2\}}^{\{1,2\}}(\ell)\ b_1^\dagger b_2^\dagger b_2 \tag{3.66g}$$
$$H_2^1(\ell) = \left(H_0^1(\ell)\right)^\dagger \tag{3.66h}$$
$$H_0^2(\ell) = h_\emptyset^{\{1,2\}}(\ell)\ b_1^\dagger b_2^\dagger \tag{3.66i}$$
$$H_2^0(\ell) = \left(H_0^2(\ell)\right)^\dagger \tag{3.66j}$$

and the two hard-core bosons b_1 and b_2 represented by

$$b_1 = \begin{pmatrix} 0 & 1 \\ 0 & 0 \end{pmatrix} \otimes \begin{pmatrix} 1 & 0 \\ 0 & 1 \end{pmatrix} \tag{3.67a}$$
$$b_2 = \begin{pmatrix} 1 & 0 \\ 0 & 1 \end{pmatrix} \otimes \begin{pmatrix} 0 & 1 \\ 0 & 0 \end{pmatrix}. \tag{3.67b}$$

As a 4×4 matrix the Hamiltonian (3.66) is given by

$$H = \begin{pmatrix} e_0 & h_{0,1} & h_{0,2} & h_{0,3} \\ h_{0,1} & e_1 & h_{1,2} & h_{1,3} \\ h_{0,2} & h_{1,2} & e_2 & h_{2,3} \\ h_{0,3} & h_{1,3} & h_{2,3} & e_3 \end{pmatrix} \tag{3.68a}$$
$$= \begin{pmatrix} h_\emptyset^\emptyset & h_\emptyset^{\{1\}} & h_\emptyset^{\{2\}} & h_\emptyset^{\{1,2\}} \\ h_\emptyset^{\{1\}} & h_\emptyset^\emptyset + h_{\{1\}}^{\{1\}} & h_{\{1\}}^{\{2\}} & h_\emptyset^{\{2\}} + h_{\{1\}}^{\{1,2\}} \\ h_\emptyset^{\{2\}} & h_{\{1\}}^{\{2\}} & h_\emptyset^\emptyset + h_{\{2\}}^{\{2\}} & h_\emptyset^{\{1\}} + h_{\{2\}}^{\{1,2\}} \\ h_\emptyset^{\{1,2\}} & h_\emptyset^{\{2\}} + h_{\{1\}}^{\{1,2\}} & h_\emptyset^{\{1\}} + h_{\{2\}}^{\{1,2\}} & h_\emptyset^\emptyset + h_{\{1\}}^{\{1\}} + h_{\{2\}}^{\{2\}} + h_{\{1,2\}}^{\{1,2\}} \end{pmatrix} \tag{3.68b}$$

where we have suppressed the ℓ-dependence of the coefficients $e_n(\ell)$, $h_{n,m}(\ell)$ and $h_{\mathbf{j}}^{\mathbf{i}}(\ell)$ to improve legibility.

Comparing the matrix representation of the MIELKE generator

$$G_{\mathrm{M}} = \begin{pmatrix} 0 & -h_{\emptyset}^{\{1\}} & -h_{\emptyset}^{\{2\}} & -h_{\emptyset}^{\{1,2\}} \\ h_{\emptyset}^{\{1\}} & 0 & -h_{\{1\}}^{\{2\}} & -h_{\emptyset}^{\{2\}} - h_{\{1\}}^{\{1,2\}} \\ h_{\emptyset}^{\{2\}} & h_{\{1\}}^{\{2\}} & 0 & -h_{\emptyset}^{\{1\}} - h_{\{2\}}^{\{1,2\}} \\ h_{\emptyset}^{\{1,2\}} & h_{\emptyset}^{\{2\}} + h_{\{1\}}^{\{1,2\}} & h_{\emptyset}^{\{1\}} + h_{\{2\}}^{\{1,2\}} & 0 \end{pmatrix} \tag{3.69}$$

and the matrix representation of the generalized generator for systems formulated in second quantization

$$G_{\mathrm{pc}} = \begin{pmatrix} 0 & -h_{\emptyset}^{\{1\}} & -h_{\emptyset}^{\{2\}} & -h_{\emptyset}^{\{1,2\}} \\ h_{\emptyset}^{\{1\}} & 0 & 0 & -h_{\emptyset}^{\{2\}} - h_{\{1\}}^{\{1,2\}} \\ h_{\emptyset}^{\{2\}} & 0 & 0 & -h_{\emptyset}^{\{1\}} - h_{\{2\}}^{\{1,2\}} \\ h_{\emptyset}^{\{1,2\}} & h_{\emptyset}^{\{2\}} + h_{\{1\}}^{\{1,2\}} & h_{\emptyset}^{\{1\}} + h_{\{2\}}^{\{1,2\}} & 0 \end{pmatrix} \tag{3.70}$$

clarifies their differences. In the case of $G_{\mathrm{pc}}(\ell)$ all matrix elements within the one-particle space are zero thus no $h_{\{1\}}^{\{2\}}(\ell)$ occurs. Likewise the matrix representation of

$$G_{\mathrm{DEO}} = \begin{pmatrix} 0 & -h_{\emptyset}^{\{1\}} & -h_{\emptyset}^{\{2\}} & -h_{\emptyset}^{\{1,2\}} \\ h_{\emptyset}^{\{1\}} & 0 & 0 & 0 \\ h_{\emptyset}^{\{2\}} & 0 & 0 & 0 \\ h_{\emptyset}^{\{1,2\}} & 0 & 0 & 0 \end{pmatrix} \tag{3.71}$$

differs from the matrix representation of

$$G_{\mathrm{gs}} = \begin{pmatrix} 0 & -h_{\emptyset}^{\{1\}} & -h_{\emptyset}^{\{2\}} & -h_{\emptyset}^{\{1,2\}} \\ h_{\emptyset}^{\{1\}} & 0 & 0 & -h_{\emptyset}^{\{2\}} \\ h_{\emptyset}^{\{2\}} & 0 & 0 & -h_{\emptyset}^{\{1\}} \\ h_{\emptyset}^{\{1,2\}} & h_{\emptyset}^{\{2\}} & h_{\emptyset}^{\{1\}} & 0 \end{pmatrix}. \tag{3.72}$$

The flow equations generated by (3.69), (3.70), (3.71) and (3.72) are given in appendix B. All four generators (3.69), (3.70), (3.71) and (3.72) decouple the ground state. Thus for the limit $\ell \to \infty$ these generators reveal the same $h_{\emptyset}^{\emptyset}(\ell) = e_0(\ell)$. Interestingly, $e_0(\ell)$ is the same for all four generators *for all* values of ℓ as shown in the left panel of figure 3.8a and in the left panel of figure 3.8b. Thus, all four generators transform the vacuum state $|0(\ell)\rangle$ exactly in the same way. It is possible to proof this statement rigorously, see section 3.3.4 and reference [Fischer *et al.*(2010)].

To quantify the speed of convergence of the flow equation for different generators, we introduce the residual off-diagonality (ROD) [Reischl *et al.*(2004), Reischl(2006)]. The ROD is defined as the square root of the sum of the moduli squared of all coefficients that contribute to the considered generator. To be more precise, in the case of generators given in matrix representation (e.g. $G_{\mathrm{M}}(\ell)$ and $G_{\mathrm{DEO}}(\ell)$) the ROD is given by

$$\mathrm{ROD}(\ell) = \left(\sum_{\substack{n,m \\ h_{n,m}(\ell) \in G(\ell)}} \left| h_{n,m}(\ell) \right|^2 \right)^{1/2} \tag{3.73}$$

and in the case of generators formulated in second quantization (e.g. $G_{\mathrm{pc}}(\ell)$ and $G_{\mathrm{gs}}(\ell)$) the ROD is defined as[7]

$$\mathrm{ROD}(\ell) = \left(\sum_{\substack{\mathbf{i},\mathbf{j} \\ h_{\mathbf{j}}^{\mathbf{i}}(\ell) \in G(\ell)}} \left| h_{\mathbf{j}}^{\mathbf{i}}(\ell) \right|^2 \right)^{1/2}. \tag{3.74}$$

The right panels of figure 3.8a and figure 3.8b show the evolution of the ROD for the toy model (3.66). For the generators $G_{\mathrm{DEO}}(\ell)$ and $G_{\mathrm{gs}}(\ell)$ the evolution of the ROD is exactly the same for all values ℓ. This is a result of the fact that for these two generators

[7] In the thermodynamic limit we consider only the representatives of the translation group.

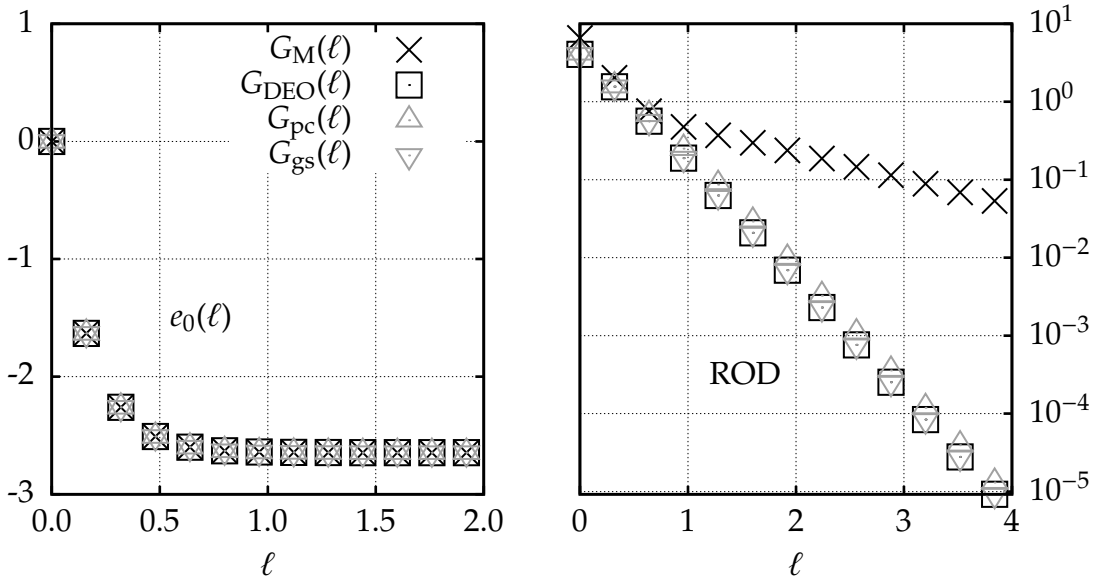

(a) Evolution of the ground state energy $e_0(\ell) = h^{\emptyset}_{\emptyset}(\ell)$ and the ROD for starting values $h^{\emptyset}_{\emptyset}(0) = 0$, $h^{\{1\}}_{\{1\}}(0) = h^{\{2\}}_{\{2\}}(0) = h^{\{2\}}_{\{1\}}(0) = h^{\{1,2\}}_{\{1,2\}}(0) = 1$, $h^{\{1\}}_{\emptyset}(0) = h^{\{2\}}_{\emptyset}(0) = 2$ and $h^{\{1,2\}}_{\{1\}}(0) = h^{\{1,2\}}_{\{2\}}(0) = h^{\{1,2\}}_{\emptyset}(0) = 1/2$.

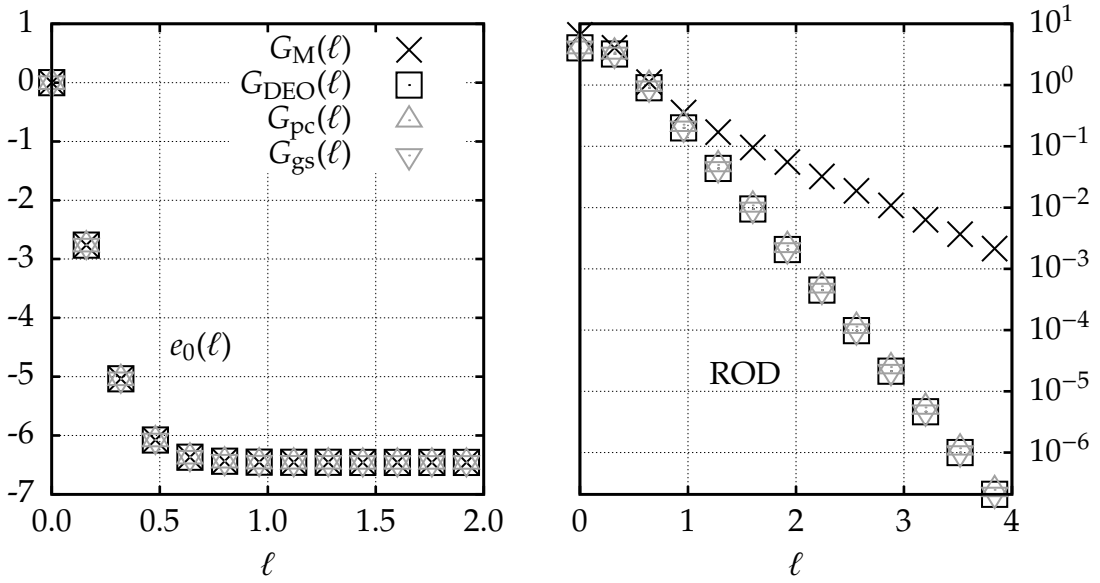

(b) Evolution of the ground state energy $e_0(\ell) = h^{\emptyset}_{\emptyset}(\ell)$ and the ROD for starting values $h^{\emptyset}_{\emptyset}(0) = 0$, $h^{\{1\}}_{\{1\}}(0) = h^{\{2\}}_{\{2\}}(0) = h^{\{2\}}_{\{1\}}(0) = h^{\{1,2\}}_{\{1,2\}}(0) = -1$, $h^{\{1\}}_{\emptyset}(0) = h^{\{2\}}_{\emptyset}(0) = 2$ and $h^{\{1,2\}}_{\{1\}}(0) = h^{\{1,2\}}_{\{2\}}(0) = h^{\{1,2\}}_{\emptyset}(0) = 1/2$.

Figure 3.8: Evolution of the ground state energy $e_0(\ell) = h^{\emptyset}_{\emptyset}(\ell)$ and the ROD of the toy model (3.66) for two different sets of initial values. The four generators $G_M(\ell)$, $G_{DEO}(\ell)$, $G_{pc}(\ell)$ and $G_{gs}(\ell)$ are considered. The ground state energy $e_0(\ell)$ is the same for all four generators *for all* values of ℓ.

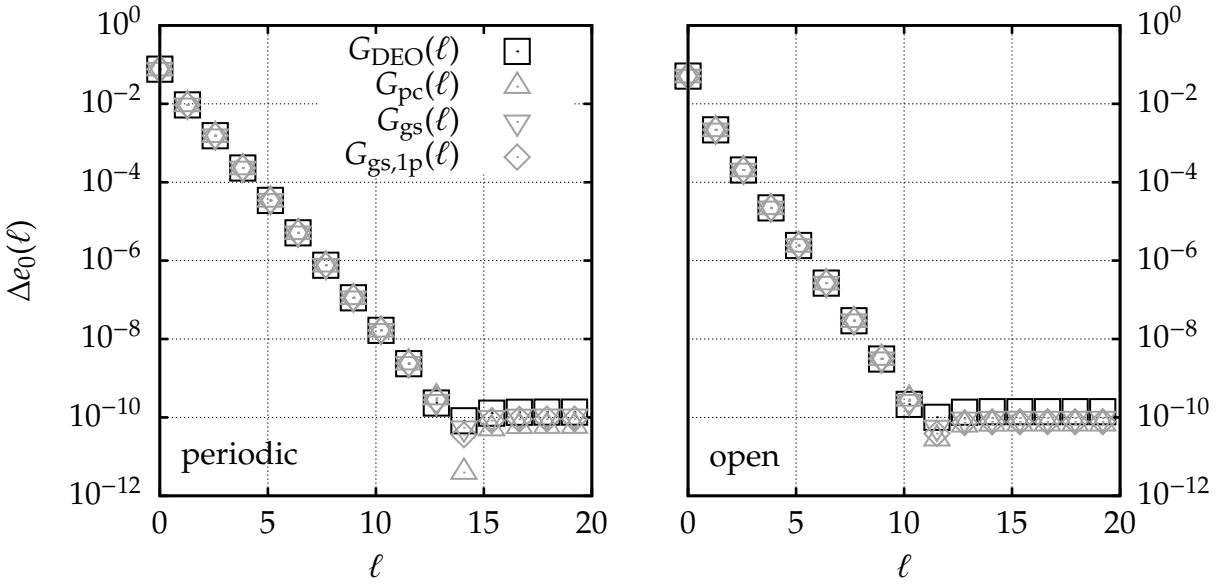

Figure 3.9: Evolution of $\Delta e_0(\ell) := |e_0(\ell) - e_{\mathrm{exact}}|$ during the flow for an antiferromagnetic spin $S = 1/2$ HEISENBERG chain with ten spins and exchange couplings $J_\perp = 1$ and $x = 0$, $y = 1$ (cf. equation (4.1)). All calculations start from the dimerized phase. The left panel shows results for periodic boundary conditions; right panel shows results for open boundary conditions.

the ROD is given by

$$\mathrm{ROD}(\ell) = -\left(\frac{\partial h_\emptyset^\emptyset(\ell)}{\partial \ell}\right)^{1/2} \tag{3.75}$$

(cf. appendix B equation (B.3a) and equation (B.4a)). Since $h_\emptyset^\emptyset(\ell)$ is identical for both generators the ROD is identical, too.

For both sets of initial values the generator $G_{\mathrm{M}}(\ell)$ converges most slowly which is a consequence of the total diagonalization induced by this generator.

3.3.3 Example: Finite antiferromagnetic spin $S = 1/2$ HEISENBERG chain

In the former section 3.3.2 it was exemplarily shown for a very simple toy model that different generators transform the vacuum state $|0(\ell)\rangle$ in the same way. Before we prove this statement generally we numerically verify this property on a more complex model.

In figure 3.9 we show numerical data verifying the equivalent transformation of the vacuum state $|0(\ell)\rangle$ by different generators. The ℓ-dependence of the difference $\Delta e_0(\ell) := |e_0(\ell) - e_{\mathrm{exact}}|$ between the vacuum expectation value $e_0(\ell) = \langle 0|H(\ell)|0\rangle$ and the

exact ground state energy e_{exact} is plotted for the generators $G_{\text{DEO}}(\ell)$, $G_{\text{pc}}(\ell)$, $G_{\text{gs}}(\ell)$ and $G_{\text{gs,1p}}(\ell)$. The system under study is an antiferromagnetic spin $S = 1/2$ HEISENBERG chain with ten spins and exchange couplings $J_\perp = 1$ and $x = 0$, $y = 1$ (cf. equation (4.1)). All calculations start from a bound operator formulation where the vacuum state is given by a product state of singlets (cf. equations (4.4) and (4.6) and figure 4.1 in section 4 for $x = 0$ and $y = 1$). We considered periodic and open boundary conditions. Figure 3.9 shows clearly that all considered generators transform the vacuum state $|0(\ell)\rangle$ in the same way. The features beyond $\ell = 12$ stem from numerical inaccuracies occurring at $\Delta e_0(\ell) \approx 10^{-10}$. These inaccuracies are shown here to illustrate where and how numerical errors make themselves felt.

In the following section 3.3.4 we prove that the considered generators transform the vacuum state $|0(\ell)\rangle$ in the same way. Additionally, we prove that the generator $G_{\text{pc}}(\ell)$ and the $G_{\text{gs,1p}}(\ell)$ transform all one-particle states identically.

3.3.4 Identical transformation of subspaces

Ground state

In section 3.3.2 and section 3.3.3 we have argued that all generators $G_{\text{M}}(\ell)$, $G_{\text{DEO}}(\ell)$, $G_{\text{pc}}(\ell)$, $G_{\text{gs}}(\ell)$ and $G_{\text{gs,1p}}(\ell)$) transform the vacuum state $|0(\ell)\rangle$ in the same way if the flow equation is solved exactly. Here we prove this statement.

Previously, we defined the ℓ-dependent Hamiltonian by $H(\ell) := U^\dagger(\ell) H U(\ell)$. Alternatively, we can keep the operators constant but make the states ℓ-dependent. This is in complete analogy to passing from the HEISENBERG picture to the SCHRÖDINGER picture. Hence, the ℓ-dependence of the vacuum state is given by $|0(\ell)\rangle = U(\ell)|0\rangle$ and the generator is given by $G(\ell) = -U^\dagger(\ell)\frac{\partial U(\ell)}{\partial \ell}$. Thus, for the derivative of $|0(\ell)\rangle$ it follows

$$\frac{\partial |0(\ell)\rangle}{\partial \ell} = \partial_l U(\ell)|0\rangle \tag{3.76a}$$

$$= U(\ell)\underbrace{U^\dagger(\ell)(\partial_l U(\ell))}_{=-G(\ell)}|0\rangle \tag{3.76b}$$

$$= -U(\ell)G(\ell)|0\rangle\ . \tag{3.76c}$$

Introducing a basis $\{|n\rangle\}$ yields

$$\frac{\partial |0(\ell)\rangle}{\partial \ell} = -\sum_n U(\ell)|n\rangle \underbrace{\langle n|G(\ell)|0\rangle}_{=g_{n,0}(\ell)}\ . \tag{3.77}$$

The key observation is that for all considered generators the definition of the matrix

element $g_{n,0}(\ell)$ is the same, namely

$$g_{n,0}(\ell) = \begin{cases} h_{n,0}(\ell) & \text{for } n > 0 \\ 0 & \text{for } n = 0 \end{cases} . \tag{3.78}$$

Applying (3.78)) to (3.77) yields

$$\frac{\partial |0(\ell)\rangle}{\partial \ell} = -\sum_{n\neq 0} U(\ell)|n\rangle\langle n|H(\ell)|0\rangle \tag{3.79a}$$

$$= -\left(\sum_{n} U(\ell)|n\rangle\langle n|H(\ell)|0\rangle\right) + U(\ell)|0\rangle\langle 0|H(\ell)|0\rangle . \tag{3.79b}$$

Shifting the ℓ-dependency to the vacuum state and using the equality $U(\ell)U^\dagger(\ell) \equiv \mathbb{1}$ provides us with

$$\frac{\partial |0(\ell)\rangle}{\partial \ell} = -H|0(\ell)\rangle + |0(\ell)\rangle\langle 0(\ell)|H|0(\ell)\rangle \tag{3.80a}$$

$$= \Big[P_0(\ell), H\Big]|0(\ell)\rangle \tag{3.80b}$$

with the ℓ-dependent projector $P_0(\ell) = |0(\ell)\rangle\langle 0(\ell)|$. According to (3.80a) the derivative of $|0(\ell)\rangle$ only depends on $|0(\ell)\rangle$ itself and the initial Hamiltonian H. Therefore, the considered generators all transform the vacuum state $|0(\ell)\rangle$ in the same way. The essential point of the proof is that for all considered generators the matrix elements $g_{n,0}(\ell)$ are defined identically by (3.78). We point out, that the statement, that all generators treat $|0\rangle$ alike, does no longer hold if approximations (truncations) are introduced.

One-particle space

The proof presented in the previous subsection can be generalized. Since the action of the generator $G_{\text{pc}}(\ell)$ and the generator $G_{\text{gs,1p}}(\ell)$ is also the same on the one-particle subspace, one can prove that they also transform all one-particle states in the same way. In the following we characterize the states by their number of (quasi)particles, so it is useful to use an eigenbasis $\{|n\rangle\}$ of the (quasi)particle number operator Q. The number of (quasi)particles of a state $|n\rangle$ is denoted by q_n. Consider the derivative of an arbitrary state $|n(\ell)\rangle$ with at most one particle ($q_n \leq 1$)

$$\frac{\partial}{\partial \ell}|n(\ell)\rangle = \partial_l U(\ell)|n\rangle \tag{3.81a}$$

$$= -U(\ell)G(\ell)|n\rangle \tag{3.81b}$$

$$= -\sum_{m} U(\ell)|m\rangle \underbrace{\langle m|G(\ell)|n\rangle}_{=g_{m,n}(\ell)} . \tag{3.81c}$$

For both generators the matrix elements $g_{m,n}(\ell)$ with $q_n \leq 1$ are given by

$$g_{m,n}(\ell) = \operatorname{sgn}(q_m - q_n) h_{m,n}(\ell) \tag{3.82}$$

according to (3.31) and (3.57). Hence we have

$$\begin{aligned} \frac{\partial}{\partial \ell} |n(\ell)\rangle = &- \sum_{\substack{m \\ q_m > 1}} U(\ell) |m\rangle \langle m| H(\ell) |n\rangle \\ &- \sum_{\substack{m \\ q_m \leq 1}} \operatorname{sgn}(q_m - q_n) U(\ell) |m\rangle \langle m| H(\ell) |n\rangle \end{aligned} \tag{3.83}$$

To the first part on the right hand side of (3.83) we add all missing contributions with $q_m \leq 1$. Hence we get

$$\begin{aligned} \frac{\partial}{\partial \ell} |n(\ell)\rangle = &- U(\ell) H(\ell) |n\rangle \\ &+ \sum_{\substack{m \\ q_m \leq 1}} U(\ell) |m\rangle \langle m| H(\ell) |n\rangle \\ &- \sum_{\substack{m \\ q_m \leq 1}} \operatorname{sgn}(q_m - q_n) U(\ell) |m\rangle \langle m| H(\ell) |n\rangle. \end{aligned} \tag{3.84}$$

Just as in the previous subsection we shift the ℓ-dependence from the Hamiltonian $H(\ell)$ to the states

$$\begin{aligned} \frac{\partial}{\partial \ell} |n(\ell)\rangle = &- H |n(\ell)\rangle \\ &+ \sum_{\substack{m \\ q_m \leq 1}} |m(\ell)\rangle \langle m(\ell)| H |n(\ell)\rangle \\ &- \sum_{\substack{m \\ q_m \leq 1}} \operatorname{sgn}(q_m - q_n) |m(\ell)\rangle \langle m(\ell)| H |n(\ell)\rangle. \end{aligned} \tag{3.85}$$

It follows that the transformation of the subspace $\{|n\rangle\}$ with $q_n \leq 1$ is independent from all other states $\{|n\rangle\}$ with $q_n > 1$. The transformation only depends on the initial Hamiltonian H. Therefore, the generator $G_{\mathrm{pc}}(\ell)$ and the generator $G_{\mathrm{gs,1p}}(\ell)$ transform the one-particle subspace in the same way. Note that this proof is not restricted to the case $q_n \leq 1$ and can easily be adapted to the case $q_n \leq M \in \mathbb{N}$. The choice (3.57) or (3.82) has to be adapted accordingly, i.e., we have pass from $G_{\mathrm{gs,1p}}(\ell)$ to $G_{\mathrm{gs,1p,\ldots,Mp}}(\ell)$ with

$$G_{\mathrm{gs,1p,\ldots,Mp}}(\ell) = \sum_{j=0}^{M} \sum_{i>j}^{N} \left(H_j^i(\ell) - H_i^j(\ell) \right) . \tag{3.86}$$

3.4 Self-similar continuous unitary transformations

So far the concept of CUTs was discussed in general. This section will focus on the self-similar realization of CUTs denoted as sCUT. Following reference [Reischl(2006)] a truncation scheme in real-space is introduced to make the CUT approach amenable for gapped infinitely large systems.

For the sCUT the Hamiltonian $H(\ell)$ is represented by a sum

$$H(\ell) = \sum_i c_i(\ell) A_i \tag{3.87}$$

of linearly independent operators A_i and their ℓ-dependent prefactors $c_i(\ell)$. During the flow only the prefactors $c_i(\ell)$ change while the operators A_i serve as a fixed basis for $H(\ell)$, which motivates the naming self-similar. Already in the first work about CUTs Wegner used such a self-similar approach [Wegner(1994)]. In principle, also all CUTs performed in matrix representation fit the definition of sCUTs given above. In this case the A_i are simply matrices where only one element is equal to one and all other are zero. But in the following the operators A_i typically are monomials of operators in second quantization, cf. equation (3.53).

The commutator $[G(\ell), H(\ell)]$ appearing on the right hand side of the flow equation (3.3) might also generate operators A_i, which do not appear in the initial Hamiltonian $H(0)$, i.e., whose prefactors $c_i(\ell)$ are zero for $\ell = 0$. These new operators A_i must be added to the Hamiltonian $H(\ell)$ and must also be considered in the generator $G(\ell)$. Then the commutator $[G(\ell), H(\ell)]$ generates even more operators, which have to be taken into account, too. For a finite dimensional Hilbert space this procedure comes to an end because the maximal number of linearly independent operators A_i is finite. Such unrestricted calculations were performed for the toy models in section 3.3.1 and section 3.3.2 and to compute the results for the ground state energy of the finite Heisenberg chain presented in section 3.3.3.

For large systems such an unrestricted approach is not possible due to the proliferating number of operators A_i. Especially in the thermodynamic limit or in bosonic systems one has to deal with an infinite number of operators A_i. Hence it is not possible to obtain a closed set of differential equations. Thus in practice one has to decide which operators A_i are important to describe the underlying physics properly and which can be neglected.

One established truncation scheme is to use a perturbative approach (pCUT) which is based on the generator $G_{\mathrm{pc}}(\ell)$ [Knetter & Uhrig(2000), Knetter *et al.*(2003b)]. But since we intend to describe the decay of (quasi)particles so that variations of the generator $G_{\mathrm{pc}}(\ell)$ have to be used (cf. section 3.2.3), we choose the self-similar approach (sCUT) where modifications to the generator $G_{\mathrm{pc}}(\ell)$ are easy to realize. But there is no fun-

damental reason why an adapted generator cannot be implemented perturbatively as well [Krull(2011)].

In actual sCUT calculations the differential equations for the prefactors $c_i(\ell)$ determined by the flow equation (3.3) are calculated by performing the following steps:

(a) If necessary, define a truncation scheme (cf. section 3.4.3) that restricts the maximal number of operators A_i.

(b) Set up a Hamiltonian $H(\ell)$ with operators A_i and prefactors $c_i(\ell)$ given by the initial Hamiltonian $H(0)$.

(c) Define a generator $G(\ell)$ by using the operators A_i and by choosing its prefactors $c_i^G(\ell)$. The only restriction on the prefactors $c_i^G(\ell)$ is that the resulting generator $G(\ell)$ is antihermitian but typically the prefactors $c_i^G(\ell)$ of the generator $G(\ell)$ will be determined by the prefactors $c_i(\ell)$ of the Hamiltonian $H(\ell)$ (cf. section 3.2).

(d) Calculate the commutator $[G(\ell), H(\ell)]$ and compare the prefactors of the operators on the left hand and on the right hand side of the flow equation (3.3). This yields differential equations for the prefactors $c_i(\ell)$ of the form

$$\frac{\partial c_i(\ell)}{\partial \ell} = \sum_{j,k} a_{ijk}\, c_j^G(\ell) c_k(\ell) \,. \tag{3.88}$$

The factors a_{ijk} are determined by the commutator $\left[A_j, A_k\right]$. If new operators emerge, the truncation scheme decides whether these operators are considered or not.

(e) Repeat step (d) until no new operators emerge which fit the truncation scheme.

(f) Solve the differential equations (3.88).

Formally, the effective Hamiltonian H_{eff} is given by

$$H_{\text{eff}} = \sum_i c_i(\infty) A_i \,. \tag{3.89}$$

Since in actual calculations an analytic integration of the system of coupled differential equations (3.88) is usually not feasible, the equations have to be solved numerically. The initial values $c_i(0)$ are determined by $H(0)$. New operators A_i emerging in step (d) start with an initial prefactor equal to zero.

The sCUT approach works for observables $O(\ell)$ in the same way as for the Hamiltonian $H(\ell)$, but usually the truncation scheme for the observables $O(\ell)$ differs from the truncation scheme for the Hamiltonian $H(\ell)$, cf. section 3.4.3. The form of the generator

$G(\ell)$ is predicted by the Hamiltonian $H(\ell)$, cf. section 3.2. Thus it is convenient to transform the Hamiltonian $H(\ell)$ and the observable $O(\ell)$ simultaneously instead of saving the Hamiltonian $H(\ell)$ for each ℓ to transform the observable $O(\ell)$.

3.4.1 Real space representation by local operators

Many problems in solid state physics are represented by localized states (e.g. WANNIER states) and local Hamiltonians in second quantization [Ashcroft & Mermin(1976)] on a lattice. By local Hamiltonians we refer to Hamiltonians whose hopping and interaction terms have a finite range in real space. An example is a tight-binding Hamiltonian for non-interacting fermions that contains only hopping terms to a few nearest neighbors. This example also illustrates that a local Hamiltonian does not necessarily describe local physics. The eigenstates of such a tight-binding Hamiltonian are momentum eigenstates which are extended over the whole lattice.

In second quantization the Hamiltonian $H(\ell)$ is given by

$$H(\ell) = \sum_{\mathbf{i},\mathbf{j}} h^{\mathbf{i}}_{\mathbf{j}}(\ell) M^{\mathbf{i}}_{\mathbf{j}} \tag{3.90}$$

with the normal ordered monomials

$$M^{\mathbf{i}}_{\mathbf{j}} = e^{\dagger}_{i_1} \cdots e^{\dagger}_{i_{N_i}} e_{j_1} \cdots e_{j_{N_j}} , \tag{3.91}$$

see reference [Knetter *et al.*(2003b)].

Let us now assume that the local HILBERT space on a lattice site r consists of four states. In chapters 4, 5 and 6 spin systems are mapped to a triplon representation (cf. appendix C) which leads to such local HILBERT spaces with four states. The generalization to any finite number of states is obvious. The four states on site r are labeled by $|r,n\rangle$ with $n \in \{0,1,2,3\}$. We define the states $|r,0\rangle := (1,0,0,0)^T_r$ as local reference states. The global reference state $|0\rangle$ is given by the product state

$$|0\rangle = \bigotimes_r |r,0\rangle \ . \tag{3.92}$$

To ensure that the CUT can transfer the global reference state $|0\rangle$ into the ground state for $\ell \to \infty$ it is important that $|0\rangle$ is connected to the ground state by the Hamiltonian, e.g., $|0\rangle$ has the same quantum numbers as the ground state. The local excitations $|r,\alpha\rangle$

with the flavor $\alpha \in \{1,2,3\}$ can be created by the creation operators $e^\dagger_{\alpha,r}$ as follows

$$|r,1\rangle = e^\dagger_{1,r}|r,0\rangle = \begin{pmatrix} 0 & 0 & 0 & 0 \\ 1 & 0 & 0 & 0 \\ 0 & 0 & 0 & 0 \\ 0 & 0 & 0 & 0 \end{pmatrix}_r \begin{pmatrix} 1 \\ 0 \\ 0 \\ 0 \end{pmatrix}_r = \begin{pmatrix} 0 \\ 1 \\ 0 \\ 0 \end{pmatrix}_r \tag{3.93a}$$

$$|r,2\rangle = e^\dagger_{2,r}|r,0\rangle = \begin{pmatrix} 0 & 0 & 0 & 0 \\ 0 & 0 & 0 & 0 \\ 1 & 0 & 0 & 0 \\ 0 & 0 & 0 & 0 \end{pmatrix}_r \begin{pmatrix} 1 \\ 0 \\ 0 \\ 0 \end{pmatrix}_r = \begin{pmatrix} 0 \\ 0 \\ 1 \\ 0 \end{pmatrix}_r \tag{3.93b}$$

$$|r,3\rangle = e^\dagger_{1,r}|r,0\rangle = \begin{pmatrix} 0 & 0 & 0 & 0 \\ 0 & 0 & 0 & 0 \\ 0 & 0 & 0 & 0 \\ 1 & 0 & 0 & 0 \end{pmatrix}_r \begin{pmatrix} 1 \\ 0 \\ 0 \\ 0 \end{pmatrix}_r = \begin{pmatrix} 0 \\ 0 \\ 0 \\ 1 \end{pmatrix}_r . \tag{3.93c}$$

The annihilation operator $e_{\alpha,r}$ are given by the hermitian conjugate of the matrices appearing in (3.93). The operators $e^\dagger_{\alpha,r}$ create so called hard-core particles, where the name hard-core particle implies that only one particle can exist on a given site r and has its origin in the description of nucleon-nucleon interaction where the force between them is singular [Fetter & Walecka(1971)]. Therefore, applying a creation operator on an occupied state yields zero, reflected by $e^\dagger_{\alpha,r}e^\dagger_{\beta,r} = 0$. The set

$$\left\{ \mathbb{1}_4 \, , e^\dagger_{\alpha,r} \, , e_{\alpha,r} \, , e^\dagger_{\alpha,r}e_{\beta,r} \;\middle|\; \alpha,\beta = 1,2,3 \right\} \tag{3.94}$$

builds a basis for the operators of the local Hilbert space and hence any local operator A_r can be decomposed into a linear combination of these basis operators. All operators except the identity operator $\mathbb{1}_4$ are normal ordered in the sense of

$$\langle 0|A_r|0\rangle = 0 \, . \tag{3.95}$$

Note that one uses the identity operator in the set (3.94) and not the operator

$$\mathbb{1}_4 - \sum_{\alpha=1}^{3} e^\dagger_{\alpha,r}e_{\alpha,r} = \begin{pmatrix} 1 & 0 & 0 & 0 \\ 0 & 0 & 0 & 0 \\ 0 & 0 & 0 & 0 \\ 0 & 0 & 0 & 0 \end{pmatrix}_r . \tag{3.96}$$

If one would use this operator instead of the identity operator, the action of a local operator on a state would depend on the form of the state on all other site, which would not correspond to the concept of second quantization. To illustrate this point let

us consider a system with N sites and a local operator A_r acting on site r. Formally, the operator A_r has the matrix representation

$$\mathbb{1}_{4,1} \otimes \ldots \otimes \mathbb{1}_{4,r-1} \otimes A_r \otimes \mathbb{1}_{4,r+1} \otimes \ldots \otimes \mathbb{1}_{4,N} \,, \tag{3.97}$$

where one usually omits all identity matrices $\mathbb{1}_4$. But exactly these identity matrices ensure that the action of the local operator A_r does not depend on states on any other site $r \neq r'$. If one used the operator (3.96) instead of the identity $\mathbb{1}_4$ in equation (3.97), the operator A_r could only yield a non vanishing result if it is applied to a state built up by the local reference states $|r,0\rangle$ for all $r \neq 0$. This illustrates why one uses the identity matrix $\mathbb{1}_4$ instead of the operator (3.96) to build up the local basis (3.94).

The commutation relations for the hard-core particle operators in (3.93) are

$$\left[e_{\alpha,r}, e^\dagger_{\beta,s}\right] = \delta_{r,s}\left(\delta_{\alpha,\beta}\left(\mathbb{1}_4 - \sum_{\gamma=1}^{3} e^\dagger_{\gamma,r} e_{\gamma,r}\right) - e^\dagger_{\beta,r} e_{\alpha,r}\right) \tag{3.98}$$

where we assumed that operators on different sites fulfill bosonic commutation relations. The additional contributions appearing in the commutator for hard-core bosons (3.98) in comparison to the commutation relations for normal bosons complicate analytical calculations with hard-core particles. For example, a usual Bogoliubov transformation will fail to diagonalize a bilinear Hamiltonian. Also, even for a non-interacting system of hard-core bosons an exact analytic expression for the partition function is not available [Troyer *et al.*(1994)] so that calculations of thermodynamic quantities are also more involved.

In this thesis only the case of a unique reference state $|0\rangle$ as described above is considered so we restrict all discussions to this case. Nevertheless, we want to mention that the sCUT method can also be applied for an ensemble of reference states. For a detailed discussion see references [Reischl *et al.*(2004), Reischl(2006), Hamerla(2009), Hamerla *et al.*(2010)].

3.4.2 Translation invariant systems and other symmetries

A favorable property of the sCUT approach is that the translational symmetry of a lattice can be implemented easily, which makes calculations in the thermodynamic limit possible. Terms in the Hamiltonian that are related by the translation symmetry have the same coefficient so only one representative term needs to be considered. Let T be the translation group. Then the Hamiltonian $H(\ell)$ can be rewritten as

$$H(\ell) = \sum_i c_i(\ell) A_i = \sum_T \sum_j \tilde{c}_j(\ell) \tilde{A}_j \tag{3.99}$$

where $\tilde{A}_j$ are the representatives of the translation group T and $\tilde{c}_j(\ell)$ their coefficients[8] . Using these representatives the flow equation (3.3) is given by

$$\begin{aligned}\frac{\partial}{\partial\ell}\sum_T\sum_i \tilde{c}_i(\ell)\tilde{A}_i &= \left[\sum_T\sum_j \tilde{c}_j^G(\ell)\tilde{A}_j, \sum_T\sum_k \tilde{c}_k(\ell)\tilde{A}_k\right] \\ &= \sum_T\left[\sum_j \tilde{c}_j^G(\ell)\tilde{A}_j, \sum_T\sum_k \tilde{c}_k(\ell)\tilde{A}_k\right] .\end{aligned} \tag{3.100}$$

Since in equation (3.100) the sum over the translation group T appears on the left hand and on the right hand side of the equal sign one can drop this sum and derive the flow equations only for the representatives.

The second sum over the translation group T on the right hand site of equation (3.100) can not be canceled. Nevertheless, if one assumes that the operators A_j have only a finite range and that the local HILBERT space has a finite dimension, the commutator $\left[\sum_j \tilde{c}_j^G(\ell)\tilde{A}_j, \sum_T\sum_k \tilde{c}_k(\ell)\tilde{A}_k\right]$ only produces a finite number of non-vanishing terms.

In the same way as the translation symmetry also other possible symmetries can be taken into account. Typical examples are lattice symmetries reflected by the corresponding space group, spin rotation symmetries or a particle-hole symmetry. Likewise, relations between coefficients caused by hermiticity of the Hamiltonian $H(\ell)$ and the antihermiticity of the generator $G(\ell)$ can be used to reduce the computational effort.

Note that the coefficients $\tilde{c}_i(\ell)$ of the representatives $\tilde{A}_i$ might be different from the corresponding coefficients $c_i(\ell)$ of A_i. This is because some terms can be invariant under a certain symmetry operation so that they occur several times in the sum over the symmetry group which must be considered in the coefficient $\tilde{c}_i(\ell)$. As an example let us assume that the hopping terms $h^{\{i\}}_{\{j\}}(\ell)\, e_i^\dagger e_j$ and $h^{\{j\}}_{\{i\}}(\ell)\, e_j^\dagger e_i$ are related by a reflection symmetry so that $h^{\{i\}}_{\{j\}}(\ell) = h^{\{j\}}_{\{i\}}(\ell)$ holds. As representatives one can choose all terms $\tilde{h}^{\{i\}}_{\{j\}}(\ell)\, e_i^\dagger e_j$ with $i \le j$. For $i < j$ indeed $\tilde{h}^{\{i\}}_{\{j\}}(\ell) = h^{\{i\}}_{\{j\}}(\ell) = h^{\{j\}}_{\{i\}}(\ell)$ holds. But for $i = j$ the coefficient of the representative is only one half of the corresponding coefficient in the unsymmetrized Hamiltonian, e.g. $2\tilde{h}^{\{i\}}_{\{j\}}(\ell) = h^{\{i\}}_{\{j\}}(\ell)$, since interchanging i and j leaves $e_i^\dagger e_j$ invariant for $i = j$. In addition some symmetry operations can also lead to a change of the sign of the coefficient.

For translational invariant systems formulated in real space by local operators we

[8] For the translation group $c_i(\ell) = \tilde{c}_i(\ell)$ holds. This does not need to be the case for other symmetry groups.

use as a notation for terms of the Hamiltonian

$$\begin{matrix}\alpha_0,\alpha_1,\ldots,\alpha_{N_c}\\ \beta_0,\beta_1,\ldots,\beta_{N_a}\end{matrix}\left[c_{H|_{N_a}^{N_c}}\right]_{l_0,l_1,\ldots,l_{N_a}}^{d_1,\ldots,d_{N_c}} e^\dagger_{\alpha_0,r}\, e^\dagger_{\alpha_1,r+d_1}\cdots e^\dagger_{\alpha_{N_c},r+d_1+\ldots+d_{N_c}}\, e_{\beta_0,r+l_0}\, e_{\beta_1,r+l_0+l_1}\cdots e_{\beta_{N_a},r+l_0+l_1+\ldots+l_{N_a}} \tag{3.101}$$

where we split the local degrees of freedom, flavors, $\alpha_0,\ldots,\alpha_{N_c},\beta_0,\ldots,\beta_{N_a}$ from the relative lattice distances $d_1,\ldots,d_{N_c},l_0,\ldots,l_{N_a}$. Note, that due to translation symmetry no d_0 occurs. If a term purely consists of annihilation operators, the parameter l_0 is superfluous and therefore does not occur in the coefficient, e.g.,

$$\beta_0,\beta_1,\ldots,\beta_{N_a}\left[c_{H|_{N_a}^{N_c}}\right]_{l_1,l_2,\ldots,l_{N_a}} e_{\beta_0,r}\, e_{\beta_1,r+l_1}\cdots e_{\beta_{N_a},r+l_1+\ldots+l_{N_a}}\,. \tag{3.102}$$

For hard-core particles $d_1,\ldots,d_{N_c},l_1,\ldots,l_{N_a}>0$ holds. The only distance that can become zero and negative is l_0. We also have neglected the ℓ-dependence of the coefficient to enhance legibility. For terms describing a local observable $O(\ell,r)$ connected to the site r we use the notation

$$\begin{aligned}&\begin{matrix}\alpha_0,\alpha_1,\ldots,\alpha_{N_c}\\ \beta_0,\beta_1,\ldots,\beta_{N_a}\end{matrix}\left[c_{O|_{N_a}^{N_c}}\right]_{l_0,l_1,\ldots,l_{N_a}}^{d_0,d_1,\ldots,d_{N_c}} e^\dagger_{\alpha_0,r+d_0}\, e^\dagger_{\alpha_1,r+d_0+d_1}\cdots e^\dagger_{\alpha_{N_c},r+d_0+d_1+\ldots+d_{N_c}}\times\\ &\quad\times e_{\beta_0,r+l_0}\, e_{\beta_1,r+l_0+l_1}\cdots e_{\beta_{N_a},r+l_0+l_1+\ldots+l_{N_a}}\end{aligned} \tag{3.103}$$

where the distance $d_0\in\mathbb{Z}$ may occur.

3.4.3 Truncation scheme

A crucial point of the sCUT approach is the choice of an appropriate truncation scheme, ideally justified by the physics under study. Formally, it is possible to estimate effects of the truncation via an inhomogeneous flow equation [Drescher(2009), Drescher *et al.*(2011)]. But unfortunately, especially in infinite systems, the errors typically are highly overestimated which makes an optimization of the truncation scheme according to these estimates nearly impossible in actual calculations.

Truncation scheme for the Hamiltonian

In the following we will describe a truncation scheme for translational invariant Hamiltonians in second quantization formulated by local operators, where the truncation scheme is based on the locality of the terms. If we consider gapped systems the correlation length ξ and the gap energy Δ satisfy the relation $\Delta\propto\xi^{-z}$ where z denotes the dynamic critical exponent [Sachdev(1999)]. Therefore, the correlations are local which implies that long-range interactions are less important. This property motivates a truncation scheme which disregards long-range interactions

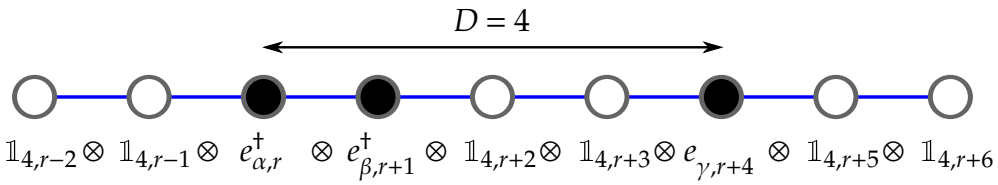

Figure 3.10: Schematical representation the monomial $e^\dagger_{\alpha,r} e^\dagger_{\beta,r+1} e_{\gamma,r+4}$ with extension $D = 4$. Filled circles indicate non-trivial operators.

Since this thesis only deals with sCUTs in one dimension we only present a truncation scheme for one-dimensional systems. Nevertheless, the presented approach can be easily generalized to higher dimensions [Reischl *et al.*(2004), Reischl(2006), Hamerla(2009), Hamerla *et al.*(2010)].

We first define a measure for the locality of a term, which we call the extension D. The extension D of a term is defined by the distance between the rightmost to the leftmost site on which the monomial acts in a nontrivial way. For example, the term $e^\dagger_{\alpha,r} e^\dagger_{\beta,r+1} e_{\gamma,r+4}$ has an extension $D = 4$, cf. figure 3.10. Second, we define the truncation scheme by choosing a maximal extension $D_{\max}$ discarding all terms with a larger extension ($D > D_{\max}$).

It turns out that it is appropriate to define not only one maximal extension for all terms but to keep terms with a different number of annihilation or creation operators up to different maximal extensions [Reischl(2006)]. Accordingly, terms with n annihilation or creation operators in total are required to have an extension D_n or less to be kept in the flow equation. As a second truncation criterion we admit only terms which create or annihilate not more than N_t (quasi)particles. Thus the total truncation scheme is defined by the value of N_t and the set of extensions $\mathbf{D} = (D_2, \ldots, D_{2N_t})$.

Note, that in translational invariant systems with a finite-dimensional local Hilbert space D_1 is superfluous. In the case of a four-dimensional local Hilbert space as considered before only six different monomials exist, which act on one site only, in particular, $e^\dagger_1$, $e^\dagger_2$, $e^\dagger_3$, e_1, e_2 and e_3. In figure 3.11 a truncation scheme with $N_t = 3$ is illustrated.

Additional, certain symmetries might cause that some blocks $H^i_j(\ell)$ of the full Hamiltonian $H(\ell)$ never occur during the flow. As an example, for the symmetric spin $S = 1/2$ Heisenberg ladder ($y = 0$, cf. section 4.1) no terms occur that consist of an odd number of operators. Therefore, we do not need to define maximum extensions $D_3, D_5, \ldots$. In the notation of the set of extensions $\mathbf{D}$ we replace such superfluous extensions by a dot, e.g. $\mathbf{D} = (8, ., 6, ., 4)$.

It is worthwhile to emphasize that this truncation scheme does not turn our approach to a calculation on a finite cluster. It is a self-similar calculation strictly in the thermodynamic limit. We only truncate the range of the interactions in real space, but not the Hilbert space.

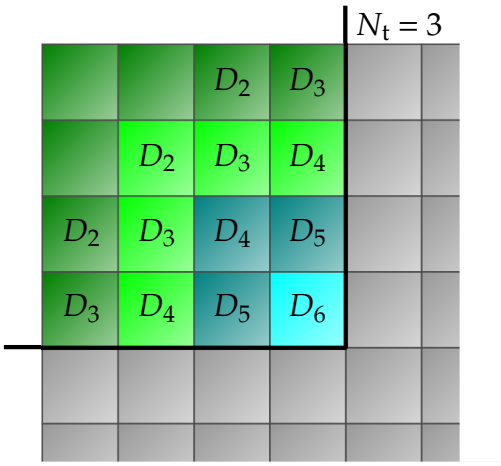

Figure 3.11: Schematical representation of a truncation scheme with $N_t = 3$. All contributions $H^i_j(\ell)$ (cf. figure 3.1) with $i, j > N_t = 3$ (grey blocks) are neglected. In a part $H^i_j(\ell)$ only those terms are considered which extension D is smaller or equal to the maximal extension D_{i+j}, i.e. $D \leq D_{i+j}$.

Truncation scheme for observables

Since a local observable is connected to a certain site one has to define a separate truncation scheme for observables [Reischl(2006)]. Let us consider a local observable $O(\ell, r)$ located at site r for $\ell = 0$. During the flow the observable delocalizes so that it also acts on sites different from r. Again we define a truncation scheme relying on the locality of the problem.

Firstly, we define an extension D^O for terms occurring in the observable $O(\ell, r)$. In contrast for terms appearing in the Hamiltonian, where only the distance between the rightmost to the leftmost site have an effect on the extension, the extension D^O of a observable $O(\ell, r)$ is defined as *the sum* of the distances of *all* its local operators to the site r.

Figure 3.12 illustrates the definition of the observable extension D^O. For $\ell = 0$ the observable $O(\ell, r)$ only acts on site r as indicated by the filled circle in panel (a). During the flow also terms with a structure depicted in panel (b), (c) and (d) might occur. Panel (b) shows a term of the observable $O(\ell, r)$ only acting on site $r-2$. Thus the observable extension of this term is $D^O = |(r-2) - r| = 2$. The term depicted in panel (c) acts on site $r-2$ and on site $r-1$. Its observable extension is $D^O = |(r-2) - r| + |(r-1) - r| = 3$. Finally, the term in panel (d) acts on four sites whereby its action on site r does not contribute to it observable extension $D^O = |(r-2) - r| + |(r-1) - r| + |(r+2) - r| = 5$.

Note, that the terms appearing in panel (b), (c) and (d) are generated by the commutator on the right hand side of equation (3.9). In this thesis the generator $G(\ell)$ is always built by terms occurring in the Hamiltonian $H(\ell)$. Thus, if the Hamiltonian $H(\ell)$ is sufficiently well described by terms with a finite extension, also the observ-

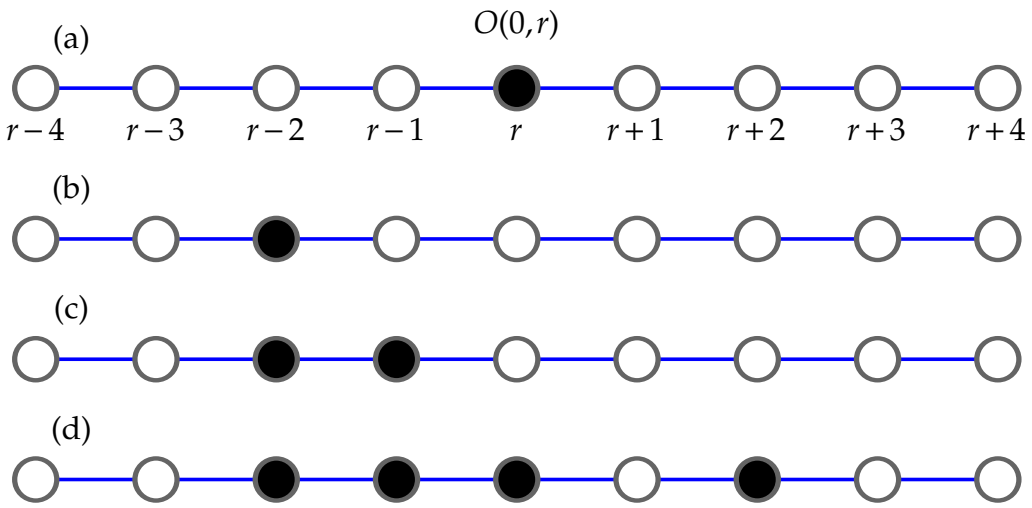

Figure 3.12: Illustration of the definition of the observable extension D^O, cf. text. Panel (a) depicts the local observable $O(0,r)$ for $\ell = 0$. Panel (b), (c) and (d) depict terms occurring during the flow for $\ell > 0$. Open circles indicate sites where the term under study acts as the identity. Filled circles indicate sites on which a non-trivial operator acts. (b) The term acts only at site $r-2$ and has the observable extension $D^O = 2$. (c) This term additionally acts on site $r-1$ and therefore has an observable extension of $D^O = 3$. (d) A term acting on four sites with observable extension $D^O = 5$. Terms beyond a certain maximal observable extension are omitted.

able $O(\ell,r)$ should be describable by terms close to the site r. Therefore, as for the Hamiltonian we define a maximum value D^O_{max} for the observable extension D^O and discard all terms with a larger observable extension ($D^O > D^O_{\text{max}}$). We also use different maximal observable extensions D^O_n depending on the total number n of annihilation and creation operators occurring in the term and admit only terms which create or annihilate not more than N^O_{t} (quasi)particles. Therefore, the total truncation scheme for the observables is defined by the value N^O_{t} and the set of observable extensions $\mathbf{D}^O = (D^O_1,\ldots,D^O_{2N^O_{\text{t}}})$. In contrast to the truncation scheme for the Hamiltonian also terms consisting of only one annihilation or creation operator must be truncated in the truncation scheme for the observable $O(\ell,r)$. For that reason D^O_1 appears in $\mathbf{D}^O$, which is a consequence of the missing translational invariance of the local observable $O(\ell,r)$.

3.5 Implementation

To perform a sCUT two basic steps are necessary. The calculation of the coupled system of coupled differential equations for the coefficients given by the flow equation (3.3) and their integration. Since the construction of the differential equations is independent of their initial values it is useful to have a separate program for each of these two steps. Once the system of differential equations is constructed the same system can be used

to describe different interaction parameters of the model under study (cf. chapter 4, chapter 5 and chapter 6).

In the following section 3.5.1 the program constructing the differential equation system is briefly described. In section 3.5.2 comments about the numerical integration of the differential equations are given.

3.5.1 Construction of the differential equations

The program to set up the differential equations induced by the flow equation (3.3) is based on the implementations by Reischl [Reischl(2006)] and Duffe [Duffe(2010)]. In the given references also more details of the implementation are given. Here only the main aspects are briefly discussed.

To optimize performance and flexibility the programming language C++ is used instead of a computer algebra program like Mathematica or Maple. Nevertheless, we use algebraical fractions to describe the factors a_{ijk} in equation (3.88) to avoid rounding errors during the setting up.

A local operator is implemented as an object of a class `op` and characterized by three elements `op_state_0`, `op_state_1` and `i`, cf. figure 3.13. The element `i` represents

```
class op
{
private:
  short op_state_0;
  short op_state_1;
  short i;

  ...
```

Figure 3.13: Representation of a local operator in the programming language C++.

the lattice site r of the local operator. Since within this thesis only one-dimensional systems are considered the lattice site can be described by just one integer. To describe higher-dimensional lattices one has to use a vector. The integer `op_state_0` determines the flavor α of the creation operator on site r while `op_state_1` determines the flavor of the annihilation operator on site r, cf. equation (3.93).

The main elements describing a term of the Hamiltonian H or an observable O are `prefactor`, `ops` and `imaginary`, see figure 3.14. Each `term` consists of a vector `ops` of local operators `op` and an algebraical fraction as `prefactor`. Additionally, the element `imaginary` determines if the prefactor is imaginary or not. It is convenient to include also other elements in the class `term` such as a hashing value to speed up comparisons of terms or values describing symmetries of a term [Duffe(2010)].

```
class term
{
private:
  fraction prefactor;
  vector<op> ops;
  bool imaginary;

  ...
```

Figure 3.14: Representation of a term of the Hamiltonian H or an observable O in the programming language C++.

In figure 3.15 the structure of the program setting up the differential equations is depicted. The program follows directly the algorithm of sCUT described in section 3.4.

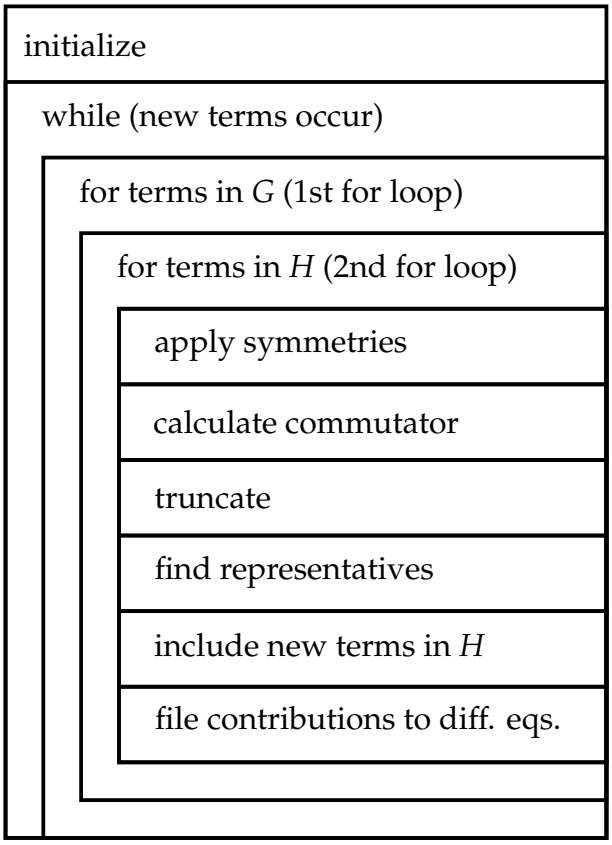

Figure 3.15: Structure diagram of the program for setting up the flow equation [Hamerla(2009)].

Firstly, the Hamiltonian H is initialized where only representative terms have to be considered due to the use of symmetries. To treat systems in the thermodynamic limit it is indispensable to use the translational symmetry. Addtionally, we use spin symmetries and the hermiticity of the Hamiltonian to reduce the number of representative terms.

Since we only consider generators determined by the Hamiltonian we do not have to save the generator separately. The main part of the program consists of two loops to

calculate the commutator of all terms occuring in the generator G and the Hamiltonian H. To get all contributions a sum over the corresponding symmetry group is necessary, cf. section 3.4.2. The commutator of two terms can be calculated efficiently by splitting it via the product rule into a sum over commutators of local operators [Reischl(2006), Duffe(2010)]. After the calculation of the commutator the resulting terms are transferred to a unique, i.e., unambiguous, representation by sorting the local operators according to their sites and local normal ordering. If a term satisfies the truncation scheme its representative term is determined and its occurrence is registered in the differential equation system. When all commutators are computed it has to be tested if new representative terms have emerged. For these new terms we have to repeat the steps explained above. As long as new terms emerge, which comply with the truncation scheme, a new run through the loop is started to compute their contributions to the system of differential equations.

Setting up the differential equations for a local observable $O(r)$ works in the same way. But one has to take into account that the local observable is not translationally invariant and that it possesses a different truncation scheme, cf. section 3.4.3.

3.5.2 Numerical solution of the differential equations

The numerical integration of the first order system of coupled differential equations is done by standard Runge-Kutta-algorithms [Press *et al.*(2002)]. We use the ROD defined in section 3.3.2 to measure the convergence. If the ROD falls below a certain threshold (typically $\approx 10^{-10}$) we consider the integration as converged.

Since the generator $G(\ell)$ is typically defined by the Hamiltonian $H(\ell)$ (cf. section 3.2) the integration of the differential equations describing a transformation of an observable $O(\ell)$ should be done simultaneously with the integration of the system of differential equation describing the transformation of the Hamiltonian $H(\ell)$.

The number of considered coefficients depends on the chosen truncation schemes. Within this thesis the order of magnitude of the number of considered coefficients is $10^5 - 10^6$.

3.6 Chapter summary

In this chapter the concept of continuous unitary transformations (CUTs) was presented. CUTs can be used to derive effective Hamiltonians whose structure is more diagonal than the original problem. The final form of the effective Hamiltonian depends on the choice of the generator generating the CUT.

After an introduction to former well-established choices of generators we introduced a generator adapted to describe systems with unstable (quasi)particles. We also derived

this generator in the context of variational calculus and discussed generalizations of this generator. Results obtained by this new generator will be presented in the following chapters 4, 5 and 6.

To illustrate differences and similarities of distinct generators small toy models were discussed. We also proved that certain different generators transform some subspaces entirely in the same way.

After these general considerations of CUTs we presented the concept of self-similar continuous unitary transformations (sCUTs) in real space by local operators. A truncation scheme based on the locality of terms to perform calculations in the thermodynamic limit was discussed as well. This approach is used in the following chapters 4, 5 and 6.

Finally we described briefly how to implement the sCUT in real space on a computer.

Chapter 4

Asymmetric antiferromagnetic spin $S = 1/2$ Heisenberg ladder

The Hamiltonian for the asymmetric antiferromagnetic spin $S = 1/2$ Heisenberg ladder (AASHL) reads

$$H = J_\perp H_\perp + J_\parallel H_\parallel + J_{\text{diag}} H_{\text{diag}} \tag{4.1a}$$

with

$$H_\perp = \sum_r \mathbf{S}_1(r)\mathbf{S}_2(r) \tag{4.1b}$$

$$H_\parallel = \sum_r \Big(\mathbf{S}_1(r)\mathbf{S}_1(r+1) + \mathbf{S}_2(r)\mathbf{S}_2(r+1)\Big) \tag{4.1c}$$

$$H_{\text{diag}} = \sum_r \mathbf{S}_1(r)\mathbf{S}_2(r+1) \tag{4.1d}$$

where the subscript $l \in 1,2$ denotes the leg and the argument $r \in \mathbb{Z}$ denotes the rung of the spin vector $\mathbf{S}_l(r)$, cf. figure 4.1. In the fully antiferromagnetic case the couplings $J_\perp$, $J_\parallel$ and J_{diag} all are positive ($J_\perp, J_\parallel, J_{\text{diag}} \geq 0$). From now onwards, we use the dimensionless parameters

$$x := \frac{J_\parallel}{J_\perp} \tag{4.2a}$$

$$y := \frac{J_{\text{diag}}}{J_\perp} \tag{4.2b}$$

and set the perpendicular coupling equal to one, i.e. $J_\perp = 1$. For calculations including dynamical structure factors $S^{\alpha\beta}(\mathbf{Q},\omega)$ also the vector $\mathbf{b}$ defining the ladder rungs is important (see figure 4.1, cf. section F).

For the case $x < y$ the Hamiltonian (4.1) is usually denoted as a dimerized and

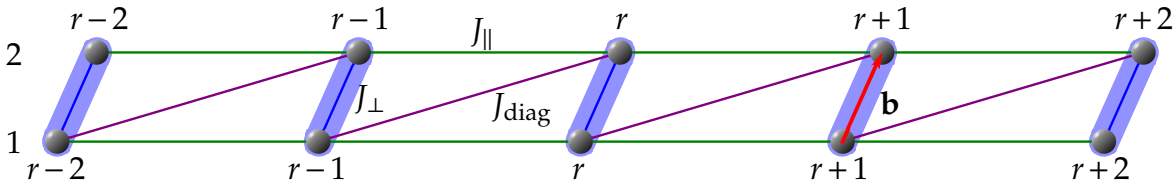

Figure 4.1: Schematic representation of the asymmetric antiferromagnetic spin $S = 1/2$ Heisenberg ladder (AASHL). Circles indicate spins with spin $S = 1/2$. Solid lines stand for couplings, where all couplings are assumed to be positive, i.e. $J_\perp, J_\parallel, J_{\text{diag}} \geq 0$. Ladder rungs are defined by the vector $\mathbf{b}$. In the following, the dimensionless parameters $x := J_\parallel/J_\perp > 0$ and $y := J_{\text{diag}}/J_\perp > 0$ are used and the perpendicular coupling is set to one, i.e. $J_\perp = 1$. The additional diagonal interaction J_{diag} breaks the reflection symmetry and hence induces a hybridization between the one-triplon states and the two-triplon continuum.

frustrated spin $S = 1/2$ chain (see reference [Schmidt *et al.*(2004)] and references therein). Since in this thesis we are mainly interested in the case $x > y$, we denote the system as AASHL instead of dimerized an frustrated chain.

The Hamiltonian (4.1) comprises some frequently discussed models as limiting cases. For example, for $x = 0$ and $y = 1$ the Hamiltonian (4.1) describes the exactly solvable isotropic antiferromagnetic spin $S = 1/2$ Heisenberg chain [Bethe(1931), Hulthén(1938), des Cloizeaux & Pearson(1962), Yang & Yang(1966a), Yang & Yang(1966b), Faddeev & Takhtajan(1981), Baxter(1982)].

In the broad field of quantum spin systems without magnetic long-range order, the limit of the symmetric spin $S = 1/2$ Heisenberg ladder [Barnes *et al.*(1993), Dagotto & Rice(1996), Sushkov & Kotov(1998), Damle & Sachdev(1998), Brehmer *et al.*(1999), Jurecka & Brenig(2000), Knetter *et al.*(2001), Zheng *et al.*(2001), Schmidt *et al.*(2001), Haga & Suga(2002), Knetter *et al.*(2003a), Schmidt & Uhrig(2005)] with $y = 0$ (cf. section 4.1 and figure 4.3) is a very popular example of a one-dimensional valence-bond solid [Affleck *et al.*(1987)].

Besides the theoretical interest, there is a large number of compounds that can be described by quantum Heisenberg spin ladders (see for example [Kojima *et al.*(1995), Schwenk *et al.*(1996), Eccleston *et al.*(1996), Kumagai *et al.*(1997), Hammar *et al.*(1998), Sugai & Suzuki(1999), Matsuda *et al.*(2000), Konstantinović *et al.*(2001), Grüninger *et al.*(2002), Notbohm *et al.*(2007), Schmidiger *et al.*(2011)] or for an overview see [Johnston *et al.*(2000)]). Special interest has been raised by the realization of coupled spin ladders in the stripe phase of cuprate superconductors [Tranquada *et al.*(1995), Vojta & Ulbricht(2004), Uhrig *et al.*(2004), Uhrig *et al.*(2005b)]. Also the experimental evidence for superconductivity in $Sr_{0.4}Ca_{13.6}Cu_{24}O_{41.84}$ under pressure [Uehara *et al.*(1996)] contributed to the interest in the spin $S = 1/2$ Heisenberg ladder and its extended versions.

The phase diagram of the asymmetric Heisenberg ladder for $x > 0$ depicted in figure

4.2 is well understood [Chitra *et al.*(1995), Brehmer *et al.*(1996), Brehmer *et al.*(1998)]. A special role plays the line $y = 1$ where the physics differs considerably

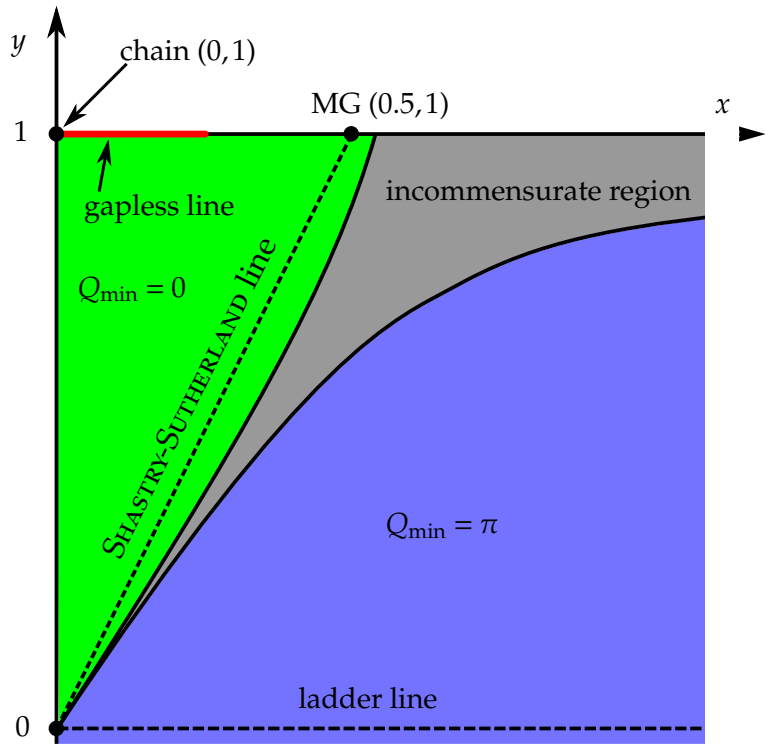

Figure 4.2: Schematic illustration of the ground state phase diagram of the AASHL as (x, y)-plane. At the chain point $(0, 1)$ and along the Shastry-Sutherland line the respective exact ground state is known. Except for $y = 1$ and $0 \leq x < x_c \approx 0.241167$ the excitation spectrum is gapped. Different colors are used to distinguish the region with the minimum of the dispersion at $Q_{min} = 0$ (green), the region with $Q_{min} = \pi$ (blue) and the incommensurate region (grey). The shown boundaries only provide a qualitative picture. They do not correspond to any calculations.

from all other parts of the phase diagram. Starting from the exactly solvable isotropic antiferromagnetic spin $S = 1/2$ Heisenberg chain for $x = 0$ the system remains gapless up to a critical value $x_c \approx 0.241167$ [Haldane(1982), Okamoto & Nomura(1992), Castilla *et al.*(1995), Eggert(1996)]. Within this interval the ground state is unique and the excitations are gapless $S = 1/2$ spinons [des Cloizeaux & Pearson(1962), Faddeev & Takhtajan(1981)]. For $x > x_c$ the ground state is twofold degenerate and dimerized, see e.g. [Haldane(1982)]. The excitations are massive spinons. In this region also lies the Majumdar-Ghosh point ($x = 0.5$, $y = 1.0$) which ground states are known exactly [Majumdar & Ghosh(1969a), Majumdar & Ghosh(1969b)].

Everywhere else ($y \neq 1$) the ground state of the model is unique and the excitations are gapped [Barnes *et al.*(1993), White(1996)]. For $y \to -\infty$ two spins connected by J_{diag}

form an effective $S = 1$ spin, since the singlet part becomes irrelevant for the physics at low energies. Therefore, for $y = \infty$ the system is equivalent to the $S = 1$ Haldane chain [Haldane(1983), Renard *et al.*(1987)] with an effective coupling $J_\perp(1+2x)/4$.

For $x = y = 0$ the model is trivial. The ground state is given by a product state of singlets. Excitations are immobile triplets. We use this point as starting point for the self-similar continuous unitary transformations (sCUTs), see below. On the Shastry-Sutherland line connecting the point $x = 0$ and $y = 0$ with the Majumdar-Ghosh point the product state of singlets is also the exact ground state [Shastry & Sutherland(1981)]. The symmetric Heisenberg ladder lies on the line $y = 0$.

Away from the line $y = 1$ the elementary excitations are triplons continuously connected to the local triplets. The momentum $Q_{\min}$ indicating the minimum of their dispersion depends on the parameters x and y [Brehmer *et al.*(1996), Brehmer *et al.*(1998), Müller & Mikeska(2000)]. In figure 4.2 different colors are used according to whether the momentum $Q_{\min}$ is 0 or π or lies between these values (incommensurate region). We did *not* calculate the exact position of the boundaries. The shown boundaries shall only provide a qualitative sketch. In this thesis we only consider parameters for which the minimum of the dispersion lies at $Q_{\min} = \pi$.

To define an appropriate starting point for the sCUT we use the bond operator representation [Chubukov(1989), Sachdev & Bhatt(1990)] (cf. chapter C). Each rung r of the ladder is separately considered has a four-dimensional Hilbert space. A possible eigenbasis of the local operator $\mathbf{S}_1(r)\mathbf{S}_2(r)$ is given by the singlet state

$$\left|r,\text{singlet}\right\rangle := \frac{1}{\sqrt{2}}\left(\left|\uparrow\downarrow\right\rangle - \left|\downarrow\uparrow\right\rangle\right)_r \tag{4.3a}$$

and the three triplet states

$$t^\dagger_{x,r}\left|r,\text{singlet}\right\rangle := \left|r,x\right\rangle = \frac{-1}{\sqrt{2}}\left(\left|\uparrow\uparrow\right\rangle - \left|\downarrow\downarrow\right\rangle\right)_r \tag{4.3b}$$

$$t^\dagger_{y,r}\left|r,\text{singlet}\right\rangle := \left|r,y\right\rangle = \frac{\mathrm{i}}{\sqrt{2}}\left(\left|\uparrow\uparrow\right\rangle + \left|\downarrow\downarrow\right\rangle\right)_r \tag{4.3c}$$

$$t^\dagger_{z,r}\left|r,\text{singlet}\right\rangle := \left|r,z\right\rangle = \frac{1}{\sqrt{2}}\left(\left|\uparrow\downarrow\right\rangle + \left|\downarrow\uparrow\right\rangle\right)_r . \tag{4.3d}$$

Without any interactions along the ladder ($x = 0$, $y = 0$) the ground state of the system is the product state of the rung singlets

$$\left|0\right\rangle := \bigotimes_r \left|r,\text{singlet}\right\rangle = \bigotimes_r \frac{1}{\sqrt{2}}\left(\left|\uparrow\downarrow\right\rangle - \left|\downarrow\uparrow\right\rangle\right)_r . \tag{4.4}$$

This reference state shall be the vacuum state of the system at $\ell = 0$. Excitations on a rung r are created by the local operators $t^\dagger_{x,r}$, $t^\dagger_{y,r}$ and $t^\dagger_{z,r}$. These operators defined by

(4.3) create a triplet on a rung r and satisfy the hard-core boson commutation relations (cf. equation (3.98))

$$\left[t_{\alpha,r}, t^\dagger_{\beta,s}\right] = \delta_{r,s}\left(\delta_{\alpha,\beta}\left(\mathbb{1}_4 - \sum_{\gamma=1}^{3} t^\dagger_{\gamma,r} t_{\gamma,r}\right) - t^\dagger_{\beta,r} t_{\alpha,r}\right) \tag{4.5}$$

where $t_{\alpha,r}$ ($\alpha \in \{x,y,z\}$) annihilate such a triplet. We consider all the excited states, which can be continuously connected to the local triplets, to be elementary magnetic excitations. These quasiparticles are called triplons [Schmidt & Uhrig(2003), Schmidt & Uhrig(2005)].

In the bond operator representation the Hamiltonian (4.1) is given in the notation (3.30) by

$$H = H_0^0 + H_1^1 + H_2^2 + H_0^2 + H_2^0 + H_1^2 + H_2^1 \tag{4.6a}$$

with

$$H_0^0 = -\sum_r \frac{3}{4} \tag{4.6b}$$

$$H_1^1 = \sum_r \sum_\alpha t^\dagger_{\alpha,r} t_{\alpha,r} + \left(\frac{1}{2}x - \frac{1}{4}y\right) \sum_r \sum_\alpha \left(t^\dagger_{\alpha,r} t_{\alpha,r+1} + t^\dagger_{\alpha,r+1} t_{\alpha,r}\right) \tag{4.6c}$$

$$H_2^2 = \left(\frac{1}{2}x + \frac{1}{4}y\right) \sum_r \sum_{\alpha\neq\beta} \left(t^\dagger_{\alpha,r} t^\dagger_{\beta,r+1} t_{\beta,r} t_{\alpha,r+1} - t^\dagger_{\alpha,r} t^\dagger_{\alpha,r+1} t_{\beta,r} t_{\beta,r+1}\right) \tag{4.6d}$$

$$H_0^2 = \left(\frac{1}{2}x - \frac{1}{4}y\right) \sum_r \sum_\alpha t^\dagger_{\alpha,r} t^\dagger_{\alpha,r+1} \tag{4.6e}$$

$$H_2^0 = \left(H_0^2\right)^\dagger \tag{4.6f}$$

$$H_1^2 = -\frac{\mathrm{i}}{4} y \sum_r \sum_{\alpha,\beta,\gamma} \varepsilon_{\alpha\beta\gamma}\, t^\dagger_{\alpha,r} t^\dagger_{\beta,r+1} \left(t_{\gamma,r} + t_{\gamma,r+1}\right) \tag{4.6g}$$

$$H_2^1 = \left(H_1^2\right)^\dagger . \tag{4.6h}$$

This representation of the Hamiltonian of the asymmetric antiferromagnetic spin $S = 1/2$ Heisenberg ladder is used as the starting point for the sCUTs. Therefore, the initial values of the sCUT are given by

$$\left[c_{H|_1^1}\right]_0 = 1 \tag{4.7a}$$

$$\left[c_{H|_1^1}\right]_1 = \left[c_{H|_1^1}\right]_{-1} = \frac{1}{2}x - \frac{1}{4}y \tag{4.7b}$$

$$\left[c_{H|_2^2}\right]^1_{0,1} = \left(\frac{1}{2}x + \frac{1}{4}y\right)\left((1-\delta_{\alpha\beta}\right) \tag{4.7c}$$

$$\begin{smallmatrix}\alpha,\alpha\\ \beta,\beta\end{smallmatrix}\left[c_{H|_2^2}\right]_{0,1}^1 = -\left(\frac{1}{2}x+\frac{1}{4}y\right)\left((1-\delta_{\alpha\beta}\right) \tag{4.7d}$$

$$\begin{smallmatrix}\alpha,\alpha\\ \end{smallmatrix}\left[c_{H|_0^2}\right]^1 = \begin{smallmatrix}\\ \alpha,\alpha\end{smallmatrix}\left[c_{H|_2^0}\right]_1 = \frac{1}{2}x-\frac{1}{4}y \tag{4.7e}$$

$$\begin{smallmatrix}\alpha,\beta\\ \gamma\end{smallmatrix}\left[c_{H|_1^2}\right]_0^1 = \begin{smallmatrix}\alpha,\beta\\ \gamma\end{smallmatrix}\left[c_{H|_1^2}\right]_1^1 = -\frac{\mathrm{i}}{4}y\ \varepsilon_{\alpha\beta\gamma} \tag{4.7f}$$

$$\begin{smallmatrix}\gamma\\ \alpha,\beta\end{smallmatrix}\left[c_{H|_2^1}\right]_0^1 = \begin{smallmatrix}\gamma\\ \alpha,\beta\end{smallmatrix}\left[c_{H|_2^1}\right]_{-1}^1 = \frac{\mathrm{i}}{4}y\ \varepsilon_{\alpha\beta\gamma}\ . \tag{4.7g}$$

For the parameter $y = 0$ the coefficients (4.7f) and (4.7g) vanish whereby decay processes of one triplon into two are prevented.

In the following section 4.1 we briefly summarize the low-energy physics of the symmetric spin $S = 1/2$ Heisenberg ladder ($y = 0$). Since in this model no decay occurs the generator $G_{\mathrm{pc}}(\ell)$ can be used. We reproduce the sCUT calculations for the energy spectrum previously performed by Reischl [Reischl(2006)]. In addition, we calculate the dynamical structure factor for the one and two quasiparticle channel using sCUTs based on the generator $G_{\mathrm{pc}}(\ell)$. These calculations serve as a basis for an investigation of the more involved model of the AASHL and they help to quantify the influence of the parameter $y > 0$.

In section 4.2 the AASHL for $x = 0.5$ and $y = 0.1$ is discussed in detail. The convergence behavior of various generators is investigated and compared to the symmetric case with $y = 0$. Also the more involved analysis of the effective model produced by the generator $G_{\mathrm{gs}}(\ell)$ is illustrated.

To describe quasiparticle decay in the AASHL results for the dynamical structure factor $S^{zz}(Q,\omega)$ for various parameters x and y are given in section 4.3.

4.1 Symmetric case ($y = 0$)

The symmetric Heisenberg spin ladder with $y = 0$ is invariant under a reflection about the centerline of the ladder, see figure 4.3. This reflection symmetry is responsible for

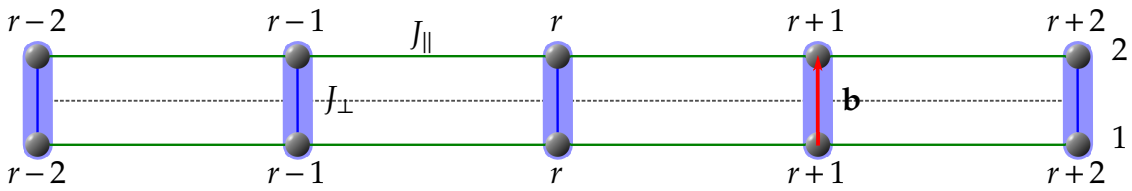

Figure 4.3: Schematic representation of a Heisenberg spin ladder. Circles indicate spins with spin $S = 1/2$. Solid lines stand for couplings where all couplings are assumed to be positive, i.e. $J_\perp, J_\parallel \geq 0$. The dashed line indicates the axis of reflection symmetry. Ladder rungs are defined by the vector $\mathbf{b}$. In the following, the dimensionless parameter $x := J_\parallel/J_\perp$ is used and the perpendicular coupling is set to one, i.e. $J_\perp = 1$.

the infinite lifetime of the triplons, which are the $S = 1$ elementary magnetic excitations of an antiferromagnetic system without long-range order [Schmidt & Uhrig(2003)]. Although the energy levels of the one-triplon dispersion and the two-triplon continuum might overlap decay is forbidden due to missing decay vertices (matrix elements), cf. chapter 2. Generally, due to the reflection symmetry no decay vertices between subspaces with an odd number of quasiparticles and subspaces with an even number of quasiparticles exist [Knetter *et al.*(2003a)].

4.1.1 Energy properties

By using the generator $G_{\mathrm{pc}}(\ell)$ subspaces with different quasiparticle numbers are separated. Thus the one-triplon dispersion is given by the coefficients of $H_{\mathrm{eff}}\big|_1^1 = \lim_{\ell\to\infty} H_1^1(\ell)$. To calculate the one-triplon dispersion we use the momentum space representation. The Fourier transformed one-particle states are defined by

$$\left|Q,\alpha_0\right\rangle := \frac{1}{\sqrt{N}} \sum_r \mathrm{e}^{\mathrm{i}Qr} \left|r,\alpha_0\right\rangle \tag{4.8}$$

with $|r,\alpha\rangle = t^\dagger_{\alpha,r}|0\rangle$. The action of $H_{\mathrm{eff}}\big|_1^1$ with respect to translational symmetry on the one-triplon state $|r,\alpha\rangle$ is given by equation (D.2) in appendix D. Due to the SU(2) symmetry of the Hamiltonian (4.1) the hopping coefficients ${}^{\alpha_0}_{\beta_0}\big[c_{H|_1^1}\big]_{l_0}$ obey the relation ${}^{\alpha_0}_{\beta_0}\big[c_{H|_1^1}\big]_{l_0} = \delta_{\alpha_0,\beta_0}\big[c_{H|_1^1}\big]_{l_0}$. This leads to the threefold degenerate one-triplon dispersion

$$\omega_1(Q) := \left\langle Q,\alpha\right| H_{\mathrm{eff}}\big|_1^1 \left|Q,\alpha\right\rangle = \sum_r \mathrm{e}^{\mathrm{i}Qr} \left[c_{H|_1^1}\right]_r \tag{4.9}$$

for $\alpha = x,y,z$.

The one-triplon dispersion $\omega_1(Q)$ also determines the two-triplon continuum

$$\omega_2(Q,q) = \omega_1(Q/2+q) + \omega_1(Q/2-q) \tag{4.10}$$

with the relative momentum $q \in [-\pi,\pi]$. The lower band edge $\omega_2^{\min}(Q)$ is given by the minimum of $\omega_2(Q,q)$ over q and the maximum of $\omega_2(Q,q)$ over q defines the upper band edge $\omega_2^{\max}(Q)$, i.e.

$$\omega_2^{\min}(Q) = \min_{q\in[-\pi,\pi]} \omega_2(Q,q) \tag{4.11a}$$

$$\omega_2^{\max}(Q) = \max_{q\in[-\pi,\pi]} \omega_2(Q,q)\,. \tag{4.11b}$$

Note, that the energies of the two-triplon continuum is entirely determined by the one-triplon dispersion. Interactions between two two-triplon states are not incorporated.

Since the generator $G_{\mathrm{pc}}(\ell)$ also separates the two-triplon subspace the whole two-triplon energy spectrum is determined by $H_{\mathrm{eff}}\big|_1^1$ and $H_{\mathrm{eff}}\big|_2^2 = \lim_{\ell\to\infty} H_2^2(\ell)$. The matrix elements determining the two-quasiparticle spectrum are given by

$$\Big\langle Q,\alpha_0\Big|\Big\langle d_1,\alpha_1\Big|\Big(H_{\mathrm{eff}}\big|_1^1 + H_{\mathrm{eff}}\big|_2^2\Big)\Big|Q,\beta_0\Big\rangle\Big|l_1,\beta_1\Big\rangle \tag{4.12}$$

with the Fourier transformed two-particle states

$$\Big|Q,\alpha_0\Big\rangle\Big|d_1,\alpha_1\Big\rangle = \frac{1}{\sqrt{\mathcal{N}}}\sum_r \mathrm{e}^{\mathrm{i}Q\left(r+\frac{d_1}{2}\right)}\,\Big|r,\alpha_0\Big\rangle\Big|r+d_1,\alpha_1\Big\rangle \tag{4.13}$$

with $d_1 > 0$. Due to the SU(2) symmetry of the Hamiltonian (4.1) the computational effort can be reduced by considering only matrix elements relevant for the description of a subspace specified by the spin quantum numbers S and m, for details see references [Knetter *et al.*(2003a)] and [Knetter(2003)]. In table 4.1 the spin eigenstates in the zero-, one- and two-triplon subspace are listed.

The two-quasiparticle interaction terms occurring in $H_{\mathrm{eff}}\big|_2^2$ can produce bound and antibound states [Uhrig & Schulz(1996), Damle & Sachdev(1998), Sushkov & Kotov(1998), Uhrig & Normand(1998), Kotov *et al.*(1999), Trebst *et al.*(2000), Jurecka & Brenig(2000), Zheng *et al.*(2001)].

Figure 4.4 depicts the energy spectrum of the symmetric spin ladder for $x = 0.5$ and $y = 0.0$ obtained by sCUTs using the generator $G_{\mathrm{pc}}(\ell)$ and a truncation scheme $N_{\mathrm{t}} = 4$ with $\mathbf{D} = (10,.,8,.,5,.,3)$, cf. section 3.4.3.

Due to the reflection symmetry of the symmetric spin ladder subspaces with an odd number of quasiparticles cannot interact with subspaces with an even number of quasiparticles. Thus the energy spectra of odd subspaces and the energy spectra of even subspaces are presented in separate graphs. The black line in the left panel of figure 4.4 depicts the one-triplon dispersion $\omega_1(Q)$. The solid blue lines in the right panel of figure 4.4 display the boundaries of the two-triplon continuum $\omega_2(Q,q)$. In this figure also the two-particle bound states are depicted. The $S = 0$ bound state is represented by the dashed blue line and the threefold degenerate $S = 1$ bound state by the dotted blue line.

For the calculations of the bound states all Fourier transformed two-particle states with $d_1 < 4000$, cf. equation (4.13), have been considered. This leads to a diagonalization of a 3999×3999 matrix for fixed spin quantum numbers S and m. The existence of bound states depends on the momentum Q. They do not exist within the whole Brillouin zone. For all momenta Q where bound states exist the spectrum of the $S = 0$ bound state lies below the spectrum of the $S = 1$ bound state.

The three-triplon and four-triplon continua are also depicted in figure 4.4 besides the one- and two-triplon energy levels. Without considering two-triplon bound states

Table 4.1: Spin eigenstates in the zero-, one- and two-triplon subspace.

S	m	zero-triplon subspace
0	0	$\left\vert \text{singlet,singlet} \right\rangle$
S	m	one-triplon subspace
1	1	$-\frac{1}{\sqrt{2}}\left(\left\vert \text{singlet},x\right\rangle + \text{i}\left\vert \text{singlet},y\right\rangle\right)$
1	0	$\left\vert \text{singlet},z\right\rangle$
1	-1	$\frac{1}{\sqrt{2}}\left(\left\vert \text{singlet},x\right\rangle - \text{i}\left\vert \text{singlet},y\right\rangle\right)$
S	m	two-triplon subspace
2	2	$\frac{1}{2}\left[\left\vert x,x\right\rangle - \left\vert y,y\right\rangle + \text{i}\left(\left\vert x,y\right\rangle + \left\vert y,x\right\rangle\right)\right]$
2	1	$-\frac{1}{2}\left[\left\vert x,z\right\rangle + \left\vert z,x\right\rangle + \text{i}\left(\left\vert y,z\right\rangle + \left\vert z,y\right\rangle\right)\right]$
2	0	$\frac{1}{\sqrt{6}}\left(2\left\vert z,z\right\rangle - \left\vert x,x\right\rangle - \left\vert y,y\right\rangle\right)$
2	-1	$\frac{1}{2}\left[\left\vert x,z\right\rangle + \left\vert z,x\right\rangle - \text{i}\left(\left\vert y,z\right\rangle + \left\vert z,y\right\rangle\right)\right]$
2	-2	$\frac{1}{2}\left[\left\vert x,x\right\rangle - \left\vert y,y\right\rangle - \text{i}\left(\left\vert x,y\right\rangle + \left\vert y,x\right\rangle\right)\right]$
1	1	$-\frac{1}{2}\left[\left\vert x,z\right\rangle - \left\vert z,x\right\rangle + \text{i}\left(\left\vert y,z\right\rangle - \left\vert z,y\right\rangle\right)\right]$
1	0	$\frac{\text{i}}{\sqrt{2}}\left(\left\vert x,y\right\rangle - \left\vert y,x\right\rangle\right)$
1	-1	$-\frac{1}{2}\left[\left\vert x,z\right\rangle - \left\vert z,x\right\rangle - \text{i}\left(\left\vert y,z\right\rangle - \left\vert z,y\right\rangle\right)\right]$
0	0	$\frac{1}{\sqrt{3}}\left(\left\vert x,x\right\rangle + \left\vert y,y\right\rangle + \left\vert z,z\right\rangle\right)$

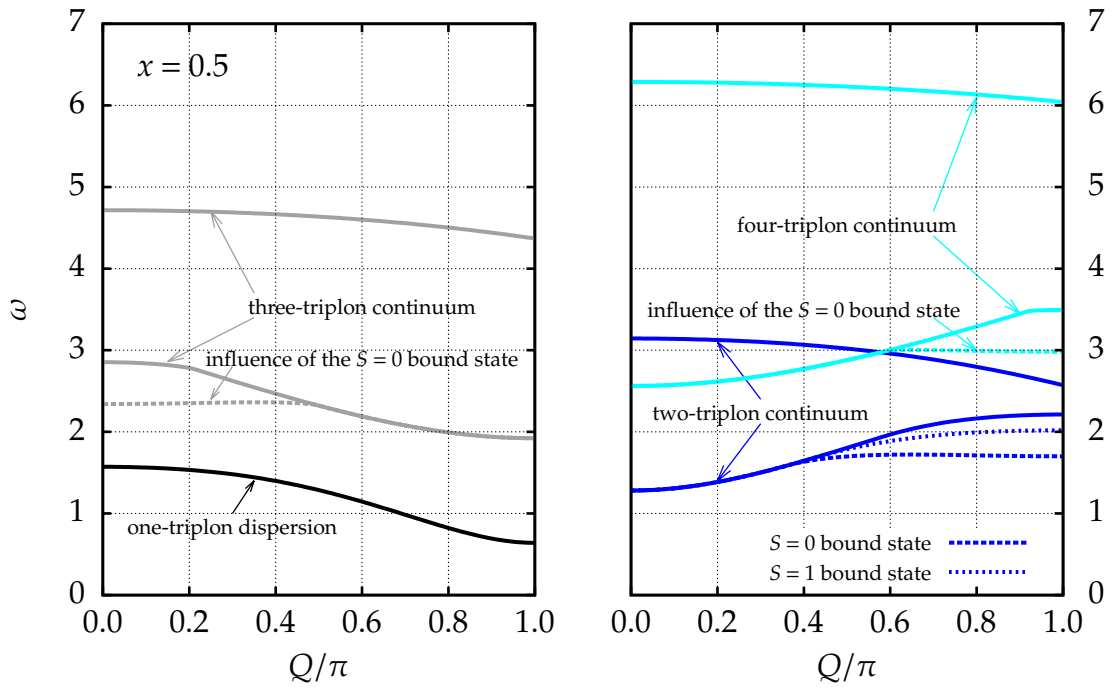

Figure 4.4: Energy spectrum for the symmetric spin ladder with $x = 0.5$ obtained by sCUT using the generator $G_{\mathrm{pc}}(\ell)$ and a truncation scheme $N_{\mathrm{t}} = 4$ with $\mathbf{D} = (10,.,8,.,5,.,3)$. Left panel: subspaces with an odd number of triplons. Right panel: subspaces with an even number of triplons. The lower edges of the three- and four-triplon continua taking into account the two-triplon $S = 0$ bound state are displayed by dashed lines.

the lower edge $\omega_3^{\mathrm{min}}(Q)$ and the upper edge $\omega_3^{\mathrm{max}}(Q)$ of the three-triplon continuum are given by

$$\omega_3^{\mathrm{min}}(Q) = \min_{q\in[-\pi,\pi]} \left(\omega_2^{\mathrm{min}}(Q/2+q) + \omega_1(Q/2-q)\right) \tag{4.14a}$$

$$\omega_3^{\mathrm{max}}(Q) = \max_{q\in[-\pi,\pi]} \left(\omega_2^{\mathrm{max}}(Q/2+q) + \omega_1(Q/2-q)\right) . \tag{4.14b}$$

The band edges of the four-triplon continuum are given analogously by

$$\omega_4^{\mathrm{min}}(Q) = \min_{q\in[-\pi,\pi]} \left(\omega_3^{\mathrm{min}}(Q/2+q) + \omega_1(Q/2-q)\right) \tag{4.15a}$$

$$\omega_4^{\mathrm{max}}(Q) = \max_{q\in[-\pi,\pi]} \left(\omega_3^{\mathrm{max}}(Q/2+q) + \omega_1(Q/2-q)\right) . \tag{4.15b}$$

In figure 4.4 these continua are represented by solid lines. To incorporate the influence of the two-triplon bound states to the three- and four-triplon continua one has to replace $\omega_2^{\mathrm{min}}(Q)$ in equation 4.14a by the dispersion of the lowest bound state ($S = 0$). The resulting lower band edges are depicted in figure 4.4 by dashed lines. Note, that the influence of terms appearing in $H_{\mathrm{eff}}\big|_3^3 = \lim_{\ell\to\infty} H_3^3(\ell)$ and $H_{\mathrm{eff}}\big|_4^4 = \lim_{\ell\to\infty} H_4^4(\ell)$ are not considered for the calculations of the three- and four-triplon spectrum.

The results shown in figure 4.4 for the truncation scheme $N_t = 4$ with $\mathbf{D} = (10,.,8,.,5,.,3)$ coincide within the linewidth with results for the truncation scheme $N_t = 4$ with $\mathbf{D} = (10,.,6,.,4,.,3)$, results obtained by perturbative continuous unitary transformations (pCUTs) [Schmidt(2004)] and directly evaluated enhanced perturbative continuous unitary transformations (deepCUTs) [Krull(2011)]. For a detailed discussion of the accuracy of the sCUT results see [Reischl(2006)].

In figure 4.5 the energy spectrum of the symmetric spin ladder with $x = 0.75$ obtained by sCUTs is depicted. Again the generator $G_{\mathrm{pc}}(\ell)$ and the truncation scheme $N_t = 4$

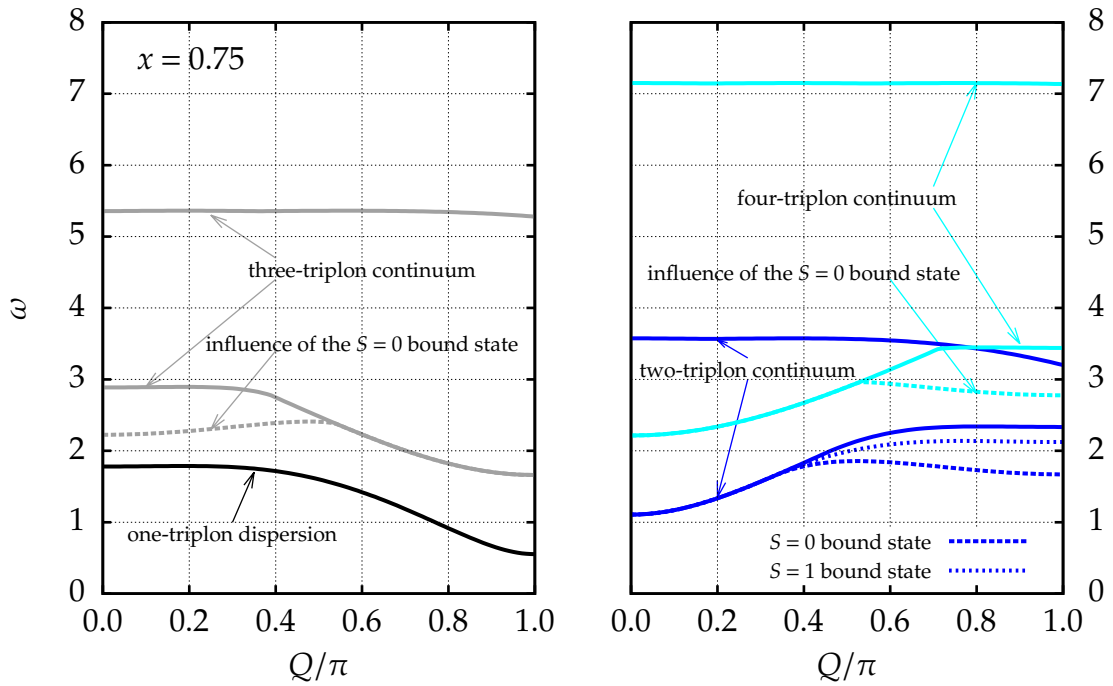

Figure 4.5: Energy spectrum for the symmetric spin ladder with $x = 0.75$ obtained by sCUT using the generator $G_{\mathrm{pc}}(\ell)$ and a truncation scheme $N_t = 4$ with $\mathbf{D} = (10,.,8,.,5,.,3)$. Left panel: subspaces with an odd number of triplons. Right panel: subspaces with an even number of triplons. The lower edges of the three- and four-triplon continua taking into account the two-triplon $S = 0$ bound state are displayed by dashed lines.

with $\mathbf{D} = (10,.,8,.,5,.,3)$ have been used. The results coincide within the linewidth with results for the truncation scheme $N_t = 4$ with $\mathbf{D} = (10,.,6,.,4,.,3)$.

Qualitatively, no differences to the symmetric spin ladder with $x = 0.5$ exist. However, the bandwidth of the one-triplon dispersion for $x = 0.75$ is considerably larger than for $x = 0.5$. This also enlarges the bandwidths of the continua and leads to a larger overlap between the two- and four-triplon continua. The one-triplon dispersion and the three-triplon continua are still well separated. Again $S = 0$ and $S = 1$ bound states exist.

By further increasing the parameter x the bandwidth of the one-triplon dispersion becomes even broader. This is depicted in figure 4.6 for $x = 1.0$. Once more, the

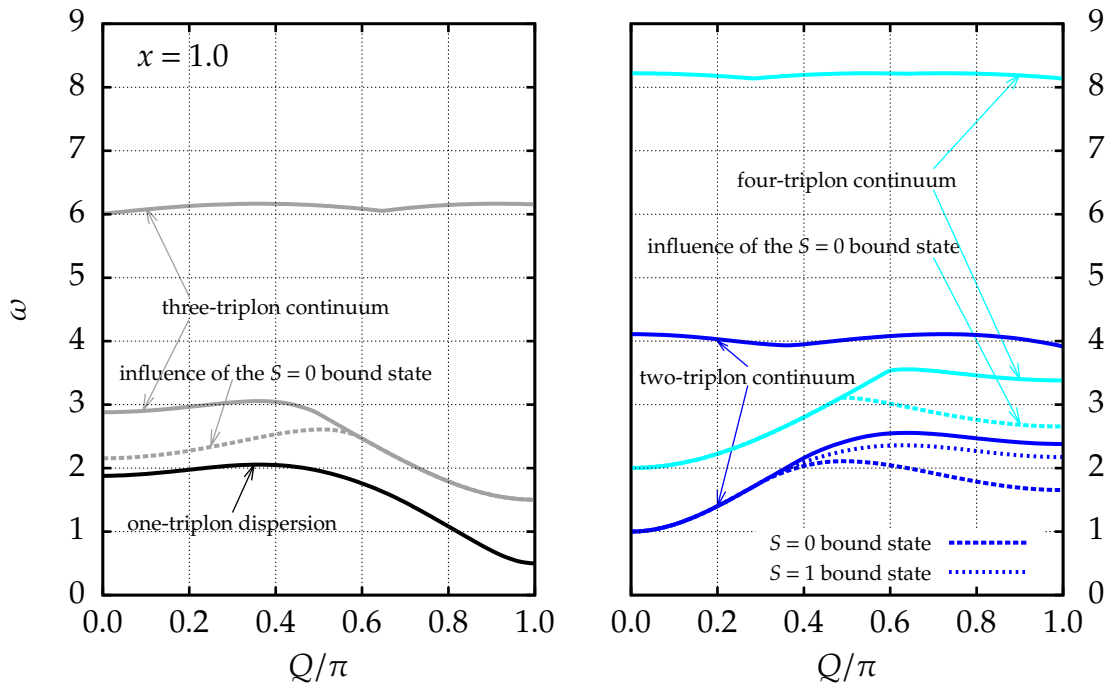

Figure 4.6: Energy spectrum for the symmetric spin ladder with $x = 1.0$ obtained by sCUT using the generator $G_{\mathrm{pc}}(\ell)$ and a truncation scheme $N_{\mathrm{t}} = 4$ with $\mathbf{D} = (10,.,8,.,5,.,3)$. Left panel: subspaces with an odd number of triplons. Right panel: subspaces with an even number of triplons. The lower edges of the three- and four-triplon continua taking into account the two-triplon $S = 0$ bound state are displayed by dashed lines.

generator $G_{\mathrm{pc}}(\ell)$ and the truncation scheme $N_{\mathrm{t}} = 4$ with $\mathbf{D} = (10,.,8,.,5,.,3)$ have been used.

For $x = 1.0$ the lower edge of the three-triplon continuum is very close to the one-triplon dispersion. At small values of the momentum Q the three-triplon continuum pushes the one triplon-dispersion to lower energy values. This leads to a dip within the one-triplon dispersion at $Q = 0$. Additionally, due to the larger bandwidth of the one-triplon dispersion the overlap between the two- and four-triplon continua is enhanced. As well as for $x = 0.5$ and $x = 0.75$ a $S = 0$ bound state and a threefold degenerate $S = 1$ bound state exist in the two-triplon sector.

The correlation length of the ladder increases with the value x. Thus for $x = 1.0$ truncations effects become considerably more noticeable as for, e.g., $x = 0.5$. In figure 4.7 results for various methods based on continuous unitary transformation (CUT) with the generator $G_{\mathrm{pc}}(\ell)$ are compared. Black and blue lines indicate sCUT calculations. Two different truncation schemes are depicted (truncation scheme I: $N_{\mathrm{t}} = 4$, $\mathbf{D} = (10,.,8,.,5,.,3)$, truncation scheme II: $N_{\mathrm{t}} = 4$, $\mathbf{D} = (10,.,6,.,4,.,3)$). Also results obtained by sCUTs (grey lines) and deepCUTs (cyan lines) are depicted. A more detailed discussion of the influence of the truncation scheme on the sCUT results is given in [Reischl(2006)].

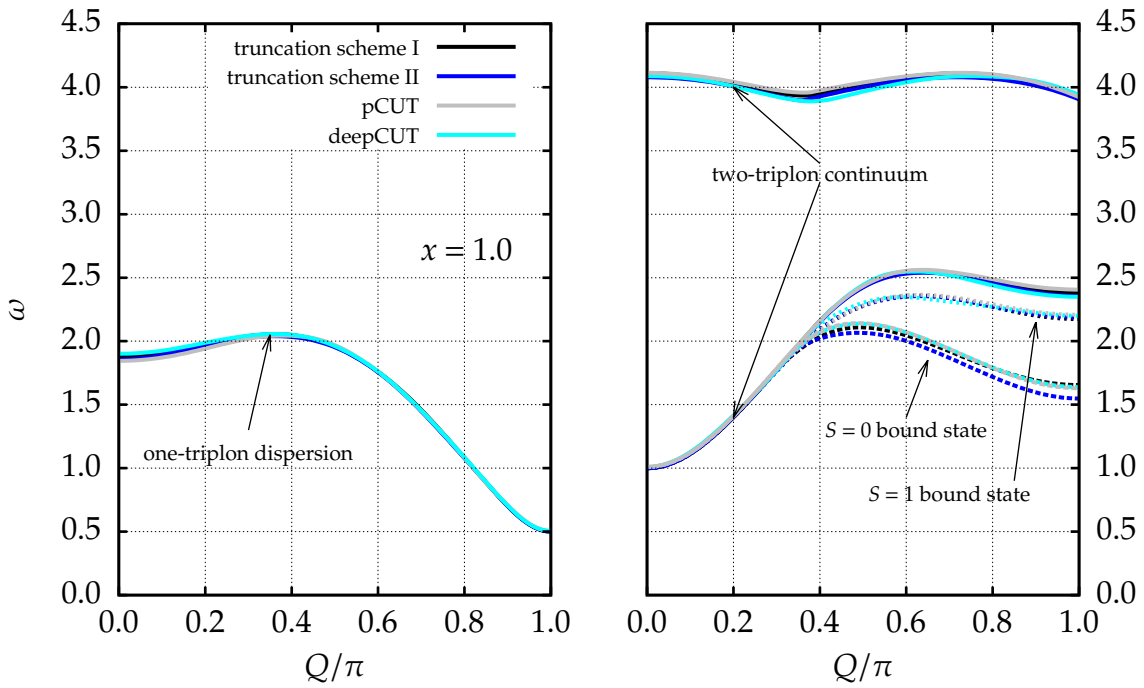

Figure 4.7: Energy spectrum of the one- and two-triplon sector for the symmetric spin ladder with $x = 1.0$ obtained by the generator $G_{\mathrm{pc}}(\ell)$ for various CUT methods. Black and blue lines indicate sCUT calculations (truncation scheme I: $N_{\mathrm{t}} = 4$, $\mathbf{D} = (10,.,8,.,5,.,3)$, truncation scheme II: $N_{\mathrm{t}} = 4$, $\mathbf{D} = (10,.,6,.,4,.,3)$). Grey lines indicate pCUT calculations [Schmidt(2004)]. Cyan lines indicate deepCUT calculations [Krull(2011)].

Especially, the results for the one-triplon dispersion for momenta $Q \gtrapprox 0.5\pi$ coincide for all four calculations (cf. left panel of figure 4.7). For momenta $Q \lessapprox 0.5\pi$ the dispersion relations slightly differ from one another. This also leads to minor deviations for the band edges of the two-triplon continuum. For most momenta also the results for the bound states coincide. Only the most stringent truncation scheme II yields considerably deviating results for the $S = 0$ bound state, cf. right panel of figure 4.7. For truncation scheme I the relative deviation to the pCUT results is less than 2%, cf. [Reischl(2006)].

A further increment of the parameter x towards values beyond $x = 1.0$ leads to larger deviations between the different calculations. Additionally, for $x \approx 1.4$ the sCUT calculations with the generator $G_{\mathrm{pc}}(\ell)$ diverge for the truncation scheme I. In section 3.2.3 it was stated that the generator $G_{\mathrm{pc}}(\ell)$ sorts the eigenvalues in ascending order of the particle number of the corresponding eigenvector if the eigenvectors are linked by a matrix element of the Hamiltonian [Mielke(1998), Heidbrink & Uhrig(2002), Fischer *et al.*(2010)]. The generator $G_{\mathrm{gs,1p}}(\ell)$ transforms the vacuum state and the one-particle subspace in the same way, see section 3.3.4 and reference [Fischer *et al.*(2010)], but it transforms states consisting of more than one particle differently. Thus the divergence occurring in the sCUT calculations with the generator $G_{\mathrm{pc}}(\ell)$ seems to be caused by reordering processes between the the two- and four-triplon states (cf. section 3.2.3) since calculations

with the generator $G_{\mathrm{gs,1p}}(\ell)$ for the same truncation scheme converge. Note, that even for $x = 1.0$ a pronounced overlap between the two- and four-triplon continua exists, cf. figure 4.6.

The truncation scheme II converges even for higher values of the parameter x, for $x = 1.5$ see [Duffe(2010)] and for $x = 1.95$ see [Krull(2011)]. But especially in sectors with more than one triplon the results differ considerably from results obtained by enhanced perturbative continuous unitary transformation (epCUT), see [Krull(2011)]. For these high values of x the one-triplon dispersion might merge with the three-triplon continua besides the overlap between the two- and four-triplon continua. Thus, decay processes from one triplon into three triplons might become possible so that even in the case of the symmetric Heisenberg ladder spontaneous quasiparticle decay (SQPD) may occur, while usually the triplons have infinite lifetime due to the reflection symmetry (see figure 4.3).

The main aim of this thesis is to investigate the SQPD of one triplon into two triplons. To avoid the very involved physics of Heisenberg spin $S = 1/2$ ladders with a large coupling x, e.g., triplon decay of one triplon into three triplons and hybridization of two- and four-triplon states, we restrict ourselves in the following to couplings $x \leq 1.0$. For these couplings sCUTs yield reliable results, see figure 4.4, figure 4.5, figure 4.6 and figure 4.7.

4.1.2 Spectral properties

In this section results for the dynamical structure factor $S^{zz}(Q,\omega)$ for the symmetric spin ladder are presented. All results are calculated by sCUTs using the generator $G_{\mathrm{pc}}(\ell)$. The dynamical structure factor $S^{zz}(Q,\omega)$ can be measured by inelastic neutron scattering (INS) experiments, cf. appendix F.

For temperature $T = 0$ the dynamical structure factor $S^{zz}(Q,\omega)$ is given by

$$S^{zz}(Q,\omega) = -\frac{1}{\pi}\mathrm{Im}\,\mathcal{G}^{zz}(Q,\omega) \tag{4.16}$$

with the retarded zero temperature Green function

$$\mathcal{G}^{zz}(Q,\omega) = \lim_{\delta\to 0^+} \left\langle g\right| S^z(-Q)\left[\omega - (H(Q) - E_0) + \mathrm{i}\delta\right]^{-1} S^z(Q)\left|g\right\rangle \quad \text{for} \quad \omega > 0\,. \tag{4.17}$$

The vector $\left|g\right\rangle$ denotes the ground state of the system. Experiments can only measure energy differences. Thus the ground state energy E_0 is subtracted in equation (4.17).

The Fourier transformed spin operator $S^z(Q)$ is defined by

$$S^z(Q) = \frac{e^{iQ\frac{\mathbf{b}}{2}}}{\sqrt{2N}} \sum_r e^{iQr} \left(e^{-iQ\frac{\mathbf{b}}{2}} S_1^z(r) + e^{iQ\frac{\mathbf{b}}{2}} S_2^z(r) \right), \tag{4.18}$$

for details see appendix F. Note, that the Fourier transformed spin operator $S^z(Q)$ depends on the inner product of the momentum vector $\mathbf{Q}$ and the basis vector $\mathbf{b}$ defining the ladder rungs. With the scalar Q we denote only the momentum along the ladder. By fixing $\mathbf{Qb}$ it is possible to investigate the odd and even quasiparticle sectors of the symmetric ladder separately. This is explained in more detail below.

The unitary transformation U induced by the generator $G_{\text{pc}}(\ell)$ yields a quasiparticle number conserving Hamiltonian H_{eff} (cf. section 3.2.3). Thus it is possible to discuss the dynamical structure factor $S^{zz}(Q,\omega)$ split in parts with different quasiparticle numbers.

Formally, this can be seen by inserting $UU^\dagger = \mathbb{1}$ in equation (4.16)

$$S^{zz}(Q,\omega) = -\frac{1}{\pi}\text{Im} \lim_{\delta\to 0^+} \left\langle g \right| UU^\dagger S^z(-Q) UU^\dagger \left[\omega - (H(Q) - E_0) + i\delta\right]^{-1} UU^\dagger S^z(Q) UU^\dagger \left| g \right\rangle \tag{4.19a}$$

$$= -\frac{1}{\pi}\text{Im} \lim_{\delta\to 0^+} \left\langle 0 \right| S^z_{\text{eff}}(-Q) \left[\omega - (H_{\text{eff}}(Q) - E_0) + i\delta\right]^{-1} S^z_{\text{eff}}(Q) \left| 0 \right\rangle \tag{4.19b}$$

$$= -\frac{1}{\pi}\text{Im} \sum_N \lim_{\delta\to 0^+} \left\langle 0 \right| S^z_{\text{eff}}(-Q)\Big|_N^0 \left[\omega - \Big(\sum_{i=0}^{N} H_{\text{eff}}(Q)\Big|_i^i - E_0\Big) + i\delta\right]^{-1} S^z_{\text{eff}}(Q)\Big|_0^N \left| 0 \right\rangle \tag{4.19c}$$

where after the CUT the ground state $|g\rangle$ is represented by the quasiparticle vacuum $|0\rangle = U^\dagger |g\rangle$. In the latter step the block-diagonality of the Hamiltonian H_{eff} is used. The N-quasiparticle sector of the dynamical structure factor we denote by

$$S^{zz}_N(Q,\omega) = -\frac{1}{\pi}\text{Im} \lim_{\delta\to 0^+} \left\langle 0 \right| S^z_{\text{eff}}(-Q)\Big|_N^0 \left[\omega - \Big(\sum_{i=0}^{N} H_{\text{eff}}(Q)\Big|_i^i - E_0\Big) + i\delta\right]^{-1} S^z_{\text{eff}}(Q)\Big|_0^N \left| 0 \right\rangle . \tag{4.20}$$

Therefore the dynamical structure factor $S^{zz}(Q,\omega)$ is given by

$$S^{zz}(Q,\omega) = \sum_N S^{zz}_N(Q,\omega) . \tag{4.21}$$

Analogously, we can split the spectral weight

$$I = \int_{-\pi}^{\pi} \frac{dQ}{2\pi} \int_{-\infty}^{\infty} d\omega \, S^{zz}(Q,\omega) \tag{4.22}$$

in parts I_N related to different quasiparticle numbers

$$I = \sum_N I_N \tag{4.23}$$

with

$$I_N = \int_{-\pi}^{\pi} \frac{\mathrm{d}Q}{2\pi} \int_{-\infty}^{\infty} \mathrm{d}\omega \; S_N^{zz}(Q,\omega) \; . \tag{4.24}$$

For the calculation of the dynamical structure factor $S^{zz}(Q,\omega)$ by means of CUTs it is necessary to determine the effective observable $S^z_{\mathrm{eff}}(Q)$, cf. equation (4.19b). This is done by transforming the local observable $S^z_1(r)$, see section 3.1.2, appendix E and appendix F. Accordingly, we also have to use a truncation scheme for observables, cf. section 3.4.3.

In the following we discuss the one- and two-quasiparticle contributions to the dynamical structure factor $S^{zz}(Q,\omega)$. By adjusting the momentum $\mathbf{Q}_\perp$ perpendicular to Q it is possible to fix the inner product $\mathbf{Qb}$ in equation (4.18). By setting $\mathbf{Qb} = \pi$ equation (4.18) yields

$$S^z(Q) = \frac{1}{\sqrt{2N}} \sum_r \mathrm{e}^{\mathrm{i}Qr} \left(S^z_1(r) - S^z_2(r) \right) \tag{4.25a}$$

$$= \frac{1}{\sqrt{2N}} \sum_r \mathrm{e}^{\mathrm{i}Qr} \left(t^\dagger_{z,r} + t_{z,r} \right) \tag{4.25b}$$

cf. equation C.1. Since in the symmetric case of the ladder no interactions between subspaces with odd quasiparticle numbers and subspaces with even quasiparticle numbers exist (cf. figure 4.3 and reference [Knetter *et al.*(2003a)]) the observable in equation (4.25) can be used to investigate odd contributions $S_N^{zz}(Q,\omega)$ with $N = 1,3,\ldots$ to the dynamical structure factor $S^{zz}(Q,\omega)$. Analogously, by setting $\mathbf{Qb} = 0$ equation (4.18) yields

$$S^z(Q) = \frac{1}{\sqrt{2N}} \sum_r \mathrm{e}^{\mathrm{i}Qr} \left(S^z_1(r) + S^z_2(r) \right) \tag{4.26a}$$

$$= -\frac{\mathrm{i}}{\sqrt{2N}} \sum_r \mathrm{e}^{\mathrm{i}Qr} \left(t^\dagger_{x,r} t_{y,r} - t^\dagger_{y,r} t_{x,r} \right) , \tag{4.26b}$$

which can be used to investigate even contributions $S_N^{zz}(Q,\omega)$ with $N = 2,4,\ldots$ to the dynamical structure factor $S^{zz}(Q,\omega)$.

One-triplon dynamical structure factor

For a translational invariant system the one-triplon dynamical structure factor can be calculated by the identity

$$\lim_{\delta\to 0^+} \frac{1}{\omega-\omega_0 \pm \mathrm{i}\delta} = \mathcal{P}\frac{1}{\omega-\omega_0} \mp \mathrm{i}\pi\delta(\omega-\omega_0) \tag{4.27}$$

with the principal value $\mathcal{P}$. Therefore, the one-triplon contribution $S_1^{zz}(Q,\omega)$ to the dynamical structure factor is given by

$$\begin{aligned} S_1^{zz}(Q,\omega) &= \left\langle 0\right| S^z_{\mathrm{eff}}(-Q)\big|_1^0\, \delta\Big(\omega - H_{\mathrm{eff}}(Q)\big|_1^1\Big)\, S^z_{\mathrm{eff}}(Q)\big|_0^1 \left|0\right\rangle && \text{(4.28a)}\\ &= \left|C^{S=1,m=0}_{S^z|_0^1}(Q)\right|^2 \; {}^{S=1}_{m=0}\!\left\langle Q\right|\, \delta\Big(\omega - H_{\mathrm{eff}}(Q)\big|_1^1\Big)\, \left|Q\right\rangle^{S=1}_{m=0} && \text{(4.28b)}\\ &= \left|C^{S=1,m=0}_{S^z|_0^1}(Q)\right|^2 \delta\left(\omega-\omega_1(Q)\right) && \text{(4.28c)}\\ &= S_1^{zz}(Q)\,\delta\left(\omega-\omega_1(Q)\right) && \text{(4.28d)} \end{aligned}$$

with the equal-time structure factor for the one-triplon part

$$S_1^{zz}(Q) = \left|C^{S=1,m=0}_{S^z|_0^1}(Q)\right|^2 \tag{4.29}$$

and

$$C^{S=1,m=0}_{S^z|_0^1}(Q) = -\sqrt{2}\mathrm{i}\mathrm{e}^{\mathrm{i}\frac{\mathbf{Qb}}{2}} \sum_{d_0} {}^z\left[c_{S_1^z|_0^1}\right]^{d_0} \sin\left(Qd_0 + \mathbf{Qb}/2\right)\,. \tag{4.30}$$

Details of the calculation of $C^{S=1,m=0}_{S^z|_0^1}(Q)$ are given in appendix F and in appendix E.

In figure 4.8 the equal-time structure factor for the one-triplon part $S_1^{zz}(Q)$ is depicted for various interaction values x. To maximize the one-triplon contribution we set $\mathbf{Qb} = \pi$. Black lines are calculated by sCUTs. Grey lines indicate results obtained by pCUTs [Schmidt(2004), Schmidt & Uhrig(2005)]. For $x = 0.5$ the results coincide within the linewidth. For the used definition of $S_1^{zz}(Q)$ (4.29) the equation $S_1^{zz}(Q)/I = 1.0$ holds in the absence of any interaction ($x = 0$). By increasing the interaction x the equal-time structure factor for the one-triplon part $S_1^{zz}(Q)$ decreases for momenta around $Q = 0$ and increases for momenta around $Q = \pi$. This observation indicates the strong tendency towards antiferromagnetism and agrees with results obtained by bosonization for weakly coupled spin chains where a peak in the dynamical structure factor around $Q = \pi$ is predicted [Shelton *et al.*(1996)].

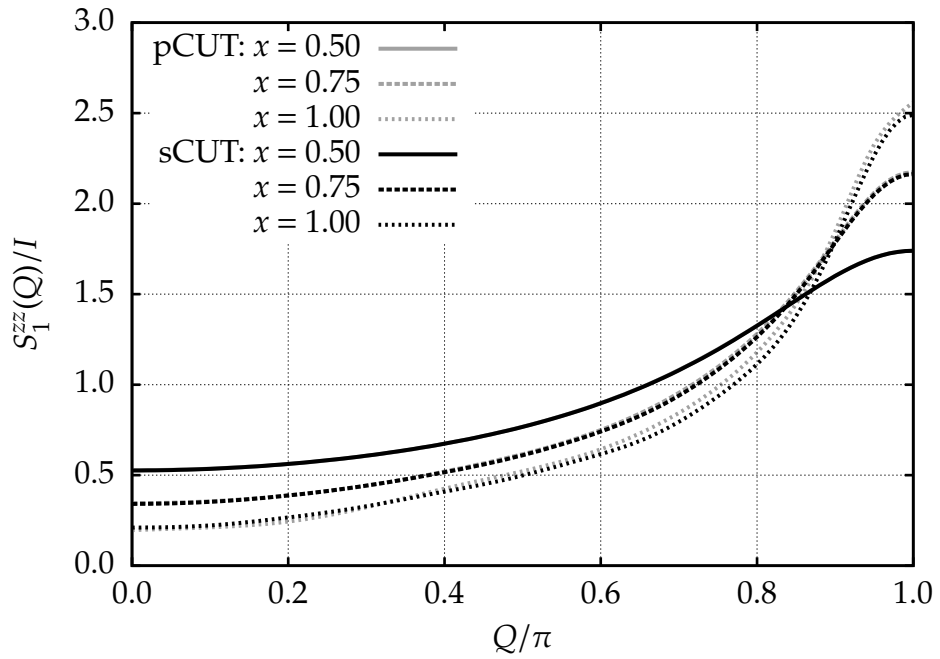

Figure 4.8: Equal-time structure factor for the one-triplon part $S_1^{zz}(Q)$ for $\mathbf{Qb} = \pi$ normalized to the total spectral weight I. Black lines: sCUT results for the generator $G_{\mathrm{pc}}(\ell)$ using the truncation scheme $N_{\mathrm{t}} = 4$, $\mathbf{D} = (10,.,8,.,5,.,3)$ and $N_{\mathrm{t}}^O = 3$, $\mathbf{D}^O = (10,10,8,8,6,6)$. Grey lines: pCUT results [Schmidt(2004), Schmidt & Uhrig(2005)]. For x=0.5 the sCUT and pCUT results agree within the linewidth. The area under a curve is equal to its relative weight $I_1^{\mathrm{rel}} = I_1/I$.

Two-triplon dynamical structure factor

To calculate the two-triplon dynamical structure factor $S_2^{zz}(Q,\omega)$ we use a Lanczos tridiagonalization, which leads to the continued fraction representation [Zwanzig(1961), Mori(1965), Gagliano & Balseiro(1987), Pettifor & Weaire(1985), Viswanath & Müller(1994)]

$$S_2^{zz}(Q,\omega) = -\frac{1}{\pi}\mathrm{Im}\,\frac{\left\langle 0\right| S^z_{\mathrm{eff}}(-Q)\big|_2^0\, S^z_{\mathrm{eff}}(Q)\big|_0^2 \left|0\right\rangle}{\omega - a_0(Q) - \dfrac{b_1^2(Q)}{\omega - a_1(Q) - \dfrac{b_2^2(Q)}{\cdots}}} \tag{4.31a}$$

$$= -\frac{1}{\pi}\mathrm{Im}\,\frac{\overset{S=1}{\underset{m=0}{\left\langle Q,l_1\right|}} \sum\limits_{l_1}\left[C^{S=1,m=0}_{S^z|_0^2}(Q)\right]^{l_1{}^*} \sum\limits_{d_1}\left[C^{S=1,m=0}_{S^z|_0^2}(Q)\right]^{d_1}\left|Q,d_1\right\rangle^{S=1}_{m=0}}{\omega - a_0(Q) - \dfrac{b_1^2(Q)}{\omega - a_1(Q) - \dfrac{b_2^2(Q)}{\cdots}}} \tag{4.31b}$$

$$= -\frac{1}{\pi}\mathrm{Im}\,\frac{\sum\limits_{d_1}\left|\left[C^{S=1,m=0}_{S^z|_0^2}(Q)\right]^{d_1}\right|^2}{\omega - a_0(Q) - \dfrac{b_1^2(Q)}{\omega - a_1(Q) - \dfrac{b_2^2(Q)}{\cdots}}}\,. \tag{4.31c}$$

The coefficients $a_n(Q)$ and $b_n(Q)$ are calculated by repeated application of $H_{\mathrm{eff}}\big|_1^1 + H_{\mathrm{eff}}\big|_2^2$ to the initial state $S^z_{\mathrm{eff}}(Q)\big|_0^2\left|0\right\rangle = \sum\limits_{d_1}\left[C^{S=1,m=0}_{S^z|_0^2}(Q)\right]^{d_1}\left|Q,d_1\right\rangle^{S=1}_{m=0}$ with momentum Q, spin $S = 1$, and S^z component $m = 0$. Details of the calculation of $\left[C^{S=1,m=0}_{S^z|_0^2}(Q)\right]^{d_1}$ are given in appendix F and in appendix E. For details about the Lanczos tridiagonalization see appendix A. All states $\left|Q,d_1\right\rangle^{S=1}_{m=0}$ with $d_1 < 4000$ are considered. The equal-time structure factor for the two-triplon part is given by

$$S_2^{zz}(Q) = \sum_{d_1}\left|\left[C^{S=1,m=0}_{S^z|_0^2}(Q)\right]^{d_1}\right|^2. \tag{4.32}$$

In figure 4.9 the two-triplon dynamical structure factor $S_2^{zz}(Q,\omega)$ is depicted for various values of x. The effective Hamiltonian and the effective observable are obtained by the generator $G_{\mathrm{pc}}(\ell)$ using the truncation scheme $N_{\mathrm{t}} = 4$, $\mathbf{D} = (10,.,8,.,5,.,3)$ and $N_{\mathrm{t}}^O = 3$, $\mathbf{D}^O = (10,10,8,8,6,6)$. The continued fraction (4.31) is terminated as described in appendix A.2 by a square-root terminator [Pettifor & Weaire(1985)].

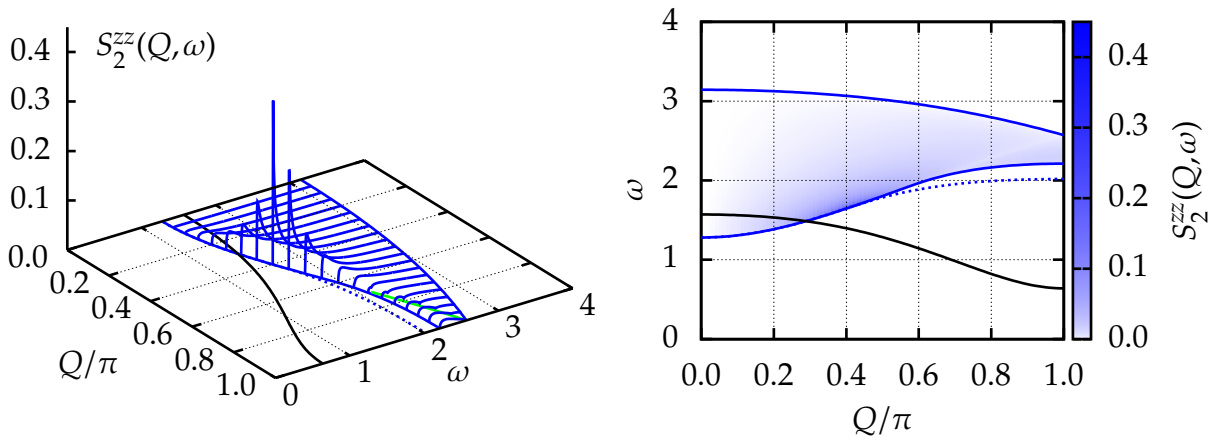

(a) $x = 0.5$

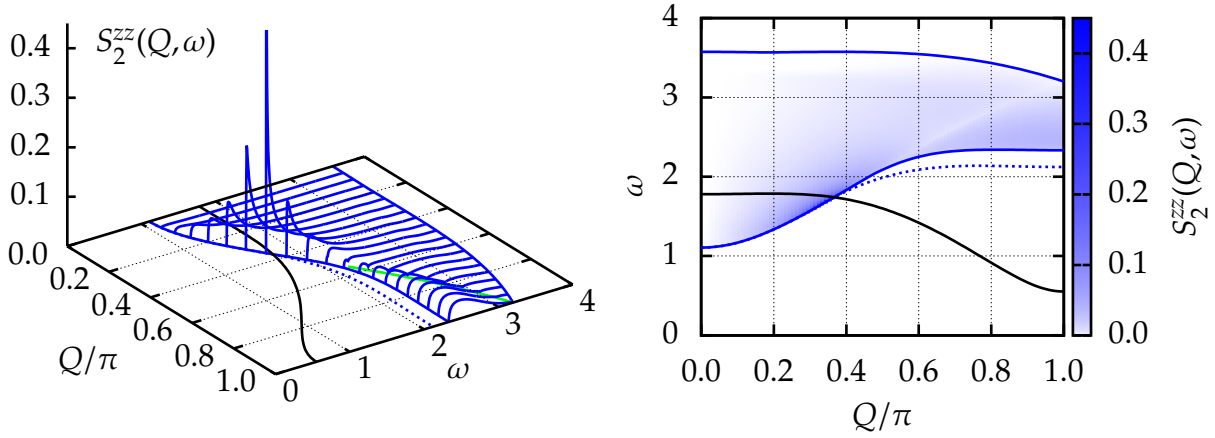

(b) $x = 0.75$

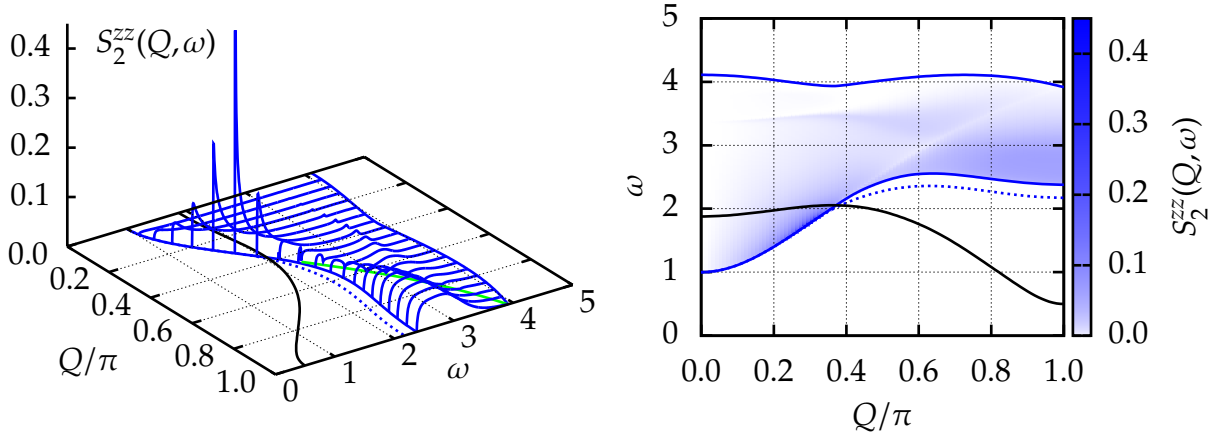

(c) $x = 1.0$

Figure 4.9: Two-triplon dynamical structure factor $S_2^{zz}(Q,\omega)$ for various values of x and $y = 0$ for $\mathbf{Qb} = 0$. The effective Hamiltonian and the effective observable are obtained by the generator $G_{\mathrm{pc}}(\ell)$ using the truncation scheme $N_{\mathrm{t}} = 4$, $\mathbf{D} = (10,.,8,.,5,.,3)$ and $N_{\mathrm{t}}^{O} = 3$, $\mathbf{D}^{O} = (10,10,8,8,6,6)$. The continued fraction (4.31) is terminated as described in appendix A.2. Solid black lines depict one-triplon dispersions. Dotted blue lines depict the $S = 1$ bound states. Green lines in the left panels indicate mid-band singularities.

In the left panel of figure 4.9a, 4.9b and 4.9c the two-triplon dynamical structure factor $S_2^{zz}(Q,\omega)$ is represented by solid blue lines in a three-dimensional plot. The right panels also show the two-triplon dynamical structure factor $S_2^{zz}(Q,\omega)$, as color plot. Here only the boundaries of the two-triplon continuum are represented by solid blue lines. Also the one-triplon dispersion is depicted by a solid black line in each panel. The dispersion of the $S = 1$ bound states is depicted by dotted blue lines. Note, that if the continued fraction for the two-triplon dynamical structure factor $S_2^{zz}(Q,\omega)$ is terminated by a square-root terminator, the bound states appear as δ-peaks. Therefore, we only depict their dispersion and not their weight in figure 4.9.

In figure 4.10 the same quantities as in figure 4.9 are depicted. This time, instead of a terminator, a slight broadening $\omega \to \omega + i\delta$ with $\delta = 0.05$[1] has been used to calculate the two-triplon dynamical structure factor $S_2^{zz}(Q,\omega)$, cf. appendix A. Coefficients $a_n(Q)$ and $b_{n+1}(Q)$ with $n < 1400$ have been used.

Most of the spectral weight inside the continuum of the two-triplon dynamical structure factor $S_2^{zz}(Q,\omega)$ is located near the lower band edge, cf. figure 4.9. Especially, in the region where the $S = 1$ bound state merges with the continuum plenty of spectral weight occurs. In figure 4.9 also mid-band singularities indicated by green lines can be observed. They can be interpreted as precursors of the upper band edge of the two-spinon continuum for the isolated spin chain [Schmidt(2004)]. However, these details of the continuum of the two-triplon dynamical structure factor $S_2^{zz}(Q,\omega)$ are barely accessibly in INS experiments. Due to the finite resolution in actual experiments the $S = 1$ bound state can be hardly separated from the continuum and thus dominates the dynamical structure factor $S_2^{zz}(Q,\omega)$. This is illustrated in figure 4.10 where a slight broadening with $\delta = 0.05$ has been used. Note, that the existence of a finite ring exchange can prevent the existence of a $S = 1$ bound state because it weakens the attractive interaction [Schmidt & Uhrig(2005), Notbohm *et al.*(2007)].

Spectral weight

Since the total spectral weight I is fixed by a sum rule, see appendix F, we define relative spectral weights by $I_N^{\text{rel}} = I_N/I$ where the N-particle part of the spectral weight is given by

$$I_N = \int_{-\pi}^{\pi} \frac{dQ}{2\pi}\, S_N^{zz}(Q) \tag{4.33}$$

with the N-particle equal-time structure factor $S_N^{zz}(Q)$. The one-particle equal-time structure factor $S_1^{zz}(Q)$ is given by equation (4.29) and the two-particle equal-time structure factor $S_2^{zz}(Q)$ by equation (4.32).

[1] As the energy ω the broadening δ is given in units of $J_\perp$, where we set $J_\perp = 1$.

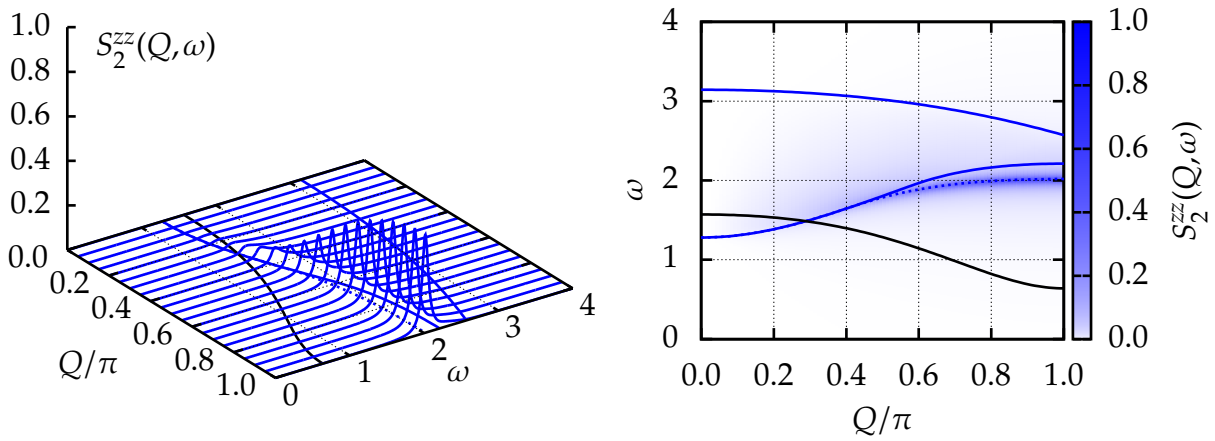

(a) $x = 0.5$

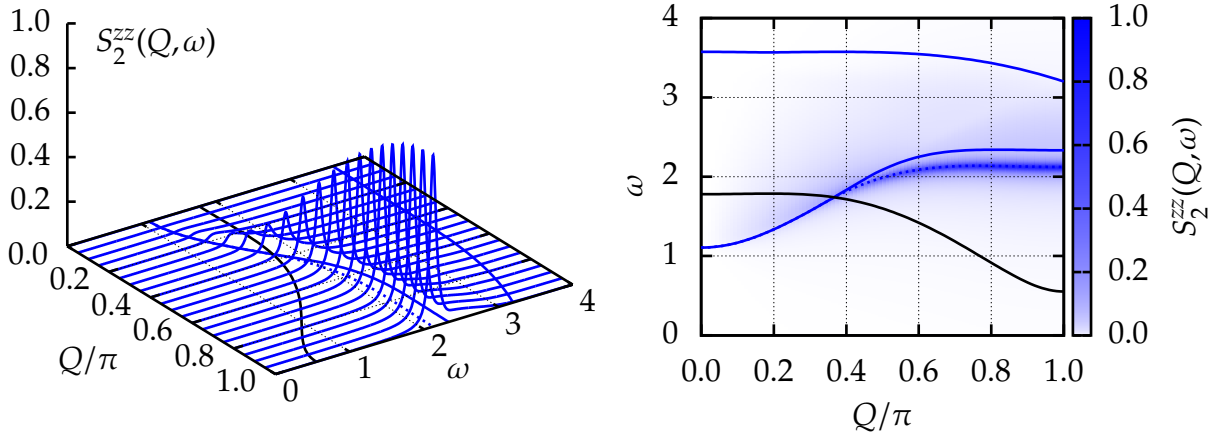

(b) $x = 0.75$

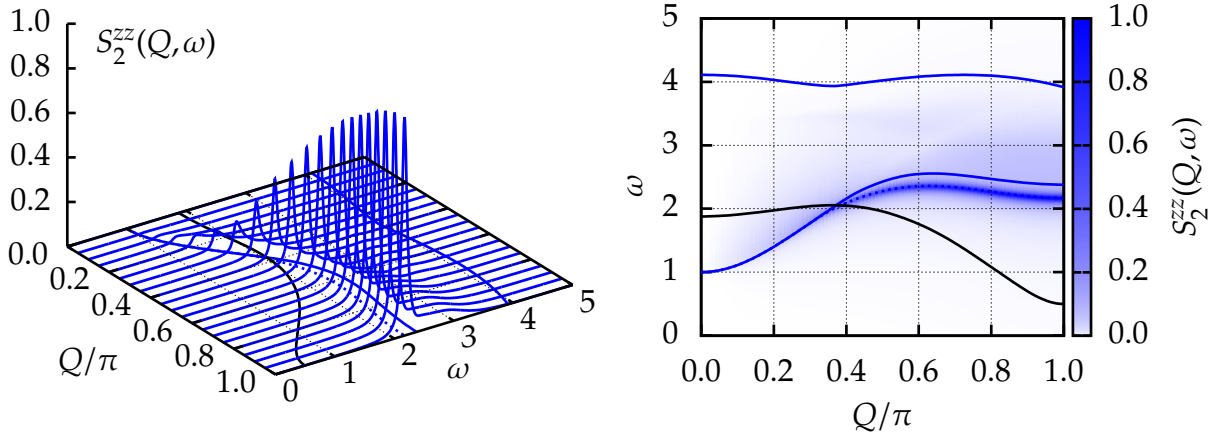

(c) $x = 1.0$

Figure 4.10: Two-triplon dynamical structure factor $S_2^{zz}(Q,\omega)$ for various values of x and $y = 0$ for $\mathbf{Qb} = 0$. The effective Hamiltonian and the effective observable are obtained by the generator $G_{\mathrm{pc}}(\ell)$ using the truncation scheme $N_{\mathrm{t}} = 4$, $\mathbf{D} = (10,.,8,.,5,.,3)$ and $N_{\mathrm{t}}^{O} = 3$, $\mathbf{D}^{O} = (10,10,8,8,6,6)$. The continued fraction (4.31) has been calculated up to $n = 1399$. A broadening with $\delta = 0.05$ has been used. Solid black lines depict one-triplon dispersions. Dotted blue lines depict the $S = 1$ bound states.

For $x = 0$ the complete spectral weight is in the one-particle sector. With increasing interaction x more and more weight is distributed in channels with more and more triplons. In table 4.2 the relative spectral weights for the one- and two-particle channel I_1^{rel} and I_2^{rel} plus their sum are listed for $x = 0.5$, $x = 0.75$ and $x = 1.0$. For the considered

Table 4.2: Relative spectral weights I_N^{rel}.

x	I_1^{rel}	I_2^{rel}	$I_1^{\text{rel}} + I_2^{\text{rel}}$
0.50	0.918	0.075	0.993
0.75	0.829	0.141	0.970
1.00	0.739	0.199	0.938

interactions x the spectral weight is dominated by the one- and two-particle sector. Even for $x = 1.0$ about 94% of the spectral weight is found in these sectors. The missing spectral weight can be found in subspaces with more than two triplons, whereby the main part of the missing spectral weight occurs in the three-triplon subspace [Schmidt(2004)].

4.2 The asymmetric antiferromagnetic spin $S = 1/2$ Heisenberg ladder for $x = 0.5$ and $y = 0.1$

In this section we study the parameter set $x = 0.5, y = 0.1$ and compare its results to those of the parameter set $x = 0.5, y = 0.0$. The scope of this section is to illustrate the general considerations concerning CUTs for unstable quasiparticles (cf. chapter 3) by a concrete example.

The low energy spectrum for $x = 0.5$ and $y = 0$ is well studied by several methods (see for instance reference [Sushkov & Kotov(1998)] and reference [Trebst *et al.*(2000)]) including methods based on CUTs [Knetter *et al.*(2003a), Schmidt(2004), Reischl(2006)], see also section 4.1. Therefore, it is a perfect starting point to discuss the more sophisticated case with $x = 0.5$ and $y = 0.1$. The additional diagonal interaction y makes the whole situation conceptionally more difficult because it breaks a symmetry. While for $y = 0$ the model is symmetric under reflection (see figure. 4.3) an arbitrary small value $y \neq 0$ breaks this reflection symmetry (see figure. 4.1).

Breaking this symmetry creates processes which enable the triplons to decay into two-triplon states. Therefore, the asymmetric spin $S = 1/2$ Heisenberg ladder is an ideal model to analyze quasiparticles with finite lifetime and to illustrate our previous theoretical considerations concerning the choice of an adaptive generator quantitatively, see section 3.2.3.

Firstly, we show that a rearrangement of the states of the Hilbert space, i.e., a continuous relabelling (for simple examples see reference [Dusuel & Uhrig(2004), Reischl(2006)] and section 3.3.1), reduces the speed of convergence (see section 4.2.1). Therefore, generators that avoid such a rearrangement induce a considerably faster convergence.

Secondly, we discuss the low-energy spectrum for the symmetric and for the asymmetric ladder (see section 4.2.2). If decay is possible the generator $G_{\mathrm{gs,1p}}(\ell)$ and the generator $G_{\mathrm{pc}}(\ell)$ indeed tend to interpret the energetically lowest states above the ground state as the elementary excitations (as stated before in section 3.2.3). This can be avoided by using the generator $G_{\mathrm{gs}}(\ell)$. Unfortunately, for this generator a simple calculation in the one-particle subspace is not sufficient to obtain reliable results for the true one-triplon dispersion. This is a consequence of the fact that in the effective Hamiltonian induced by $G_{\mathrm{gs}}(\ell)$ the one-particle subspace still couples to higher particle subspaces (see figure 3.3). To obtain reliable results for the single triplon dispersion we include states which consist of up to three particles in our calculations (see section 4.2.2). Especially, we show results for a spectral density at zero temperature in which the (quasi)particle decay is manifest as a Lorentzian resonance of finite width.

4.2.1 Convergence

As for the toy model discussed in section 3.3.2 we use the residual off-diagonality (ROD) [Reischl *et al.*(2004), Reischl(2006)] to quantify the speed of convergence of the flow equation. The ROD is given by

$$\mathrm{ROD}(\ell) = \left(\sum_{\substack{\mathbf{i},\mathbf{j} \\ h^{\mathbf{i}}_{\mathbf{j}}(\ell) \in G(\ell)}} \left| h^{\mathbf{i}}_{\mathbf{j}}(\ell) \right|^2 \right)^{1/2} . \tag{4.34}$$

where the range of the sum $\sum_{\mathbf{i},\mathbf{j}}$ depends on the choice of the generator $G(\ell)$, cf. section 3.3.2 equation (3.74). For translational invariant systems in the thermodynamic limit only one representative of the translational symmetry group is included. Otherwise the ROD would grow proportional to the system size. In addition, the partial ROD^i_j with $i \geq j$ denotes the square root of the sum of the moduli squared of all coefficients belonging to terms with i creation and j annihilation operators or to their hermitian conjugate terms, i.e.,

$$\mathrm{ROD}^i_j(\ell) = \left(\sum_{\substack{\mathbf{i},\mathbf{j} \\ h^{\mathbf{i}}_{\mathbf{j}}(\ell) \in H^i_j(\ell), H^j_i(\ell)}} \left| h^{\mathbf{i}}_{\mathbf{j}}(\ell) \right|^2 \right)^{1/2} . \tag{4.35}$$

Figure 4.11a shows the evolution of the ROD during the flow for different generators $G(\ell)$ and different truncation schemes for $x = 0.5$ and $y = 0$. For all generators the RODs

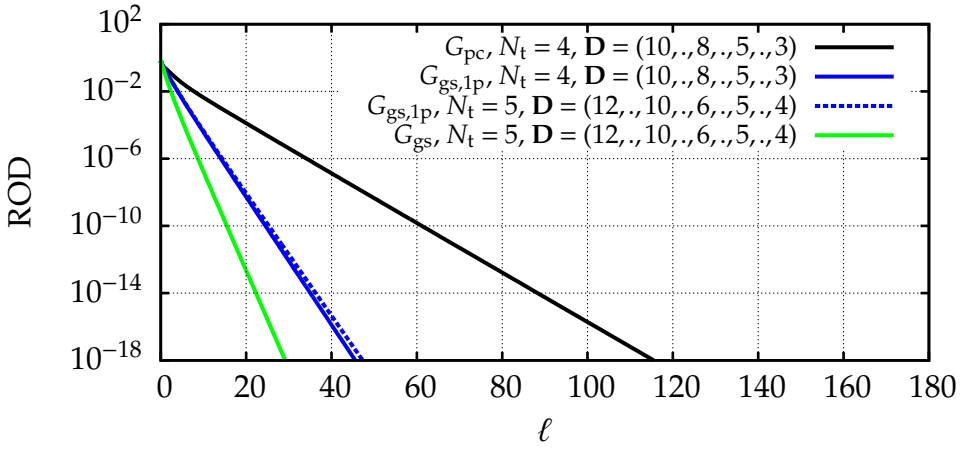

(a) RODs for the symmetric ladder with $x = 0.5$ and $y = 0$.

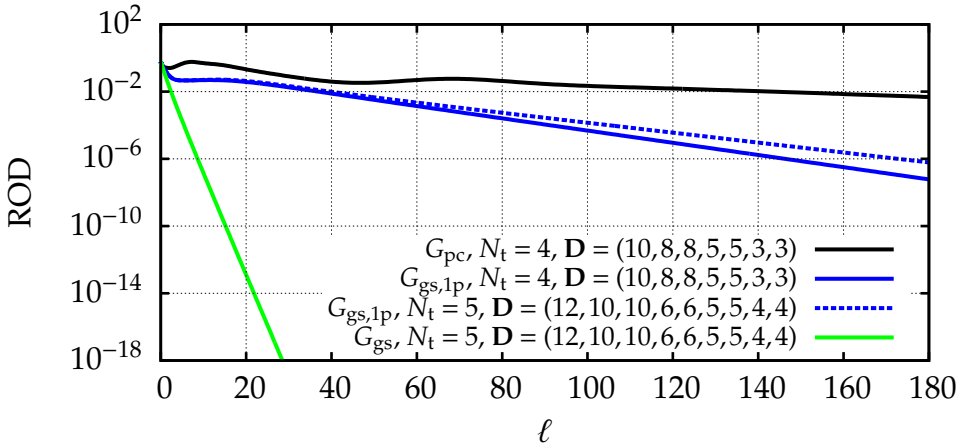

(b) RODs for the asymmetric ladder with $x = 0.5$ and $y = 0.1$.

Figure 4.11: Convergence of flow equations. Panel (a) shows the evolution of the ROD during the flow for various generators and various truncation schemes for the symmetric ladder. In all cases, the ROD decreases strictly monotonically. Panel (b) shows the evolution of the ROD for various generators and various truncation schemes for the asymmetric ladder. The RODs of the generator $G_{\mathrm{gs,1p}}(\ell)$ and the generator $G_{\mathrm{pc}}(\ell)$ increase temporarily during the flow. This indicates a significant rearrangement of the states in the HILBERT space.

decrease strictly monotonically. The ROD of the generator $G_{\mathrm{gs}}(\ell)$ decreases faster than the ROD of the generator $G_{\mathrm{gs,1p}}(\ell)$. This a consequence of the fact that the generator $G_{\mathrm{gs,1p}}(\ell)$ contains more coefficients than the generator $G_{\mathrm{gs}}(\ell)$. The convergence of these additional coefficients is slower because they connect states that differ less in their eigenenergies (cf. equation (3.43)), for example, the energy gap between one- and three-triplon states is smaller than the energy gap between the vacuum state and the two-triplon states. This also explains why the generator $G_{\mathrm{gs,1p}}(\ell)$ converges faster than the generator $G_{\mathrm{pc}}(\ell)$.

The convergence behavior clearly changes if one includes the diagonal interaction, even if y is small ($y = 0.1, 0.01$). In figure 4.11b the ROD during the flow for various generators and various truncation schemes for $x = 0.5$ and $y = 0.1$ is depicted. Only the ROD of the generator $G_{\mathrm{gs}}(\ell)$ decreases strictly monotonically, whereas the RODs of the generator $G_{\mathrm{gs,1p}}(\ell)$ and the generator $G_{\mathrm{pc}}(\ell)$ increase temporarily during the flow. These increases indicate a rearrangement in the Hilbert space, cf., reference [Dusuel & Uhrig(2004)] for simple examples. . If all eigenstates were ordered in such a way that states with more triplons had higher eigenenergies, the ROD would decrease exponentially (cf. equation (3.42)).

The generator $G_{\mathrm{pc}}(\ell)$ sorts the eigenvalues in ascending order of the particle number of the corresponding states [Mielke(1998), Heidbrink & Uhrig(2002), Fischer *et al.*(2010)]. These rearrangements affect the results for the one-triplon dispersion as we illustrate in section 4.2.2.

Figure 4.12 shows the ROD of the generator $G_{\mathrm{pc}}(\ell)$ split in the partial RODs ROD^i_j defined above for $x = 0.5$ and $y = 0.1, 0.01$. Clearly, the contributions ROD^i_j of the ROD changing the number of triplons only by one ($|i - j| = 1$) provide the main contributions to the total ROD, although the corresponding initial couplings are proportional to y which is small ($y = 0.1, 0.01$). From this we infer that the convergence of the flow equation is mainly influenced by terms in the generator that induce a rearrangement of the Hilbert space if they are to be eliminated by the CUT. It is less important whether the corresponding coupling parameter is large or not. This is an important property of the CUTs that distinguishes them from conventional diagrammatic perturbation theories.

In summary, we state that a rearrangement of the states of the Hilbert space reduces the speed of convergence. Omitting the corresponding terms from the generator stabilizes the flow in the sense that the convergence is monotonic and robust. Hence, especially the generator $G_{\mathrm{gs}}(\ell)$ yields a very fast converging and robust flow. We point out that a fast convergence is advantageous because it minimizes the interval in ℓ during which significant terms are truncated. Hence as a rule of thumb, the faster the convergence, the smaller the truncation errors.

4.2.2 Low-energy spectrum

In this section we discuss the low-energy spectrum of the effective Hamiltonian H_{eff}. The CUTs were always stopped at $\ell = 200$. At this value the remaining effect on the one-particle subspace is very small for all generators and truncation schemes (cf. figure 4.11) so that a further integration of the flow equation would not change the results for the one-triplon dispersion as shown in figure 4.13.

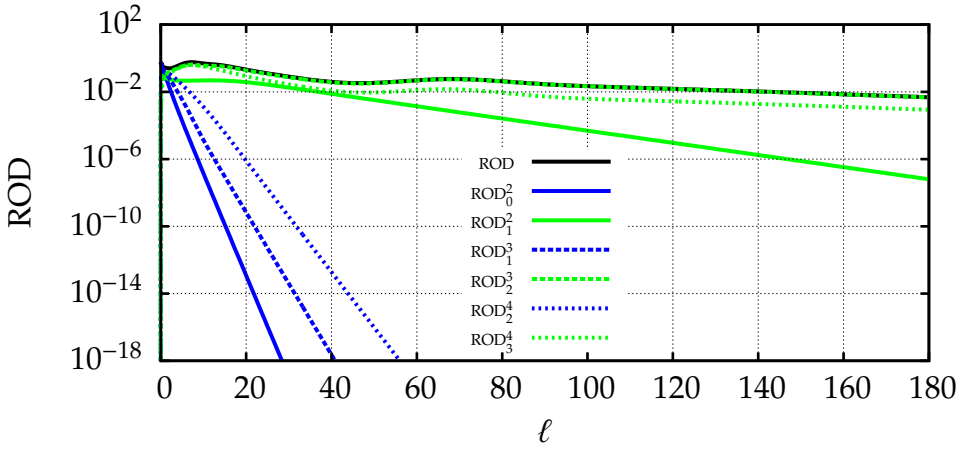

(a) ROD_j^i for the generator $G_{\mathrm{pc}}(\ell)$ for the asymmetric ladder with $x = 0.5$ and $y = 0.1$. Truncation scheme: $N_{\mathrm{t}} = 4$, $\mathbf{D} = (10,8,8,5,5,3,3)$.

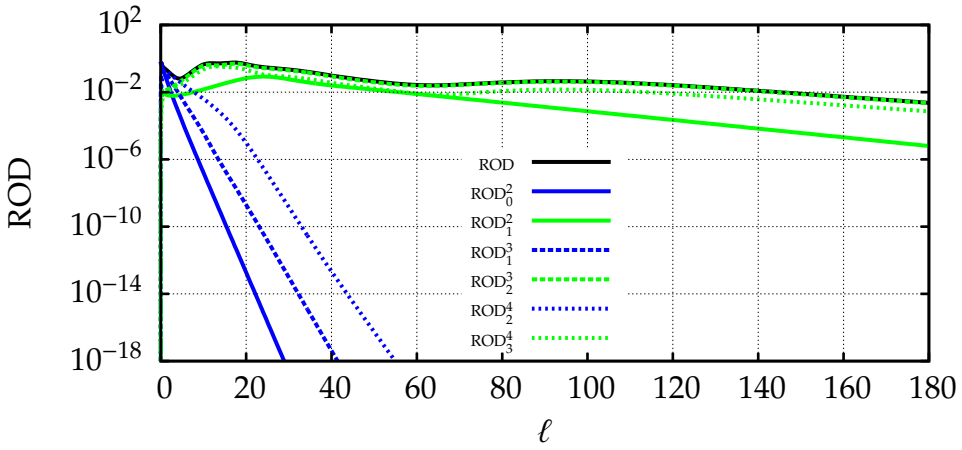

(b) ROD_j^i for the generator $G_{\mathrm{pc}}(\ell)$ for the asymmetric ladder with $x = 0.5$ and $y = 0.01$. Truncation scheme: $N_{\mathrm{t}} = 4$, $\mathbf{D} = (10,8,8,5,5,3,3)$.

Figure 4.12: ROD of the generator $G_{\mathrm{pc}}(\ell)$ split into the parts ROD_j^i for the asymmetric ladder for $x = 0.5$ and $y = 0.1, 0.01$. The main contributions to the total ROD is due to ROD_j^i with $|i - j| = 1$.

Energy properties

The generator $G_{\mathrm{pc}}(\ell)$ and the generator $G_{\mathrm{gs,1p}}(\ell)$ separate the one-particle subspace from the other subspaces. Consequently, for these two generators the one-triplon dispersion $\omega_1(Q)$, cf. equation (4.9), yields eigenvalues of the effective Hamiltonian H_{eff} in the one-particle subspace. In contrast, the generator $G_{\mathrm{gs}}(\ell)$ does not separate the one-particle space. Therefore, the effective Hamiltonian H_{eff} still contains terms that connect the one-particle subspace with states of more particles, see figure 3.3. In this case the quantity $\omega_1(Q)$ only gives an approximation of the eigenvalues of the effective Hamiltonian H_{eff}, cf. figure D.1.

In figure 4.13a the one-triplon dispersion $\omega_1(Q)$ is displayed for $x = 0.5$ and $y = 0.0$. Results for all three generators $G_{\mathrm{pc}}(\ell)$, $G_{\mathrm{gs,1p}}(\ell)$ and $G_{\mathrm{gs}}(\ell)$ and various truncation

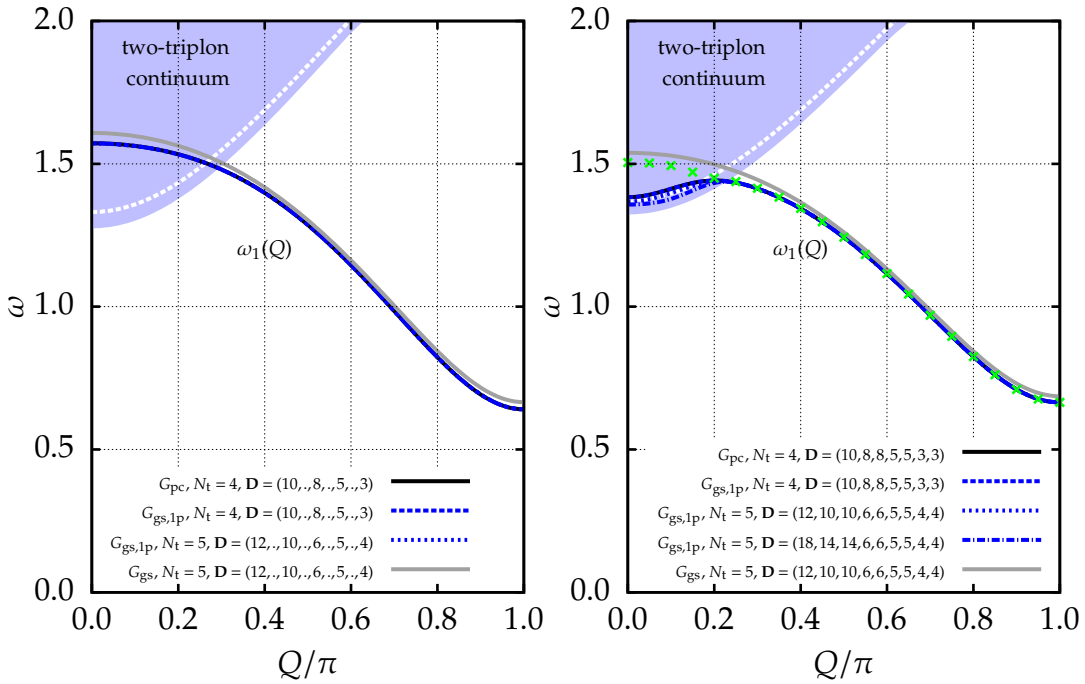

(a) $x = 0.5$, $y = 0.0$ **(b)** $x = 0.5$, $y = 0.1$

Figure 4.13: Low-energy spectrum of the symmetric and asymmetric spin $S = 1/2$ Heisenberg ladder. Panel (a) shows results for the one-triplon dispersion $\omega_1(Q)$ for the symmetric ladder with $x = 0.5$ and $y = 0.0$. Results for different generators and different truncation schemes are depicted. Additionally, the lower part of the two-particle continuum is shown (light blue area). The dashed white line represents an approximation of the lower edge of the two-particle continuum obtained by the approximate one-triplon dispersion $\omega_1(Q)$ in the case of the generator $G_{\mathrm{gs}}(\ell)$. Panel (b) shows the corresponding quantities for the asymmetric ladder with $x = 0.5$ and $y = 0.1$. Green crosses represent the renormalized one-triplon dispersion (see text).

schemes are shown. The two generators $G_{\mathrm{pc}}(\ell)$ and $G_{\mathrm{gs,1p}}(\ell)$ separating the one-particle space yield almost the same results and barely depend on the chosen truncation scheme. Together with the good convergence, see figure 4.11a, this implies that the results are

reliable. By construction, for the generator $G_{\mathrm{gs}}(\ell)$ the quantity $\omega_1(Q)$ as defined above (cf. equation (4.9)) yields only an approximation of the true one-triplon dispersion. The resulting $\omega_1(Q)$ is an upper variational bound to the results obtained from the other two generators if truncation errors are negligible. This fact is based on the variational principle that a minimum in a restricted subspace is an upper bound to the minimum in an unrestricted subspace. To improve the results in this case one has to consider subspaces with more particles as well, see below.

Figure 4.13a also displays the lower part of the two-particle continuum $\omega_2(Q)$, cf. equation (4.10), using the one-triplon dispersion $\omega_1(Q)$ obtained from the generator $G_{\mathrm{pc}}(\ell)$. The additional dashed white line represents an approximation of the lower edge of the two-particle continuum obtained by the approximate one-triplon dispersion $\omega_1(Q)$ obtained from the generator $G_{\mathrm{gs}}(\ell)$.

We emphasize again that due to the reflection symmetry for $y = 0$, see figure 4.3, no interaction exists between the one-triplon states and the two-triplon continuum. As a result the quasiparticles are well defined and infinitely long lived for the whole Brillouin zone, although the two-particle continuum starts below the one-triplon dispersion for certain momenta Q. In addition, this symmetry prevents any rearrangement between the one- and two-particle subspaces during the flow, see section 3.2.3. This situation changes abruptly if a diagonal interaction is switched on, even if y is infinitesimally small.

In figure 4.13b the one-triplon dispersion $\omega_1(Q)$ is displayed for $x = 0.5$ and a small additional interaction $y = 0.1$. Again, results for all three generators $G_{\mathrm{pc}}(\ell)$, $G_{\mathrm{gs,1p}}(\ell)$ and $G_{\mathrm{gs}}(\ell)$ and various truncation schemes are shown as well as the lower part of the two-particle continuum $\omega_2(Q,q)$ determined from the one-triplon dispersion obtained from the generator $G_{\mathrm{pc}}(\ell)$. Likewise, the approximate results for the lower edge of the two-particle continuum obtained from the generator $G_{\mathrm{gs}}(\ell)$ are shown.

The use of the two generators $G_{\mathrm{pc}}(\ell)$ and $G_{\mathrm{gs,1p}}(\ell)$ implies significantly lower energies for the one-triplon dispersion, see figure 4.13b, where $\omega_1(Q)$ overlaps with the two-triplon continuum. The results strongly depend on the truncation scheme in this region. This can be explained as follows. Since for $y \neq 0$ the one-particle and the two-particle space are interacting with each other, the two generators $G_{\mathrm{pc}}(\ell)$ and $G_{\mathrm{gs,1p}}(\ell)$ try to sort the eigenvalues in such a way that the eigenvalues of the one-triplon dispersion lie below the two-particle continuum, see figure 3.2 and section 3.2.3. Therefore, the one-triplon dispersion of the effective model H_{eff} lies at the lower edge of the two-particle continuum in the region where the one-triplon dispersion merges with the two-particle continuum. This is not completely achieved in practice because of the finite range of processes which can be described by our truncation scheme in real space.

We truncate the range of the decay processes in real space. This means that the distance between the generated two triplons is limited although the true scattering

state comprises contributions up to infinite distance. As a result, the rearrangement of the eigenvalues is only incomplete. Figure 4.13b illustrates that increasing the range of the decay processes (e.g. increasing D_3) implies that $\omega_1(Q)$ approaches the lower band edge of $\omega_2(Q,q)$ from above more and more.

As stated before, the rearrangements of the states are unfavorable for two reasons. Firstly, they imply a slow convergence, which may cause growing truncation errors. Secondly, one usually defines the state with the largest spectral weight above the ground state as the elementary excitation of the system and not a state with almost no spectral weight, even if it is lower in energy. Strictly speaking, *one* scattering state inside the continuum in an infinite large system has no spectral weight. To define a weight inside the continuum an integration over a finite energy interval is necessary.

To avoid the rearrangement of the eigenstates, which leads to a potentially misleading (quasi)particle picture, we employ the operator $G_{\mathrm{gs}}(\ell)$ (cf. figure 4.13b). The generator $G_{\mathrm{gs}}(\ell)$ only yields an approximation for the one-triplon eigenvalues of the effective Hamiltonian H_{eff}. This is the case even in the region of the Brillouin zone where the (quasi)particles are well defined. Due to our treatment of the problem in real space, we cannot distinguish processes in different regions in momentum space easily. To improve the results for the one-triplon dispersion one must include transitions to states that consist of more than one particle. This is discussed below.

Here, we first want to show the results for the two-, three- and four-particle continua (cf. equation (4.10), equation (4.14) and equation (4.15)) resulting from the approximate one-triplon dispersion $\omega_1(Q)$ in the case of the generator $G_{\mathrm{gs}}(\ell)$ for $x = 0.5$ and $y = 0.1$. The boundaries of these continua are shown in figure 4.14b by solid lines. Additionally, figure 4.14b shows the lower boundaries of the three- and four-particle continua[2] emerging from the combination of the approximate one-triplon dispersion $\omega_1(Q)$ and the $S = 0$ bound state.

The two-particle bound states for $S = 0$ and $S = 1$ shown in figure 4.14b are calculated by diagonalizing the effective Hamiltonian H_{eff} in the subspace spanned by the single triplon states (4.8) and the two-triplon states (4.13) with $0 < d_1 < 120$ for each given value of Q (for details see appendix D)[3]. Since the subspace spanned by the states (4.8) and (4.13) is not separated from states with higher number of triplons (cf. figure D.1) we obtain, as for the one-triplon dispersion $\omega_1(Q)$, only an approximation for the bound states. Consequently, the depicted continua only represent approximations. The restriction of the relative distance d_1 in the two-triplon states (4.13) is less important. Increasing d_1 does not change the results perceivably.

For comparison, figure 4.14a shows the same quantities for the symmetric

[2] The names "three- and four-particle continuum" refer to the fact that the corresponding states consist of three, respectively four, triplons in the basis of the effective Hamiltonian.

[3] Here we considered $d_1 < 120$ only to be consistent with the later calculations which also include the three-particle space. In principle, $d_1 \approx 4000$ is easily accessible in the two-particle space.

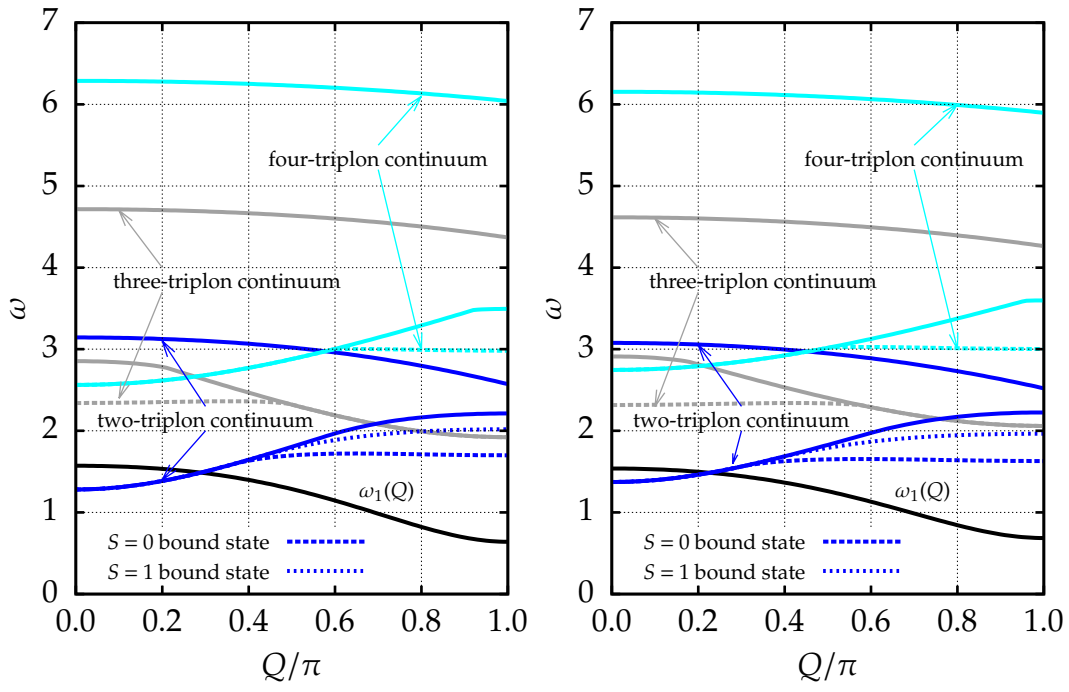

(a) $x = 0.5$, $y = 0.0$ **(b)** $x = 0.5$, $y = 0.1$

Figure 4.14: Panel (b): Two-, three- and four-triplon continua of the AASHL with $x = 0.5$ and $y = 0.1$. The solid blue lines represent the lower and upper boundaries of the two-particle continuum. The other blue lines represent the $S = 0$ and the $S = 1$ two-particle bound states. Grey lines illustrate the boundaries of the three-particle continuum, where the type of line corresponds to the two-particle state(s) used to determine the three-particle continuum. Cyan lines illustrate the boundaries of the four-particle continuum, where the type of line corresponds to the three-particle state(s) used to determine the four-particle continuum. Panel (a): Analogous results for the symmetric case with $x = 0.5$ and $y = 0.0$.

case $x = 0.5$ and $y = 0$, cf. section 4.1 and references [Uhrig & Schulz(1996), Uhrig & Normand(1998), Damle & Sachdev(1998), Sushkov & Kotov(1998), Trebst *et al.*(2000), Knetter *et al.*(2001)].

Note that the whole complex structure of the low-energy spectrum shown in figure 4.14 follows from the one-triplon dispersion, the triplon-triplon interaction, and from the diagonalization of the effective Hamiltonian within the one- and two-triplon subspace.

Spectral properties

In this subsection we improve the results presented in the former section for the one-triplon dispersion which we obtained with the generator $G_{\mathrm{gs}}(\ell)$ for $x = 0.5$ and $y = 0.1$. This is achieved by including transitions to three-triplon states. To describe the triplon decay we calculate the zero temperature spectral density.

We start by analyzing the frequency and momentum resolved retarded zero tem-

perature Green function

$$\mathcal{G}(Q,\omega) = \lim_{\delta\to 0^+} {}^{S=1}_{m=0}\!\left\langle Q\right| \left[\omega - (H_{\text{eff}}(Q) - E_0) + \mathrm{i}\delta\right]^{-1} \left|Q\right\rangle^{S=1}_{m=0} . \tag{4.36}$$

The corresponding spectral density $\rho(Q,\omega)$ follows by taking the negative imaginary part of $\mathcal{G}(Q,\omega)$ divided by π

$$\rho(Q,\omega) = -\frac{1}{\pi}\mathrm{Im}\,\mathcal{G}(Q,\omega) . \tag{4.37}$$

We only investigate the action of the effective Hamiltonian H_{eff} on the state $\left|Q\right\rangle^{S=1}_{m=0}$ to illustrate the description of quasiparticle decay by using the generator $G_{\text{gs}}(\ell)$. We do not transform any observables as before, cf. section 4.1.2. An investigation of the dynamical structure factor of the AASHL is given in section 4.3.

The Green function is evaluated by tridiagonalization (Lanczos algorithm, cf. appendix A), which leads to the continued fraction representation [Zwanzig(1961), Mori(1965), Gagliano & Balseiro(1987), Pettifor & Weaire(1985), Viswanath & Müller(1994)]

$$\mathcal{G}(Q,\omega) = \cfrac{1}{\omega - a_0(Q) - \cfrac{b_1^2(Q)}{\omega - a_1(Q) - \cfrac{b_2^2(Q)}{\cdots}}} . \tag{4.38}$$

The coefficients $a_n(Q)$ and $b_n(Q)$ are calculated by repeated application of $H_{\text{eff}}(Q) - E_0$ on the initial state $\left|Q\right\rangle^{S=1}_{m=0}$ with wave vector Q, spin $S = 1$, and S^z component $m = 0$ (for details see appendix A). Note that the continued fraction in the denominator on the right hand side of (4.38) (proportional to $b_1^2(Q)/\omega\ldots$) can be taken as a standard self-energy whose imaginary part determines the decay rate.

In all practical calculations, we have to restrict ourselves to a certain subspace. For this calculation, we considered the subspace spanned by

$$\left|Q\right\rangle^{S=1}_{m=0} \tag{4.39a}$$

$$\left|Q,d_1\right\rangle^{S=1}_{m=0} \tag{4.39b}$$

$$\left|Q,d_1,d_2,a\right\rangle^{S=1}_{m=0} \tag{4.39c}$$

with $a = 1,2,3$ and $d_1,d_2 > 0$ and $d_1,d_1 + d_2 < 120$, cf. table D.1 in appendix D. Thus we

consider the restricted effective Hamiltonian

$$H_{\text{eff}}^{\text{res}} = H_1^1(\infty) + H_2^2(\infty) + H_3^3(\infty) + H_1^2(\infty) + H_2^1(\infty) + H_1^3(\infty) + H_3^1(\infty) + H_2^3(\infty) + H_3^2(\infty) \,. \tag{4.40}$$

The action of this restricted effective Hamiltonian $H_{\text{eff}}^{\text{res}}$ on the considered subspace is presented in appendix D. More details of the calculation of the spectral density are given in appendix A.

Figure 4.15a shows the spectral density $\rho(Q,\omega)$ for $x = 0.5$ and $y = 0.1$. For $Q \lessapprox 0.2\pi$

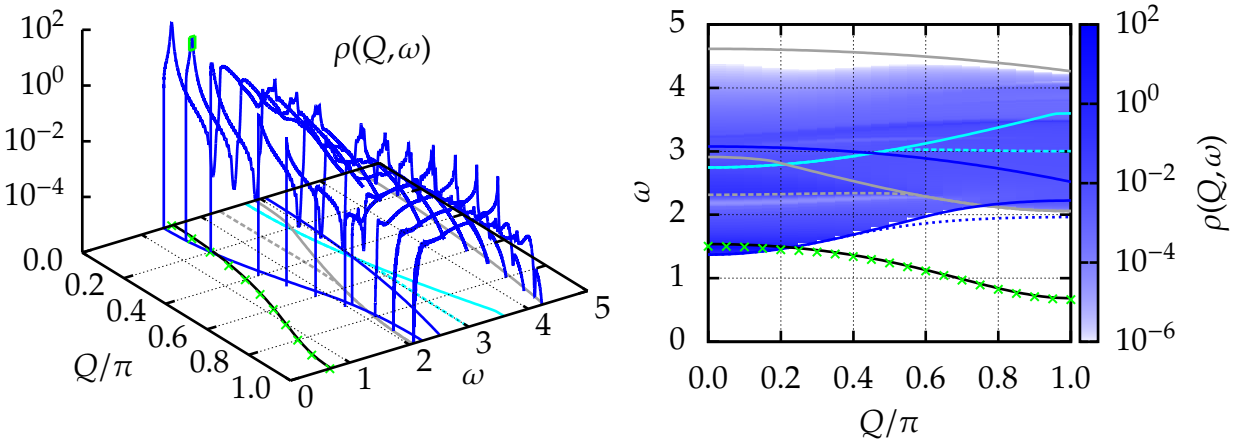

(a) Spectral density of the AASHL for $x = 0.5$ and $y = 0.1$.

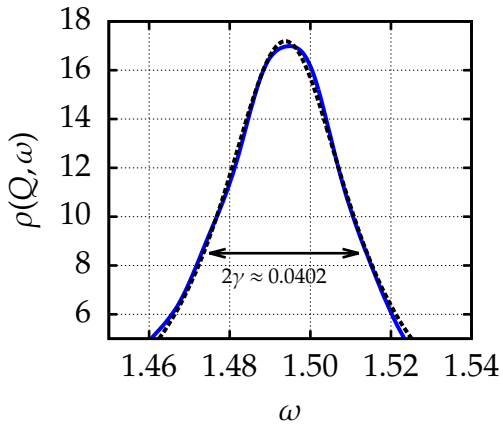

(b) Lorentzian fit of the spectral density

Figure 4.15: Spectral density of the AASHL. Panel (a) shows the spectral density of the AASHL for $x = 0.5$ and $y = 0.1$. Green crosses depict the renormalized one-triplon dispersion obtained by using the generator $G_{\text{gs}}(\ell)$ (truncation scheme: $N_{\text{t}} = 5$, $\mathbf{D} = (12,10,10,6,6,5,5,4,4)$) and (tri)diagonalization in the subspace (4.39). In panel (b), a Lorentzian is fitted to the spectral density. The described quasiparticle exhibits an inverse lifetime of $\gamma \approx 0.0201$.

decaying triplons are observed. Their maximum density lies in the vicinity of the approximate one-triplon dispersion. The region framed in green is shown in detail in

figure 4.15b. In this region, we can fit our data to a Lorentzian

$$L(\omega) = \frac{A}{\pi} \frac{\gamma}{(\omega - \omega_0)^2 + \gamma^2} \tag{4.41}$$

with

$$A \approx 1.0848/J_\perp \tag{4.42a}$$

$$\omega_0 \approx 1.4938\ J_\perp \tag{4.42b}$$

and the inverse lifetime

$$\gamma \approx 0.0201\ J_\perp\ . \tag{4.42c}$$

Note, that the fitting parameter A is greater than one which would correspond to a quasiparticle weight greater than one. This illustrates once more that the usual Fermi liquid like definition of the quasiparticle weight does not hold in this system, cf. section 2.2.

Besides the strong one-triplon peaks for $Q \lessapprox 0.2\pi$ the spectral density increases distinctly at the beginning of the three-particle continuum involving the $S = 0$ bound state for $Q \lessapprox 0.5\pi$, cf. figure 4.15a. This illustrates that the existence of bound states influences the form of the spectral density significantly. For an additional discussion of the influence of the $S = 1$ bound state and a $S = 2$ anti-bound state on the spectral density $\rho(Q,\omega)$ see [Fischer *et al.*(2010)].

Finally, we want to discuss the shift of the one-triplon dispersion caused by the hybridization with two- and three-particle states. In the sequel, we refer to this shifted one-triplon dispersion as renormalized one-triplon dispersion. The results for the renormalized one-triplon dispersion are depicted in figure 4.13b and figure 4.15a by green crosses.

We obtain the renormalized one-triplon dispersion by fixing the total momentum Q and determining the root of the real part of the Green function $\mathcal{G}(Q,\omega)$ (4.38) using the subspace (4.39). To good accuracy, we retrieve the results obtained before by the generators $G_{\mathrm{pc}}(\ell)$ and $G_{\mathrm{gs,1p}}(\ell)$ in the region of the Brillouin zone where the quasiparticles are stable. Therefore, it is sufficient to consider the subspace (4.39) if one wants to describe the one-triplon dispersion of the AASHL with $x = 0.5$ and $y = 0.1$ using the generator $G_{\mathrm{gs}}(\ell)$.

Note that the calculation in the subspace (4.39) does not lead to the correct band edges of the triplon continuum because the shift of the one-triplon dispersion makes itself felt only if we included four-particle states as well. Hence, this kind of calculation is not fully self-consistent. In principle, there are possibilities to achieve consistency

between the one-triplon dispersion and the band edges of the continua. But this issue is beyond the scope of the present thesis.

In the region where the one-triplon dispersion hybridizes with the two-triplon continuum the renormalized one-triplon dispersion indicates the energies with the maximum spectral intensity $\rho(Q,\omega)$. These energies represent what is usually seen as the energy of a quasiparticle with finite lifetime. The energies determined in this way lie between what is obtained from the generator $G_{\mathrm{gs}}(\ell)$ in the one-triplon sector (grey line in figure 4.13b) and what is obtained from the generator $G_{\mathrm{pc}}(\ell)$ or from the generator $G_{\mathrm{gs,1p}}(\ell)$.

We emphasize that the advantage of the generator $G_{\mathrm{gs}}(\ell)$ compared to the generator $G_{\mathrm{pc}}(\ell)$ or $G_{\mathrm{gs,1p}}(\ell)$ is that also the quasiparticle decay is described in the region of the Brillouin zone where the one-triplon dispersion merges with the two-triplon continuum. The generator $G_{\mathrm{gs}}(\ell)$ avoids rearrangement processes during the flow, which lead to a potentially misleading quasiparticle picture. Thereby the CUT becomes more robust. Hence, the proposed adapted generator achieves the initial goal to describe decaying quasiparticles properly.

4.3 Dynamical structure factors for the asymmetric antiferromagnetic spin $S = 1/2$ Heisenberg ladder

In the previous section it was shown that decaying quasiparticles can be described by CUTs using the generator $G_{\mathrm{gs}}(\ell)$. Additionally, in this section observables are transformed to determine the dynamical structure factor $S^{zz}(Q,\omega)$ for the AASHL which is experimentally accessible by inelastic neutron scattering (INS), cf. appendix F.

To determine the dynamical structure factor $S^{zz}(Q,\omega)$ we use a continued fraction representation of equation (4.19b)

$$S^{zz}(Q,\omega) = -\frac{1}{\pi}\mathrm{Im}\,\mathcal{G}^{zz}(Q,\omega) \tag{4.43}$$

with the retarded zero temperature Green function

$$\mathcal{G}^{zz}(Q,\omega) = \lim_{\delta\to 0^+} \left\langle 0\right| S^z_{\text{eff}}(-Q) \left[\omega - (H_{\text{eff}}(Q) - E_0) + \mathrm{i}\delta\right]^{-1} S^z_{\text{eff}}(Q) \left|0\right\rangle \tag{4.44a}$$

$$= \cfrac{\left\langle 0\right| S^z_{\text{eff}}(-Q)\, S^z_{\text{eff}}(Q) \left|0\right\rangle}{\omega - a_0(Q) - \cfrac{b_1^2(Q)}{\omega - a_1(Q) - \cfrac{b_2^2(Q)}{\cdots}}} \tag{4.44b}$$

$$= \cfrac{S^{zz}(Q)}{\omega - a_0(Q) - \cfrac{b_1^2(Q)}{\omega - a_1(Q) - \cfrac{b_2^2(Q)}{\cdots}}}, \tag{4.44c}$$

where again the coefficients $a_n(Q)$ and $b_n(Q)$ are calculated by a Lanczos tridiagonalization, see appendix A. The effective Hamiltonian $H_{\text{eff}}(Q)$ and the effective observable $S^z_{\text{eff}}(Q)$ have been obtained by the generator $G_{\text{gs}}(\ell)$ using the truncation scheme $N_{\text{t}} = 5$, $\mathbf{D} = (12,10,10,6,6,5,5,4,4)$ and $N_{\text{t}}^O = 3$, $\mathbf{D}^O = (10,10,8,8,6,6)$ (cf. section 3.4.3) and a Fourier transformation (cf. appendix D, appendix E and appendix F). Again we stopped the sCUTs at $\ell = 200$. As in section 4.2.2 we restrict ourselves to the subspace (4.39) given by $\left|Q\right\rangle^{S=1}_{m=0}$, $\left|Q,d_1\right\rangle^{S=1}_{m=0}$ and $\left|Q,d_1,d_2,a\right\rangle^{S=1}_{m=0}$ with $a = 1,2,3$ and $d_1,d_2 > 0$ and $d_1, d_1 + d_2 < 120$ (cf. appendix D) and consider the restricted effective Hamiltonian $H^{\text{res}}_{\text{eff}}$ (4.40). Thus the initial state of the Lanczos tridiagonalization $\left|\psi_0\right\rangle$ is given by

$$\left|\psi_0\right\rangle = S^z_{\text{eff}}(Q) \left|0\right\rangle \tag{4.45a}$$

$$\begin{aligned} &= C^{S=1,m=0}_{S^z|^1_0}(Q) \left|Q\right\rangle^{S=1}_{m=0} \\ &\quad + \sum_{d_1} \left[C^{S=1,m=0}_{S^z|^2_0}(Q)\right]^{d_1} \left|Q,d_1\right\rangle^{S=1}_{m=0} \\ &\quad + \sum_{d_1,d_2} \sum_{a=1}^{3} {}^{a}\left[C^{S=1,m=0}_{S^z|^3_0}(Q)\right]^{d_1,d_2} \left|Q,d_1,d_2,a\right\rangle^{S=1}_{m=0}. \end{aligned} \tag{4.45b}$$

For the definition of $C^{S=1,m=0}_{S^z|^1_0}(Q)$, $\left[C^{S=1,m=0}_{S^z|^2_0}(Q)\right]^{d_1}$ and ${}^{a}\left[C^{S=1,m=0}_{S^z|^3_0}(Q)\right]^{d_1,d_2}$ see equation (F.16), (F.18) and (F.20). Then the equal-time structure factor $S^{zz}(Q)$ is given by

$$S^{zz}(Q) = \left|C^{S=1,m=0}_{S^z|^1_0}(Q)\right|^2 + \sum_{d_1} \left|\left[C^{S=1,m=0}_{S^z|^2_0}(Q)\right]^{d_1}\right|^2 + \sum_{d_1,d_2} \sum_{a=1}^{3} \left|{}^{a}\left[C^{S=1,m=0}_{S^z|^3_0}(Q)\right]^{d_1,d_2}\right|^2. \tag{4.46}$$

Due to the restriction $d_1 + d_2 < 120$ for the distances d_1 and d_2 a proper termination of the continued fraction (4.44) is difficult, cf. appendix A.2. Thus in the following we

use a slight broadening $\omega \to \omega + \mathrm{i}\delta$ with $\delta = 0.05$. The number of used Lanczos steps n is quoted in the respective figure captions.

In figure 4.16 the dynamical structure factor $S^{zz}(Q,\omega)$ (4.43) of the AASHL for $x = 0.5$ and various values $y > 0$ is depicted. We use three-dimensional plots (left panels) and color plots (right panels) to visualize the dynamical structure factor $S^{zz}(Q,\omega)$. The inner product **Qb** is set to **Qb** $= \pi$. In addition to results obtained by the generator $G_{\mathrm{gs}}(\ell)$ and a Lanczos tridiagonalization as described above also the one-triplon dispersion (4.9) (black line) and the ensuing two-triplon continuum (4.10) (blue lines in the (Q,ω)-plane) obtained by the generator $G_{\mathrm{gs,1p}}(\ell)$ are shown. We want to emphasize once more that the generator $G_{\mathrm{gs,1p}}(\ell)$ tends to interpret the energetically lowest states above the ground state as the elementary excitations and not the state with the largest spectral weight, cf. section 4.2. Nevertheless, its results help to check the validity of the results obtained by the generator $G_{\mathrm{gs}}(\ell)$, especially in the region of the Brillouin zone where the quasiparticles have infinite lifetime. The green crosses depict the renormalized one-triplon dispersion determined by the root of the real part of the Green function $\mathcal{G}^{zz}(Q,\omega)$ (4.44), i.e.,

$$\mathrm{Re}\,\mathcal{G}^{zz}(Q,\omega) = \mathrm{Re}\left\langle 0\right| S^z_{\mathrm{eff}}(-Q)\left[\omega - (H_{\mathrm{eff}}(Q) - E_0) + \mathrm{i}\delta\right]^{-1} S^z_{\mathrm{eff}}(Q)\left|0\right\rangle = 0 \tag{4.47}$$

for $\delta = 0.05$ and **Qb** $= \pi$ which corresponds to $\omega - \omega_1(Q) - \mathrm{Re}\,\Sigma(Q,\omega) = 0$. The red circles depict the lowest energy level obtained by a diagonalization of $H^{\mathrm{res}}_{\mathrm{eff}}$ (4.40) in the subspace (4.39).

For $x = 0.5$ and $y = 0.25$ and for $x = 0.5$ and $y = 0.5$ the one-triplon dispersions do *not* merge with the two-triplon continuum, see figure 4.16b and figure 4.16c. Therefore, stable excitations exist in the whole Brillouin zone. This is a consequence of the fact that with increasing coupling y the quasiparticles become less and less mobile (in first order the next-neighbor hopping is given by $x/2 - y/4$, cf. equation (4.7b)). Thus increasing y does not necessarily enhance the quasiparticle decay. It can also lead to stable excitations.

For $x = 0.5$ and $y = 0.1$ quasiparticle decay occurs but still a marked peak exists inside the continuum, see figure 4.16a. A discussion of the width of the excitations is given below, cf. section 4.3.2.

In figure 4.17 the dynamical structure factor $S^{zz}(Q,\omega)$ (4.43) of the AASHL for $x = 0.5$ and $y = 0.1, 0.25, 0.5$ is depicted for **Qb** $= 0$. For all considered values of y a $S = 1$ bound state exists for momenta $Q \gtrapprox 0.5$ due to triplon-triplon interactions. Note, that in the case of unstable quasiparticles ($x = 0.5$, $y = 0.1$) the definition of the continuum is in some way arbitrary since one has to choose which states define the one-triplon dispersion $\omega_1(Q)$ inside the continuum, cf. equation (4.10). The depicted boundaries of the two-triplon continuum (blue lines in the (Q,ω)-plane) are determined by the

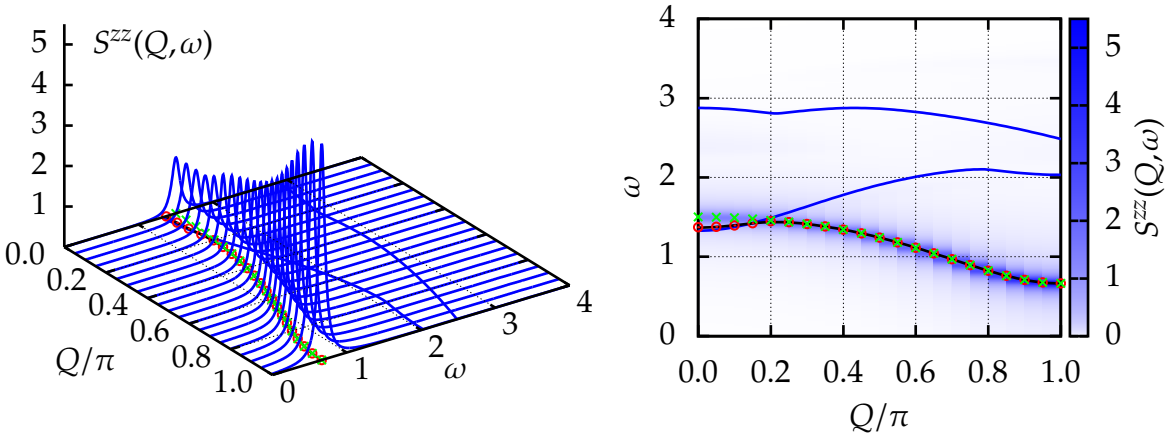

(a) $x = 0.5$, $y = 0.1$, number of Lanczos steps $n = 80$

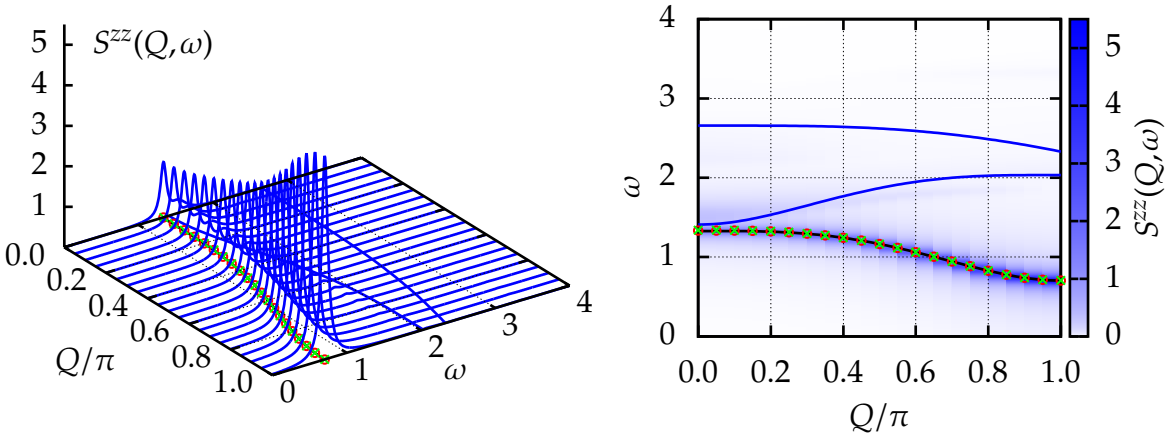

(b) $x = 0.5$, $y = 0.25$, number of Lanczos steps $n = 80$

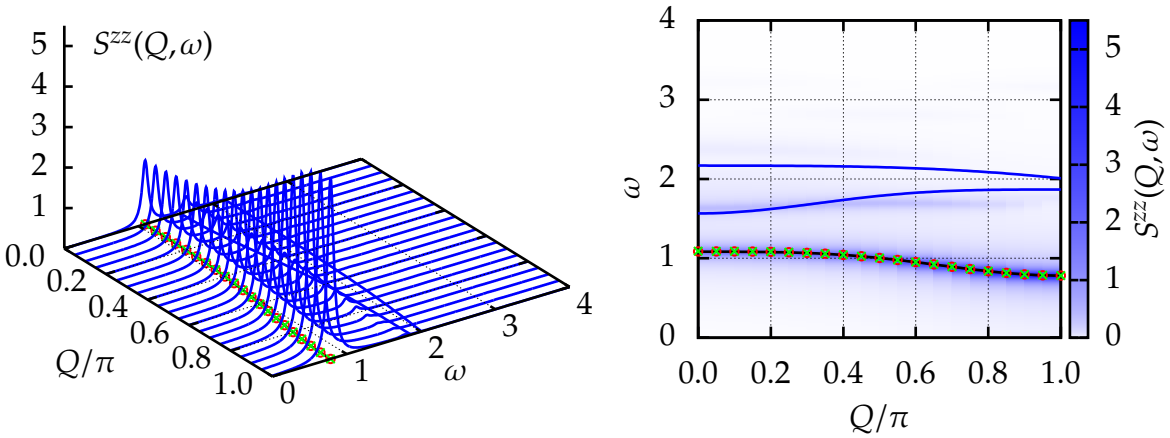

(c) $x = 0.5$, $y = 0.5$, number of Lanczos steps $n = 80$

Figure 4.16: Dynamical structure factor $S^{zz}(Q,\omega)$ of the AASHL for $x = 0.5$, **Qb** $= \pi$ and various values $y > 0$ calculated by using the generator $G_{\mathrm{gs}}(\ell)$ and Lanczos tridiagonalization as described in the text (broadening: $\delta = 0.05$). The solid black line depicts the one-triplon dispersion and blue lines in the (Q,ω)-plane depict the borders of the two-triplon continuum obtained by the generator $G_{\mathrm{gs,1p}}(\ell)$. Green crosses depict the renormalized one-triplon dispersion obtained by the generator $G_{\mathrm{gs}}(\ell)$ and equation (4.47). Red circles depict the lowest energy level obtained by a diagonalization in the subspace (4.39).

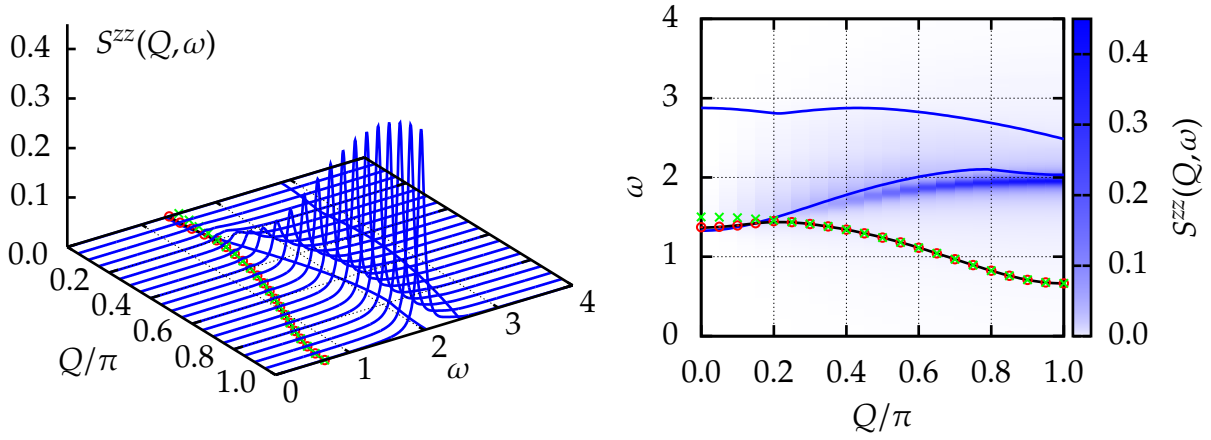

(a) $x = 0.5$, $y = 0.1$, number of Lanczos steps $n = 80$

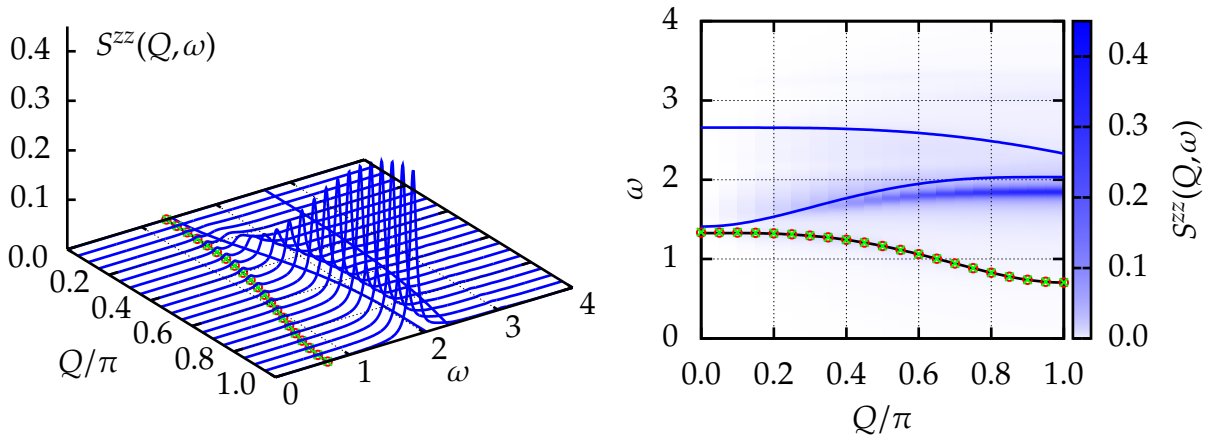

(b) $x = 0.5$, $y = 0.25$, number of Lanczos steps $n = 80$

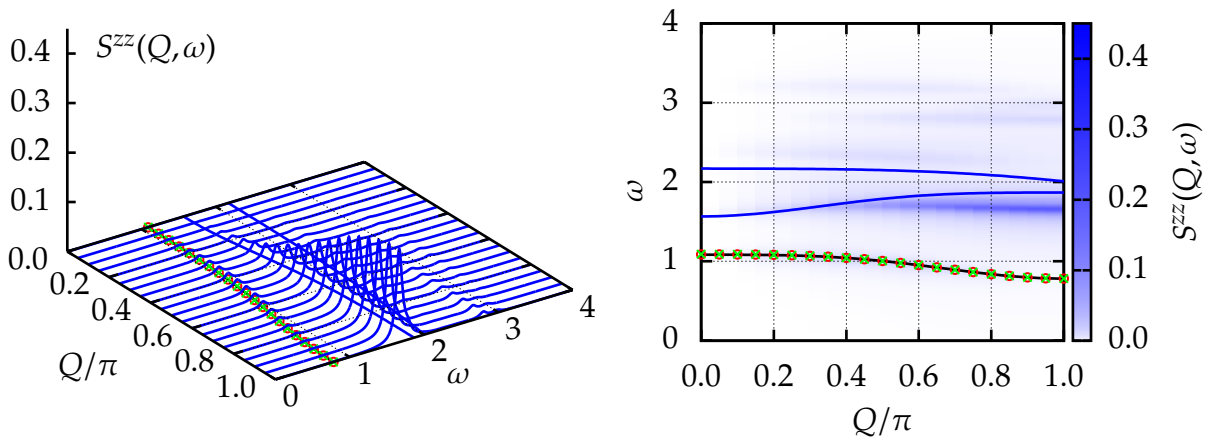

(c) $x = 0.5$, $y = 0.5$, number of Lanczos steps $n = 80$

Figure 4.17: Dynamical structure factor $S^{zz}(Q,\omega)$ of the AASHL for $x = 0.5$, **Qb** $= 0$ and various values $y > 0$ calculated by using the generator $G_{\mathrm{gs}}(\ell)$ and Lanczos tridiagonalization as described in the text (broadening: $\delta = 0.05$). The solid black line depicts the one-triplon dispersion and blue lines in the (Q,ω)-plane depict the borders of the two-triplon continuum obtained by the generator $G_{\mathrm{gs,1p}}(\ell)$. Green crosses depict the renormalized one-triplon dispersion obtained by the generator $G_{\mathrm{gs}}(\ell)$ and equation (4.47). Red circles depict the lowest energy level obtained by a diagonalization in the subspace (4.39).

one-triplon dispersion obtained by the generator $G_{\mathrm{gs,1p}}(\ell)$ (black line). Nonetheless, if one used the renormalized one-triplon dispersion (green crosses) to define the two-triplon continuum the boundaries of the two-triplon continuum would lie even higher in energy since the renormalized one-triplon dispersion lies above the one-triplon dispersion obtained by the generator $G_{\mathrm{gs,1p}}(\ell)$. Thus for momenta $Q \gtrapprox 0.5$, in any case, a stable excitation exists between the one-triplon dispersion and the two-triplon continuum, the so-called $S = 1$ bound state. Since $y \neq 0$ traces of the $S = 1$ bound state can also be found in the dynamical structure factor $S^{zz}(Q, \omega)$ for $\mathbf{Qb} = \pi$, cf. figure 4.16c.

As mentioned before, for $x = 0.5$ and $y = 0.1$ decay occurs but still marked peaks inside the continuum can be observed. A possibility to increase the width of these peaks is to increase the interaction y. Unfortunately, increasing y leads to quasiparticles which are less mobile. This may produce stable excitations within the whole Brillouin zone, see figure 4.16b and figure 4.16c. To prevent the formation of a stable excitation for larger y one has to increase the interaction x as well. Another possibility is to consider asymmetric ferro-antiferromagnetic spin $S = 1/2$ Heisenberg ladders (AFASHLs) with $y < 0$. In first order the mobility of the triplons is given by $x/2 - y/4$, cf. equation 4.6. According to this, a positive interaction $y > 0$ decreases the mobility of the triplons while a negative interaction $y < 0$ increases their mobility. The width is in first order proportional to y^2 (see equation (4.6)) and thereby insensitive to the sign of y. AFASHLs are discussed in the next chapter 5.

Figure 4.18 shows the dynamical structure factor $S^{zz}(Q, \omega)$ of the AASHL for $x = 0.75$ and $y = 0.1,\ 0.25,\ 0.5$ for $\mathbf{Qb} = \pi$. The analogous quantities for $\mathbf{Qb} = 0$ are depicted in figure 4.19. Figure 4.20 and figure 4.21 display results for $x = 1.0$ and $y = 0.1,\ 0.25,\ 0.5$.

For $x = 0.75$, $y = 0.5$ (cf. figure 4.18c) and for $x = 1.0$, $y = 0.5$ (cf. figure 4.20c) the renormalized one-triplon dispersion (green crosses) and the lowest $S = 1$ eigenvalues obtained by the generator $G_{\mathrm{gs}}(\ell)$ and a diagonalization of the Hamiltonian $H_{\mathrm{eff}}^{\mathrm{res}}$ in the subspace 4.39 (red circles) coincide in the whole Brillouin zone. This indicates that stable elementary excitations exist for all momenta Q. For $x = 0.75$, $y = 0.5$ the scenario of stable quasiparticles within the whole Brillouin zone is supported by results obtained by the generator $G_{\mathrm{gs,1p}}(\ell)$, see figure 4.18c. The one-triplon dispersion (black line) lies below the lower edge of the continuum (blue line) for all momenta Q. In contrast, for $x = 1.0$, $y = 0.5$ the one-triplon dispersion (black line) merges with the continuum (blue line) for $Q \lessapprox 0.1\pi$. Thus calculations with the generator $G_{\mathrm{gs,1p}}(\ell)$ indicate unstable quasiparticles for $x = 1.0$, $y = 0.5$ and $Q \lessapprox 0.1\pi$.

The differences between the results obtained by the generator $G_{\mathrm{gs}}(\ell)$ and the results obtained by the generator $G_{\mathrm{gs,1p}}(\ell)$ seem to be mainly caused by the incomplete self-consistency in the analysis of the effective Hamiltonian $H_{\mathrm{eff}}^{\mathrm{res}}$. The energy of the lower band edge of the continuum around $Q \approx 0$ is determined by the one-triplon dispersion around $Q \approx \pi$. For $Q = 0$ the lower band edge should lie at 2Δ with the gap energy Δ

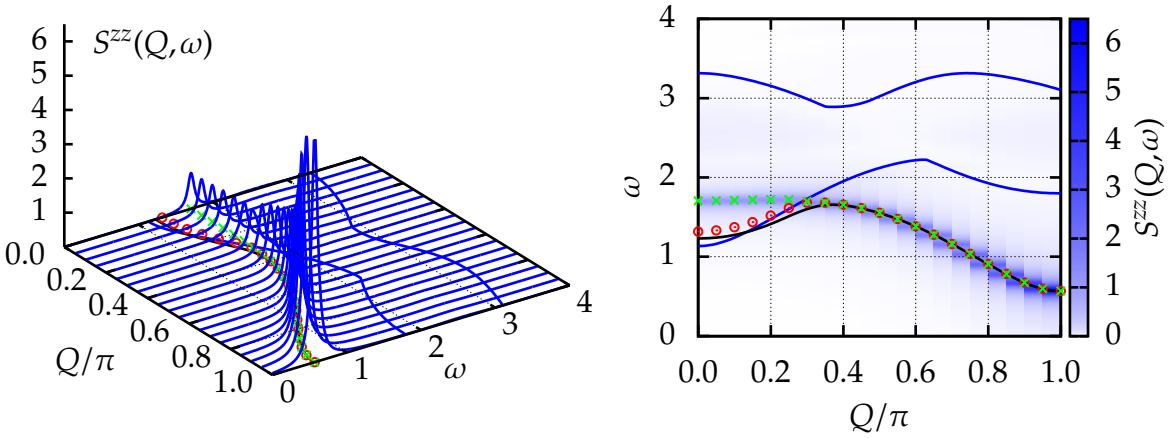

(a) $x = 0.75$, $y = 0.1$, number of Lanczos steps $n = 60$

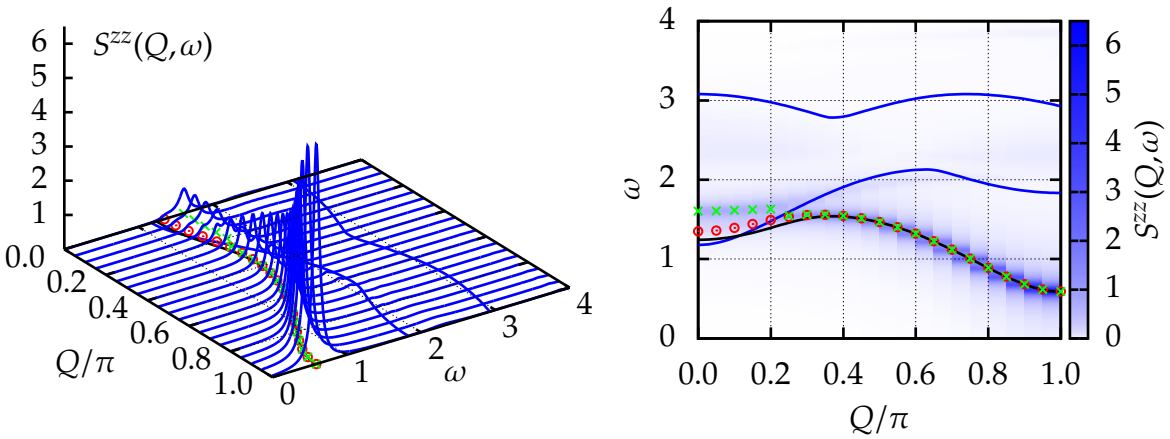

(b) $x = 0.75$, $y = 0.25$, number of Lanczos steps $n = 60$

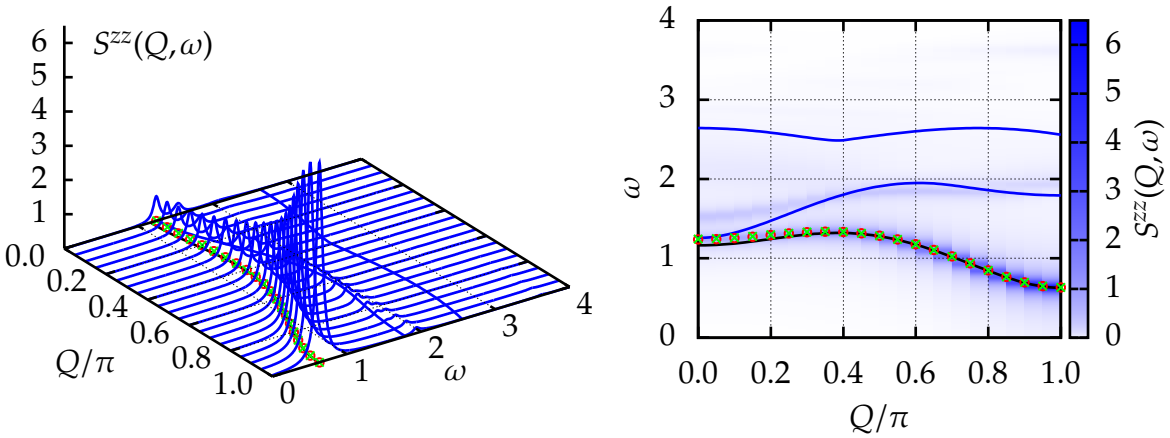

(c) $x = 0.75$, $y = 0.5$, number of Lanczos steps $n = 70$

Figure 4.18: Dynamical structure factor $S^{zz}(Q,\omega)$ of the AASHL for $x = 0.75$, **Qb** $= \pi$ and various values $y > 0$ calculated by using the generator $G_{\mathrm{gs}}(\ell)$ and Lanczos tridiagonalization as described in the text (broadening: $\delta = 0.05$). The solid black line depicts the one-triplon dispersion and blue lines in the (Q,ω)-plane depict the borders of the two-triplon continuum obtained by the generator $G_{\mathrm{gs,1p}}(\ell)$. Green crosses depict the renormalized one-triplon dispersion obtained by the generator $G_{\mathrm{gs}}(\ell)$ and equation (4.47). Red circles depict the lowest energy level obtained by a diagonalization in the subspace (4.39).

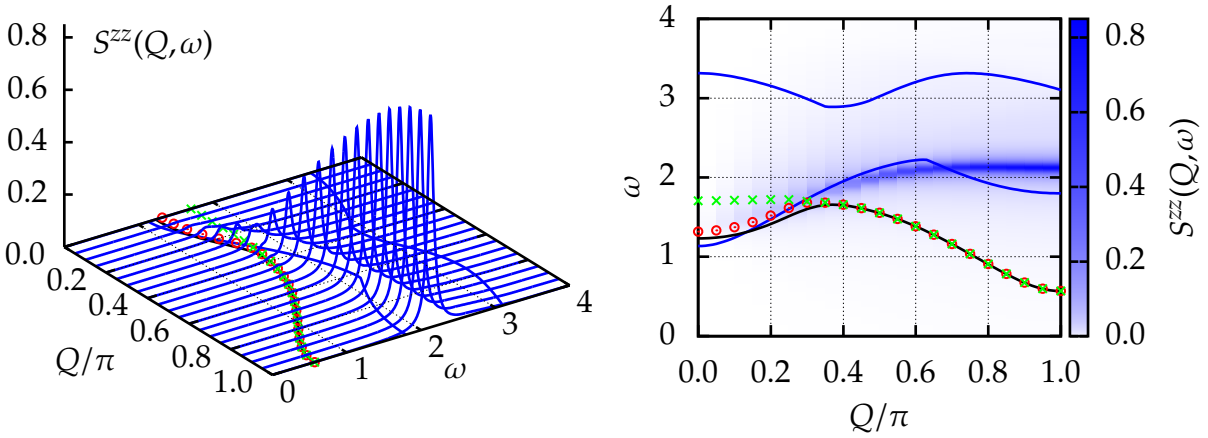

(a) $x = 0.75$, $y = 0.1$, number of Lanczos steps $n = 60$

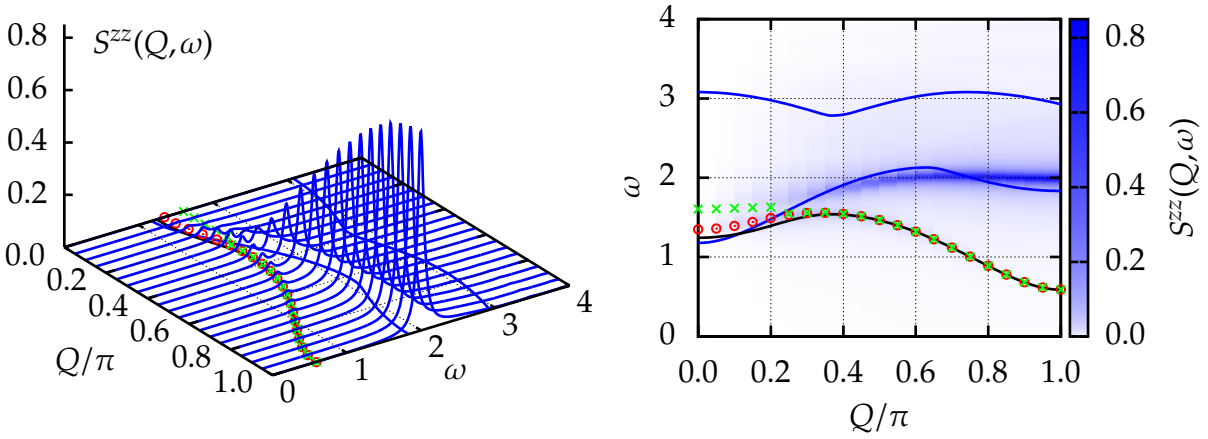

(b) $x = 0.75$, $y = 0.25$, number of Lanczos steps $n = 60$

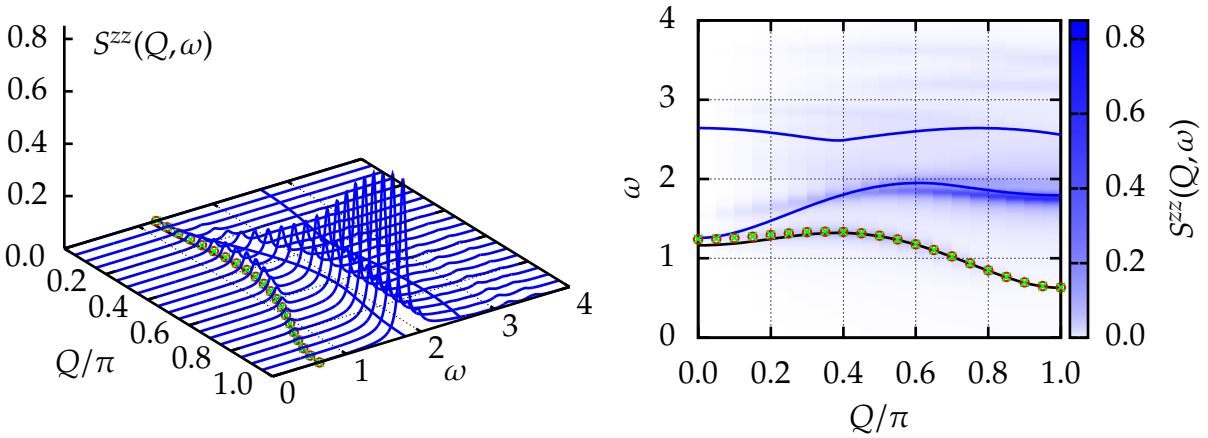

(c) $x = 0.75$, $y = 0.5$, number of Lanczos steps $n = 70$

Figure 4.19: Dynamical structure factor $S^{zz}(Q,\omega)$ of the AASHL for $x = 0.75$, **Qb** $= 0$ and various values $y > 0$ calculated by using the generator $G_{\mathrm{gs}}(\ell)$ and Lanczos tridiagonalization as described in the text (broadening: $\delta = 0.05$). The solid black line depicts the one-triplon dispersion and blue lines in the (Q,ω)-plane depict the borders of the two-triplon continuum obtained by the generator $G_{\mathrm{gs,1p}}(\ell)$. Green crosses depict the renormalized one-triplon dispersion obtained by the generator $G_{\mathrm{gs}}(\ell)$ and equation (4.47). Red circles depict the lowest energy level obtained by a diagonalization in the subspace (4.39).

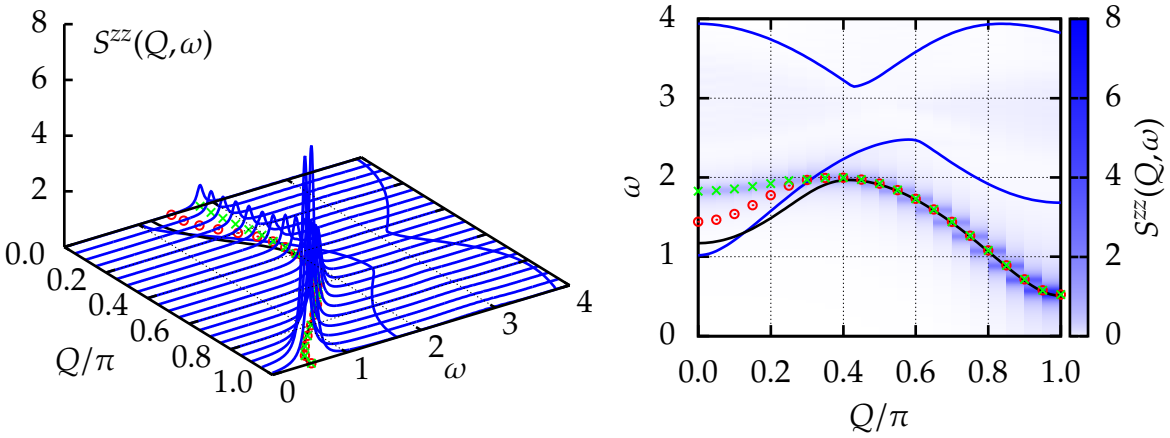

(a) $x = 1.0$, $y = 0.1$, number of Lanczos steps $n = 50$

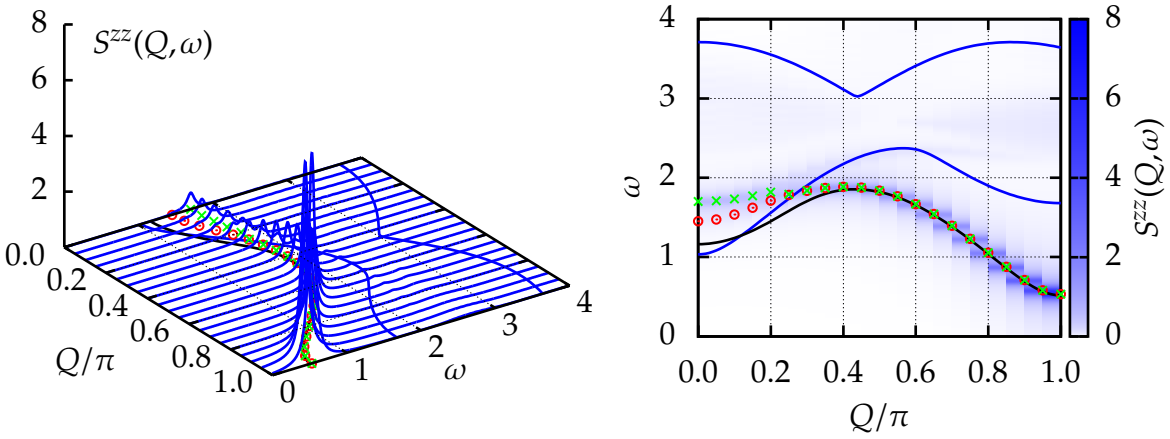

(b) $x = 1.0$, $y = 0.25$, number of Lanczos steps $n = 50$

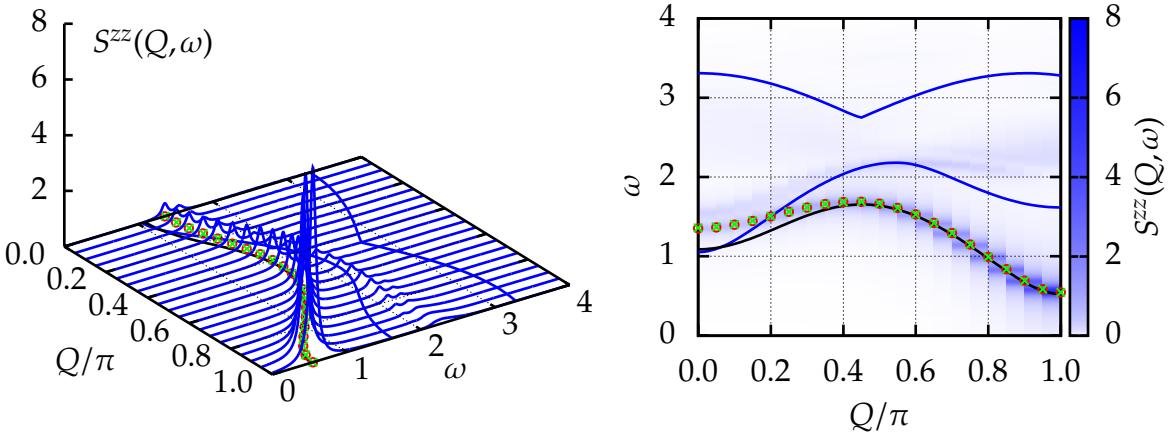

(c) $x = 1.0$, $y = 0.5$, number of Lanczos steps $n = 50$

Figure 4.20: Dynamical structure factor $S^{zz}(Q,\omega)$ of the AASHL for $x = 1.0$, **Qb** $= \pi$ and various values $y > 0$ calculated by using the generator $G_{\mathrm{gs}}(\ell)$ and Lanczos tridiagonalization as described in the text (broadening: $\delta = 0.05$). The solid black line depicts the one-triplon dispersion and blue lines in the (Q,ω)-plane depict the borders of the two-triplon continuum obtained by the generator $G_{\mathrm{gs,1p}}(\ell)$. Green crosses depict the renormalized one-triplon dispersion obtained by the generator $G_{\mathrm{gs}}(\ell)$ and equation (4.47). Red circles depict the lowest energy level obtained by a diagonalization in the subspace (4.39).

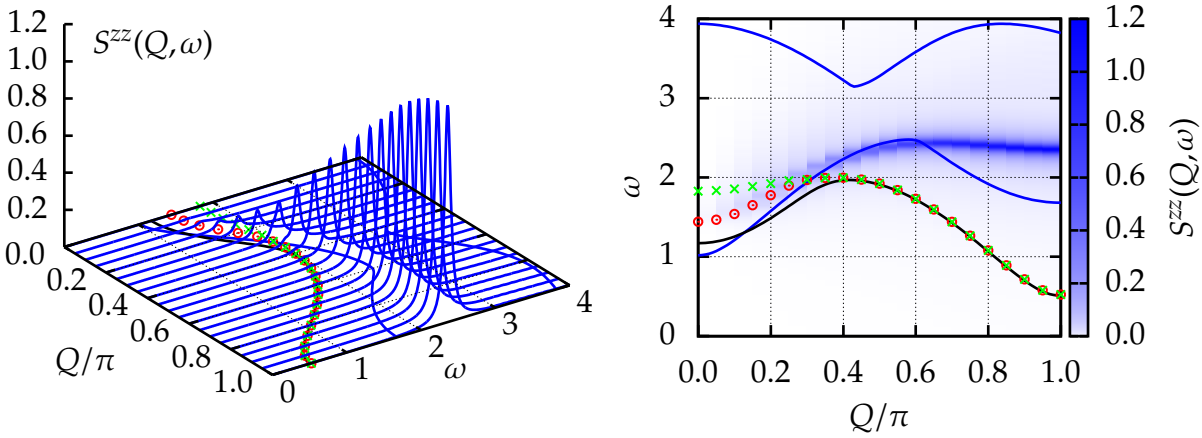

(a) $x = 1.0$, $y = 0.1$, number of Lanczos steps $n = 50$

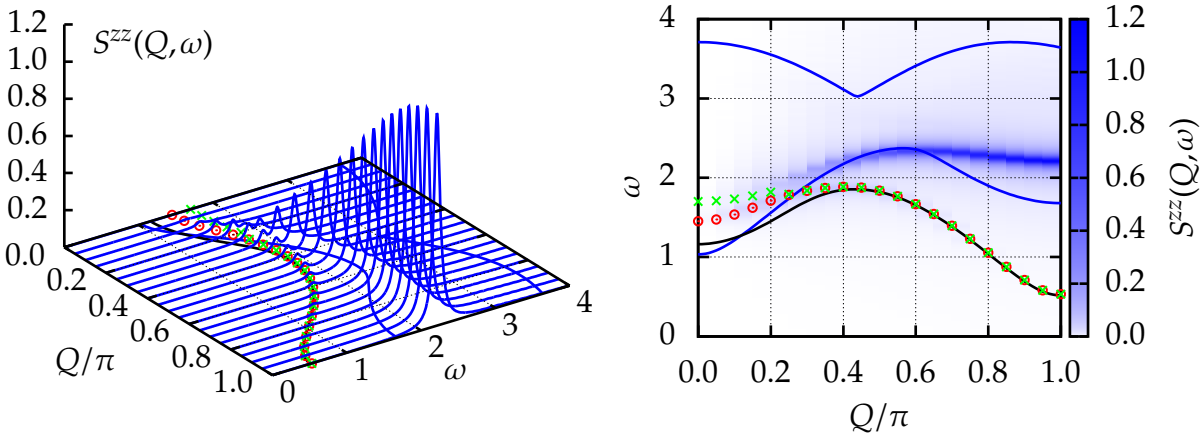

(b) $x = 1.0$, $y = 0.25$, number of Lanczos steps $n = 50$

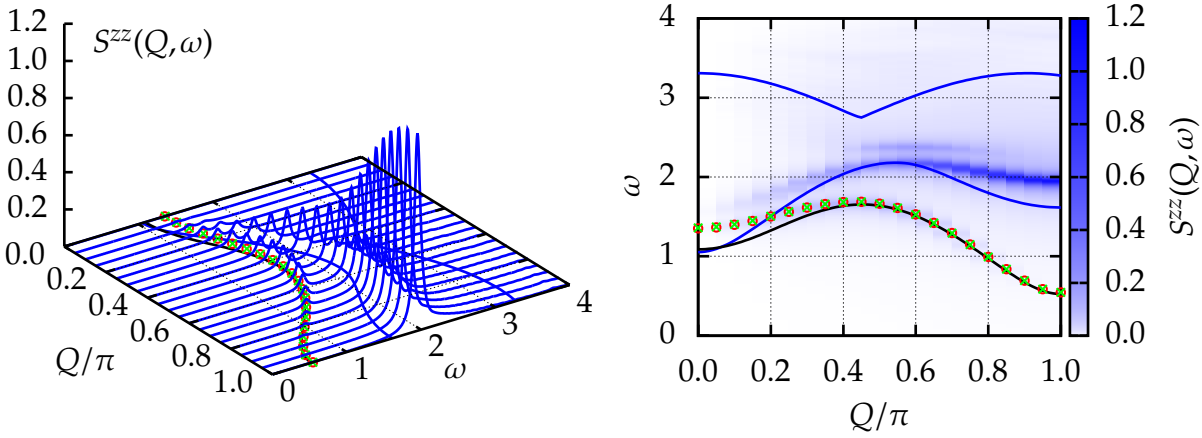

(c) $x = 1.0$, $y = 0.5$, number of Lanczos steps $n = 50$

Figure 4.21: Dynamical structure factor $S^{zz}(Q,\omega)$ of the AASHL for $x = 1.0$, **Qb** $= 0$ and various values $y > 0$ calculated by using the generator $G_{\mathrm{gs}}(\ell)$ and Lanczos tridiagonalization as described in the text (broadening: $\delta = 0.05$). The solid black line depicts the one-triplon dispersion and blue lines in the (Q,ω)-plane depict the borders of the two-triplon continuum obtained by the generator $G_{\mathrm{gs,1p}}(\ell)$. Green crosses depict the renormalized one-triplon dispersion obtained by the generator $G_{\mathrm{gs}}(\ell)$ and equation (4.47). Red circles depict the lowest energy level obtained by a diagonalization in the subspace (4.39).

located at $Q = \pi$. For $Q \gtrapprox 0.5\pi$ the lowest $S = 1$ eigenvalues obtained by a diagonalization of the Hamiltonian $H_{\text{eff}}^{\text{res}}$ in the subspace 4.39 (red circles) coincide with the one-triplon dispersion obtained by the generator $G_{\text{gs,1p}}(\ell)$. Therefore, for a fully self-consistent calculation the lowest $S = 1$ eigenvalue (red circles) should coincide with the lower edge of the continuum (blue line) in the vicinity of $Q = 0$ for unstable excitations. Especially for $x = 1.0$ the incomplete self-consistency becomes obvious. Note, that in the case of quasiparticle decay the black line around $Q = 0$ has no significance in describing the excitations with maximal spectral weight, cf. section 4.2.

For $x = 0.75, 1.0$ and $x = 0.1, 0.25$ quasiparticle decay can be observed, see figure 4.18a, figure 4.18b, figure 4.20a and figure 4.20b. As expected the width of the excitations inside the continuum increases with increasing interaction y.

Figure 4.19 and figure 4.21 show results for $\mathbf{Qb} = 0$. In all cases an excitation can be observed for $Q \gtrapprox 0.4\pi$ close to the lower band edge of the continuum. The question arises, if this excitation is a bound state with infinite lifetime. For $x = 0.75$, $y = 0.1,\ 0.25$ and $x = 1.0$, $y = 0.1,\ 0.25,\ 0.5$ the blue line specifying the lower edge of the continuum dips below the excitation around $Q \approx \pi$. Thus in this region of the Brillouin zone the excitation most likely will have a (small) finite width. Nevertheless, it seems that a $S = 1$ bound state with infinite lifetime exists in the middle of the Brillouin zone around $Q \approx 0.5\pi$ which becomes a resonance for $Q \to \pi$.

For all pairs (x, y) for which the AASHL shows quasiparticle decay the one-triplon dispersion $\omega_1(Q) = a_0(Q)$ does *not* allow for additional minima within the two-particle continuum effecting the decay, cf. section 2.4. Therefore, the peaks inside the continuum are either continued by the one-triplon branch (scenario (i), cf. section 2.2) or by the two-triplon bound state (scenario (ii), cf. section 2.3) while the one-triplon branch is pushed below the continuum and stays stable in the region where the bound state starts to decay.

For $x = 0.5$ and $y = 0.1$ it seems that the peaks inside the continuum are continued by the one-triplon branch (scenario (i)), cf. figure 4.16a. In contrast, for $x = 0.75,\ 1.0$ and $y = 0.25$ a two-peak structure occur around $Q \approx 0.2\pi$ in the dynamical structure factor $S^{zz}(Q, \omega)$, see figure 4.18b and 4.20b. This suggest, that the decay is influenced by the bound state (scenario (ii)). Calculations for $y = 0.75,\ 1.0$ and $x = 0.0$ support this scenario. They show that the one-triplon dispersion crosses the two-particle $S = 1$ bound state below the continuum, see figure 4.9b and figure 4.9c. According to this, scenario (ii) should also occur for $x = 0.75,\ 1.0$ and $y = 0.1$. Unfortunately, no evidence for scenario (ii) can be found in figures 4.18a, 4.19a, 4.20a and 4.21a. This might be caused by the fact that the interaction $y = 0.1$ is too small to produce a pronounced level repulsion which can be observed in the broadened result shown in figures 4.18a–4.21a.

4.3.1 Equal-time structure factors $S^{zz}(Q)$ and spectral weights

Next, we want to discuss the equal-time structure factor $S^{zz}(Q)$. Figure 4.22 displays $S^{zz}(Q)$ for $\mathbf{Qb} = \pi$ (dashed lines), $S^{zz}(Q)$ for $\mathbf{Qb} = 0$ (dotted lines) and the sum of these two quantities (solid lines) normalized to the total spectral weight I (F.13) for various interactions x and y. Most of the spectral weight is gathered in the channel with $\mathbf{Qb} = \pi$. As in the symmetric case for $y = 0$ (cf. section 4.1.2), increasing x shifts more and more spectral weight from momenta around $Q = 0$ to momenta around $Q = \pi$, see figure 4.22a, figure 4.22b and figure 4.22c. Increasing y has the opposite effect. By increasing y more and more spectral weight is shifted from momenta around $Q = \pi$ to momenta around $Q = 0$.

In table 4.3 the relative spectral weights $I^{\mathrm{rel}}\big|_{\mathbf{Qb}} := I\big|_{\mathbf{Qb}}/I$ for $\mathbf{Qb} = \pi$ and $\mathbf{Qb} = 0$ are listed. We emphasize that the sum of $I^{\mathrm{rel}}\big|_{\mathbf{Qb}=\pi}$ and $I^{\mathrm{rel}}\big|_{\mathbf{Qb}=0}$ fulfills the sum rule (F.13)

Table 4.3: Relative spectral weights $I^{\mathrm{rel}}\big|_{\mathbf{Qb}}$.

x	y	$I^{\mathrm{rel}}\big\|_{\mathbf{Qb}=\pi}$	$I^{\mathrm{rel}}\big\|_{\mathbf{Qb}=0}$	$I^{\mathrm{rel}}\big\|_{\mathbf{Qb}=\pi} + I^{\mathrm{rel}}\big\|_{\mathbf{Qb}=0}$
0.50	0.10	0.93272	0.06732	1.00004
0.50	0.25	0.94408	0.05598	1.00006
0.50	0.50	0.96402	0.03605	1.00007
0.75	0.10	0.86405	0.13608	1.00013
0.75	0.25	0.87012	0.12999	1.00011
0.75	0.50	0.88017	0.12000	1.00017
1.00	0.10	0.80877	0.19238	1.00115
1.00	0.25	0.80926	0.19170	1.00096
1.00	0.50	0.80790	0.19303	1.00093

very well. This justifies the restriction to the subspace 4.39, at least for the transformed local spin operator $S^z_l(r)$. The spectral weight of states with four or more triplons seems to be negligible.

The distribution of the spectral weight is mainly influenced by the parameter x. Increasing x shifts more and more spectral weight from the channel with $\mathbf{Qb} = \pi$ to the channel with $\mathbf{Qb} = 0$. For $x = 0.5$ and $x = 0.75$ increasing y slightly thwarts this shift. Interestingly, for $x = 1.0$ the effect of the interaction y is negligible.

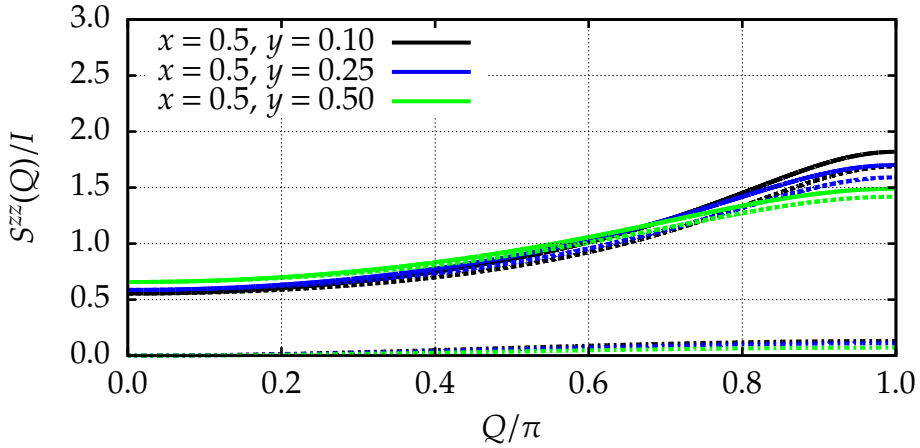

(a) Equal-time structure factor $S^{zz}(Q)$ normalized to the total spectral weight I for $x = 0.5$ and various $y > 0$.

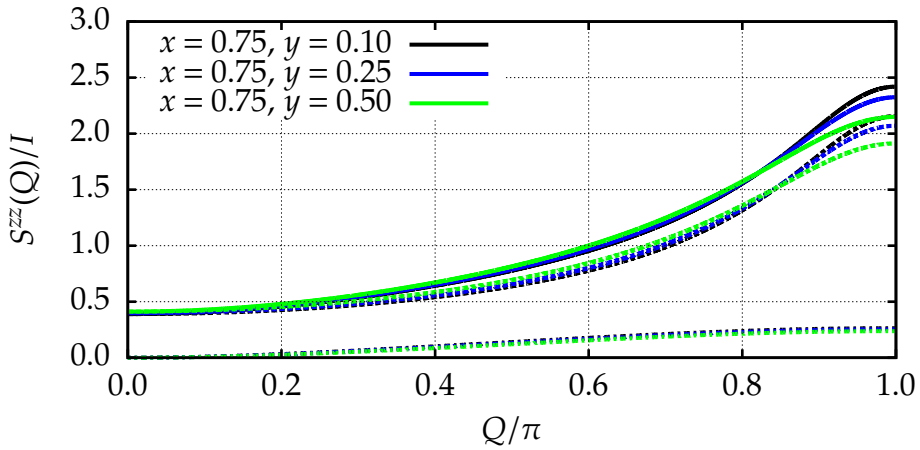

(b) Equal-time structure factor $S^{zz}(Q)$ normalized to the total spectral weight I for $x = 0.75$ and various $y > 0$.

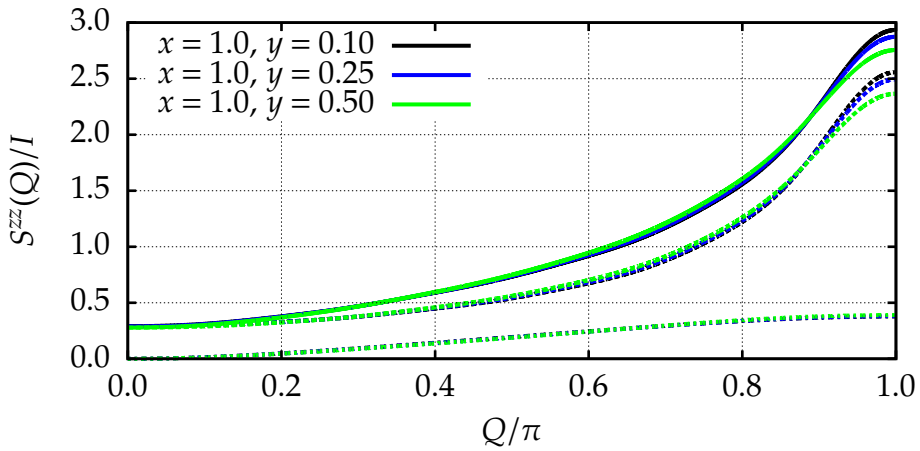

(c) Equal-time structure factor $S^{zz}(Q)$ normalized to the total spectral weight I for $x = 1.0$ and various $y > 0$.

Figure 4.22: Equal-time structure factor $S^{zz}(Q)$ normalized to the total spectral weight I for various interactions x and $y > 0$. Dashed lines indicate $S^{zz}(Q)$ for $\mathbf{Qb} = \pi$, dotted lines indicate $S^{zz}(Q)$ for $\mathbf{Qb} = 0$ and solid lines indicate the sum of the two structure factors.

4.3.2 Quasiparticle lifetime

In section 2.2 we have shown that the usual definition of the quasiparticle weight $Z(Q)$ does not apply inside the continuum for the spin systems under study. Therefore, we solely use the inverse quasiparticle lifetime, respectively the width of the resonances, to describe the decay processes.

To determine the width we use a continued fraction representation of the self-energy $\Sigma(Q,\omega)$ given by

$$\mathcal{G}^{zz}(Q,\omega) = \frac{S^{zz}(Q)}{\omega - a_0(Q) - \Sigma^{zz}(Q,\omega)} \tag{4.48}$$

and

$$\Sigma^{zz}(Q,\omega) = \cfrac{b_1^2(Q)}{\omega - a_1(Q) - \cfrac{b_2^2(Q)}{\omega - a_2(Q) - \cfrac{b_3^2(Q)}{\dots}}}, \tag{4.49}$$

cf. equation (4.44) for $\mathbf{Qb} = \pi$. The width of the quasiparticle is then given by

$$\gamma(Q) = -\mathrm{Im}\,\Sigma^{zz}(Q,\omega_{1,\mathrm{r}}(Q))\,, \tag{4.50}$$

where the renormalized one-triplon dispersion $\omega_{1,\mathrm{r}}(Q)$ is given by the roots of the real part on the Green function $G^{zz}(Q,\omega)$ indicated by green crosses in figure 4.16-4.21.

It turns out to be convenient to use a slightly broadened Green function $G^{zz}(Q,\omega)$ to determine the position of a renormalized quasiparticle and to use a terminated (cf. appendix A.2) self-energy $\Sigma^{zz}(Q,\omega)$ to calculate the width of the renormalized quasiparticle.

Figure 4.23 shows the width $\gamma(Q)$ in units of $J_\perp = 1$ for pairs (x,y) for which the AASHL shows quasiparticle decay. The triplons start to decay when they merge with the continuum. As expected the width $\gamma(Q)$ increases with increasing interaction y. But interestingly, the width $\gamma(Q)$ decreases with increasing interaction x. Typically, however, the width is quite small ($\gamma(Q) \lessapprox 0.08$). For all considered interactions x and y the width has a maximum close to the point where the one-triplon dispersion merges with the continuum indicating the relevance of two-particle interactions (cf. figure 2.19) and hopping terms exceeding nearest-neighbor interactions (cf. figure 2.24). The dashed grey line indicates the width $\gamma(Q)$ obtained by a broadened ($\delta = 0.05$) self-energy $\Sigma^{zz}(Q,\omega)$ for $x = 0.75$ and $y = 0.25$. The broadening smears out the transition from stable excitations with infinite lifetime to unstable excitations with finite lifetime inside the continuum. For that reason, we usually use a terminated self-energy $\Sigma^{zz}(Q,\omega)$ to

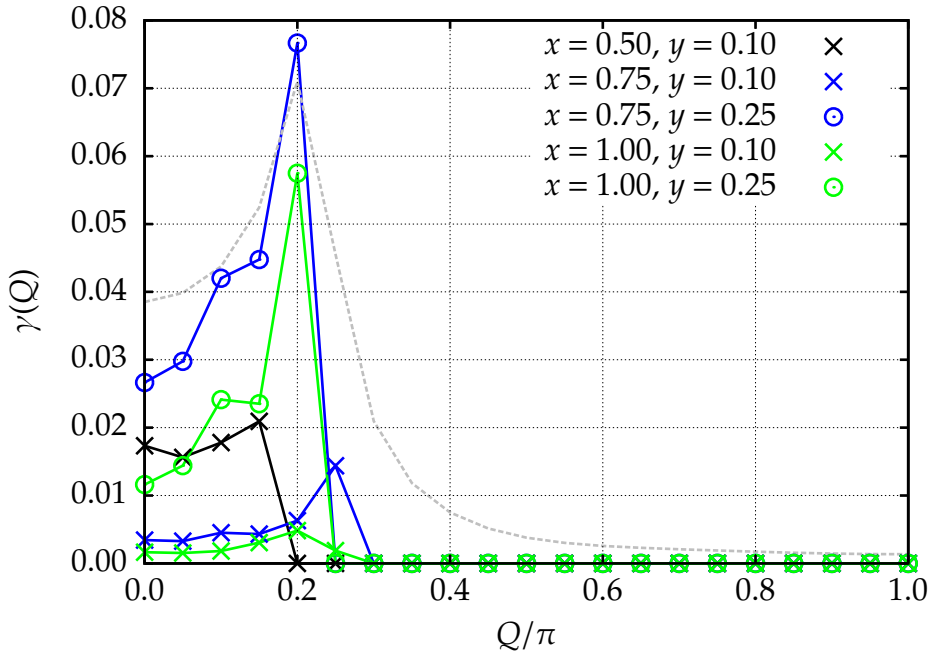

Figure 4.23: Width $\gamma(Q)$ for various interactions $x > 0$ and $y > 0$. For $Q \lessapprox 0.2\pi$ the triplons decay. The dashed grey line indicates the width $\gamma(Q)$ obtained by a broadened ($\delta = 0.05$) self-energy $\Sigma^{zz}(Q,\omega)$ for $x = 0.75$ and $y = 0.25$.

determine the width of the renormalized quasiparticle. Note, that the dashed grey line is convex up to $Q = 0.2\pi$. This is not the case for the corresponding width obtained by a terminated self-energy $\Sigma^{zz}(Q,\omega)$ which indicates numerical inaccuracies due to the previously mentioned difficulties of a proper termination.

In summary we found, that quasiparticle decay indeed occurs in the AASHL. But generically marked peaks inside the continuum can still be observed (cf. figure 4.16, figure 4.18 and figure 4.20) since the width of the excitations is small, see figure 4.23. Basically, one observes a reduction of spectral weight within the equal-time structure factor $S^{zz}(Q)$, cf. figure 4.22. The fact that increasing the interaction y leads to less mobile quasiparticles and thus may lead to stable excitations within the whole Brillouin zone counteracts the tendency of increasing line width on increasing y. Therefore, in the next chapter 5 we discuss the AFASHL with $y < 0$. We will see that the decay in the AFASHL is considerably larger than in the AASHL.

4.4 Chapter summary

In this chapter the low energy spectrum of the asymmetric antiferromagnetic spin $S = 1/2$ Heisenberg ladder (AASHL) was investigated by self-similar continuous unitary transformations (sCUTs). Energy properties as well as spectral properties are discussed.

Starting from the symmetric ladder where quasiparticle decay is not permitted due

to a reflection symmetry, the AASHL is discussed in detail. In that model an interaction breaking the reflection symmetry leads to spontaneous quasiparticle decay (SQPD). The behavior of the flow equations for different generators is illustrated. In the case of SQPD only the generator $G_{\mathrm{gs}}(\ell)$ leads to a robust flow which is consistent with the general considerations presented in chapter 3.

Finally, results for the dynamical structure factors of the AASHL are shown. It turns out, that the SQPD in the AASHL can be influenced by a $S = 1$ bound state. Additionally the SQPD remains quite small, i.e., the decaying quasiparticles have a large lifetime. This follows from the fact that increasing the parameter which causes the decay simultaneously decreases the mobility of the triplon whereby stable quasiparticles below the continuum are produced. Thus the AASHL where all interaction are antiferromagnetic is not an ideal model to study large SQPD. We will see in the next chapter 5 that an asymmetric ladder with one ferromagnetic interaction is more suitable to study quasiparticle decay.

Chapter 5

Asymmetric ferro-antiferromagnetic spin $S = 1/2$ Heisenberg ladder

The model of the asymmetric ferro-antiferromagnetic spin $S = 1/2$ Heisenberg ladder (AFASHL) is depicted in figure 5.1. As in the case of the asymmetric antiferromagnetic

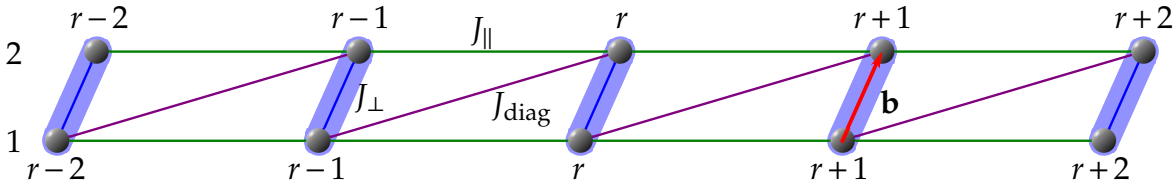

Figure 5.1: Schematic representation of the asymmetric ferro-antiferromagnetic spin $S = 1/2$ Heisenberg ladder (AFASHL). Circles indicate spins with spin $S = 1/2$. Solid lines stand for couplings. The coupling $J_\perp$ and $J_\parallel$ are assumed to be positive, i.e. $J_\perp, J_\parallel > 0$ while the diagonal coupling is assumed to be negative, i.e. $J_{\text{diag}} < 0$. Ladder rungs are defined by the vector $\mathbf{b}$. In the following, the dimensionless parameters $x := J_\parallel/J_\perp > 0$ and $y := J_{\text{diag}}/J_\perp < 0$ are used and the perpendicular coupling is set to be one, i.e. $J_\perp = 1$. The additional diagonal interaction J_{diag} breaks the reflection symmetry and hence induces a hybridization between the one-triplon states and the two-triplon continuum.

spin $S = 1/2$ Heisenberg ladder (AASHL), the AFASHL is described by the Hamiltonian (4.1). Again we use the dimensionless parameters $x = J_\parallel/J_\perp$ and $y = J_{\text{diag}}/J_\perp$, where we set the perpendicular coupling to unity, i.e. $J_\perp = 1$. In contrast to the previous chapter 4 where the model of the (4.1) was discussed for solely positive interactions $x > 0$ and $y > 0$, in this chapter we focus on the case with a ferromagnetic interaction $y < 0$. We will see, that a ferromagnetic coupling $y < 0$ is more suited for an investigation of large quasiparticle decay in the asymmetric ladder (4.1) than an antiferromagnetic coupling $y > 0$.

As mentioned before, cf. chapter 4, for $y \to -\infty$ the model is equivalent to the $S = 1$ Haldane chain. Note, that in the $S = 1$ Haldane chain quasiparticle decay was indeed observed experimentally [Zaliznyak *et al.*(2001)]. Zaliznyak *et al.* observed a gradual

crossing of the single-particle mode over to a narrow continuum for momenta $Q \leq 0.5\pi$ in inelastic neutron scattering (INS) data of $CsNiCl_3$.

5.1 Dynamical structure factors for the asymmetric ferro-antiferromagnetic spin $S = 1/2$ Heisenberg ladder

To investigate spontaneous quasiparticle decay (SQPD) in the AFASHL we calculate the dynamical structure factor $S^{zz}(Q,\omega)$ by self-similar continuous unitary transformations (sCUTs). In this section only the results for the dynamical structure factor $S^{zz}(Q,\omega)$ are given and discussed. Details of the calculations were given in section 4.3.

Figures 5.2-5.7 depict the dynamical structure factor $S^{zz}(Q,\omega)$ (4.43) of the AFASHL for $x = 0.5,\ 0.75$ and $x = 1.0$ and various values $y < 0$. Results for the dynamical structure factor $S^{zz}(Q,\omega)$, the renormalized one-triplon dispersion (green crosses) and the lowest energy level of $H_{\text{eff}}^{\text{res}}$ (4.40) in the subspace (4.39) (red circles) are determined from the generator $G_{\text{gs}}(\ell)$, cf. section 4.3. Additionally, the one triplon dispersion (4.9) (black line) and the ensuing two-triplon continuum (4.10) (blue lines in the (Q,ω)-plane) obtained by the generator $G_{\text{gs,1p}}(\ell)$ are depicted.

In figure 5.2, figure 5.4 and in figure 5.6 the inner product **Qb** is set to $\mathbf{Qb} = \pi$. The main difference to the dynamical structure factors $S^{zz}(Q,\omega)$ with solely antiferromagnetic interactions is that quasiparticle decay can still be observed for interactions $y < 0$ with larger absolute value. Stable quasiparticles within the whole Brillouin zone do not emerge. Thus it is possible to discuss decay for $y = -0.5$.

In figure 5.3, figure 5.5 and in figure 5.7 the inner product **Qb** is set to $\mathbf{Qb} = 0$. As for positive y a marked peak can be observed for momenta around $Q \approx \pi$ which vanishes for small momenta around $Q \approx 0$. Decreasing the parameter y reduces binding effects (in first order binding effects are proportional to $x/2 + y/4$, cf. equation (4.7c) and equation (4.7d)). This can be seen in figure 5.3, figure 5.5 and in figure 5.7. Only for $x = 0.5$, $y = -0.1,\ -0.25$ and for $x = 0.75$, $y = -0.1$, and only around $Q \approx 0.5\pi$, marked peaks lie below the two-particle continuum obtained by the generator $G_{\text{gs,1p}}(\ell)$ which indicate $S = 1$ bound states. Around momenta $Q \approx \pi$ the peaks always lie inside the continuum.

The incomplete self-consistency of the results obtained by the generator $G_{\text{gs}}(\ell)$ and a subsequent (tri)diagonalization can again be observed in the shown results. The red circles do not coincide with the lower edge of the continuum (blue line in the (Q,ω)-plane) obtained by the generator $G_{\text{gs,1p}}(\ell)$ for $Q \approx 0$ although they do for $Q \approx \pi$.

As for the AASHL the one-triplon branch does not allow for additional minima within the two-triplon continuum effecting the decay, cf. section 2.4. But again, two-triplon interactions seem to be important (scenario (ii), cf. section 2.3). Especially, for $x = 0.75,\ 1.0$ and $y = -0.25,\ -0.5$ a two peak structure occur around $Q = 0.3\pi$ in

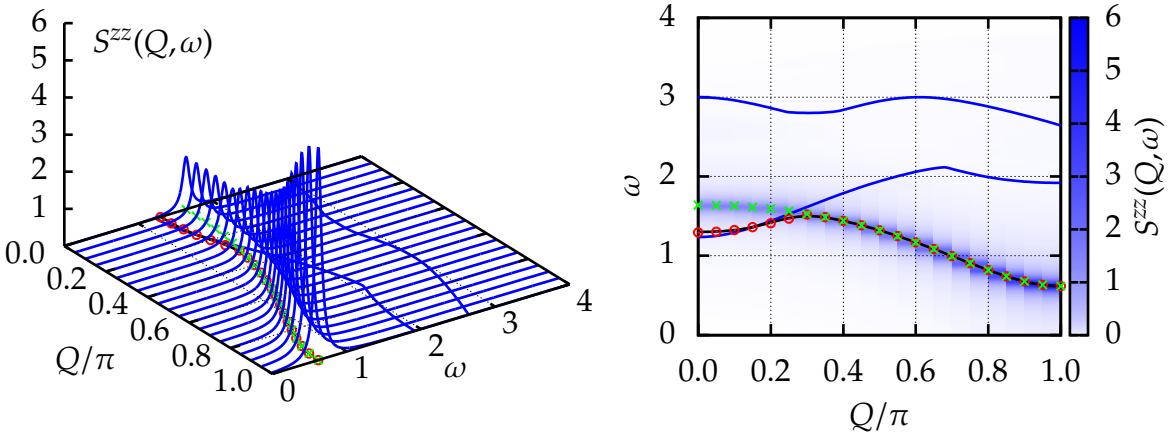

(a) $x = 0.5$, $y = -0.1$, number of Lanczos steps $n = 80$

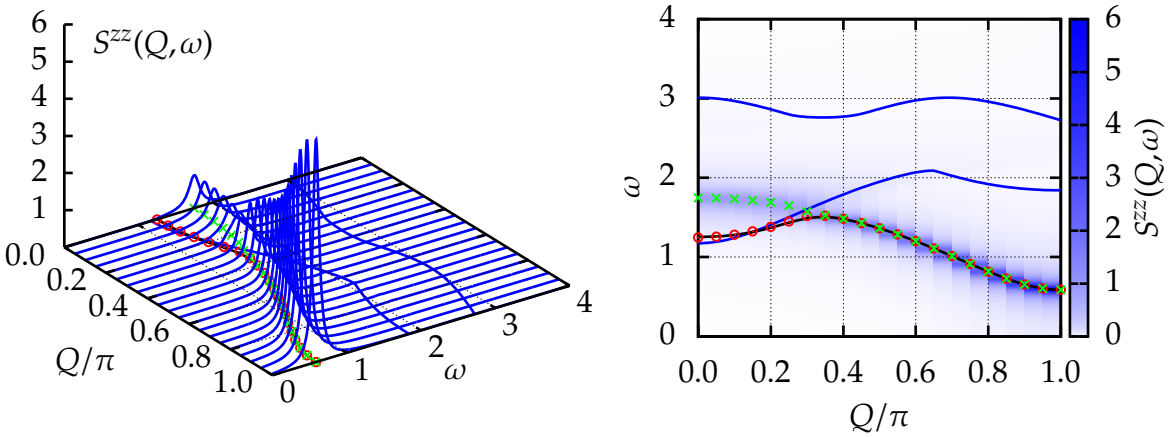

(b) $x = 0.5$, $y = -0.25$, number of Lanczos steps $n = 70$

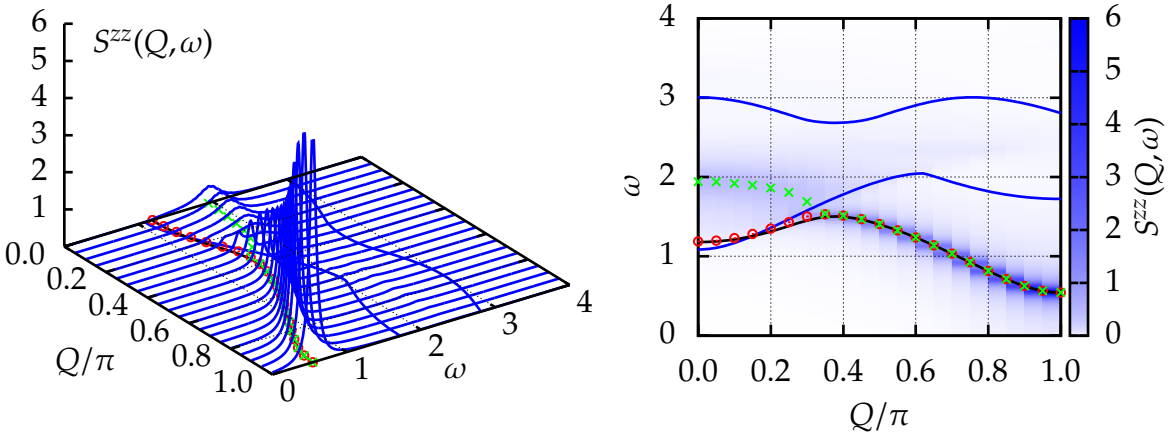

(c) $x = 0.5$, $y = -0.5$, number of Lanczos steps $n = 70$

Figure 5.2: Dynamical structure factor $S^{zz}(Q,\omega)$ of the AFASHL for $x = 0.5$, **Qb** $= \pi$ and various values $y < 0$ calculated by using the generator $G_{\mathrm{gs}}(\ell)$ and Lanczos tridiagonalization as described in the text (broadening: $\delta = 0.05$). The solid black line depicts the one-triplon dispersion and blue lines in the (Q,ω)-plane depict the borders of the two-triplon continuum obtained by the generator $G_{\mathrm{gs,1p}}(\ell)$. Green crosses depict the renormalized one-triplon dispersion obtained by the generator $G_{\mathrm{gs}}(\ell)$ and equation (4.47). Red circles depict the lowest energy level obtained by a diagonalization in the subspace (4.39).

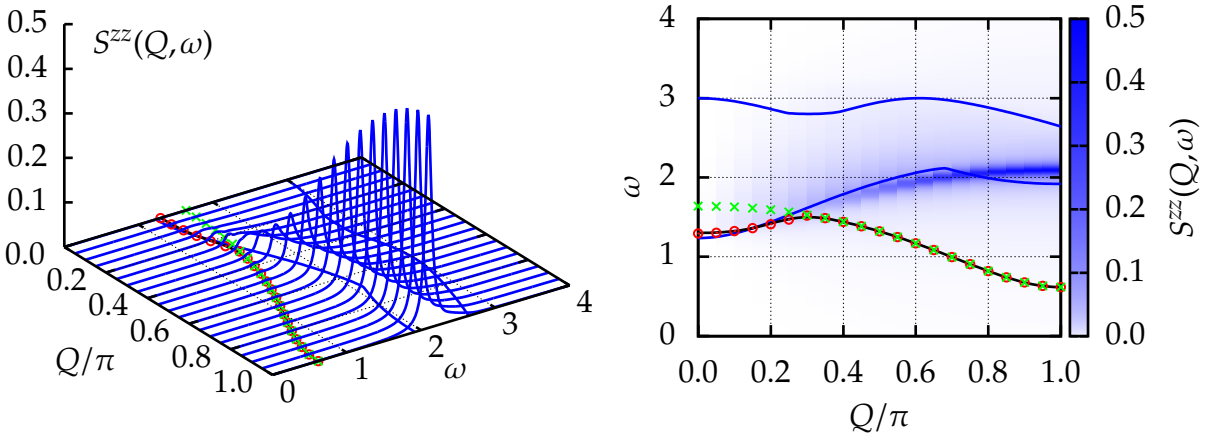

(a) $x = 0.5$, $y = -0.1$, number of Lanczos steps $n = 80$

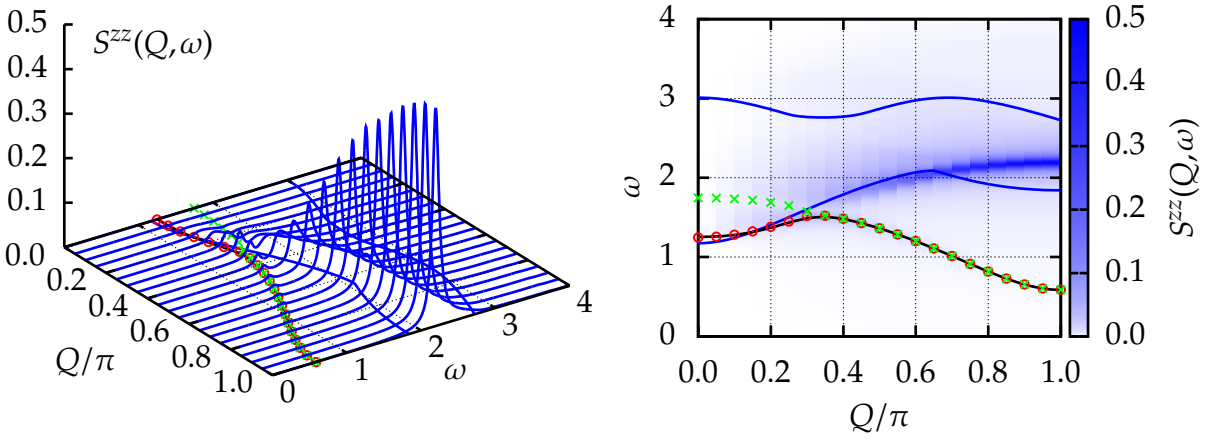

(b) $x = 0.5$, $y = -0.25$, number of Lanczos steps $n = 70$

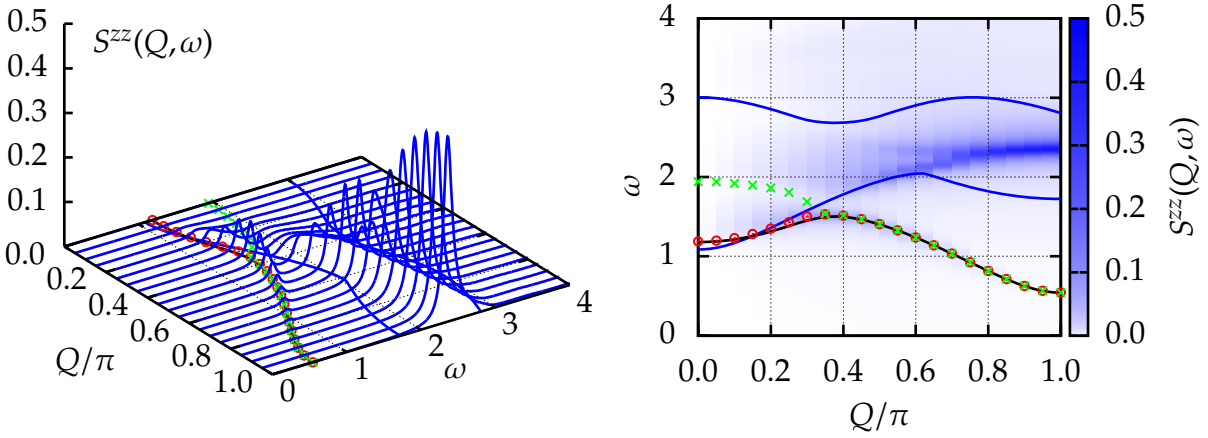

(c) $x = 0.5$, $y = -0.5$, number of Lanczos steps $n = 70$

Figure 5.3: Dynamical structure factor $S^{zz}(Q,\omega)$ of the AFASHL for $x = 0.5$, **Qb** $= 0$ and various values $y < 0$ calculated by using the generator $G_{\text{gs}}(\ell)$ and Lanczos tridiagonalization as described in the text (broadening: $\delta = 0.05$). The solid black line depicts the one-triplon dispersion and blue lines in the (Q,ω)-plane depict the borders of the two-triplon continuum obtained by the generator $G_{\text{gs,1p}}(\ell)$. Green crosses depict the renormalized one-triplon dispersion obtained by the generator $G_{\text{gs}}(\ell)$ and equation (4.47). Red circles depict the lowest energy level obtained by a diagonalization in the subspace (4.39).

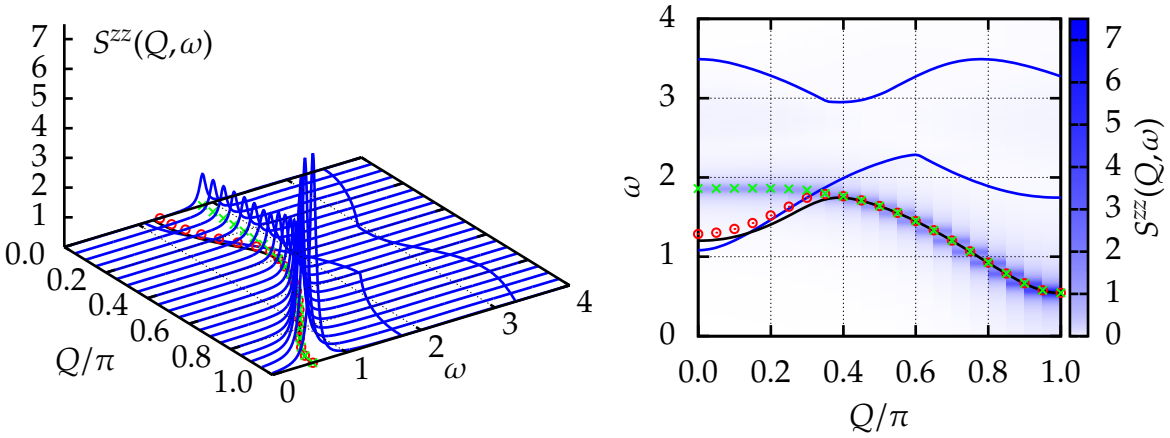

(a) $x = 0.75$, $y = -0.1$, number of Lanczos steps $n = 60$

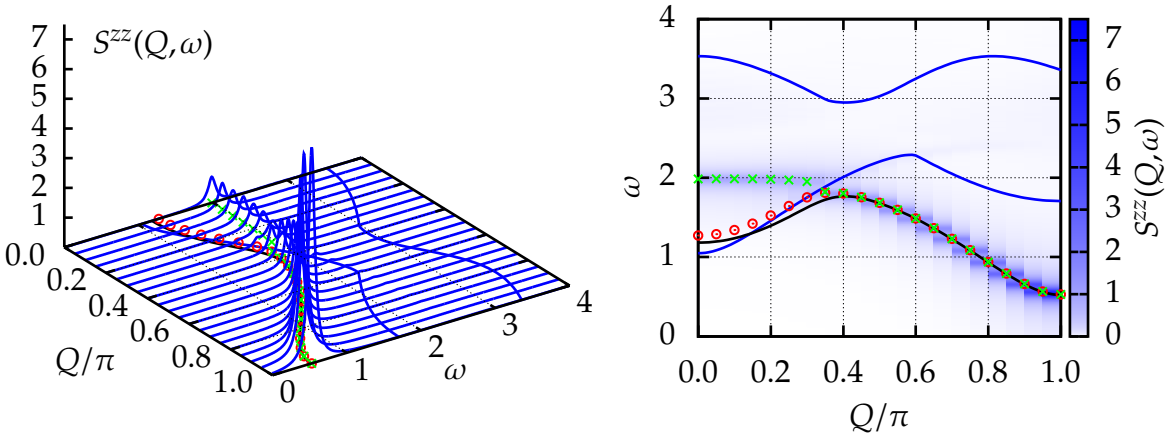

(b) $x = 0.75$, $y = -0.25$, number of Lanczos steps $n = 60$

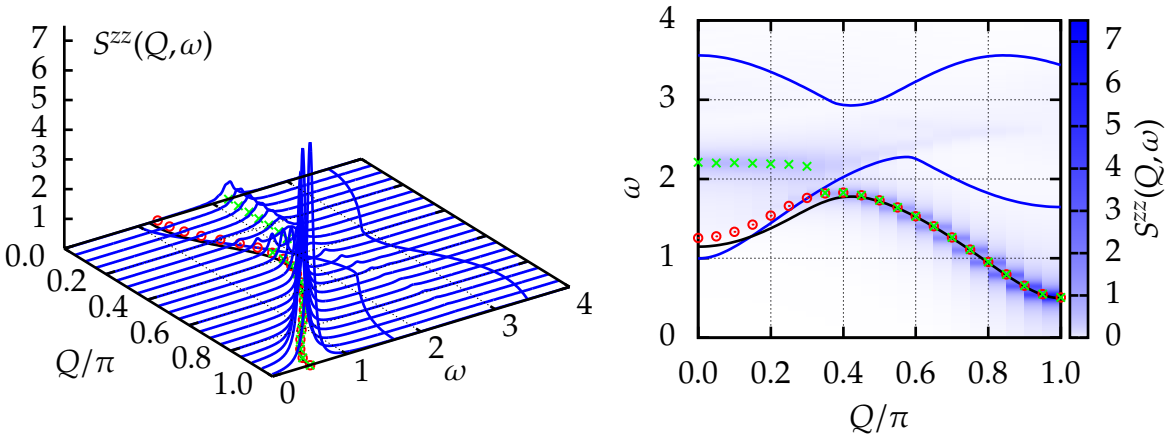

(c) $x = 0.75$, $y = -0.5$, number of Lanczos steps $n = 60$

Figure 5.4: Dynamical structure factor $S^{zz}(Q,\omega)$ of the AFASHL for $x = 0.75$, **Qb** $= \pi$ and various values $y < 0$ calculated by using the generator $G_{\mathrm{gs}}(\ell)$ and Lanczos tridiagonalization as described in the text (broadening: $\delta = 0.05$). The solid black line depicts the one-triplon dispersion and blue lines in the (Q,ω)-plane depict the borders of the two-triplon continuum obtained by the generator $G_{\mathrm{gs,1p}}(\ell)$. Green crosses depict the renormalized one-triplon dispersion obtained by the generator $G_{\mathrm{gs}}(\ell)$ and equation (4.47). Red circles depict the lowest energy level obtained by a diagonalization in the subspace (4.39).

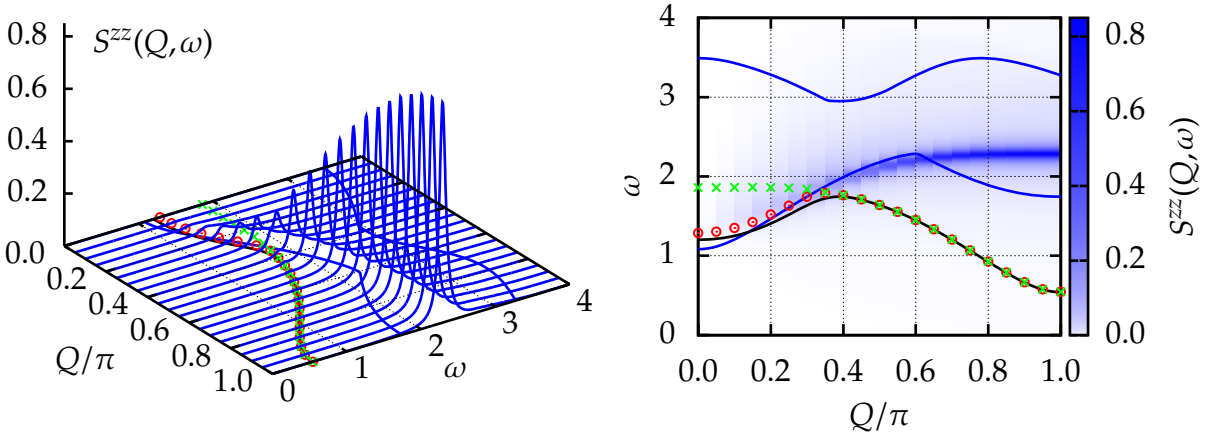

(a) $x = 0.75$, $y = -0.1$, number of Lanczos steps $n = 60$

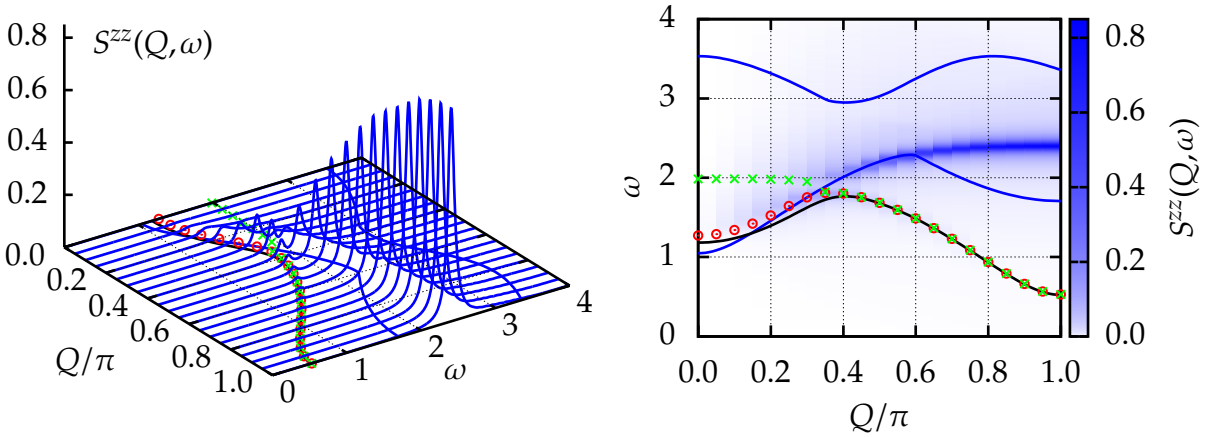

(b) $x = 0.75$, $y = -0.25$, number of Lanczos steps $n = 60$

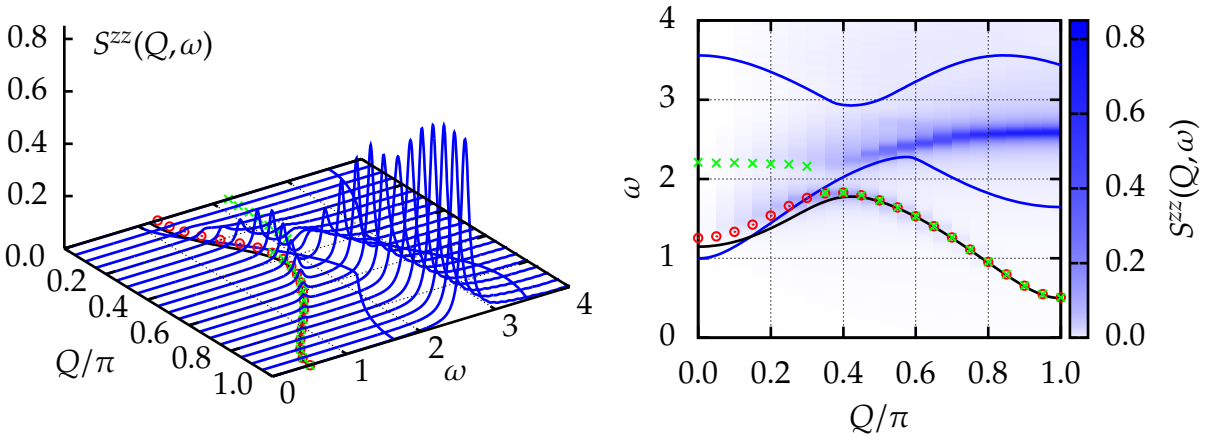

(c) $x = 0.75$, $y = -0.5$, number of Lanczos steps $n = 60$

Figure 5.5: Dynamical structure factor $S^{zz}(Q,\omega)$ of the AFASHL for $x = 0.75$, **Qb** $= 0$ and various values $y < 0$ calculated by using the generator $G_{\mathrm{gs}}(\ell)$ and Lanczos tridiagonalization as described in the text (broadening: $\delta = 0.05$). The solid black line depicts the one-triplon dispersion and blue lines in the (Q,ω)-plane depict the borders of the two-triplon continuum obtained by the generator $G_{\mathrm{gs,1p}}(\ell)$. Green crosses depict the renormalized one-triplon dispersion obtained by the generator $G_{\mathrm{gs}}(\ell)$ and equation (4.47). Red circles depict the lowest energy level obtained by a diagonalization in the subspace (4.39).

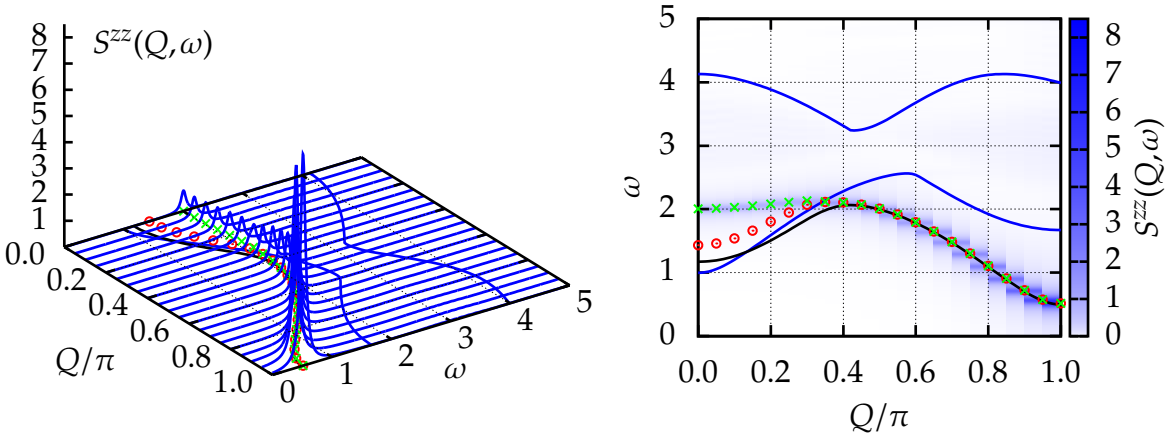

(a) $x = 1.0$, $y = -0.1$, number of Lanczos steps $n = 50$

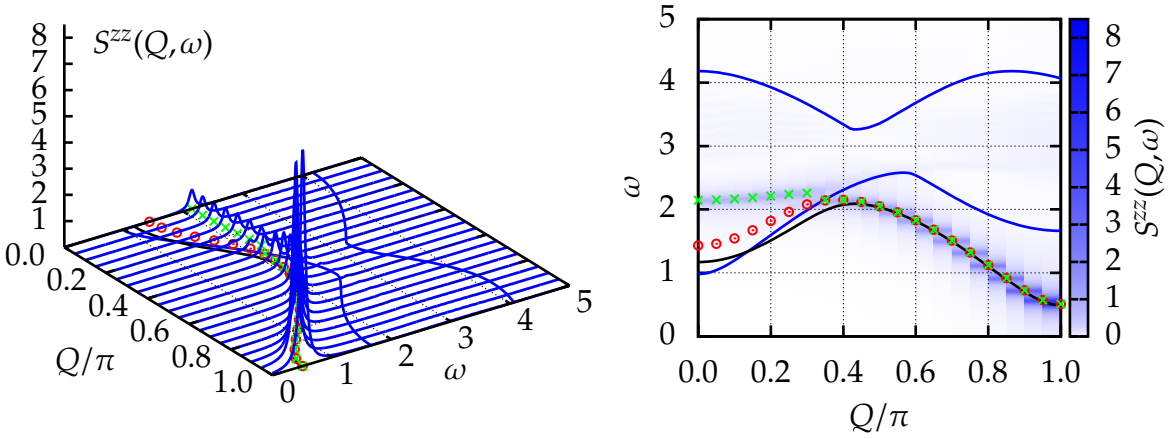

(b) $x = 1.0$, $y = -0.25$, number of Lanczos steps $n = 50$

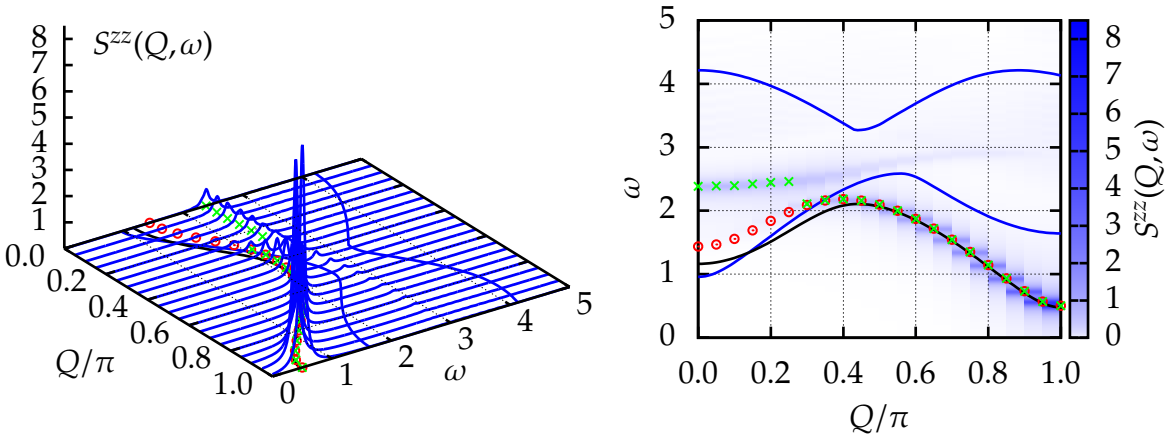

(c) $x = 1.0$, $y = -0.5$, number of Lanczos steps $n = 50$

Figure 5.6: Dynamical structure factor $S^{zz}(Q,\omega)$ of the AFASHL for $x = 1.0$, **Qb** $= \pi$ and various values $y < 0$ calculated by using the generator $G_{\mathrm{gs}}(\ell)$ and Lanczos tridiagonalization as described in the text (broadening: $\delta = 0.05$). The solid black line depicts the one-triplon dispersion and blue lines in the (Q,ω)-plane depict the borders of the two-triplon continuum obtained by the generator $G_{\mathrm{gs,1p}}(\ell)$. Green crosses depict the renormalized one-triplon dispersion obtained by the generator $G_{\mathrm{gs}}(\ell)$ and equation (4.47). Red circles depict the lowest energy level obtained by a diagonalization in the subspace (4.39).

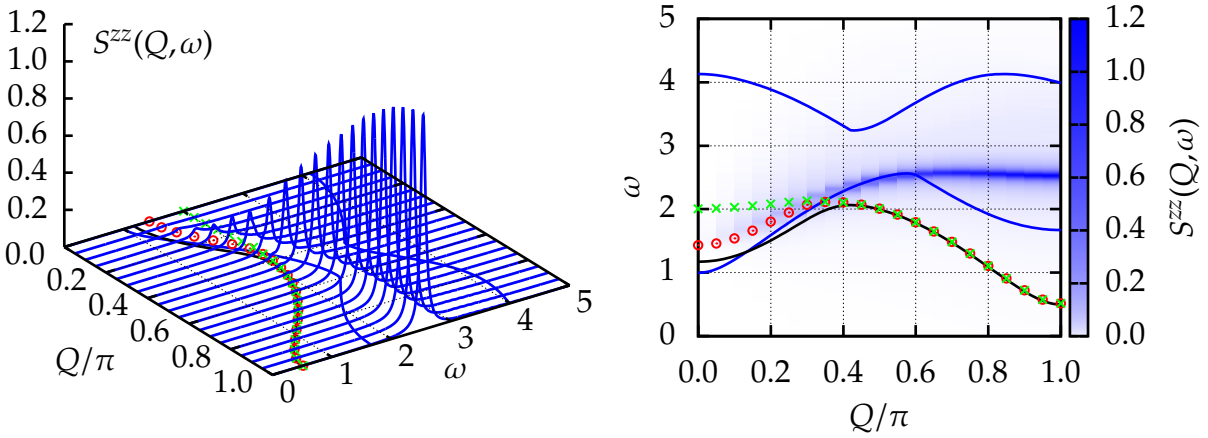

(a) $x = 1.0$, $y = -0.1$, number of Lanczos steps $n = 50$

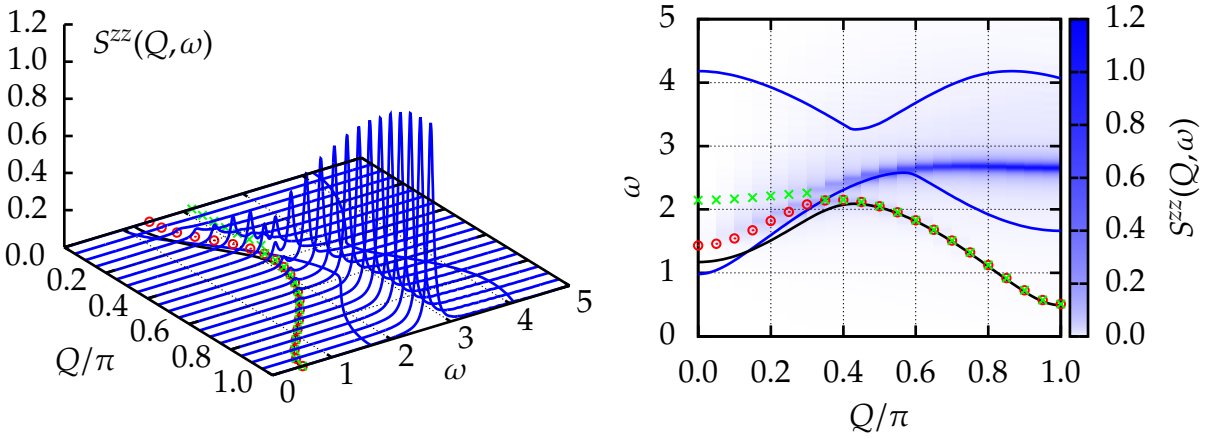

(b) $x = 1.0$, $y = -0.25$, number of Lanczos steps $n = 50$

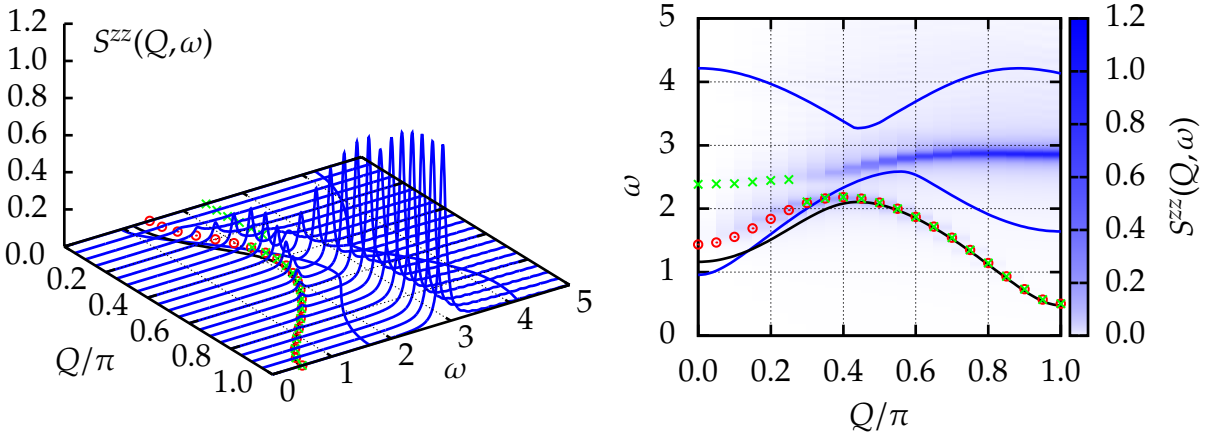

(c) $x = 1.0$, $y = -0.5$, number of Lanczos steps $n = 50$

Figure 5.7: Dynamical structure factor $S^{zz}(Q,\omega)$ of the AFASHL for $x = 1.0$, **Qb** $= 0$ and various values $y < 0$ calculated by using the generator $G_{\mathrm{gs}}(\ell)$ and Lanczos tridiagonalization as described in the text (broadening: $\delta = 0.05$). The solid black line depicts the one-triplon dispersion and blue lines in the (Q,ω)-plane depict the borders of the two-triplon continuum obtained by the generator $G_{\mathrm{gs,1p}}(\ell)$. Green crosses depict the renormalized one-triplon dispersion obtained by the generator $G_{\mathrm{gs}}(\ell)$ and equation (4.47). Red circles depict the lowest energy level obtained by a diagonalization in the subspace (4.39).

the dynamical structure factor $S^{zz}(Q,\omega)$, cf. figures 5.4–5.7 panels (b) and (c). The small peaks for $Q \lessapprox 0.3\pi$ occurring in figures 5.4b, 5.4c, 5.6b and figure 5.6c for $\mathbf{Qb} = \pi$ indicated by the green crosses are continued by resonances for $\mathbf{Qb} = 0$ and $Q \gtrapprox 0.3\pi$, see figures 5.5b, 5.5c, 5.7b and figure 5.7c. This supports a scenario of level repulsion.

5.1.1 Equal-time structure factors $S^{zz}(Q)$ and spectral weights

In figure 5.8 the equal-time structure factor $S^{zz}(Q)$ for $x = 0.5,\ 0.75,\ 1.0$ and various values $y < 0$ is depicted for $\mathbf{Qb} = \pi$ (dashed lines) and for $\mathbf{Qb} = 0$ (dotted lines). The solid lines depict the sum of the equal-time structure factor $S^{zz}(Q)$ for $\mathbf{Qb} = \pi$ and $\mathbf{Qb} = 0$.

Most of the spectral weight is found in the channel with $\mathbf{Qb} = \pi$. Again, (cf. section 4.1.2 and section 4.3.1) increasing the coupling x shifts more and more weight from momenta around $Q = 0$ to momenta around $Q = \pi$, see figure 5.8a, figure 5.8b and figure 5.8c. This effect is slightly enhanced by decreasing y.

In table 5.1 the relative spectral weights $I^{\mathrm{rel}}\big|_{\mathbf{Qb}} := I\big|_{\mathbf{Qb}}/I$ for $\mathbf{Qb} = \pi$ and $\mathbf{Qb} = 0$ are listed. Also for $y < 0$ the sum rule (F.13) is very well fulfilled. Thus for the transformed

Table 5.1: Relative spectral weights $I^{\mathrm{rel}}\big|_{\mathbf{Qb}}$.

x	y	$I^{\mathrm{rel}}\big\|_{\mathbf{Qb}=\pi}$	$I^{\mathrm{rel}}\big\|_{\mathbf{Qb}=0}$	$I^{\mathrm{rel}}\big\|_{\mathbf{Qb}=\pi} + I^{\mathrm{rel}}\big\|_{\mathbf{Qb}=0}$
0.50	-0.10	0.91848	0.08155	1.00002
0.50	-0.25	0.90853	0.09150	1.00004
0.50	-0.50	0.89344	0.10672	1.00015
0.75	-0.10	0.85632	0.14395	1.00027
0.75	-0.25	0.85090	0.15956	1.00046
0.75	-0.50	0.84264	0.15827	1.00091
1.00	-0.10	0.80740	0.19415	1.00154
1.00	-0.25	0.80607	0.19585	1.00192
1.00	-0.50	0.80361	0.19903	1.00264

local spin operator $S^z_l(r)$ the restriction to the subspace 4.39 is well justified.

By increasing the coupling x more and more spectral weight is shifted from the channel with $\mathbf{Qb} = \pi$ to the channel with $\mathbf{Qb} = 0$. Decreasing the interaction y slightly amplifies this shift, so that for the considered parameters x and y the parameter set $x = 1.0$ and $y = -0.5$ shows the largest shift.

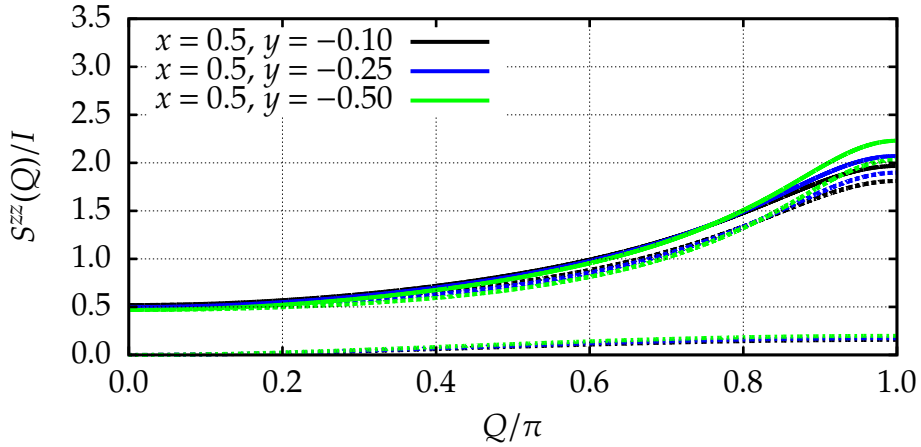

(a) Equal-time structure factor $S^{zz}(Q)$ normalized to the total spectral weight I for $x = 0.5$ and various $y < 0$.

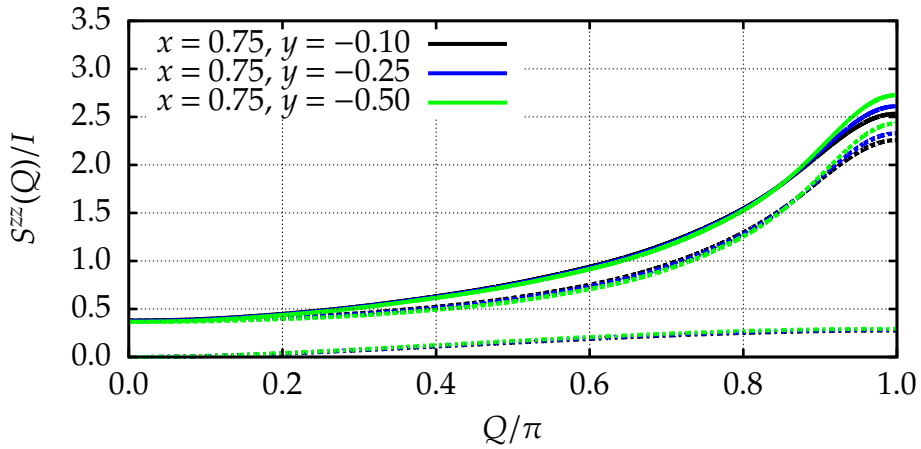

(b) Equal-time structure factor $S^{zz}(Q)$ normalized to the total spectral weight I for $x = 0.75$ and various $y < 0$.

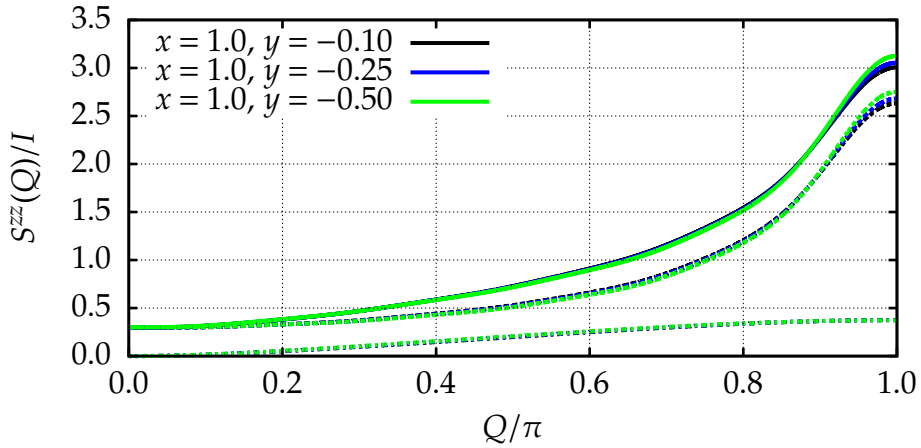

(c) Equal-time structure factor $S^{zz}(Q)$ normalized to the total spectral weight I for $x = 1.0$ and various $y < 0$.

Figure 5.8: Equal-time structure factor $S^{zz}(Q)$ normalized to the total spectral weight I for various interactions x and $y < 0$. Dashed lines indicate $S^{zz}(Q)$ for $\mathbf{Qb} = \pi$, dotted lines indicate $S^{zz}(Q)$ for $\mathbf{Qb} = 0$ and solid lines indicate their sum.

5.1.2 Quasiparticle lifetime

Finally, we discuss the inverse lifetime, the line width respectively, of the elementary excitations in the AFASHL.

As described in section 4.3.2 we use a terminated continued fraction representation of the self-energy $\Sigma(Q,\omega)$ (4.49) to determine the width $\gamma(Q)$ (4.50) of the renormalized quasiparticles indicated by green crosses in figures 5.2–5.7. Details of the termination of the continued fractions are given in appendix A.2.

Figure 5.9 shows the width $\gamma(Q)$ for various values of $x > 0$ and $y < 0$. For all

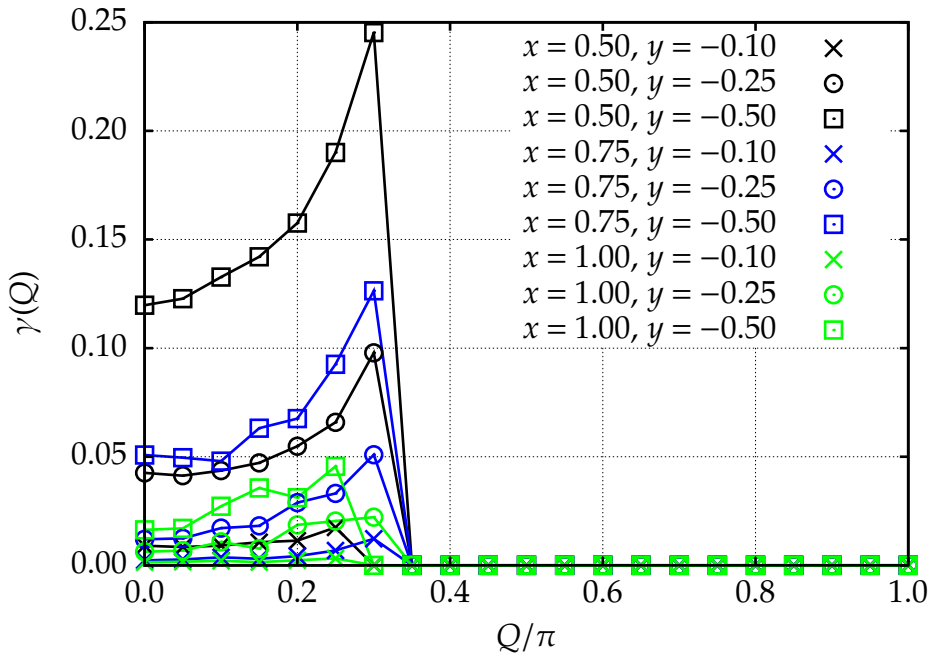

Figure 5.9: Width $\gamma(Q)$ for various interactions $x > 0$ and $y < 0$. For $Q \lessapprox 0.3\pi$ the triplons decay.

considered parameter pairs (x, y) the triplons decay. The maximal width ($\gamma(Q) \approx 0.25$) occurs for the parameter set $x = 0.5$ and $y = -0.5$ at $Q = 0.3\pi$. Note, that for these parameters and $Q = 0.3\pi$ still an excitation with considerable weight exist below the renormalized quasiparticle (green cross), see figure 5.2c. Thus it is possible that a stable quasiparticle still exists below the continuum. Nevertheless, for smaller momenta Q only the excitation inside the continuum remains.

As expected, the width $\gamma(Q)$ increases by increasing the absolute value of y. As for the AASHL increasing the interaction x leads to a smaller width.

The possibility to use higher absolute values of the parameter y in the AFASHL compared to the AASHL leads to the appearance of larger widths in the AFASHL, cf. figure 4.23 and figure 5.9.

The previously mentioned (cf. section 4.3.2) maximum of the width close to the point where the one-triplon dispersion merges with the continuum appears in the AFASHL,

as well.

In figure 5.10 the width $\gamma(Q)$ is depicted for $Q = 0$ as function of y^2 for various interactions $x > 0$ and $y < 0$. Approximately the width $\gamma(Q)$ at $Q = 0$ is given by a

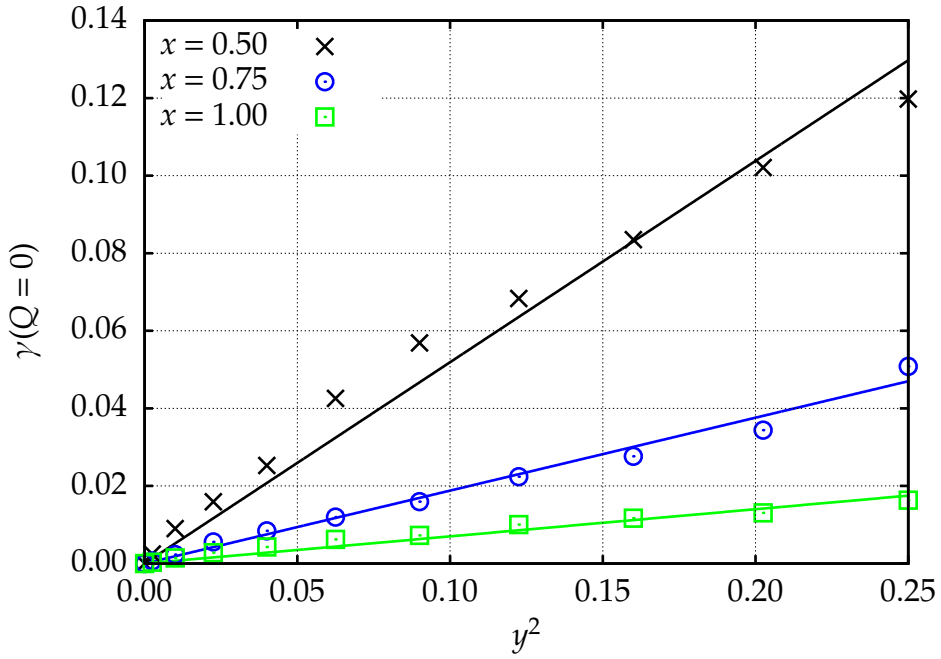

Figure 5.10: Width $\gamma(Q)$ at $Q = 0$ as function of y^2 for various interactions $x > 0$ and $y < 0$. Solid lines are linear fits ($\gamma(Q = 0) = ay^2$).

quadratic function of y, e.g. $\gamma(Q = 0) = ay^2$. In table 5.2 the fitting parameter a is listed for $x = 0.5,\ 0.75,\ 1.0$.

Table 5.2: Fitting parameter a for $x = 0.5,\ 0.75,\ 1.0$ ($\gamma(Q = 0) = ay^2$).

x	a
0.50	0.5187 ± 0.0173
0.75	0.1878 ± 0.0050
1.00	0.0763 ± 0.0032

5.2 Chapter summary

In this chapter dynamical structure factors of asymmetric ferro-antiferromagnetic spin $S = 1/2$ Heisenberg ladder (AFASHL) were discussed. Self-similar continuous unitary transformations sCUTs were used to calculate the dynamical structure factors. Thereby

a quantitative description of spontaneous quasiparticle decay (SQPD) in the AFASHL was achieved.

The AFASHL shows a significant SQPD for larger absolute values of the reflection symmetry breaking interaction, in contrast to the asymmetric antiferromagnetic spin $S = 1/2$ HEISENBERG ladder (AASHL). Thus the AFASHL is more suitable to study large quasiparticle decay. Again, for sufficiently large interactions x the SQPD is influenced by two-triplon interactions.

The results presented in this chapter explain why SQPD was observed in isopropylammonium trichlorocuprate(II) $(CH_3)_2CHNH_3CuCl_3$ (IPA-$CuCl_3$) partly described by an AFASHL. A detailed discussion of IPA-$CuCl_3$ is given in the next chapter 6.

Chapter 6

IPA-$CuCl_3$

The salt isopropylammonium trichlorocuprate(II) $(CH_3)_2CHNH_3CuCl_3$ (IPA-$CuCl_3$) is an excellent system to study two fascinating phenomena recently observed in low-dimensional quantum spin systems. The elementary $S = 1$ excitations, triplons [Schmidt & Uhrig(2003)], show spontaneous quasiparticle decay (SQPD) at higher energies so that the triplons exist only in a restricted part of the Brillouin zone [Masuda *et al.*(2006)]. Additionally, inelastic neutron scattering (INS) provides evidence for an almost exact realization of a Bose-Einstein condensation (BEC) in IPA-$CuCl_3$ for strong enough magnetic fields [Garlea *et al.*(2007), Zheludev *et al.*(2007)], which was theoretically proposed for coupled spin ladders [Giamarchi & Tsvelik(1999)].

Since the characterization of IPA-$CuCl_3$ by Roberts *et al.* [Roberts *et al.*(1981)] various spin models were discussed. Manaka *et al.* pointed out that the magnetic susceptibility of IPA-$CuCl_3$ can be explained by a ferro-antiferromagnetically alternating spin $S = 1/2$ Heisenberg chain with a ferromagnetic coupling twice as large as the antiferromagnetic coupling [Manaka *et al.*(1997)]. According to Hida [Hida(1992)] the magnetic ground state is thus given by a gapped Haldane state [Haldane(1983)].

The dispersion measured by INS [Masuda *et al.*(2006)] and the crystal structure of IPA-$CuCl_3$ indicates that the system is quasi two-dimensional. It is described by weakly coupled asymmetric spin $S = 1/2$ Heisenberg ladders, see figure 6.1. The Hamiltonian reads

$$H_{\text{IPA-CuCl}_3} = H_{1\mathcal{D}} + H_{\text{int}} \tag{6.1a}$$

$$\begin{aligned} H_{1\mathcal{D}} = J_1 \sum_{r,s} \mathbf{S}_1(r,s)\mathbf{S}_2(r+1,s) + J_3 \sum_{r,s} \mathbf{S}_1(r,s)\mathbf{S}_2(r,s) \\ + J_2 \sum_{r,s} \Big(\mathbf{S}_1(r,s)\mathbf{S}_1(r+1,s) + \mathbf{S}_2(r,s)\mathbf{S}_2(r+1,s) \Big) \end{aligned} \tag{6.1b}$$

$$H_{\text{int}} = J_4 \sum_{r,s} \mathbf{S}_1(r,s)\mathbf{S}_2(r+1,s+1) \tag{6.1c}$$

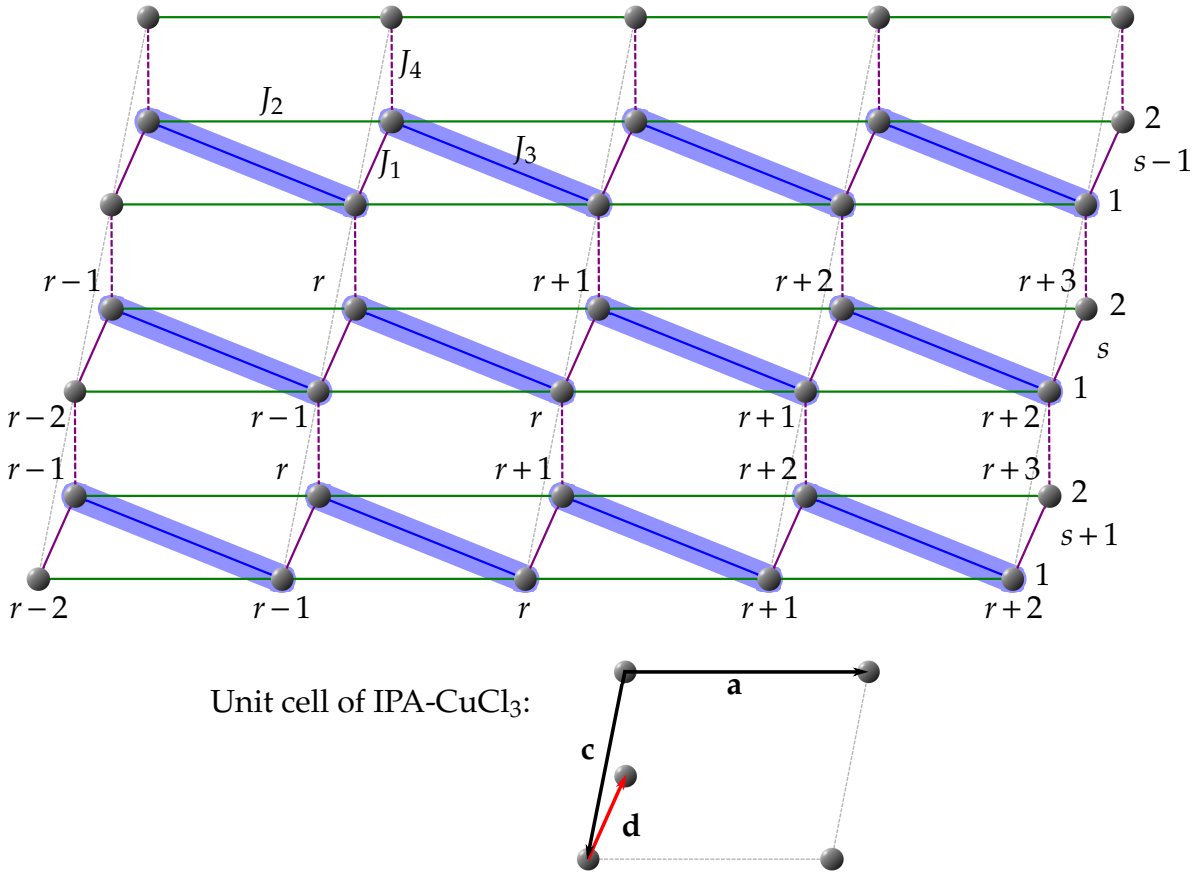

Figure 6.1: Sketch of IPA-CuCl$_3$. Circles indicate Cu ions with spin $S = 1/2$. The couplings J_1 and J_4 are ferromagnetic ($J_1, J_4 < 0$) while J_2 and J_3 are antiferromagnetic ($J_2, J_3 > 0$). Two spins linked by J_3 form a dimer. A unit cell of IPA-CuCl$_3$ is spanned by the vectors **a** and **c** and a basis vector **d**, cf. reference [Masuda *et al.*(2006)].

with two ferromagnetic couplings J_1, $J_4 < 0$ and two antiferromagnetic couplings J_2, $J_3 > 0$. The dominant dimer coupling is J_3 so that we use the dimensionless ratios $x = J_2/J_3$, $y = J_1/J_3$ and $z = J_4/J_3$ to characterize the system. Let us first consider the ladders as isolated because the interladder coupling J_4 is small. The standard view of these ladders takes the J_3 bonds to form the rungs of the ladder. Then J_1 is a diagonal bond, cf. chapter 4 and chapter 5, see figure 6.2.

The key element of this model is the asymmetry of the spin ladders controlled by J_1. On the one hand, the presence of J_1 spoils the reflection symmetry about the center line of the ladder between the legs, cf. section 4.1. This symmetry would imply a conserved parity such that the triplons on the dimers could be changed only by an even number [Knetter *et al.*(2001), Schmidt & Uhrig(2005)] so that no decay of a triplon into a pair of triplons could occur. Hence the very presence of J_1 in IPA-CuCl$_3$ opens an important decay channel for quasiparticle decay.

On the other hand, the two bonds J_2 and J_1 represent the coupling of adjacent dimers. Both contribute to the hopping of the triplons which is given in leading

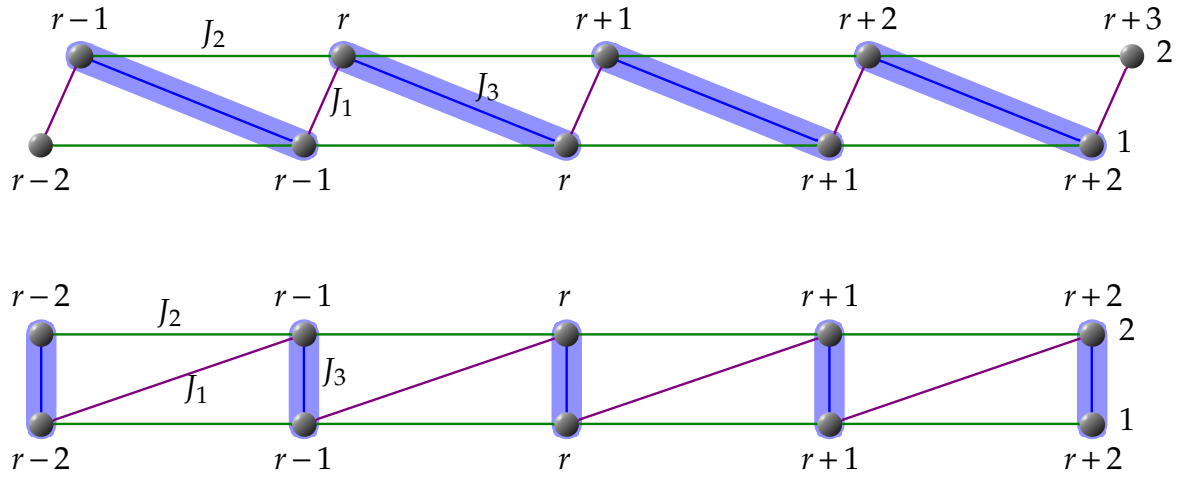

Figure 6.2: Upper panel: Ladder structure in IPA-$CuCl_3$. Lower panel: Standard view of this ladder.

order by $2J_2 - J_1$ [Uhrig & Schulz(1996)] (cf. chapter 4) while the interaction of adjacent triplons is proportional to $2J_2 + J_1$. With information only on the dispersion [Masuda *et al.*(2006)] it is impossible to determine J_1 and J_2 separately. Hence, the same feature that induces the interesting quasiparticle decay makes it particularly difficult to establish a microscopic model. Thus, in spite of many years of intensive studies [Roberts *et al.*(1981), Manaka *et al.*(1997), Manaka & Yamada(2000), Masuda *et al.*(2006), Garlea *et al.*(2007), Manaka *et al.*(2007), Hong *et al.*(2010)] no quantitative microscopic model for IPA-$CuCl_3$ is established. This chapter aims at filling this gap. Theoretically, the determination of the magnetic couplings J_1, J_2, J_3 and J_4 in IPA-$CuCl_3$ is based on self-similar continuous unitary transformations (sCUTs) of models with quasiparticle decay, see chapter 3, chapter 4 and chapter 5, to describe INS. To describe the magnetic susceptibility $\chi(T)$ high temperature series expansions (HTSEs) for asymmetric spin ladders which are topologically equivalent to dimerized and frustrated spin chains [Bühler *et al.*(2001)] are used. The experimental input used are INS data [Masuda *et al.*(2006)] and magnetic susceptibility $\chi(T)$ data [Manaka *et al.*(1997)]. We illustrate why it is intrinsically difficult to determine the microscopic model.

After we will have determined the microscopic model of IPA-$CuCl_3$ (cf. section 6.1) we calculate the dynamical structure factor $S^{zz}(Q,\omega)$ to describe the SQPD occurring in IPA-$CuCl_3$, see section 6.2. Since IPA-$CuCl_3$ is to a great extent described by asymmetric ferro-antiferromagnetic spin $S = 1/2$ Heisenberg ladders (AFASHLs) it is not surprising that SQPD was observed in this compound, cf. reference [Masuda *et al.*(2006)] and chapter 5.

Finally, we compute the magnetic field and the temperature dependence of the lowest magnetic modes in the Bose-condensed phase, cf. section 6.3 and section 6.4.

The calculation of the magnetic field dependence as well as the calculation of the temperature dependence are based on the effective model previously obtained by sCUTs.

6.1 Magnetic couplings of IPA-$CuCl_3$

To determine the magnetic couplings of IPA-$CuCl_3$ we start with sCUTs using the generator $G_{\mathrm{gs,1p}}(\ell)$, cf. section 3.2.3. In chapter 4 and in chapter 5 it was illustrated that this generator produces reliable results for the one-triplon dispersion in the region of the Brillouin zone where the excitations are stable.

As mentioned before INS data [Masuda *et al.*(2006)] imply that the interladder coupling J_4 is small compared to the remaining couplings J_1, J_2 and J_3. Thus, we start with the limit of isolated asymmetric ladders described by $H_{1\mathcal{D}}$ (6.1b). The Hamiltonian $H_{1\mathcal{D}}$ is precisely described by the AFASHL discussed in chapter 5.

The sCUT maps the Hamiltonian $H_{1\mathcal{D}}$ to an effective model where the one-triplon sector is given by

$$H_{1\mathcal{D},\mathrm{eff}}\big|_1^1 = J_3 \sum_{r,s} \sum_{\alpha} \sum_{d} \left[c_{H_{1\mathcal{D}}|_1^1}\right]_d t^\dagger_{\alpha,r,s} t_{\alpha,r+d,s} \tag{6.2}$$

with the triplon creation operators $t^\dagger_{\alpha,r,s}$ and annihilation operators $t_{\alpha,r,s}$ in real space and the spin polarization $\alpha \in \{x,y,z\}$. Here we use the generator $G_{\mathrm{gs,1p}}(\ell)$ and the truncation scheme $N_\mathrm{t} = 4$ with $\mathbf{D} = (10,8,8,6,6,4,4)$. The Hamiltonian $H_{1\mathcal{D},\mathrm{eff}}\big|_1^1$ can be diagonalized by a Fourier transformation

$$t^\dagger_{\alpha,r,s} := \frac{1}{\sqrt{N}} \frac{1}{\sqrt{N}} \sum_{h,l} \mathrm{e}^{2\pi \mathrm{i}(hr+ls)}\, t^\dagger_{\alpha,h,l} \tag{6.3a}$$

$$t_{\alpha,r,s} := \frac{1}{\sqrt{N}} \frac{1}{\sqrt{N}} \sum_{h,l} \mathrm{e}^{-2\pi \mathrm{i}(hr+ls)}\, t_{\alpha,h,l} \tag{6.3b}$$

$$\tag{6.3c}$$

yielding

$$H_{1\mathcal{D},\mathrm{eff}}\big|_1^1 = J_3 \sum_{h,l} \sum_{\alpha} \omega_1(h)\, t^\dagger_{\alpha,h,l} t_{\alpha,h,l} \tag{6.4}$$

in terms of triplon creation operators $t^\dagger_{\alpha,h,l}$ and annihilation operators $t_{\alpha,h,l}$ in momentum space, where h is the wave vector component along the ladders, l the one perpendicular to them. These operators are the Fourier transforms of the bond operators $t^\dagger_{\alpha,r,s}$ and $t_{\alpha,r,s}$ [Chubukov(1989), Sachdev & Bhatt(1990)] (cf. appendix C) defined on the dimers

in figure 6.1.

The dispersion $\omega_1(h)$, given by

$$\omega_1(h) = \left[c_{H_{1\mathcal{D}}|_1^1}\right]_0 + 2\sum_{d=1}^{D_2}\left[c_{H_{1\mathcal{D}}|_1^1}\right]_d \cos(2\pi dh) \tag{6.5}$$

(cf. appendix D). It depends only on h because the sCUT is applied to the isolated ladders which still have to be coupled. This coupling is achieved in leading order following the approach in references [Uhrig *et al.*(2004), Uhrig *et al.*(2005a)]. The spin component $S_i^\alpha(r,s)$ is taken as observable and transformed into the new basis by the sCUT. The truncation scheme for the observable has been $N_\mathrm{t}^O = 3$ and $\mathbf{D}^O = (10,10,8,8,6,6)$. Then it reads

$$S_{i,\mathrm{eff}}^\alpha(r,s) := U^\dagger S_i^\alpha(r,s) U \tag{6.6a}$$

$$= \sum_{\delta=-D_1^O}^{D_1^O}\left[c_{S_i^\alpha|_0^1}\right]^\delta \left(t^\dagger_{\alpha,r+\delta,s} + t_{\alpha,r+\delta,s}\right) + \dots\,, \tag{6.6b}$$

where the dots stand for normal-ordered higher terms in the real space triplon operators $t^\dagger_{\alpha,r,s}$ ($t_{\alpha,r,s}$). Knowing $S_{i,\mathrm{eff}}^\alpha(r,s)$ allows us in a second step to write down the effective bilinear interladder coupling $H_{\mathrm{int,eff}}^{\mathrm{bilinear}}$ in real space

$$H_{\mathrm{int,eff}}^{\mathrm{bilinear}} = J_4 \sum_{r,s}\sum_{\alpha}\sum_{\delta,\delta'}\left[c_{S_1^\alpha|_0^1}\right]^\delta\left[c_{S_2^\alpha|_0^1}\right]^{\delta'}\left[t^\dagger_{\alpha,r,s}\left(t^\dagger_{\alpha,r+1+(\delta'-\delta),s+1} + t_{\alpha,r+1+(\delta'-\delta),s+1}\right) + \mathrm{H.c.}\right], \tag{6.7}$$

where trilinear and higher contributions are neglected. Therefore, the bilinear part of the complete two-dimensional effective model for IPA-$CuCl_3$ reads

$$\begin{aligned} H_{\mathrm{IPA\text{-}CuCl_3,eff}}^{\mathrm{bilinear}} = {} & J_3 \sum_{r,s}\sum_{\alpha}\sum_{d}\left[c_{H_{1\mathcal{D}}|_1^1}\right]_d t^\dagger_{\alpha,r,s} t_{\alpha,r+d,s} \\ & + J_4 \sum_{r,s}\sum_{\delta,\delta'}\sum_{\alpha}\left[c_{S_1^\alpha|_0^1}\right]^\delta\left[c_{S_2^\alpha|_0^1}\right]^{\delta'}\left[t^\dagger_{\alpha,r,s}\left(t^\dagger_{\alpha,r+1+(\delta'-\delta),s+1} + t_{\alpha,r+1+(\delta'-\delta),s+1}\right) + \mathrm{H.c.}\right]. \end{aligned} \tag{6.8}$$

This approach is highly accurate for intraladder effects and it considers interladder couplings in leading order. Fourier transformation leads to

$$H_{\mathrm{IPA\text{-}CuCl_3,eff}}^{\mathrm{bilinear}} = J_3 \sum_{h,l}\sum_{\alpha}\left[\Omega(h,l)\, t^\dagger_{\alpha,h,l} t_{\alpha,h,l} + \frac{\Lambda(h,l)}{2}\left(t^\dagger_{\alpha,h,l} t^\dagger_{\alpha,-h,-l} + t_{\alpha,h,l} t_{\alpha,-h,-l}\right)\right] \tag{6.9}$$

with

$$\Omega(h,l) = \omega_1(h) + \Lambda(h,l) \tag{6.10}$$

and

$$\Lambda(h,l) = 2z \sum_{\delta,\delta'=-D_1^O}^{D_1^O} \left[c_{S_1^\alpha|_0^1}\right]^\delta \left[c_{S_2^\alpha|_0^1}\right]^{\delta'} \cos(2\pi h(1+\delta'-\delta)+2\pi l) \tag{6.11}$$

$$= -2z \sum_{\delta,\delta'=-D_1^O}^{D_1^O} \left[c_{S_1^\alpha|_0^1}\right]^\delta \left[c_{S_1^\alpha|_0^1}\right]^{\delta'} \cos(2\pi h(\delta+\delta'-1)-2\pi l) \tag{6.12}$$

where in the latter step $\left[c_{S_2^\alpha|_0^1}\right]^{\delta'} = -\left[c_{S_1^\alpha|_0^1}\right]^{-\delta'}$ has been used. The dispersion relation $\omega(h,l)$ of the Hamiltonian $H^{\text{bilinear}}_{\text{IPA-CuCl}_3,\text{eff}}$ (6.9) can be obtained by a bosonic Bogoliubov transformation

$$b_{\alpha,h,l} := u(h,l)\, t_{\alpha,h,l} + v(h,l)\, t^\dagger_{\alpha,-h,-l} \tag{6.13a}$$

$$b^\dagger_{\alpha,h,l} := u(h,l)\, t^\dagger_{\alpha,h,l} + v(h,l)\, t_{\alpha,-h,-l} \tag{6.13b}$$

with

$$u^2(h,l) - v^2(h,l) = 1 \tag{6.14}$$

leading to

$$\omega(h,l) = J_3 \sqrt{\Omega^2(h,l) - \Lambda^2(h,l)} \tag{6.15a}$$

$$= J_3 \sqrt{\omega_1^2(h) + 2\omega_1(h)\Lambda(h,l)}\,. \tag{6.15b}$$

In the Bogoliubov diagonalization the hard-core property of the bosons is neglected. However, this does not concern the large intraladder couplings, but only the small interladder couplings so that the approach is still very accurate [Exius(2010)]. The dispersion $\omega(h,l)$ makes a direct comparison with INS results possible.

To determine the microscopic parameters we fix the value $y = J_1/J_3$ and fit the two ratios $x = J_2/J_3$, $z = J_4/J_3$, and the energy scale J_3 to reproduce the INS result (equation (2) in reference [Masuda *et al.*(2006)])

$$\omega^2(h,l) = a^2\cos^2(\pi h) + \left[\Delta^2 + 4b^2\sin^2(\pi l)\right]\sin^2(\pi h) + c^2\sin^2(2\pi h) \tag{6.16}$$

with $a = 4.08(9)$meV, $\Delta = 1.17(1)$meV, $b = 0.67(1)$meV and $c = 2.15(9)$meV. To be more

specific, comparing equation 6.15 and equation 6.16 for $h = 0.5$ yields

$$J_3^2\,\omega_1^2(0.5) = \Delta^2 + 2b^2 \tag{6.17a}$$

$$4J_3J_4\,\omega_1(0.5)\left(\sum_\delta (-1)^\delta \left[c_{S_1^{\alpha}|_0^1}\right]^\delta\right)^2 = -2b^2 \tag{6.17b}$$

which fixes the couplings J_3 and J_4. To fit J_2 we use the experimental value of $\omega(0.4, 0.0)$. Thus, we obtain the triples (x, y, z) in table 6.1. They all essentially imply the same

Table 6.1: Parameters for IPA-$CuCl_3$ compatible with INS [Masuda *et al.*(2006)]

J_3 [meV]	$x = J_2/J_3$	$y = J_1/J_3$	$z = J_4/J_3$
3.743	0.133	-2.0	-0.076
3.288	0.268	-1.4	-0.088
3.158	0.317	-1.2	-0.092
3.038	0.369	-1.0	-0.096
2.929	0.424	-0.8	-0.100
2.830	0.480	-0.6	-0.103

dispersion, see figure 6.3. Hence, on the basis of the the INS data, one cannot decide which of the triples applies to IPA-$CuCl_3$. The quasiparticle decay occurs where the dispersion enters the tow-triplon continuum.

In complement to the INS data we use the temperature dependence of the magnetic susceptibility $\chi(T)$ [Manaka *et al.*(1997)]. Starting from the spin isotropic Hamiltonian (6.1) the susceptibilities in different spatial direction have to be the same up to scaling proportional to the squares of the Landé g-factors. This means that $\chi_A : \chi_B : \chi_C$ equals $g_A^2 : g_B^2 : g_C^2$ where A, B, C indicate the directions normal to the corresponding surfaces of the crystal [Manaka *et al.*(1997)]. Figure 6.4b displays that the three susceptibilities can be scaled to coincide for $g_A = 2.08$, $g_B = 2.06$, and $g_C = 2.25$ within about 3%. In the region of the maximum, between $T = 15$ K and 50 K the scaling even holds within less than 0.5%. This choice of g-factors fulfills the experimental constraints [Manaka *et al.*(1997), Manaka & Yamada(2000)] $g_A, g_B \in [2.06, 2.11]$ and $g_C = 2.25 - 2.26$ best. We conclude that a spin isotropic Hamiltonian such as (6.1) provides a very good description, although anisotropies, e.g., Dzyaloshinskii-Moriya terms, can be present with a relative size of a few percent. This agrees with findings from electron paramagnetic resonance [Manaka & Yamada(2000)].

Theoretically, we use the HTSE for the isolated asymmetric ladder

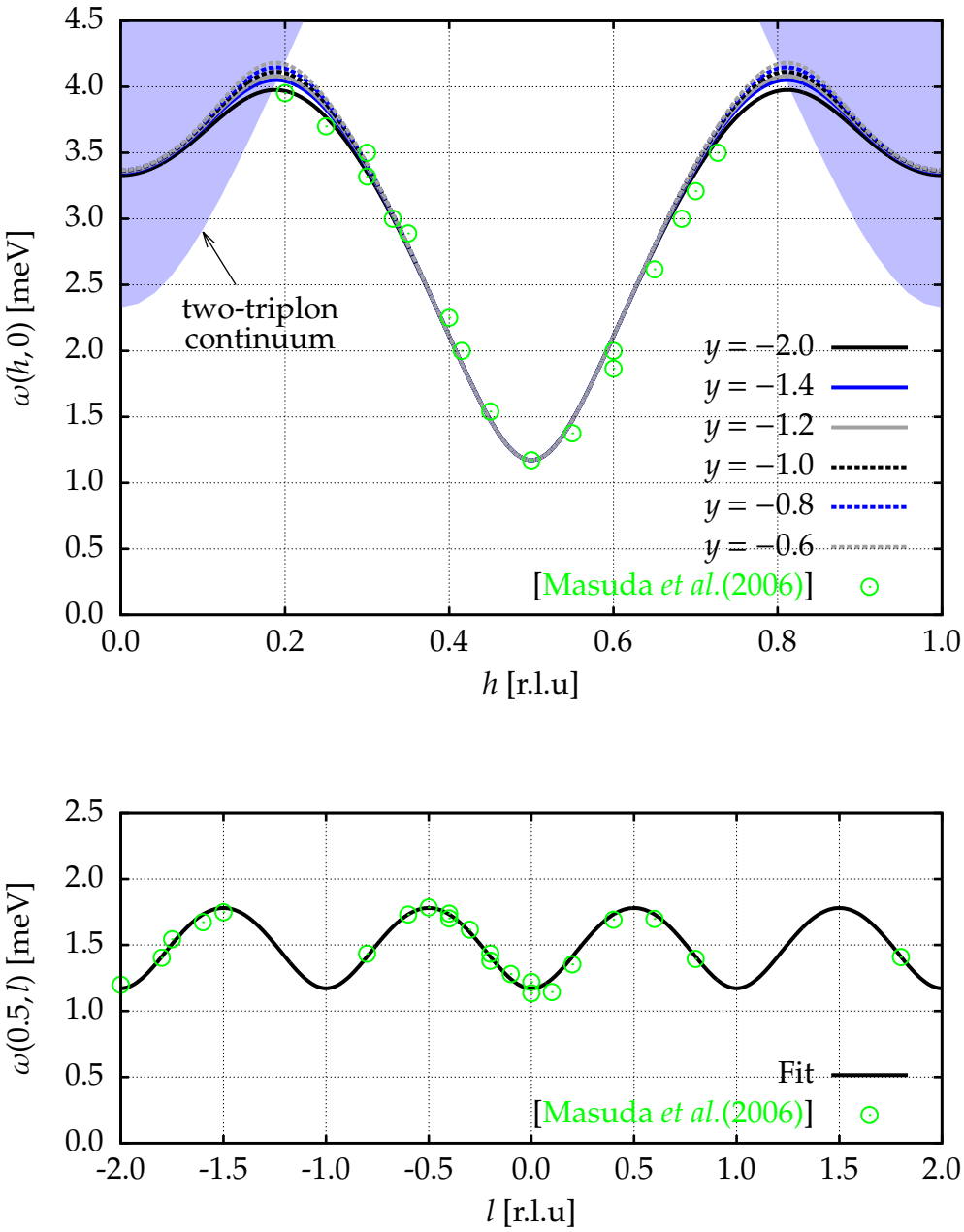

Figure 6.3: Circles are INS data [Masuda *et al.*(2006)]. Upper panel: Dispersions $\omega(h,0)$ for (x,y,z) triples in table 6.1. The quasiparticle decay takes place where the dispersion enters the light blue area indicating the two-triplon continuum. Lower panel: Dispersion $\omega(0.5,l)$. All triples lead to coinciding curves.

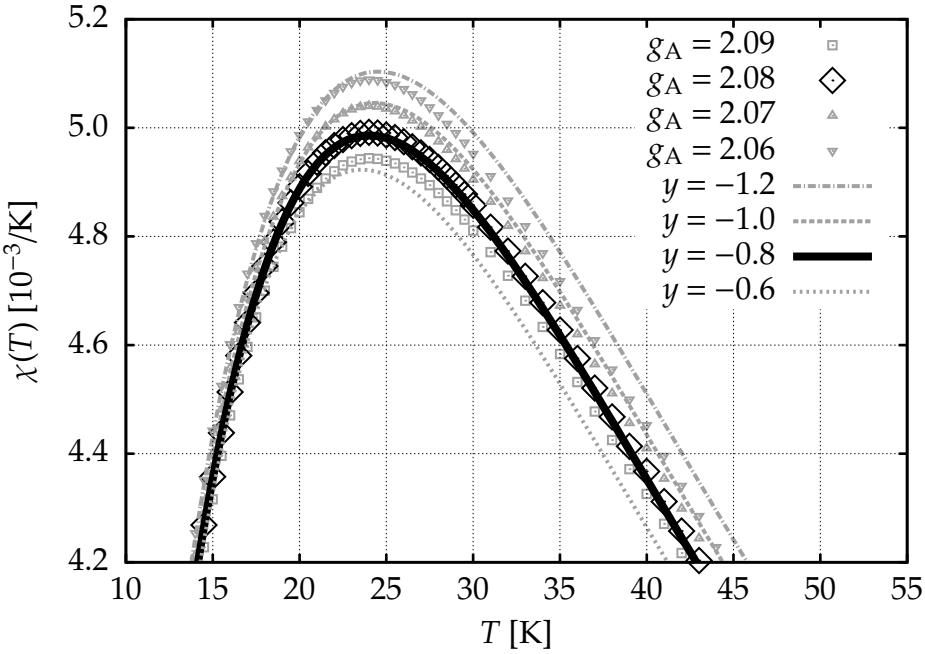

(a) Comparison of $\chi_A(T)$ for various values g_A with theoretical results obtained by [7,4] Dlog–Padé approximated high temperature series expansions [Bühler *et al.*(2001)] for the (x, y, z) triples from table 6.1.

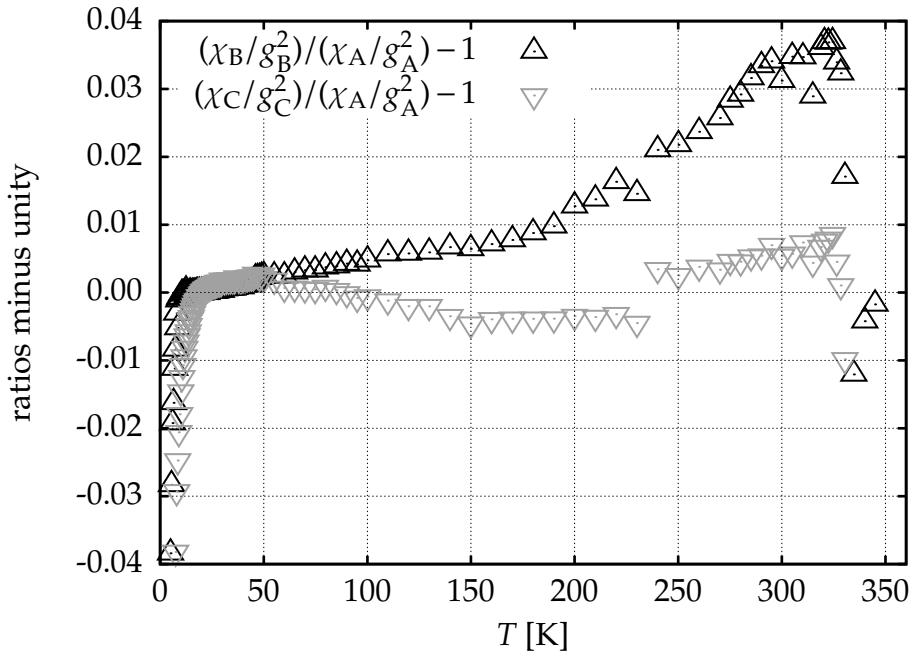

(b) Deviations of the experimental magnetic susceptibilities [Manaka *et al.*(1997)] $\chi_B(T)$ and $\chi_C(T)$ in B and C direction relative to $\chi_A(T)$ for $g_A = 2.08$, $g_B = 2.06$ and $g_C = 2.25$, indicating anisotropies.

Figure 6.4: Magnetic susceptibility $\chi(T)$.

[Bühler *et al.*(2001)] providing series in $\beta = 1/T$ up to order β^{n+1} with $n = 10$ denoted by $\chi_{1\mathcal{D}}(\beta)$ and a Dlog–Padé representation [Domb & Green(1972)] to enhance the region of validity and to include interladder interactions in IPA-$CuCl_3$ on a mean-field level.

The magnetization m of isolated ladders in an external magnetic field in z-direction

$$H_h = -h \sum_{r,s} \left(S_1^z(r,s) + S_2^z(r,s) \right) \tag{6.18}$$

is given by

$$m = \chi_{1\mathcal{D}}\, h\,. \tag{6.19}$$

Applying a mean-field approximation to the part H_{int} (6.1c) describing the interladder interaction yields

$$\begin{aligned}
H_{\text{int}} &= J_4 \sum_{r,s} \mathbf{S}_1(r,s)\mathbf{S}_2(r+1,s+1) && \text{(6.20a)}\\
&= J_4 \sum_{r,s} \sum_{\alpha} S_1^\alpha(r,s) S_2^\alpha(r+1,s+1) && \text{(6.20b)}\\
&\approx J_4 \sum_{r,s} \sum_{\alpha} S_1^\alpha(r,s) \left\langle S_2^\alpha(r+1,s+1) \right\rangle + S_2^\alpha(r+1,s+1) \left\langle S_1^\alpha(r,s) \right\rangle && \text{(6.20c)}\\
&= J_4 m \sum_{r,s} \left(S_1^z(r,s) + S_2^z(r,s) \right) && \text{(6.20d)}
\end{aligned}$$

where we assume $\left\langle S_i^z(r,s) \right\rangle = m$ and $\left\langle S_i^x(r,s) \right\rangle = \left\langle S_i^y(r,s) \right\rangle = 0$ for $i \in \{1,2\}$, and all sites r,s. Thus, the interladder interaction acts like an additional external magnetic field leading to an effective total magnetic field $h_{\text{eff}} = h - J_4 m$. This can be used to define a two-dimensional magnetic susceptibility $\chi_{2\mathcal{D}}$ via

$$\begin{aligned}
m &= \chi_{1\mathcal{D}}\, h_{\text{eff}} && \text{(6.21a)}\\
&= \chi_{1\mathcal{D}} (h - J_4 m) && \text{(6.21b)}\\
\Rightarrow \quad m &= \underbrace{\frac{\chi_{1\mathcal{D}}}{1 + J_4 \chi_{1\mathcal{D}}}}_{=:\chi_{2\mathcal{D}}} h && \text{(6.21c)}\\
\Rightarrow \quad \chi_{2\mathcal{D}}^{-1} &= \chi_{1\mathcal{D}}^{-1} + J_4 && \text{(6.21d)}
\end{aligned}$$

in interladder mean-field approximation.

A Dlog–Padé approximant of a expansion of the two-dimensional magnetic suscep-

tibility $\chi_{2\mathcal{D}}(\beta)$ is given by

$$\chi(\beta) = \frac{\beta}{4} \exp\left(\int_0^\beta P_l^k(\beta') \, \mathrm{d}\beta' \right) \tag{6.22}$$

where $P_l^k(\beta)$ is the rational Dlog-Padé approximant with a polynomial of degree k in the numerator and a polynomial of degree l in the denominator of

$$f(\beta) = \frac{\partial}{\partial \beta} \ln\left(\frac{\chi_{2\mathcal{D}}(\beta)}{\beta} \right) \tag{6.23}$$

$$= -\frac{\partial}{\partial \beta} \ln\left(\frac{1}{\chi_{1\mathcal{D}}(\beta)/\beta + A\beta^{n+1} + B\beta^{n+2}} + J_4\beta \right) . \tag{6.24}$$

Possible orders $[k,l]$ of $P_l^k(\beta)$ have to fulfill $k+l = n+1$ where n is the order of the truncated series available. The parameters A and B are introduced to incorporate zero-temperature information to the HTSE. The term $J_4\beta$ considers the interaction J_4 on a mean-field level, cf. equation (6.21).

From the asymptotic low-temperature behavior

$$\chi_{\mathcal{D}}(\beta) \approx \beta^{1-\frac{\mathcal{D}}{2}} \exp(-\Delta\beta) \quad \text{for} \quad 1/\beta \ll \Delta \tag{6.25}$$

of a gapped $\mathcal{D}$-dimensional system with a quadratic dispersion (cf. reference [Troyer *et al.*(1994)] and reference [Bühler(2003)]) follows for the low-temperature behavior of the approximant in a two-dimensional system

$$P_l^k(\beta) \approx -\Delta - \frac{1}{\beta} . \tag{6.26}$$

A finite value of $P_l^k(\beta)$ for $\beta \to \infty$ is only possible for $k = l$. To circumvent this constraint on the possible degrees of the Dlog–Padé approximant we perform an Euler transformation

$$u = \beta/(1+\beta) \quad \Leftrightarrow \quad \beta = u/(1-u) . \tag{6.27}$$

Then, the asymptotic behavior (6.26) yields the two conditions

$$P_l^k(u)\big|_{u=1} = -\Delta \tag{6.28a}$$

$$\frac{\partial}{\partial u} P_l^k(u)\big|_{u=1} = 1 \tag{6.28b}$$

which fix the additional parameters A and B in equation (6.23).

The result[1] is plotted in figure 6.4a and compared to χ_m measured in [emu/g] and

[1] All theory curves rely on the [7,4] Dlog–Padé approximant in $u = \beta/(1+\beta)$. Data from other Dlog–

converted according to

$$\chi(T) = m_{\text{mol}} k_B (g\mu_B)^{-2} N_A^{-1} \chi_m(T) \,. \tag{6.29}$$

Here m_{mol} is the molar mass of IPA-$CuCl_3$, k_B the Boltzmann constant, μ_B the Bohr magneton and N_A the Avogadro constant.

Figure 6.4a illustrates that theory and experiment agree indeed best for $g_A = 2.08$ and the triple of $y = -0.8$. As an asset, we stress that even without the value of g_A, the *position* and the *shape* of the maximum of $\chi(T)$ fits best for the triple of $y = -0.8$ and one can deduce that the g_A-factor is around 2.08. As a caveat, we stress the very weak dependence of $\chi(T)$ on y in a triple tuned to the INS data. By assuming $g_A = 2.08 \pm 0.01$ we estimate the error of our analysis to be $x = 0.42 \pm 0.06$, $y = -0.8 \pm 0.2$ and $z = -0.100 \pm 0.004$ implying $J_1 = -2.3 \pm 0.6$ meV, $J_2 = 1.2 \pm 0.2$ meV, $J_3 = 2.9 \pm 0.1$ meV and $J_4 = -0.292 \pm 0.001$ meV. These values establish the microscopic model for IPA-$CuCl_3$. We highlight that the ferromagnetic coupling J_1 does not dominate over the antiferromagnetic coupling J_3 because $|y| \lessapprox 1$, in contrast to the previous purely $1\mathcal{D}$ analysis [Manaka *et al.*(1997)].

6.2 Quasiparticle decay in IPA-$CuCl_3$

In the previous section 6.1 the magnetic couplings of IPA-$CuCl_3$ were determined. Theory and experiment agree best for $x = J_2/J_3 = 0.42$, $y = J_1/J_3 = -0.8$, $z = J_4/J_3 = -0.1$ and $J_3 = 2.929$ meV. For these couplings we present in the following results for the dynamical structure factor $S^{zz}(Q,\omega)$ along the ladder direction h.

6.2.1 Dynamical structure factors for IPA-$CuCl_3$

Without the interladder interaction J_4, IPA-$CuCl_3$ is described by a one-dimensional AFASHL. For this model dynamical structure factors were calculated in chapter 5. In the following we describe how we incorporate the interladder interaction J_4 to the one-dimensional calculations performed in chapter 5 for the AFASHL.

For $l = 0$ the interladder interaction J_4 reduces the gap of IPA-$CuCl_3$ at $h = 0.5$, see figure 6.3. As a consequence, J_4 also reduces the energy of the two-triplon continuum around $h = 0$ and $l = 0$. In this way, the interladder interaction J_4 supports the SQPD in IPA-$CuCl_3$. In an one-dimensional AFASHL with $x = 0.42$ and $y = -0.8$ decay is hardly noticeable.

Padé approximants, e.g., [9,2], agrees within line width except at very low temperatures.

The gap of IPA-$CuCl_3$ is reduced by J_4 by

$$\Delta_{J_4} = \frac{\sqrt{\Delta^2 + 4b^2} - \sqrt{\Delta^2}}{2} \tag{6.30}$$

with $\Delta = 1.17(1)$meV and $b = 0.67(1)$meV, cf. equation (6.16). By assuming that this reduction is the same within the whole Brillouin zone we can incorporate the two-dimensionality of IPA-$CuCl_3$ to the one-dimensional effective model (6.2) by using a reduced coefficient

$$\left[c^{\text{reduced}}_{H_{1\mathcal{D}}|^1_1}\right]_0 = \left[c_{H_{1\mathcal{D}}|^1_1}\right]_0 - \Delta_{J_4}/J_3 \tag{6.31}$$

for the local terms $t^\dagger_{\alpha,r,s}t_{\alpha,r,s}$. We stress that this represents a simplifying approximation. Thus, to determine the dynamical structure factors of IPA-$CuCl_3$ we calculate an effective Hamiltonian H_{eff} by sCUTs using the generator $G_{\text{gs}}(\ell)$ and the truncation scheme $N_{\text{t}} = 5$, $\mathbf{D} = (12,10,10,6,6,5,5,4,4)$ and $N^O_{\text{t}} = 3$, $\mathbf{D}^O = (10,10,8,8,6,6)$ for $x = 0.42$ and $y = -0.8$. Then we replace the coefficient $\left[c_{H_{1\mathcal{D}}|^1_1}\right]_0$ in the effective model by $\left[c^{\text{reduced}}_{H_{1\mathcal{D}}|^1_1}\right]_0$. Subsequently, we calculate the dynamical structure factor by a Lanczos tridiagonalization, as described in section 4.3.

Figure 6.5 depicts results for the dynamical structure factors $S^{zz}(Q,\omega)$ of IPA-$CuCl_3$ along the ladder direction $Q = 2\pi h$.

In figure 6.5a the inner product **Qb** is set to $\mathbf{Qb} = \pi$ and in figure 6.5b the inner product **Qb** is set to $\mathbf{Qb} = 0$. Results for the dynamical structure factor $S^{zz}(Q,\omega)$, the renormalized one-triplon dispersion (green crosses) and the lowest energy level of $H^{\text{res}}_{\text{eff}}$ (4.40) in the subspace (4.39) (green circles) determined by the generator $G_{\text{gs}}(\ell)$, cf. section 4.3, are shown. In addition, the one triplon dispersion given by equation (6.16) (black line) and the ensuing two-triplon continuum (blue lines in the (Q,ω)-plane) are depicted, cf. reference [Masuda *et al.*(2006)].

On the whole, the one-dimensional approach which incorporates the two-dimensionality of IPA-$CuCl_3$ by equation (6.31) only leads to very good results for the one-triplon dispersion where the excitations are stable, cf. black line and green crosses in figure 6.5. Additionally, the lowest energy level of $H^{\text{res}}_{\text{eff}}$ (4.40) in the subspace (4.39) (green circles) are very close to the minimum of the two-triplon continuum (lower blue line in the (Q,ω)-plane) so that the missing self-consistency (cf. section 4.2.2) of the results plays a minor role. Thus, our approach for the dynamical structure factor seems to yield reliable results.

In figure 6.5a the decay of the excitations is clearly visible. For momenta $Q \lessapprox 0.3\pi$ no marked peaks can be observed. Interestingly, for $\mathbf{Qb} = 0$ marked peaks can be observed in the region around $Q \approx 0.3\pi$ close to the lower edge of the two-triplon continuum, cf. figure 6.5b. Nevertheless, the intensity of these peaks is very small compared to the

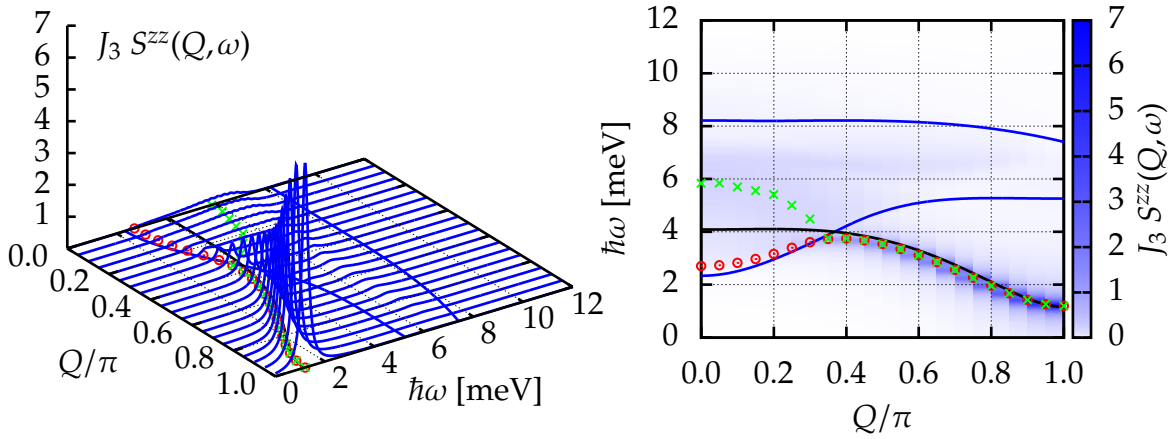

(a) Qb = π, number of Lanczos steps $n = 70$

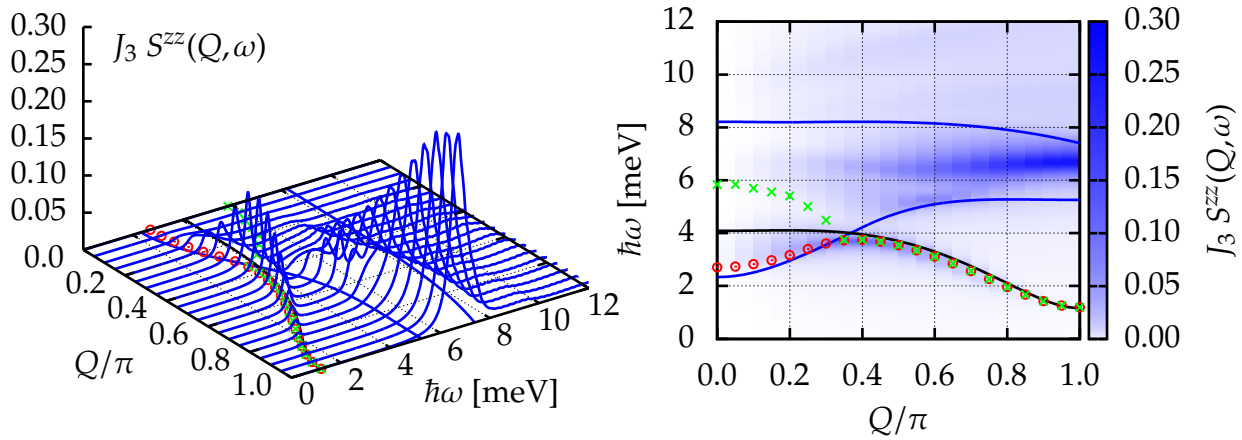

(b) Qb = 0, number of Lanczos steps $n = 70$

Figure 6.5: Dynamical structure factor $S^{zz}(Q,\omega)$ of IPA-CuCl$_3$ calculated by using the generator $G_{\text{gs}}(\ell)$ and Lanczos tridiagonalization as described in the text (broadening: $\delta = 0.05$). The solid black line depicts the one-triplon dispersion and blue lines in the (Q,ω)-plane depict the borders of the two-triplon continuum given by equation (6.16), cf. reference [Masuda *et al.*(2006)]. Green crosses depict the renormalized one-triplon dispersion obtained by the generator $G_{\text{gs}}(\ell)$ and equation (4.47). Red circles depict the lowest energy level obtained by a diagonalization in the subspace (4.39).

intensity of the peaks occurring for **Qb** = π for $Q \gtrapprox 0.3\pi$, see figure 6.5a. Most of the spectral weight for **Qb** = 0 is gathered inside the two-triplon continuum for momenta $Q \gtrapprox 0.4\pi$, see figure 6.5b.

6.2.2 Equal-time structure factors $S^{zz}(Q)$ and spectral weights

In figure 6.6 the equal-time structure factor $S^{zz}(Q)$ of IPA-$CuCl_3$ is depicted for **Qb** = π (dashed line) and for **Qb** = 0 (dotted line). The solid line depicts the sum of the equal-

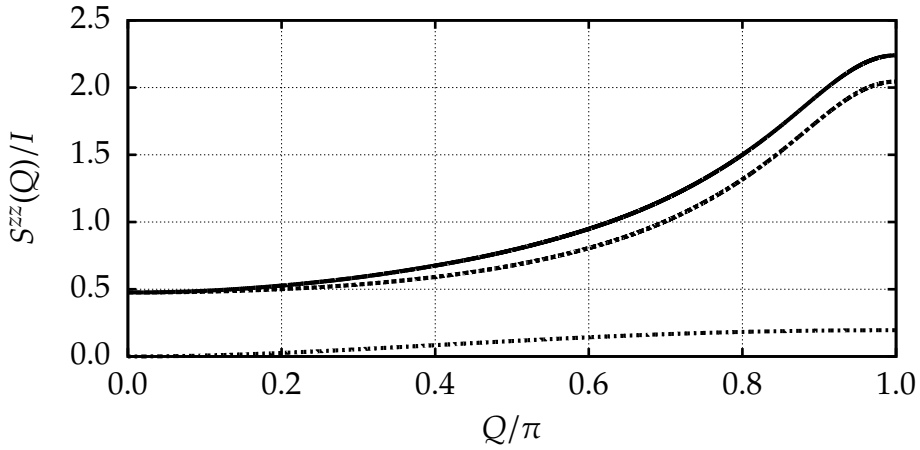

Figure 6.6: Equal-time structure factor $S^{zz}(Q)$ normalized to the total spectral weight I of IPA-$CuCl_3$. Dashed line indicates $S^{zz}(Q)$ for **Qb** = π, dotted line indicates $S^{zz}(Q)$ for **Qb** = 0 and solid line indicates the sum of the two structure factors.

time structure factor $S^{zz}(Q)$ for **Qb** = π and **Qb** = 0.

Most of the spectral weight is distributed in the channel with **Qb** = π. For **Qb** = 0 and **Qb** = π the equal-time structure factor $S^{zz}(Q)$ increases with the momentum Q.

The relative spectral weights $I^{\mathrm{rel}}\big|_{\mathbf{Qb}} := I\big|_{\mathbf{Qb}}/I$ for **Qb** = π and **Qb** = 0 are

$$I^{\mathrm{rel}}\big|_{\mathbf{Qb}=\pi} = 0.89353 \tag{6.32a}$$

$$I^{\mathrm{rel}}\big|_{\mathbf{Qb}=0} = 0.10672\,. \tag{6.32b}$$

The sum rule (F.13) is fulfilled to high accuracy ($I^{\mathrm{rel}}\big|_{\mathbf{Qb}=\pi} + I^{\mathrm{rel}}\big|_{\mathbf{Qb}=0} = 1.00025$) which indicates that for the transformed local spin operator $S_i^z(r)$ the restriction to the subspace 4.39 is again justified.

6.2.3 Quasiparticle lifetime

Figure 6.7 shows the inverse lifetime, respectively the width $\gamma(Q)$ determined from the imaginary part of the self-energy, of IPA-$CuCl_3$ in the **Qb** = π channel. As described in the previous sections 4.3.2 and 5.1.2 we use a terminated continued fraction

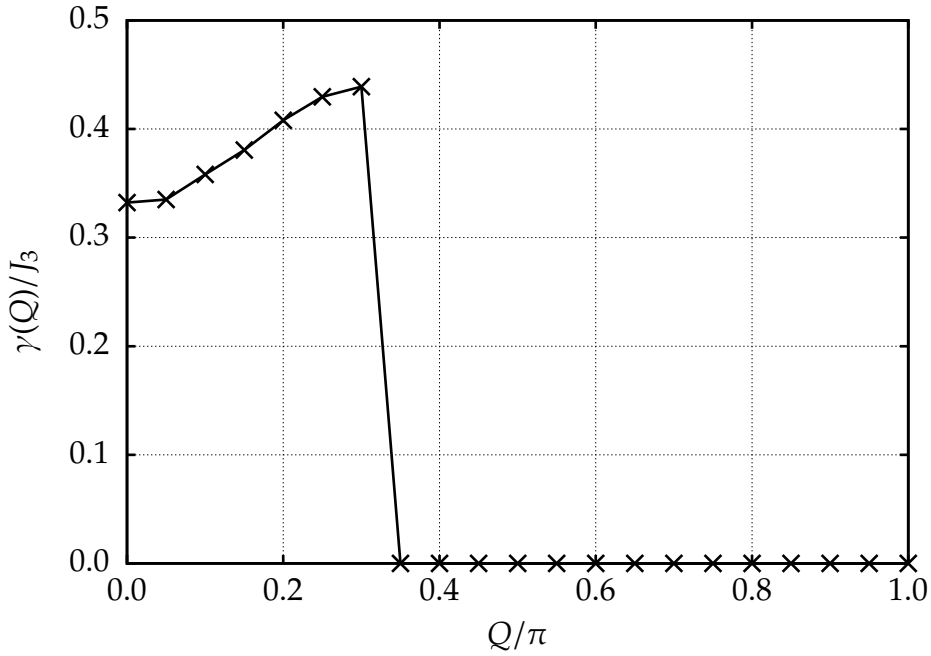

Figure 6.7: Width $\gamma(Q)$ of IPA-$CuCl_3$ for $\mathbf{Qb} = \pi$. For $Q \lessapprox 0.3\pi$ the triplons decay.

representation of the self-energy $\Sigma(Q,\omega)$ (4.49) to determine the width $\gamma(Q)$ (4.50) of the renormalized quasiparticles indicated by green crosses in figure 6.5. Details of the termination of the continued fractions are given in appendix A.2.

We draw the reader's attention to the fact, that the widths appearing in IPA-$CuCl_3$, see figure 6.7, exceed all widths occurring in the previously discussed models, cf. figure 4.23 and figure 5.9, due to the small coupling x and relatively large coupling y. Additionally, the two-dimensionality of IPA-$CuCl_3$ supports the decay by reducing the gap, see equation (6.30).

6.2.4 Comparison with experimental data

Masuda *et al.* performed INS experiments along the ladder direction $\mathbf{Q} = (2\pi h, 0, 0)$ [Masuda *et al.*(2006)]. Therefore, the effective Fourier transformed spin operator $S^z_{\text{eff}}(Q)$ appearing in the dynamical structure factor (cf. equation (4.43)) is given by

$$S^z(Q) = \frac{e^{iQ\frac{b}{2}}}{\sqrt{2}}\left(e^{-iQ\frac{b}{2}}\, S^z_{1,\text{eff}}(Q) + e^{iQ\frac{b}{2}}\, S^z_{2,\text{eff}}(Q)\right), \tag{6.33}$$

cf. equation (F.14), where b is the projection of the vector $\mathbf{b}$ in ladder direction $\mathbf{Q}$. The vector $\mathbf{b}$ defining the ladder rungs is given by

$$\mathbf{b} = \mathbf{d} - \mathbf{a}\,, \tag{6.34}$$

cf. figure 6.1 and figure 5.1, with **d** given by[2] **d** = (0.0854, 0.1316, −0.4432) [Masuda *et al.*(2006)]. Thus b in equation (6.33) is given by

$$b = 0.0854 - 1.0000 = -0.9146 \tag{6.35}$$

in units of **a**. Note, that equation (6.33) is *not* 2π-symmetric in Q due to the appearance of the product Qb. As a consequence the results for the dynamical structure factor $S^{zz}(Q,\omega)$ are *not* identical in different branches of the Brillouin zone. Except for the use of equation (6.33) instead of equation (F.14) for a fixed inner product **Qb** all calculations in this section are performed in the same way as in section 6.2.1 and in section 6.2.2.

Dynamical structure factors for IPA-$CuCl_3$

Figure 6.8 depicts INS data [Masuda *et al.*(2006)]. In figure 6.9 the corresponding theoretical results for the dynamical structure factor $S^{zz}(Q,\omega)$ are shown.

Theory and experiment coincide to a great extent. Peak positions, weights and the abrupt disappearance of the triplon branch are excellently captured by the microscopic model (6.1) for $J_1 = -2.3$ meV, $J_2 = 1.2$ meV, $J_3 = 2.9$ meV and $J_4 = -0.292$ meV.

The most distinct deviations appear close to the merging point. For example, the position of the maximum of $S^{zz}(Q,\omega)$ for $\mathbf{Q} = (1.2\pi, 0, 0)$ and $\mathbf{Q} = (1.15\pi, 0, 0)$ differs from the experimental data. These deviations might be caused by the missing self-consistency or by the only rough consideration of the interladder interaction J_4 in the calculations for the dynamical structure factor $S^{zz}(Q,\omega)$. Interestingly, for $\mathbf{Q} = (1.5\pi, 0, 0)$ a small second peak appears around $\hbar\omega \approx 6.7$ meV, cf. figure 6.10. Unfortunately, Masuda *et al.* have not presented any data for these higher energies [Masuda *et al.*(2006)].

Equal-time structure factor $S^{zz}(Q)$ and spectral weight

Figure 6.11 shows the measured h dependence of the equal-time structure factor in IPA-$CuCl_3$. In figure 6.12 the corresponding theoretical results for the equal-time structure factor $S^{zz}(Q)$ normalized to the total spectral weight I are depicted. For $b = -0.9146$ the equal-time structure factor $S^{zz}(Q)$ vanishes for

$$h = \frac{Q}{2\pi} = \frac{n}{b} \quad \text{with} \quad n \in \mathbb{Z}, \tag{6.36}$$

see figure 6.12. This follows directly from equation 6.33. If $Q/2\pi = n/b$, the Fourier transformed spin operator $S^z(Q)$ is proportional to the operator of the total spin in

[2] Actually, Masuda *et al.* state **d** = (−0.0854, −0.1316, 0.4432). But this sign of the vector **d** is not consistent with their own figure depicting the structure of IPA-$CuCl_3$ while **d** = (0.0854, 0.1316, −0.4432) is, see [Masuda *et al.*(2006)].

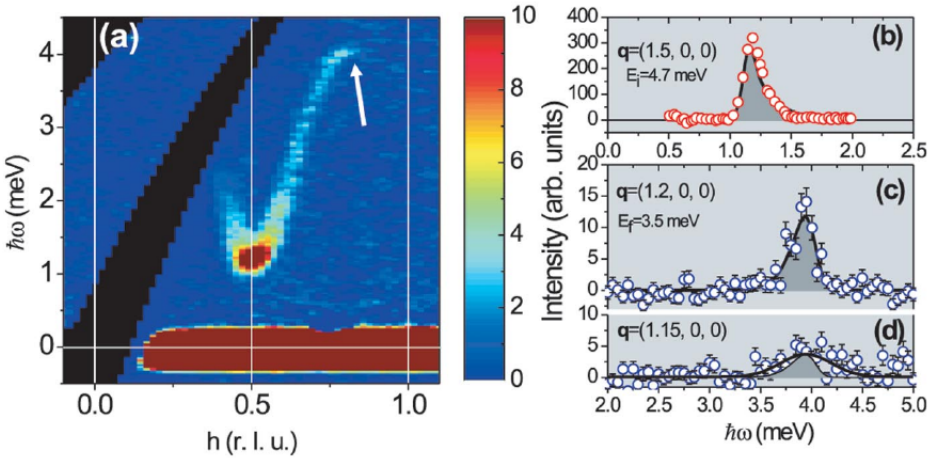

Figure 6.8: Time-of-flight **(a)** and 3-axis **(b)**, **(c)**, **(d)** inelastic neutron data measured in IPA-CuCl$_3$ at $T = 1.5$K. In **(b)**, **(c)**, **(d)** the shaded areas are calculated peak shapes due to resolution. (Figure and caption are taken from reference [Masuda *et al.*(2006)]).

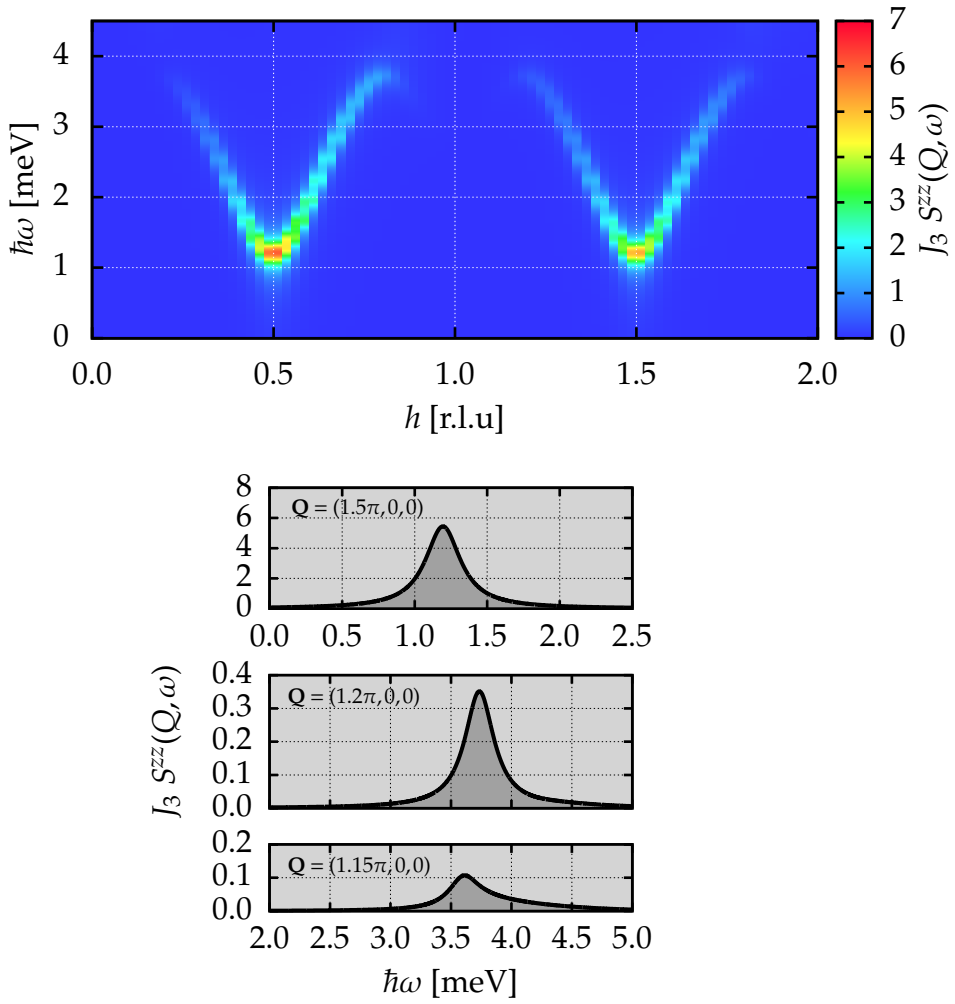

Figure 6.9: Dynamical structure factor $S^{zz}(Q,\omega)$ of IPA-CuCl$_3$ for $b = -0.9146$ calculated by using the generator $G_{gs}(\ell)$ and Lanczos tridiagonalization as described in the text (broadening: $\delta = 0.05$).

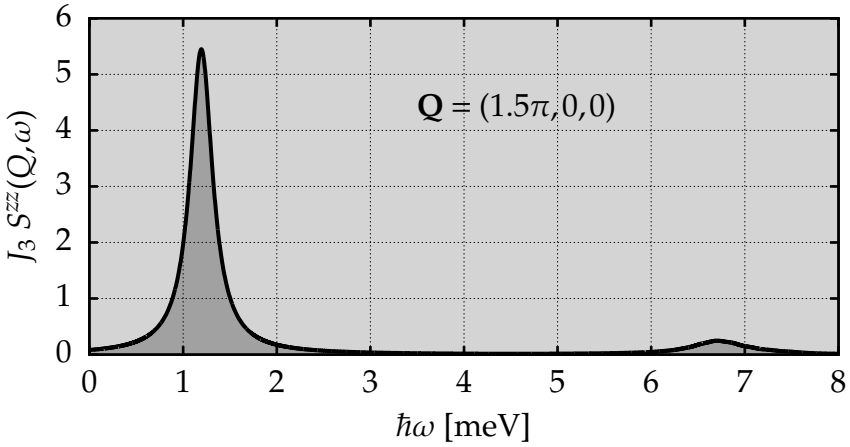

Figure 6.10: Dynamical structure factor $S^{zz}(Q,\omega)$ of IPA-CuCl$_3$ for $b = -0.9146$ and $\mathbf{Q} = (1.5\pi, 0, 0)$ calculated by using the generator $G_{gs}(\ell)$ and Lanczos tridiagonalization as described in the text (broadening: $\delta = 0.05$). Around $\hbar\omega = 6.7$ a small second peak appears.

z-direction

$$S^z_{\text{total}} = \sum_{r,s} \left(S^z_1(r,s) + S^z_2(r,s) \right) . \tag{6.37}$$

Applying this operator to the ground state, given by a spin singlet state, yields zero. Thus the disappearance of the signal for $b = -0.9146$ close to $Q/2\pi = n/b$ is supported by static properties. It is not necessarily a result of the dynamics induced by the Hamiltonian, i.e., the decay vertices. Therefore, it is more meaningful to study the decay for a fixed inner product $\mathbf{Qb} = \pi$ as done in section 6.2.1 till section 6.2.3.

Another consequence of $b = -0.9146$ is that the equal-time structure factor $S^{zz}(Q)$ is no longer symmetric about reflection at $Q/\pi = 2h = n$ for $n \in \mathbb{Z}$, see figure 6.5. Unfortunately, not enough experimental data is available to observe these asymmetries, cf. figure 6.11. Note, that also contributions from higher energies can influence the equal-time structure factor $S^{zz}(Q)$, e.g. the peak occurring for $Q = (1.5\pi, 0, 0)$ around $\omega \approx 6.7$, cf. figure 6.10.

The relative spectral weight I^{rel} is equal to $I^{\text{rel}} = 0.7073$ for $h \in [0,1]$ and equal to $I^{\text{rel}} = 0.6580$ for $h \in [1,2]$.

6.3 IPA-CuCl$_3$ in a magnetic field

Generically, the phase diagram of a gapped quantum-disordered antiferromagnet in an external magnetic field exhibits three different phases. For magnetic fields smaller than a critical magnetic field H_{c_1} , determined by the gap, the systems remains in a gapped

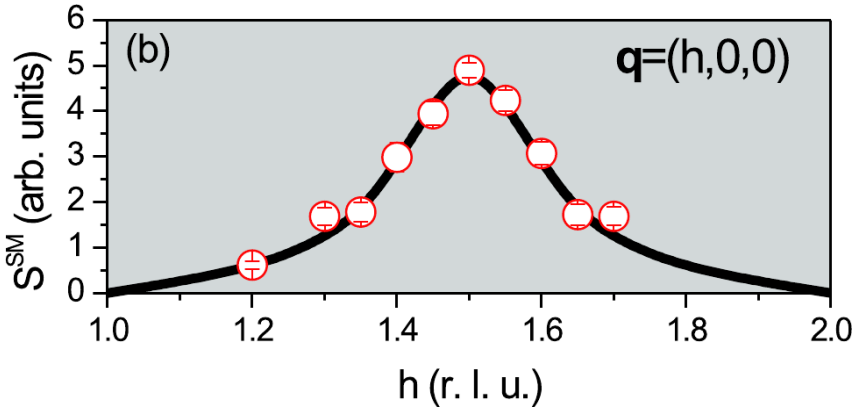

Figure 6.11: Measured h dependence of single-triplon excitation intensities in IPA-$CuCl_3$ (symbols). Solid line depicts a simulation, described in reference [Masuda *et al.*(2006)] (Figure is taken from reference [Masuda *et al.*(2006)]).

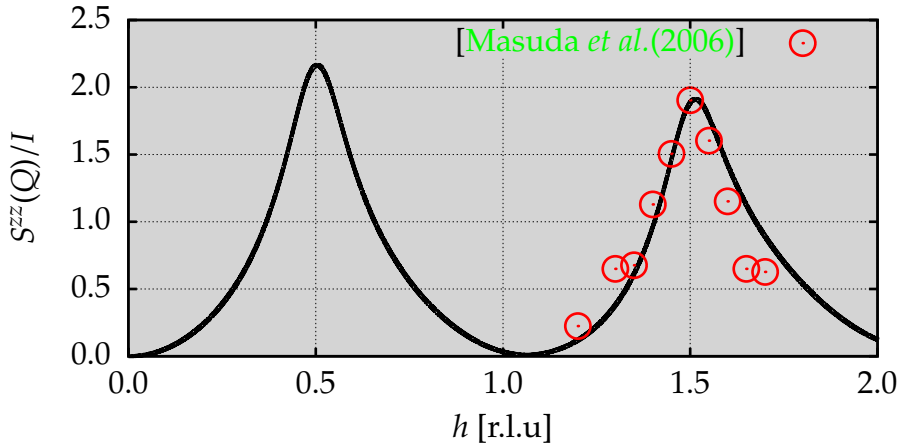

Figure 6.12: Equal-time structure factor $S^{zz}(Q)$ normalized to the total spectral weight I of IPA-$CuCl_3$ for $b = -0.9146$. Red circles are INS data [Masuda *et al.*(2006)] scaled by a factor 0.38.

disordered phase. If the magnetic field exceeds the critical value H_{c_1} a BEC occurs characterized by a long-range antiferromagnetically ordered gapless phase. Further increasing the magnetic field beyond a upper critical magnetic field H_{c_2} leads again to a gapped phase, which is fully polarized.

To describe BEC in IPA-$CuCl_3$ we follow the bond-operator approach used in the references [Sommer *et al.*(2001), Matsumoto *et al.*(2002), Matsumoto *et al.*(2004)]. With this approach Matsumoto *et al.* successfully described the BEC occurring in $TlCuCl_3$. But this approach to spin-dimer systems is quantitatively reliable only as long as the inter-dimer couplings J_{inter} are significantly smaller than the dimer coupling J_{dimer}, cf. $|J_{\text{inter}}| < J_{\text{dimer}}/2$ [Normand & Rüegg(2011)]. This limit requires $|J_i| < J_3/2$ for $i \in \{1,2,4\}$ which does not hold for IPA-$CuCl_3$, see table 6.1 and reference [Manaka *et al.*(1997)]. Thus we do *not* start with the original spin model, as in previous work [Sommer *et al.*(2001), Matsumoto *et al.*(2002), Matsumoto *et al.*(2004)], but with the effective bilinear model $H^{\text{bilinear}}_{\text{IPA-CuCl}_3,\text{eff}}$ (6.8) in real space obtained by the generator $G_{\text{gs,1p}}(\ell)$.

In the presence of an external magnetic field in z-direction

$$H_h = -h \sum_{\mathbf{r}} \left(S^z_1(\mathbf{r}) + S^z_2(\mathbf{r}) \right) \tag{6.38}$$

($\mathbf{r} = (r,s)$) the bond operator $t^\dagger_{+,\mathbf{r}}$, $t^\dagger_{-,\mathbf{r}}$ and $t^\dagger_{0,\mathbf{r}}$ defined by

$$t^\dagger_{x,\mathbf{r}} = \frac{1}{\sqrt{2}} \left(t^\dagger_{+,\mathbf{r}} + t^\dagger_{-,\mathbf{r}} \right) \tag{6.39a}$$

$$t^\dagger_{y,\mathbf{r}} = \frac{-\mathrm{i}}{\sqrt{2}} \left(t^\dagger_{+,\mathbf{r}} - t^\dagger_{-,\mathbf{r}} \right) \tag{6.39b}$$

$$t^\dagger_{x,\mathbf{r}} = t^\dagger_{0,\mathbf{r}} \,. \tag{6.39c}$$

are commonly used, cf. appendix C. For the external field H_h (6.38) follows

$$H_h = \mathrm{i}h \sum_{\mathbf{r}} \left(t^\dagger_{x,\mathbf{r}} t_{y,\mathbf{r}} - t^\dagger_{y,\mathbf{r}} t_{x,\mathbf{r}} \right) \tag{6.40a}$$

$$= -h \sum_{\mathbf{r}} \left(t^\dagger_{+,\mathbf{r}} t_{+,\mathbf{r}} - t^\dagger_{-,\mathbf{r}} t_{-,\mathbf{r}} \right) \tag{6.40b}$$

Then the effective bilinear model $H^{\text{bilinear}}_{\text{IPA-CuCl}_3,\text{eff}}$ (6.8) is given by

$$\begin{aligned} H^{\text{bilinear}}_{\text{IPA-CuCl}_3,\text{eff}} = J_3 \sum_{r,s} \sum_{m} \sum_{d} \left[c_{H_{1\mathcal{D}}|^1_1}\right]_d t^\dagger_{m,r,s} t_{m,r+d,s} \\ + J_4 \sum_{r,s} \sum_{\delta,\delta'} \sum_{m} \left[c_{S^m_1|^1_0}\right]^\delta \left[c_{S^m_2|^1_0}\right]^{\delta'} \left[t^\dagger_{m,r,s}\left(t^\dagger_{\overline{m},r+1+(\delta'-\delta),s+1} + t_{m,r+1+(\delta'-\delta),s+1}\right) + \text{H.c.}\right] \\ - h \sum_{r,s} \left(t^\dagger_{+,r,s} t_{+,r,s} - t^\dagger_{-,r,s} t_{-,r,s}\right) \end{aligned} \tag{6.41}$$

where $\overline{m} = -m$.

Following reference [Sommer *et al.*(2001)] and references [Matsumoto *et al.*(2002), Matsumoto *et al.*(2004)] we perform the local transformation

$$|\tilde{s}_{\mathbf{r}}\rangle = u\,|s_{\mathbf{r}}\rangle + v e^{i\mathbf{Q}_0\mathbf{r}}\left(f\,|t_{+,\mathbf{r}}\rangle + g\,|t_{-,\mathbf{r}}\rangle\right) \tag{6.42a}$$

$$|\tilde{t}_{+,\mathbf{r}}\rangle = u\left(f\,|t_{+,\mathbf{r}}\rangle + g\,|t_{-,\mathbf{r}}\rangle\right) - v e^{i\mathbf{Q}_0\mathbf{r}}\,|s_{\mathbf{r}}\rangle \tag{6.42b}$$

$$|\tilde{t}_{0,\mathbf{r}}\rangle = |t_{0,\mathbf{r}}\rangle \tag{6.42c}$$

$$|\tilde{t}_{-,\mathbf{r}}\rangle = f\,|t_{-,\mathbf{r}}\rangle - g\,|t_{+,\mathbf{r}}\rangle \tag{6.42d}$$

in real space with $u = \cos(\theta)$, $v = \sin(\theta)$, $f = \cos(\varphi)$ and $g = \sin(\varphi)$, the position $\mathbf{r} = (r,s)$ and the wave vector $\mathbf{Q}_0 = (\pi, 0)$ of the minimum of the dispersion. The two independent variables θ and φ are varied to minimize the classical ground state energy. This choice also ensures that firstly all linear terms in the triplon operators vanish and secondly a massless Goldstone mode appears at a critical magnetic field H_{c_1} as it has to be if a continuous symmetry is spontaneously broken. For details of the calculations, see appendix G.

Fourier transformation and Bogoliubov diagonalization of the resulting bilinear terms finally provides the lowest lying modes. Their resulting gap energies are displayed in figure 6.13. *No* parameters are adjusted.

Second, the upper critical field H_{c_2} can be determined exactly for the spin model (6.1) to be $H_{c_2} = (2J_2 + J_3)/(g\mu_B) \approx 2/g \cdot 45.8$ T. After the transformation (6.42) is applied to the dispersion obtained from sCUT we obtain $H_{c_2} \approx 2/g \cdot 45.1$ T. The very good agreement of these two values strongly supports the approximations made. Additionally, the theoretical values also match the experimental result [Manaka *et al.*(2008)] $H_{c_2} = (43.9 \pm 0.1)$ T$(2/g)$ within 4%. In view of the neglect of anisotropies and magneto-elastic effects, cf. reference [Johannsen *et al.*(2005)], this nice agreement lends independent support to the advocated microscopic model.

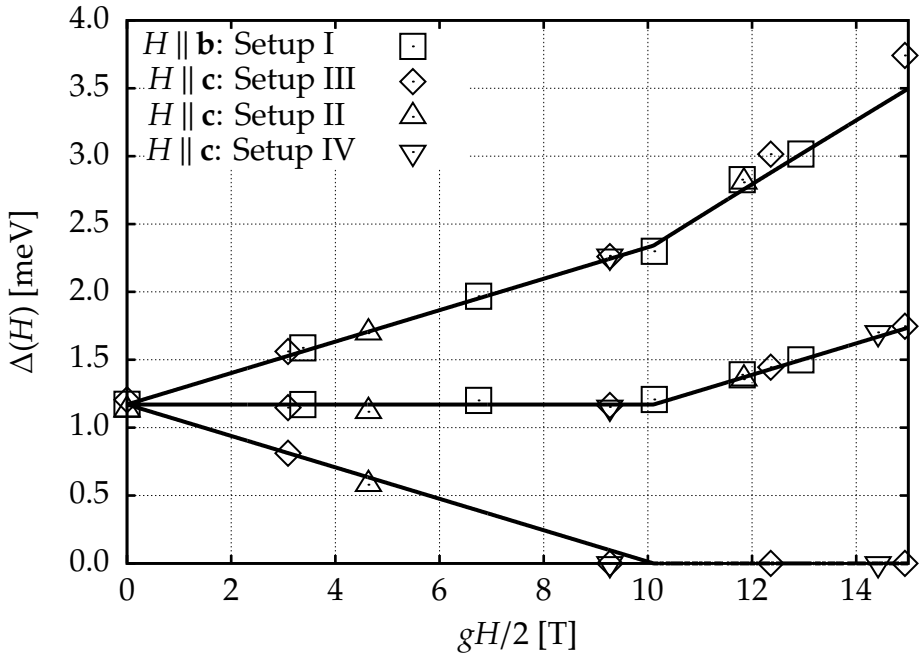

Figure 6.13: Gaps in IPA-$CuCl_3$ vs. the reduced magnetic field $gH/2$. Solid lines show theoretical results, see text. Symbols mark experimental data from references [Zheludev *et al.*(2007)] (Setup I & IV) and [Garlea *et al.*(2007)] (Setup II & III).

6.4 Temperature dependence of the spin gap

Finally, we discuss the temperature dependence of the gap $\Delta(T)$ as test for our microscopic model. To calculate the temperature dependence of the effective low-energy model obtained by continuous unitary transformations (CUTs) we apply the mean-field approach in reference [Exius *et al.*(2010)] which is based on the mean-field approach used by [Sachdev & Bhatt(1990), Troyer *et al.*(1994), Rüegg *et al.*(2005), Normand & Rüegg(2011)] to $H^{\text{bilinear}}_{\text{IPA-CuCl}_3,\text{eff}}$ (6.8). In each nonlocal term ($t^\dagger_{m,\mathbf{r}} t_{m,\mathbf{r}'}$ or $t^\dagger_{m,\mathbf{r}} t^\dagger_{-m,\mathbf{r}'}$ or $t_{m,\mathbf{r}} t_{-m,\mathbf{r}'}$ with $\mathbf{r} \neq \mathbf{r}'$) all creation operators $t^\dagger_{m,\mathbf{r}}$ are multiplied by the singlet annihilation $s_\mathbf{r}$ and the annihilation operators $t_{m,\mathbf{r}}$ by the singlet creation $s^\dagger_\mathbf{r}$. Local terms remain unchanged because they do not change the local singlet number. Finally all singlet operators are replaced by the condensate value $s(T) = \langle s^\dagger \rangle = \langle s \rangle$ with $s \in [0,1]$. In a nutshell, a factor s^2 appears in front of each nonlocal term. This is a way to account for the hard-core property at finite temperature.

This implies a dependence of the dispersion on s and hence on temperature [Troyer *et al.*(1994), Exius *et al.*(2010), Normand & Rüegg(2011)], denoted by $\omega_{s(T)}(h,l)$. The self-consistent solution is found from the hard-core condition

$$1 = \left\langle s^\dagger_\mathbf{r} s_\mathbf{r} + \sum_m t^\dagger_{m,\mathbf{r}} t_{m,\mathbf{r}} \right\rangle \tag{6.43}$$

leading to

$$s^2(T) = 1 - 3z/(1+3z) \tag{6.44}$$

with

$$z = \int_{-1/2}^{1/2} \mathrm{d}h \int_{-1/2}^{1/2} \mathrm{d}l \, \mathrm{e}^{-\beta\omega_{s(T)}(h,l)} \,, \tag{6.45}$$

see [Troyer *et al.*(1994)]. Figure 6.14 compares the result (solid line) of this simple approximation to INS data [Zheludev *et al.*(2008), Náfrádi *et al.*(2011)]. Up to 15 K

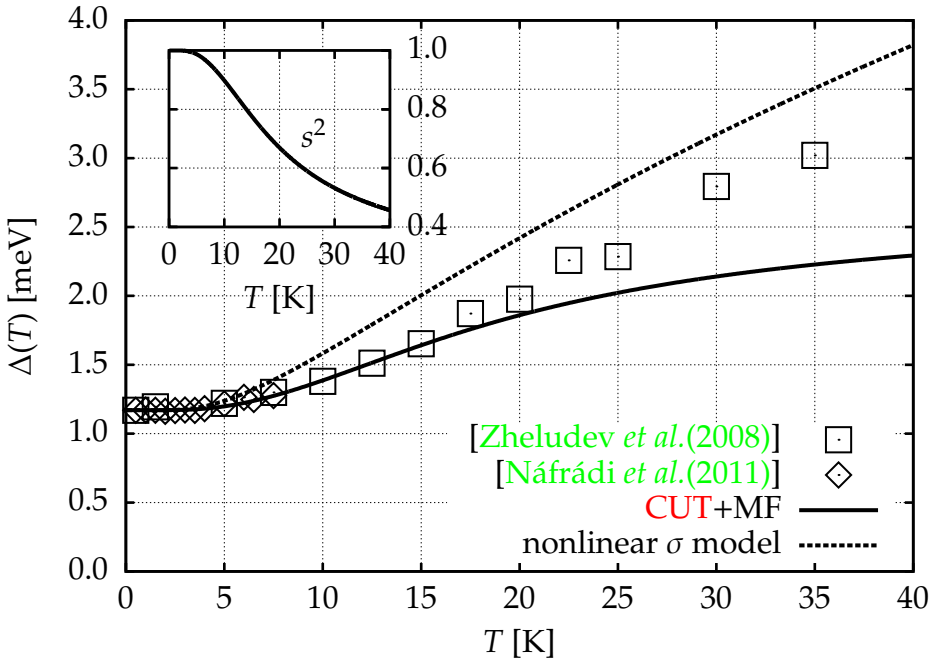

Figure 6.14: Spin gap in IPA-$CuCl_3$ vs. temperature T. Lines show theoretical results from CUTs and finite-temperature mean-field (solid line) and from the nonlinear σ model (dashed line), respectively. Inset: Temperature dependence of the condensate fraction s^2.

the experimental data is matched perfectly. We attribute the discrepancy at higher temperatures to the insufficient treatment of the hard-core constraint by the above approach (for 15 K the condensate fraction s^2 is only 0.77). Note that we only apply the mean-field theory to the dispersion obtained from sCUT, not to the original spin model as done previously [Rüegg *et al.*(2005), Normand & Rüegg(2011)] because IPA-$CuCl_3$ is not far enough in the dimer limit. The results follow directly from the effective low-energy model $H^{\text{bilinear}}_{\text{IPA-CuCl}_3,\text{eff}}$ (6.8) at $T = 0$ with $x = J_2/J_3 = 0.42$, $y = J_1/J_3 = -0.8$, $z = J_4/J_3 = -0.1$ and $J_3 = 2.929$ meV. *No* additional parameters were adjusted.

For comparison, we also include $\Delta(T)$ as derived from the nonlinear σ model on

one-loop level [Sénéchal(1993)] in figure 6.14 (dashed line). It is obtained from

$$C = \int_{-1/2}^{1/2} \mathrm{d}h \int_{-1/2}^{1/2} \mathrm{d}l \, \frac{\coth(\beta\omega(h,l,T)/2)}{\omega(h,l,T)} \tag{6.46}$$

with

$$\omega(h,l,T) := \sqrt{\omega^2(h,l) + \Delta^2(T) - \Delta^2(0)} \, . \tag{6.47}$$

The constant C is determined for $T = 0$. Interestingly, this approach describes the experimental data less accurately if the experimental dispersion at $T = 0$ is used for $\omega(h,l)$ (6.16), cf. reference [Náfrádi *et al.*(2011)]. We presume that the hard-core constraint is not accounted for sufficiently well by equation (6.46).

6.5 Chapter summary

In this chapter we showed that the available experimental evidence for isopropylammonium trichlorocuprate(II) $(CH_3)_2CHNH_3CuCl_3$ (IPA-$CuCl_3$) is consistent with a quantitative model of weakly coupled asymmetric ferro-antiferromagnetic spin $S = 1/2$ Heisenberg ladders (AFASHLs) with hard-core triplons as excitations. The magnetic couplings in IPA-$CuCl_3$ were determined by an analysis of inelastic neutron scattering (INS) data and of the temperature dependence of the magnetic susceptibility based on self-similar continuous unitary transformations (sCUTs) and high temperature series expansions (HTSEs), respectively. The magnetic couplings describing IPA-$CuCl_3$ best are $J_1 \approx -2.3$ meV, $J_2 \approx 1.2$ meV, $J_3 \approx 2.9$ meV and $J_4 \approx -0.3$ meV.

Based on the determined microscopic model for IPA-$CuCl_3$ we used sCUTs based on the generator $G_{\mathrm{gs}}(\ell)$ introduced in chapter 3 to describe the quasiparticle decay in IPA-$CuCl_3$. The theoretical results agree very well with the experimental data, leading further support for the advocated microscopic model.

The derived microscopic model also passes three additional checks. Firstly, the BEC of the energetically lowest modes is well described. Secondly, the upper critical field H_{c_2} agrees to experimental data and, finally, the temperature dependence of the spin gap matches recent data from spin-echo neutron scattering.

Concomitantly, we exemplarily showed how CUT results in one dimension at zero temperature and zero magnetic field can be extended to render a quantitative description in two dimensions at finite temperature and finite magnetic field possible.

Chapter 7

Summary & Outlook

7.1 Summary

In this section the results of the present thesis are summarized. It is divided into three parts: (i) Physical aspects concerning spontaneous quasiparticle decay (SQPD) in dimerized quantum antiferromagnets. (ii) Methodical aspects concerning continuous unitary transformations (CUTs) in systems with SQPD and (iii) their applications in low-dimensional spin systems.

7.1.1 Spontaneous quasiparticle decay

The first part of this thesis consists of an introduction to SQPD in dimerized quantum antiferromagnets. For a sufficiently large dimerization the elementary excitations are given by gapped spin $S = 1$ triplon quasiparticles. Although these triplons are protected by a gap at low energies they may decay spontaneously at temperature $T = 0$ into two or more triplons at higher energies. Such a SQPD can only occur in systems which fulfill two conditions. Firstly, the one-triplon dispersion and the two-triplon continuum have to overlap and, secondly, decay processes have to exist enabling a single triplon to decay into the continuum.

The introduction to SQPD in dimerized quantum antiferromagnets is given on the basis of an one-dimensional bosonic toy model which fulfills the two conditions mentioned above. A nice feature of the discussed toy model is that its self-energy can be calculated analytically in leading order. Therefore, the SQPD occurring in that model can be discussed in detail.

Interestingly, the SQPD in the model can not be described by adapting the concepts commonly used in Fermi liquids based on Lorentzian excitations. For example, close to the merging point of the one-particle dispersion and the two-particle continuum the width of the excitations inside the continuum is *always* arbitrarily large compared to the distance to the lower edge of the continuum. This is in marked contrast to a standard

FERMI liquid where the quasiparticles become better and better defined by approaching the FERMI surface. In addition, using the usual formula to determine the quasiparticle weight *always* leads to weights larger than one which is physically meaningless. In this sense the quasiparticle concept breaks down. Nevertheless, the vicinity of a resonance, but not its tails, inside the continuum is well described by a LORENTZIAN, i.e. by the real part of the self-energy.

Furthermore, we discussed the influence of two-particle interactions and next-nearest-neighbor hopping on the SQPD. Level repulsion between the one-particle branch and the two-particle bound state occurs if the two-particle interaction is large enough to produce a bound state in the region of the BRILLOUIN zone where the one-particle dispersion would merges with the two-particle continuum. As a result, at first the two-particle bound state merges with the two-particle continuum and starts to decay while the one-particle branch is pushed below the lower edge of the continuum. Whether the one-particle branch is stable in the whole BRILLOUIN zone or merges with the continuum at a small momentum and ceases to exist depends on the strength of the two-particle interaction.

Next-nearest-neighbor hopping can lead to stable excitation within the whole BRILLOUIN zone. In the model discussed this is the case when the next-nearest-neighbor hopping shifts the minimum of the one-particle dispersion to momenta $Q < \pi$.

7.1.2 Method: Continuous unitary transformations

The main topic of the present thesis is how to describe SQPD by means of CUTs. In general CUTs are used to derive effective low-energy models in a systematic way. By introducing a continuous auxiliary variable a flow equation for the Hamiltonian is derived. The right side of the differential equation is given by a commutator of a generator and the Hamiltonian itself. Then the crucial point is to choose a generator which simplifies the initial Hamiltonian reliably.

The starting point to describe SQPD in the framework of CUTs is a well-established and frequently used generator which generates quasiparticle conserving effective Hamiltonians. Although this generator exhibits many favorable properties there are two drawbacks if one wants to describe systems with unstable quasiparticles. Firstly, the generator interprets the energetically lowest states above the ground state as the elementary excitations. In systems with SQPD this might result in a misleading quasiparticle picture since states with very low or zero spectral weight are regarded as the elementary excitations. Additionally, the rearrangement during the flow, which generates this misleading quasiparticle picture, causes convergence problems in practice. Secondly, by construction the generator produces an effective Hamiltonian with stable excitations. All information about decay is stored in the transformation.

This makes an additional transformation of observables indispensable.

To circumvent these disadvantages a new generator is introduced here. This adapted generator leads to an effective Hamiltonian formulated in second quantization where only the ground state is completely decoupled. The effective Hamiltonian still contains information about the decay. A significant advantage of the adapted generator is that even in the case of unstable quasiparticles it yields a robust flow. As a concomitant caveat, the analysis of the effective model is more difficult, which is a consequence of the more involved physics one wants to describe.

To illustrate our general considerations about the description of SQPD by CUTs we perform self-similar continuous unitary transformations (sCUTs) on the model of asymmetric spin $S = 1/2$ Heisenberg ladders. Thereby, the concept of sCUTs is illustrated in detail.

7.1.3 Applications: Spontaneous quasiparticle decay in low-dimensional spin systems

Asymmetric spin ladders

Not the least because of their relation to high-temperature superconductivity symmetric antiferromagnetic spin $S = 1/2$ Heisenberg ladders are widely studied by many different approaches including CUTs. In symmetric ladders the reflection symmetry about the centerline implies stable excitations. By adding an additional interaction this symmetry can be broken, which induces SQPD.

Starting with the symmetric ladder we illustrate the calculation of the low-energy spectrum by sCUTs. By opposing the symmetric and asymmetric case we illustrate our former general considerations about the description of SQPD by means of CUTs. We perform tridiagonalizations in momentum space to calculate spectral densities of the effective models generated by CUTs adapted for SQPD. States which consist of up to three quasiparticles are considered. In particular, the dynamical structure factors are calculated to make a direct comparison with inelastic neutron scattering (INS) data possible. This makes an additional CUT of observables necessary.

For the case of an asymmetric antiferromagnetic spin $S = 1/2$ Heisenberg ladder (AASHL) SQPD is found, but it remains weak because for larger antiferromagnetic diagonal coupling the triplon mode drops below the continuum preventing decay. Much larger SQPD occurs in asymmetric ferro-antiferromagnetic spin $S = 1/2$ Heisenberg ladders (AFASHLs). Here the symmetry breaking coupling is ferromagnetic which prevents the decrease of the mobility of the quasiparticles. Hence for larger values of the symmetry breaking coupling still SQPD occurs and it is significant.

The SQPD in AASHLs as well as in AFASHLs is influenced by two-particle interactions. Results for the dynamical structure factor support the scenario of level repulsion

if two-particle interactions are strong enough.

The results show, that the concept of CUTs can be extended to systems that exhibit unstable quasiparticles.

IPA-$CuCl_3$

To apply the above developments to an experimental system, in the last chapter of the present thesis the salt isopropylammonium trichlorocuprate(II) $(CH_3)_2CHNH_3CuCl_3$ (IPA-$CuCl_3$) is discussed. Although INS performed in 2006 has revealed IPA-$CuCl_3$ as a system of weakly coupled AFASHLs a determination of the values of the magnetic couplings was still missing. Using sCUTs and high temperature series expansions (HTSEs) allow us to analyze data of INS and of magnetic susceptibility to establish a microscopic model for IPA-$CuCl_3$ by determining the four magnetic couplings $J_1 \approx -2.3$ meV, $J_2 \approx 1.2$ meV, $J_3 \approx 2.9$ meV and $J_4 \approx -0.3$ meV.

Based on the microscopic model we use sCUTs adapted for SQPD to describe the recently observed SQPD in IPA-$CuCl_3$. Theory and experiment agree very well without further adjustment of parameters which supports the established microscopic model.

Additionally, we show how the application range of classical and mean-field approaches can be extended by starting from an effective model previously determined by CUTs which incorporate quantum fluctuations. In this way the Bose-Einstein condensation (BEC) of triplons in an external magnetic field and the temperature dependence of the gap are calculated. Again the results are consistent with the experimental data.

In conclusion, we show that CUTs are a powerful tool to describe the low energy physics of low-dimensional dimerized quantum antiferromagnets, even in the presence of unstable excitations. The systematically derived effective models can readily serve as starting point for further calculations for phenomena such as BEC or finite temperature properties.

7.2 Outlook

Unstable quasiparticles are a commonly occurring phenomena in many-particle systems. Thus, extending the applicability of CUTs to systems with SQPD leads to a large number of additionally possible investigations.

In one dimension SQPD also has been observed in the spin $S = 1$ antiferromagnet $CsNiCl_3$ [Zaliznyak *et al.*(2001)]. Since the $S = 1$ chain is included in the AFASHL an investigation of the SQPD occurring in $CsNiCl_3$ should be possible in very much the same way as it has been done in this thesis for the AFASHL.

Our calculations on the one-dimensional bosonic toy model suggest that in the

incommensurate region of the phase digram of the AASHL always stable excitations below the continuum exist. However, for small momenta the weight of these excitations should be very small so that most of the spectral weight should be gathered inside the continuum. A test of this hypothesis might be possible by CUTs.

The method of CUTs is not restricted to one-dimensional systems. Therefore, one could try to describe the SQPD in the two-dimensional quantum spin $S = 1/2$ system piperazinium hexachlorodicuprate (PHCC) by CUTs. A complete two-dimensional analysis of IPA-$CuCl_3$ making the used mean-field approximations dispensable should be possible as well.

Unfortunately, the analysis of the effective model generated by CUTs designed for system with unstable excitations is very elaborate. To achieve the right one-particle dispersion also states consisting of up to three particles have had to be considered. This is hardly possible in two dimensions. One way to simplify the analysis of the effective model is to decouple more states during the CUT.

Convergence of the CUT is generically hindered by energetically overlapping states. In systems with SQPD the one-particle dispersion and the two-particle continuum overlap. But usually, in gapped systems the one-particle dispersion does not merge with the three-particle continuum. In that case it should be possible to eliminate all processes leading from one-particle states to three-particle states by the CUT. Such a CUT would not decouple the one- and two-particle sector from higher particle states since processes which induce the one-particle decay also yield decay from two particles into three particles. Nevertheless, for such a CUT it is possible that an analysis of the effective model with states only in the one- and two-particle sector yields reasonable results. Such a calculation would also be possible in two dimensions. At this level, it is also conceivable to include self-consistency by diagrammatic approaches with justifiable expenditure. Diagrammatic approaches could also be used to calculate finite temperature properties of an effective model previously determined by a CUT.

Although the theoretical part about the adapted CUT is quite general, only the case of a unique ground state is discussed in detail. Generalizations where the adapted CUT separates a complete low-energy subspace can also be considered. This is already done to generate generalized $t-J$ models from the Hubbard model for finite doping [Hamerla(2009), Hamerla *et al.*(2010)].

Appendix A

Lanczos tridiagonalization

To calculate the coefficients $a_n(Q)$ and $b_n(Q)$ of the continued fraction representation of a Green function

$$\mathcal{G}(Q,\omega) = \cfrac{1}{\omega - a_0(Q) - \cfrac{b_1^2(Q)}{\omega - a_1(Q) - \cfrac{b_2^2(Q)}{\dots}}} \tag{A.1}$$

a Lanczos tridiagonalization can be used [Viswanath & Müller(1994)]. The Lanczos recursion scheme for a Hamiltonian $H(Q)$ and a starting vector $\left|\psi_0\right\rangle$ is given by

$$\left|\psi_0\right\rangle \tag{A.2a}$$
$$\left|\psi_1\right\rangle = \Big(H(Q) - a_0(Q)\Big)\left|\psi_0\right\rangle \tag{A.2b}$$
$$\left|\psi_2\right\rangle = \Big(H(Q) - a_1(Q)\Big)\left|\psi_1\right\rangle - b_1^2(Q)\left|\psi_0\right\rangle \tag{A.2c}$$
$$\left|\psi_3\right\rangle = \Big(H(Q) - a_2(Q)\Big)\left|\psi_2\right\rangle - b_2^2(Q)\left|\psi_1\right\rangle \tag{A.2d}$$
$$\vdots$$

with

$$a_n(Q) = \frac{\left\langle\psi_n\middle|H(Q)\middle|\psi_n\right\rangle}{\left\langle\psi_n\middle|\psi_n\right\rangle} \quad \text{for} \quad n = 0,1,2,\dots \tag{A.2e}$$

$$b_n^2(Q) = \frac{\left\langle\psi_n\middle|\psi_n\right\rangle}{\left\langle\psi_{n-1}\middle|\psi_{n-1}\right\rangle} \quad \text{for} \quad n = 1,2,3,\dots \tag{A.2f}$$

$$b_0(Q) = 0\,. \tag{A.2g}$$

The LANCZOS recursion scheme generates a set of orthogonal states $\left|\psi_n\right\rangle$. In the generated basis $\left\{\left|\psi_n\right\rangle\right\}$ the matrix of the Hamiltonian H is tridiagonal, where the $a_n(Q)$ are the diagonal matrix elements and the $b_n(Q)$ are the elements on the second diagonal. All other matrix elements are zero.

A.1 Termination: General theory

A GREEN function $\mathcal{G}(Q,\omega)$ (A.1) at fixed momentum Q represented by a finite continued fraction has poles at the zeros of the denominator. Thus, the GREEN function $\mathcal{G}(Q,\omega)$ is a collection of δ-peaks. One standard approach to obtain a continuous density is to introduce a slight broadening of $\mathcal{G}(Q,\omega)$ via $\omega \to \omega + \mathrm{i}\delta$ with a small real number δ. This procedure corresponds to smearing out δ-peaks as LORENTZIAN function of width δ. The caveat is that also all truly sharp features such as band edges or VAN HOVE singularities are smeared out. However, a notably improved resolution of $\mathcal{G}(Q,\omega)$ can be achieved by introducing an appropriate termination of the continued fraction [Viswanath & Müller(1994)].

In actual calculations the states $\left|\psi_n\right\rangle$ always have a finite size. If one wants to simulate an infinite large system in the thermodynamic limit one has to stop the recursion before the finiteness of the considered subspace becomes conspicuous.

The lower band edge $E_\mathrm{l}(Q)$ and the upper band edge $E_\mathrm{u}(Q)$ of the GREEN function $\mathcal{G}(Q,\omega)$ are connected to the limits $a_\infty(Q) := \lim_{n\to\infty} a_n(Q)$ and $b_\infty(Q) := \lim_{n\to\infty} b_n(Q)$ of the LANCZOS coefficients via

$$E_\mathrm{u}(Q) = a_\infty(Q) + 2b_\infty(Q) \tag{A.3a}$$

$$E_\mathrm{l}(Q) = a_\infty(Q) - 2b_\infty(Q)\,, \tag{A.3b}$$

see e.g. [Pettifor & Weaire(1985)]. By assuming that for all $n > n_0$ the coefficients $a_n(Q)$ and $b_{n+1}(Q)$ can sufficiently well be approximated by $a_\infty(Q)$ and $b_\infty(Q)$, the continued fraction of the GREEN function $\mathcal{G}(Q,\omega)$ can be terminated by the square root terminator $T(Q,\omega)$ given by

$$T(Q,\omega) = \frac{1}{2b_\infty^2(Q)}\left(\omega - a_\infty(Q) - \sqrt{-D(Q,\omega)}\right) \quad \text{for} \quad \omega \geq E_\mathrm{u}(Q) \tag{A.4a}$$

$$T(Q,\omega) = \frac{1}{2b_\infty^2(Q)}\left(\omega - a_\infty(Q) - \mathrm{i}\sqrt{D(Q,\omega)}\right) \quad \text{for} \quad E_\mathrm{l}(Q) \leq \omega \leq E_\mathrm{u}(Q) \tag{A.4b}$$

$$T(Q,\omega) = \frac{1}{2b_\infty^2(Q)}\left(\omega - a_\infty(Q) + \sqrt{-D(Q,\omega)}\right) \quad \text{for} \quad \omega \leq E_\mathrm{l}(Q) \tag{A.4c}$$

with

$$D(Q,\omega) = 4b_\infty^2(Q) - (\omega - a_\infty(Q))^2 \ . \tag{A.4d}$$

In this way one can reliably approximate the thermodynamic limit of the GREEN function $\mathcal{G}(q,\omega)$ by calculations in a finite subspace.

The discussed way of termination is ideal for square root singularities at the band edges as given in one-dimensional systems with quadratic dispersions. Otherwise, other termination are better suited, but also technically more difficult.

A.2 Termination: Details

In figure A.1a the LANCZOS coefficients $a_n(Q)$ and $b_n(Q)$ for the two-triplon dynamical spin structure factor $S_2^{zz}(Q,\omega)$ for $Q = 0.1\pi$ are depicted, cf. equation (4.31) in section 4.1.2. We have restricted our system size by considering vectors $\left|Q,d_1\right\rangle_{m=0}^{S=1}$ with $d_1 < 4000$ only. Thus, our vector space has the dimension 3999. At least up to $n = 1500$ the coefficients show no sign of finiteness, i.e., they behave consistently to equation (A.3), see inset in figure A.1a. To approximate the limits $a_\infty(Q)$ and $b_\infty(Q)$ we use the arithmetic mean of $a_n(Q)$ and $b_n(Q)$ for $n \in [1400,1490]$. Finally, we use the directly calculated coefficients $a_n(Q)$ and $b_{n+1}(Q)$ for $n = 0\ldots1399$ and subsequently the square root terminator defined by the approximate limits for $a_\infty(Q)$ and $b_\infty(Q)$. By doing this, we assume that all following coefficients $a_n(K)$ and $b_{n+1}(K)$ with $n \geq 1400$ are constant. All results shown in figure 4.9 in section 4.1.2 are terminated in that way.

Figure A.1b shows the results for the coefficients $a_n(Q)$ and $b_n(Q)$ of the GREEN function $\mathcal{G}(Q,\omega)$ (4.38) for the spectral density $\rho(Q,\omega)$ discussed in section 4.2.2 for $x = 0.5$, $y = 0.1$ and $Q = 0.1\pi$. First it appears that both coefficients $a_n(Q)$ and $b_n(Q)$ ($n \lessapprox 115$) converge to fixed values $a_\infty(Q)$ and $b_\infty(Q)$ as it should be for a bounded and gapless spectral density of an infinite large system [Pettifor & Weaire(1985)]. The existence of an upper boundary of the spectral density $\rho(Q,\omega)$ is a consequence of our restriction to a subspace which contains three quasiparticles at maximum. But for $n \gtrapprox 115$ both coefficients start to change their values again noticeably. This is a consequence of the fact that we had to restrict the relative distances d_1 and $d_1 + d_2$ to a maximum of 119 rungs (cf. equation (4.39)) in our numerical calculations. Note, that the dimension of the subspace (4.39) with $0 < d_1, d_1 + d_2 < 120$ is 21183. Here we compute the average value of $a_n(Q)$ and $b_n(Q)$ for $n = 80\ldots100$ (cf. figure A.1b) to obtain a good approximation for the limits $a_\infty(Q)$ and $b_\infty(Q)$. Subsequently, we use the directly calculated coefficients $a_n(Q)$ and $b_{n+1}(Q)$ for $n = 0\ldots79$ and a terminator defined by the approximate limits for $a_\infty(Q)$ and $b_\infty(Q)$. All results for the spectral density $\rho(Q,\omega)$ depicted in figure 4.15a are obtained in this way.

Terminated continued fractions are also used to determine the width of the excitations via the self-energy $\Sigma(Q,\omega)$ in the asymmetric antiferromagnetic spin $S = 1/2$ HEISENBERG ladder (AASHL) (see figure 4.23), in the asymmetric ferro-antiferromagnetic spin $S = 1/2$ HEISENBERG ladder (AFASHL) (see figure 5.9) and in isopropylammonium trichlorocuprate(II) $(CH_3)_2CHNH_3CuCl_3$ (IPA-$CuCl_3$) (see figure 6.5 and figure 6.9). In table A.1 the number n of directly calculated coefficients and the interval $[n+1, n_{\max}]$ used to determine an approximation for the limits $a_\infty(Q)$ and $b_\infty(Q)$ are listed. For all momenta Q the same n and the same interval $[n+1, n_{\max}]$ have been used for a given pair (x, y) of interactions.

Table A.1: Number n of directly calculated coefficients and the interval $[n+1, n_{\max}]$ used to determine an approximation for the limits $a_\infty(Q)$ and $b_\infty(Q)$ for different interactions x and y.

x	y	n	$[n+1, n_{\max}]$
0.50	0.10	79	[80,100]
0.50	0.25	79	[80,100]
0.50	0.50	79	[80,100]
0.75	0.10	59	[60,75]
0.75	0.25	59	[60,75]
0.75	0.50	69	[70,90]
1.00	0.10	49	[50,60]
1.00	0.25	49	[50,60]
1.00	0.50	49	[50,60]
0.50	-0.10	79	[80,100]
0.50	-0.25	69	[70,90]
0.50	-0.50	69	[70,90]
0.75	-0.10	59	[60,75]
0.75	-0.25	59	[60,75]
0.75	-0.50	59	[60,75]
1.00	-0.10	49	[50,60]
1.00	-0.25	49	[50,60]
1.00	-0.50	49	[50,60]
IPA-$CuCl_3$		69	[70,90]

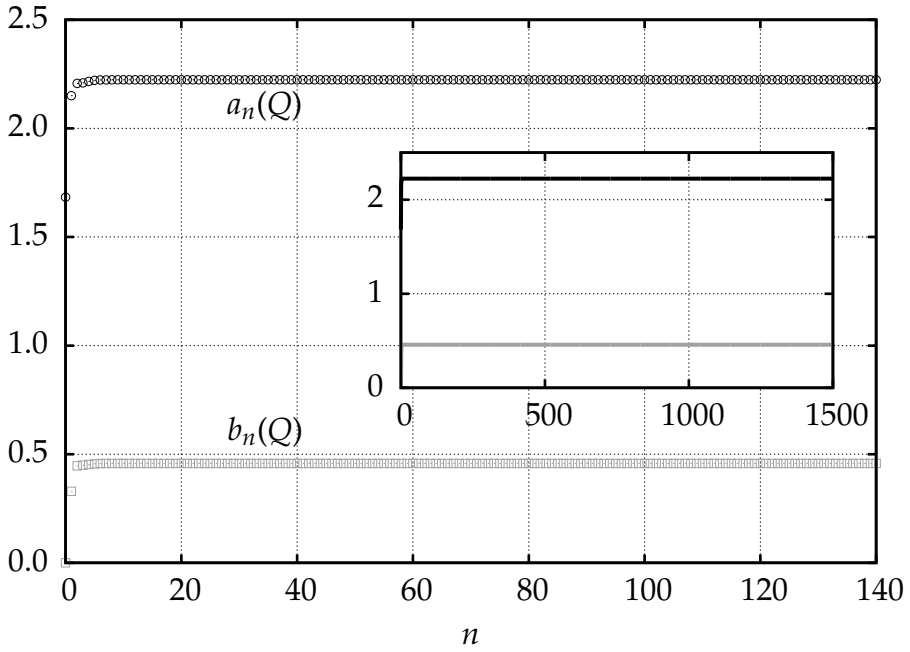

(a) Coefficients $a_n(Q)$ and $b_n(Q)$ for the two-triplon dynamical spin structure factor $S_2^{zz}(Q,\omega)$ for $Q = 0.1\pi$, cf. equation (4.31) in section 4.1.2.

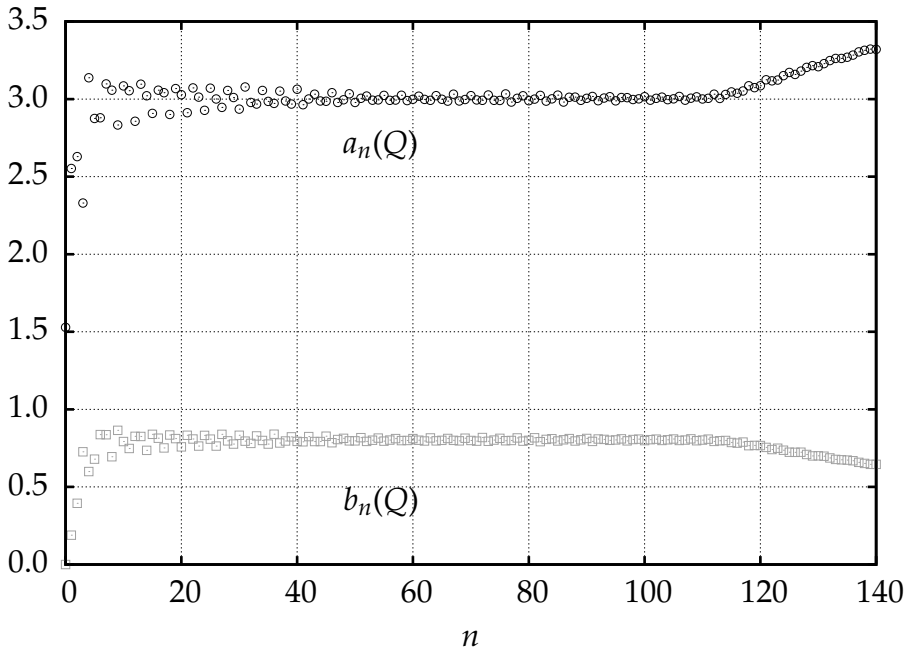

(b) Coefficients $a_n(Q)$ and $b_n(Q)$ of the spectral density $\rho(Q,\omega)$ discussed in section 4.2.2 for $x = 0.5$, $y = 0.1$ and $Q = 0.1\pi$. The restriction of the considered subspace becomes conspicuous at $n \approx 115$.

Figure A.1: Coefficients from Lanczos tridiagonalization.

Appendix B

Flow equations for hard-core toy model

Below the differential equations for the two hard-core bosons toy model discussed in section 3.3.2 are listed. To improve legibility all ℓ-dependencies are neglected.

B.1 Flow equations for the generator G_{M}

Using the generator G_{M} given by equation (3.69) yields the flow equations

$$\frac{\partial h_{\emptyset}^{\emptyset}}{\partial \ell} = -2\left(h_{\emptyset}^{\{1\}}\right)^2 - 2\left(h_{\emptyset}^{\{2\}}\right)^2 - 2\left(h_{\emptyset}^{\{1,2\}}\right)^2 \tag{B.1a}$$

$$\frac{\partial h_{\{1\}}^{\{1\}}}{\partial \ell} = 4\left(h_{\emptyset}^{\{1\}}\right)^2 + 2\left(h_{\emptyset}^{\{1,2\}}\right)^2 - 2\left(h_{\{1\}}^{\{1,2\}}\right)^2 - 4\, h_{\emptyset}^{\{2\}} h_{\{1\}}^{\{1,2\}} - 2\left(h_{\{1\}}^{\{2\}}\right)^2 \tag{B.1b}$$

$$\frac{\partial h_{\{2\}}^{\{2\}}}{\partial \ell} = 4\left(h_{\emptyset}^{\{2\}}\right)^2 + 2\left(h_{\emptyset}^{\{1,2\}}\right)^2 - 2\left(h_{\{2\}}^{\{1,2\}}\right)^2 - 4\, h_{\emptyset}^{\{1\}} h_{\{2\}}^{\{1,2\}} + 2\left(h_{\{1\}}^{\{2\}}\right)^2 \tag{B.1c}$$

$$\frac{\partial h_{\{1\}}^{\{2\}}}{\partial \ell} = h_{\{1\}}^{\{2\}}\left(h_{\{1\}}^{\{1\}} - h_{\{2\}}^{\{2\}}\right) - 2\, h_{\emptyset}^{\{1\}} h_{\{1\}}^{\{1,2\}} - 2\, h_{\emptyset}^{\{2\}} h_{\{2\}}^{\{1,2\}} - 2\, h_{\{1\}}^{\{1,2\}} h_{\{2\}}^{\{1,2\}} \tag{B.1d}$$

$$\frac{\partial h_{\{1,2\}}^{\{1,2\}}}{\partial \ell} = 8\, h_{\emptyset}^{\{1\}} h_{\{2\}}^{\{1,2\}} + 8\, h_{\emptyset}^{\{2\}} h_{\{1\}}^{\{1,2\}} + 4\left(h_{\{1\}}^{\{1,2\}}\right)^2 + 4\left(h_{\{2\}}^{\{1,2\}}\right)^2 \tag{B.1e}$$

$$\frac{\partial h_{\emptyset}^{\{1\}}}{\partial \ell} = -h_{\emptyset}^{\{1\}} h_{\{1\}}^{\{1\}} - 2\, h_{\emptyset}^{\{1,2\}}\left(h_{\emptyset}^{\{2\}} + h_{\{1\}}^{\{1,2\}}\right) - 2\, h_{\emptyset}^{\{2\}} h_{\{1\}}^{\{2\}} \tag{B.1f}$$

$$\frac{\partial h_{\emptyset}^{\{2\}}}{\partial \ell} = -h_{\emptyset}^{\{2\}} h_{\{2\}}^{\{2\}} - 2\, h_{\emptyset}^{\{1,2\}}\left(h_{\emptyset}^{\{1\}} + h_{\{2\}}^{\{1,2\}}\right) \tag{B.1g}$$

$$\frac{\partial h_{\emptyset}^{\{1,2\}}}{\partial \ell} = -h_{\emptyset}^{\{1,2\}}\left(h_{\{1\}}^{\{1\}} + h_{\{2\}}^{\{2\}} + h_{\{1,2\}}^{\{1,2\}}\right) \tag{B.1h}$$

$$\frac{\partial h_{\{1\}}^{\{1,2\}}}{\partial \ell} = 2\, h_{\emptyset}^{\{1,2\}}\left(2\, h_{\emptyset}^{\{1\}} + h_{\{2\}}^{\{1,2\}}\right) - h_{\{1,2\}}^{\{1,2\}}\left(h_{\emptyset}^{\{2\}} + h_{\{1\}}^{\{1,2\}}\right) - h_{\{1\}}^{\{1,2\}} h_{\{2\}}^{\{2\}} \tag{B.1i}$$

$$\frac{\partial h_{\{2\}}^{\{1,2\}}}{\partial \ell} = 2\, h_{\emptyset}^{\{1,2\}}\left(2\, h_{\emptyset}^{\{2\}} + h_{\{1\}}^{\{1,2\}}\right) - h_{\{1,2\}}^{\{1,2\}}\left(h_{\emptyset}^{\{1\}} + h_{\{2\}}^{\{1,2\}}\right) - h_{\{2\}}^{\{1,2\}} h_{\{1\}}^{\{1\}} + 2\, h_{\{1\}}^{\{2\}}\left(2\, h_{\emptyset}^{\{2\}} + h_{\{1\}}^{\{1,2\}}\right). \tag{B.1j}$$

B.2 Flow equations for the generator G_{pc}

Using the generator G_{pc} given by equation (3.70) yields the flow equations

$$\frac{\partial h_{\emptyset}^{\emptyset}}{\partial \ell} = -2\left(h_{\emptyset}^{\{1\}}\right)^2 - 2\left(h_{\emptyset}^{\{2\}}\right)^2 - 2\left(h_{\emptyset}^{\{1,2\}}\right)^2 \tag{B.2a}$$

$$\frac{\partial h_{\{1\}}^{\{1\}}}{\partial \ell} = 4\left(h_{\emptyset}^{\{1\}}\right)^2 + 2\left(h_{\emptyset}^{\{1,2\}}\right)^2 - 2\left(h_{\{1\}}^{\{1,2\}}\right)^2 - 4\, h_{\emptyset}^{\{2\}} h_{\{1\}}^{\{1,2\}} \tag{B.2b}$$

$$\frac{\partial h_{\{2\}}^{\{2\}}}{\partial \ell} = 4\left(h_{\emptyset}^{\{2\}}\right)^2 + 2\left(h_{\emptyset}^{\{1,2\}}\right)^2 - 2\left(h_{\{2\}}^{\{1,2\}}\right)^2 - 4\, h_{\emptyset}^{\{1\}} h_{\{2\}}^{\{1,2\}} \tag{B.2c}$$

$$\frac{\partial h_{\{1\}}^{\{2\}}}{\partial \ell} = -2\, h_{\emptyset}^{\{1\}} h_{\{1\}}^{\{1,2\}} - 2\, h_{\emptyset}^{\{2\}} h_{\{2\}}^{\{1,2\}} - 2\, h_{\{1\}}^{\{1,2\}} h_{\{2\}}^{\{1,2\}} \tag{B.2d}$$

$$\frac{\partial h_{\{1,2\}}^{\{1,2\}}}{\partial \ell} = 8\, h_{\emptyset}^{\{1\}} h_{\{2\}}^{\{1,2\}} + 8\, h_{\emptyset}^{\{2\}} h_{\{1\}}^{\{1,2\}} + 4\left(h_{\{1\}}^{\{1,2\}}\right)^2 + 4\left(h_{\{2\}}^{\{1,2\}}\right)^2 \tag{B.2e}$$

$$\frac{\partial h_{\emptyset}^{\{1\}}}{\partial \ell} = -h_{\emptyset}^{\{1\}} h_{\{1\}}^{\{1\}} - 2\, h_{\emptyset}^{\{1,2\}}\left(h_{\emptyset}^{\{2\}} + h_{\{1\}}^{\{1,2\}}\right) - h_{\emptyset}^{\{2\}} h_{\{1\}}^{\{2\}} \tag{B.2f}$$

$$\frac{\partial h_{\emptyset}^{\{2\}}}{\partial \ell} = -h_{\emptyset}^{\{2\}} h_{\{2\}}^{\{2\}} - 2\, h_{\emptyset}^{\{1,2\}}\left(h_{\emptyset}^{\{1\}} + h_{\{2\}}^{\{1,2\}}\right) - h_{\emptyset}^{\{1\}} h_{\{1\}}^{\{2\}} \tag{B.2g}$$

$$\frac{\partial h_{\emptyset}^{\{1,2\}}}{\partial \ell} = -h_{\emptyset}^{\{1,2\}}\left(h_{\{1\}}^{\{1\}} + h_{\{2\}}^{\{2\}} + h_{\{1,2\}}^{\{1,2\}}\right) \tag{B.2h}$$

$$\frac{\partial h_{\{1\}}^{\{1,2\}}}{\partial \ell} = 2\, h_{\emptyset}^{\{1,2\}}\left(2\, h_{\emptyset}^{\{1\}} + h_{\{2\}}^{\{1,2\}}\right) - h_{\{1,2\}}^{\{1,2\}}\left(h_{\emptyset}^{\{2\}} + h_{\{1\}}^{\{1,2\}}\right) - h_{\{1\}}^{\{1,2\}} h_{\{2\}}^{\{2\}} + h_{\{1\}}^{\{2\}}\left(2\, h_{\emptyset}^{\{1\}} + h_{\{2\}}^{\{1,2\}}\right) \tag{B.2i}$$

$$\frac{\partial h_{\{2\}}^{\{1,2\}}}{\partial \ell} = 2\, h_{\emptyset}^{\{1,2\}}\left(2\, h_{\emptyset}^{\{2\}} + h_{\{1\}}^{\{1,2\}}\right) - h_{\{1,2\}}^{\{1,2\}}\left(h_{\emptyset}^{\{1\}} + h_{\{2\}}^{\{1,2\}}\right) - h_{\{2\}}^{\{1,2\}} h_{\{1\}}^{\{1\}} + h_{\{1\}}^{\{2\}}\left(2\, h_{\emptyset}^{\{2\}} + h_{\{1\}}^{\{1,2\}}\right). \tag{B.2j}$$

B.3 Flow equations for the generator G_{DEO}

Using the generator G_{DEO} given by equation (3.71) yields the flow equations

$$\frac{\partial h_{\emptyset}^{\emptyset}}{\partial \ell} = -2\left(h_{\emptyset}^{\{1\}}\right)^2 - 2\left(h_{\emptyset}^{\{2\}}\right)^2 - 2\left(h_{\emptyset}^{\{1,2\}}\right)^2 \tag{B.3a}$$

$$\frac{\partial h_{\{1\}}^{\{1\}}}{\partial \ell} = 4\left(h_{\emptyset}^{\{1\}}\right)^2 + 2\left(h_{\emptyset}^{\{2\}}\right)^2 + 2\left(h_{\emptyset}^{\{1,2\}}\right)^2 \tag{B.3b}$$

$$\frac{\partial h_{\{2\}}^{\{2\}}}{\partial \ell} = 4\left(h_{\emptyset}^{\{2\}}\right)^2 + 2\left(h_{\emptyset}^{\{1\}}\right)^2 + 2\left(h_{\emptyset}^{\{1,2\}}\right)^2 \tag{B.3c}$$

$$\frac{\partial h_{\{1\}}^{\{2\}}}{\partial \ell} = 2\, h_{\emptyset}^{\{1\}} h_{\emptyset}^{\{2\}} \tag{B.3d}$$

$$\frac{\partial h_{\{1,2\}}^{\{1,2\}}}{\partial \ell} = -4\left(h_{\emptyset}^{\{1\}}\right)^2 - 4\left(h_{\emptyset}^{\{2\}}\right)^2 \tag{B.3e}$$

$$\frac{\partial h_{\emptyset}^{\{1\}}}{\partial \ell} = -h_{\emptyset}^{\{1\}} h_{\{1\}}^{\{1\}} - h_{\emptyset}^{\{1,2\}}\left(h_{\emptyset}^{\{2\}} + h_{\{1\}}^{\{1,2\}}\right) - h_{\emptyset}^{\{2\}} h_{\{1\}}^{\{2\}} \tag{B.3f}$$

$$\frac{\partial h_{\emptyset}^{\{2\}}}{\partial \ell} = -h_{\emptyset}^{\{2\}} h_{\{2\}}^{\{2\}} - h_{\emptyset}^{\{1,2\}}\left(h_{\emptyset}^{\{1\}} + h_{\{2\}}^{\{1,2\}}\right) - h_{\emptyset}^{\{1\}} h_{\{1\}}^{\{2\}} \tag{B.3g}$$

$$\frac{\partial h_{\emptyset}^{\{1,2\}}}{\partial \ell} = -h_{\emptyset}^{\{1,2\}}\left(h_{\{1\}}^{\{1\}} + h_{\{2\}}^{\{2\}} + h_{\{1,2\}}^{\{1,2\}}\right) - 2\, h_{\emptyset}^{\{1\}} h_{\emptyset}^{\{2\}} - h_{\emptyset}^{\{1\}} h_{\{1\}}^{\{1,2\}} - h_{\emptyset}^{\{2\}} h_{\{2\}}^{\{1,2\}} \tag{B.3h}$$

$$\frac{\partial h_{\{1\}}^{\{1,2\}}}{\partial \ell} = h_{\emptyset}^{\{1,2\}}\left(3\, h_{\emptyset}^{\{1\}} + h_{\{2\}}^{\{1,2\}}\right) + h_{\emptyset}^{\{1\}} h_{\{1\}}^{\{2\}} + h_{\emptyset}^{\{2\}} h_{\{1\}}^{\{1\}} \tag{B.3i}$$

$$\frac{\partial h_{\{2\}}^{\{1,2\}}}{\partial \ell} = h_{\emptyset}^{\{1,2\}}\left(3\, h_{\emptyset}^{\{2\}} + h_{\{1\}}^{\{1,2\}}\right) + h_{\emptyset}^{\{2\}} h_{\{1\}}^{\{2\}} + h_{\emptyset}^{\{1\}} h_{\{2\}}^{\{2\}}\,. \tag{B.3j}$$

B.4 Flow equations for the generator G_{gs}

Using the generator G_{gs} given by equation (3.72) yields the flow equations

$$\frac{\partial h_{\emptyset}^{\emptyset}}{\partial \ell} = -2\left(h_{\emptyset}^{\{1\}}\right)^2 - 2\left(h_{\emptyset}^{\{2\}}\right)^2 - 2\left(h_{\emptyset}^{\{1,2\}}\right)^2 \tag{B.4a}$$

$$\frac{\partial h_{\{1\}}^{\{1\}}}{\partial \ell} = 4\left(h_{\emptyset}^{\{1\}}\right)^2 + 2\left(h_{\emptyset}^{\{1,2\}}\right)^2 - 2\, h_{\emptyset}^{\{2\}} h_{\{1\}}^{\{1,2\}} \tag{B.4b}$$

$$\frac{\partial h_{\{2\}}^{\{2\}}}{\partial \ell} = 4\left(h_{\emptyset}^{\{2\}}\right)^2 + 2\left(h_{\emptyset}^{\{1,2\}}\right)^2 - 2\, h_{\emptyset}^{\{1\}} h_{\{2\}}^{\{1,2\}} \tag{B.4c}$$

$$\frac{\partial h_{\{1\}}^{\{2\}}}{\partial \ell} = -h_{\emptyset}^{\{1\}} h_{\{1\}}^{\{1,2\}} - h_{\emptyset}^{\{2\}} h_{\{2\}}^{\{1,2\}} \tag{B.4d}$$

$$\frac{\partial h_{\{1,2\}}^{\{1,2\}}}{\partial \ell} = 4\, h_{\emptyset}^{\{1\}} h_{\{2\}}^{\{1,2\}} + 4\, h_{\emptyset}^{\{2\}} h_{\{1\}}^{\{1,2\}} \tag{B.4e}$$

$$\frac{\partial h_{\emptyset}^{\{1\}}}{\partial \ell} = -h_{\emptyset}^{\{1\}} h_{\{1\}}^{\{1\}} - h_{\emptyset}^{\{1,2\}}\left(2\, h_{\emptyset}^{\{2\}} + h_{\{1\}}^{\{1,2\}}\right) - h_{\emptyset}^{\{2\}} h_{\{1\}}^{\{2\}} \tag{B.4f}$$

$$\frac{\partial h_{\emptyset}^{\{2\}}}{\partial \ell} = -h_{\emptyset}^{\{2\}} h_{\{2\}}^{\{2\}} - h_{\emptyset}^{\{1,2\}}\left(2\, h_{\emptyset}^{\{1\}} + h_{\{2\}}^{\{1,2\}}\right) - h_{\emptyset}^{\{1\}} h_{\{1\}}^{\{2\}} \tag{B.4g}$$

$$\frac{\partial h_{\emptyset}^{\{1,2\}}}{\partial \ell} = -h_{\emptyset}^{\{1,2\}}\left(h_{\{1\}}^{\{1\}} + h_{\{2\}}^{\{2\}} + h_{\{1,2\}}^{\{1,2\}}\right) - h_{\emptyset}^{\{1\}} h_{\{1\}}^{\{1,2\}} - h_{\emptyset}^{\{2\}} h_{\{2\}}^{\{1,2\}} \tag{B.4h}$$

$$\frac{\partial h_{\{1\}}^{\{1,2\}}}{\partial \ell} = h_{\emptyset}^{\{1,2\}}\left(4\, h_{\emptyset}^{\{1\}} + h_{\{2\}}^{\{1,2\}}\right) + 2\, h_{\emptyset}^{\{1\}} h_{\{1\}}^{\{2\}} - h_{\emptyset}^{\{2\}} h_{\{1,2\}}^{\{1,2\}} \tag{B.4i}$$

$$\frac{\partial h_{\{2\}}^{\{1,2\}}}{\partial \ell} = h_{\emptyset}^{\{1,2\}}\left(4\, h_{\emptyset}^{\{2\}} + h_{\{1\}}^{\{1,2\}}\right) + 2\, h_{\emptyset}^{\{2\}} h_{\{1\}}^{\{2\}} - h_{\emptyset}^{\{1\}} h_{\{1,2\}}^{\{1,2\}}\,. \tag{B.4j}$$

Appendix C

Bond operator representation

A pair of spin $S = 1/2$ operators $\mathbf{S}_1$ and $\mathbf{S}_2$ can be represented by a bond operator representation [Chubukov(1989), Sachdev & Bhatt(1990)], where the spin components S_1^α and S_2^α with $\alpha \in \{x, y, z\}$ are represented by bond operators $t_\alpha^\dagger$ (t_α) via the equations

$$S_1^\alpha := \frac{1}{2}\left[\left(t_\alpha^\dagger + t_\alpha\right) - \mathrm{i} \sum_{\beta,\gamma} \varepsilon_{\alpha\beta\gamma}\, t_\beta^\dagger t_\gamma \right] \tag{C.1a}$$

$$S_2^\alpha := \frac{1}{2}\left[-\left(t_\alpha^\dagger + t_\alpha\right) - \mathrm{i} \sum_{\beta,\gamma} \varepsilon_{\alpha\beta\gamma}\, t_\beta^\dagger t_\gamma \right] . \tag{C.1b}$$

The bond operators $t_\alpha^\dagger$ (t_α) obey the hard-core commutation relations (3.98).

An eigenbasis of the operator $\mathbf{S}_1\mathbf{S}_2$ is given by the singlet state

$$\left|\text{singlet}\right\rangle := \frac{1}{\sqrt{2}}\left(\left|\uparrow\downarrow\right\rangle - \left|\downarrow\uparrow\right\rangle \right) \tag{C.2a}$$

and the triplet states

$$t_x^\dagger \left|\text{singlet}\right\rangle := \left|x\right\rangle = \frac{-1}{\sqrt{2}}\left(\left|\uparrow\uparrow\right\rangle - \left|\downarrow\downarrow\right\rangle \right) \tag{C.2b}$$

$$t_y^\dagger \left|\text{singlet}\right\rangle := \left|y\right\rangle = \frac{\mathrm{i}}{\sqrt{2}}\left(\left|\uparrow\uparrow\right\rangle + \left|\downarrow\downarrow\right\rangle \right) \tag{C.2c}$$

$$t_z^\dagger \left|\text{singlet}\right\rangle := \left|z\right\rangle = \frac{1}{\sqrt{2}}\left(\left|\uparrow\downarrow\right\rangle + \left|\downarrow\uparrow\right\rangle \right) . \tag{C.2d}$$

In this basis the spin operators (C.1) have the matrix representation

$$S_1^x = \frac{1}{2}\begin{pmatrix} 0 & 1 & 0 & 0 \\ 1 & 0 & 0 & 0 \\ 0 & 0 & 0 & -\mathrm{i} \\ 0 & 0 & \mathrm{i} & 0 \end{pmatrix} \qquad S_2^x = \frac{1}{2}\begin{pmatrix} 0 & -1 & 0 & 0 \\ -1 & 0 & 0 & 0 \\ 0 & 0 & 0 & -\mathrm{i} \\ 0 & 0 & \mathrm{i} & 0 \end{pmatrix} \tag{C.3a}$$

$$S_1^y = \frac{1}{2}\begin{pmatrix} 0 & 0 & 1 & 0 \\ 0 & 0 & 0 & \mathrm{i} \\ 1 & 0 & 0 & 0 \\ 0 & -\mathrm{i} & 0 & 0 \end{pmatrix} \qquad S_2^y = \frac{1}{2}\begin{pmatrix} 0 & 0 & -1 & 0 \\ 0 & 0 & 0 & \mathrm{i} \\ -1 & 0 & 0 & 0 \\ 0 & -\mathrm{i} & 0 & 0 \end{pmatrix} \tag{C.3b}$$

$$S_1^z = \frac{1}{2}\begin{pmatrix} 0 & 0 & 0 & 1 \\ 0 & 0 & -\mathrm{i} & 0 \\ 0 & \mathrm{i} & 0 & 0 \\ 1 & 0 & 0 & 0 \end{pmatrix} \qquad S_2^z = \frac{1}{2}\begin{pmatrix} 0 & 0 & 0 & -1 \\ 0 & 0 & -\mathrm{i} & 0 \\ 0 & \mathrm{i} & 0 & 0 \\ -1 & 0 & 0 & 0 \end{pmatrix} \tag{C.3c}$$

yielding

$$\mathbf{S}_1\mathbf{S}_2 = \frac{1}{4}\begin{pmatrix} -3 & 0 & 0 & 0 \\ 0 & 1 & 0 & 0 \\ 0 & 0 & 1 & 0 \\ 0 & 0 & 0 & 1 \end{pmatrix}. \tag{C.4}$$

The basis vectors (C.2) are *not* building an eigenbasis of the operator $S^z_{\mathrm{tot}} = S^z_1 + S^z_2$. Therefore, in the presence of an external magnetic field proportional to S^z_{tot} one usually changes into a basis where the operator S^z_{tot} is diagonal, too. A possible basis is[1]

$$\left|\mathrm{singlet}\right\rangle := \frac{1}{\sqrt{2}}\left(\left|\uparrow\downarrow\right\rangle - \left|\downarrow\uparrow\right\rangle\right) \tag{C.5a}$$

$$t_+^\dagger \left|\mathrm{singlet}\right\rangle := -\left|\uparrow\uparrow\right\rangle \tag{C.5b}$$

$$t_0^\dagger \left|\mathrm{singlet}\right\rangle := \frac{1}{\sqrt{2}}\left(\left|\uparrow\downarrow\right\rangle + \left|\downarrow\uparrow\right\rangle\right) \tag{C.5c}$$

$$t_-^\dagger \left|\mathrm{singlet}\right\rangle := \left|\downarrow\downarrow\right\rangle \tag{C.5d}$$

where the indices $+, -$ and 0 denote the corresponding eigenvalues $1, -1$ and 0 of the operator S^z_{tot}.

The bond operators $t_x^\dagger, t_y^\dagger$ and $t_z^\dagger$ appearing in equation (C.2) and the operators $t_+^\dagger, t_-^\dagger$

[1] In the literature different definitions of $t_+^\dagger$ exist as well. Here we use the definition *with* the minus sign, as used, e.g., in [Matsumoto *et al.*(2004)]. The definition *without* the minus sign is used e.g. in [Knetter & Uhrig(2000)].

and $t_0^\dagger$ appearing in equation (C.5) are connected by

$$t_x^\dagger = \frac{1}{\sqrt{2}}\left(t_+^\dagger + t_-^\dagger\right) \tag{C.6a}$$

$$t_y^\dagger = \frac{-\mathrm{i}}{\sqrt{2}}\left(t_+^\dagger - t_-^\dagger\right) \tag{C.6b}$$

$$t_x^\dagger = t_0^\dagger\,. \tag{C.6c}$$

For sums over x, y and z we usually use the index α. For sums over $+, -$ and 0 we use the index m. Additionally, we use the definition $\overline{m} := -m$.

Within this thesis, spin interactions $\mathbf{S}_i(\mathbf{r})\mathbf{S}_j(\mathbf{r}')$ with $i, j \in \{1,2\}$ acting on the same dimer ($\mathbf{r} = \mathbf{r}'$) or acting on different dimers ($\mathbf{r} \neq \mathbf{r}'$) are considered. The equations listed below specify how the spin interactions are represented by the operators $t_x^\dagger, t_y^\dagger$ and $t_z^\dagger$ and $t_+^\dagger, t_-^\dagger$ and $t_0^\dagger$.

For $\mathbf{r} = \mathbf{r}'$ the only non-trivial combination for $\mathbf{S}_i(\mathbf{r})\mathbf{S}_j(\mathbf{r})'$ is

$$\mathbf{S}_1(\mathbf{r})\mathbf{S}_2(\mathbf{r}) = -\frac{3}{4}\mathbb{1}_4 + \sum_\alpha t_{\alpha,\mathbf{r}}^\dagger t_{\alpha,\mathbf{r}} \tag{C.7a}$$

$$= -\frac{3}{4}\mathbb{1}_4 + \sum_m t_{m,\mathbf{r}}^\dagger t_{m,\mathbf{r}}\,. \tag{C.7b}$$

For $\mathbf{r} \neq \mathbf{r}'$ four possible combinations $\mathbf{S}_i(\mathbf{r})\mathbf{S}_j(\mathbf{r}')$ exist

$$4\,\mathbf{S}_1(\mathbf{r})\mathbf{S}_1(\mathbf{r}') = \quad T_2(\mathbf{r},\mathbf{r}') + T_{3+}(\mathbf{r},\mathbf{r}') + T_4(\mathbf{r},\mathbf{r}') \tag{C.8a}$$

$$4\,\mathbf{S}_2(\mathbf{r})\mathbf{S}_2(\mathbf{r}') = \quad T_2(\mathbf{r},\mathbf{r}') - T_{3+}(\mathbf{r},\mathbf{r}') + T_4(\mathbf{r},\mathbf{r}') \tag{C.8b}$$

$$4\,\mathbf{S}_1(\mathbf{r})\mathbf{S}_2(\mathbf{r}') = -T_2(\mathbf{r},\mathbf{r}') + T_{3-}(\mathbf{r},\mathbf{r}') + T_4(\mathbf{r},\mathbf{r}') \tag{C.8c}$$

$$4\,\mathbf{S}_2(\mathbf{r})\mathbf{S}_1(\mathbf{r}') = -T_2(\mathbf{r},\mathbf{r}') - T_{3-}(\mathbf{r},\mathbf{r}') + T_4(\mathbf{r},\mathbf{r}') \tag{C.8d}$$

with

$$T_2(\mathbf{r},\mathbf{r}') = \sum_\alpha \left(t_{\alpha,\mathbf{r}}^\dagger t_{\alpha,\mathbf{r}'} + t_{\alpha,\mathbf{r}}^\dagger t_{\alpha,\mathbf{r}'}^\dagger\right) + \text{H.c.} \tag{C.9a}$$

$$T_{3\pm}(\mathbf{r},\mathbf{r}') = \sum_{\alpha,\beta,\gamma} \mathrm{i}\varepsilon_{\alpha\beta\gamma}\left(t_{\alpha,\mathbf{r}}^\dagger t_{\beta,\mathbf{r}'}^\dagger t_{\gamma,\mathbf{r}'} \pm t_{\alpha,\mathbf{r}'}^\dagger t_{\beta,\mathbf{r}}^\dagger t_{\gamma,\mathbf{r}}\right) + \text{H.c.} \tag{C.9b}$$

$$T_4(\mathbf{r},\mathbf{r}') = \sum_{\alpha\neq\beta}\left(t_{\alpha,\mathbf{r}}^\dagger t_{\beta,\mathbf{r}} t_{\beta,\mathbf{r}'}^\dagger t_{\alpha,\mathbf{r}'} - t_{\alpha,\mathbf{r}}^\dagger t_{\beta,\mathbf{r}} t_{\alpha,\mathbf{r}'}^\dagger t_{\beta,\mathbf{r}'}\right) \tag{C.9c}$$

or

$$T_2(\mathbf{r},\mathbf{r}') = \sum_m \left(t^\dagger_{m,\mathbf{r}} t_{m,\mathbf{r}'} + t^\dagger_{m,\mathbf{r}} t^\dagger_{\overline{m},\mathbf{r}'}\right) + \text{H.c.} \tag{C.10a}$$

$$\begin{aligned} T_{3\pm}(\mathbf{r},\mathbf{r}') = &-\left(t^\dagger_{+,\mathbf{r}} t^\dagger_{-,\mathbf{r}'} - t^\dagger_{-,\mathbf{r}} t^\dagger_{+,\mathbf{r}'}\right) t_{0,\mathbf{r}'} \mp \left(t^\dagger_{+,\mathbf{r}'} t^\dagger_{-,\mathbf{r}} - t^\dagger_{-,\mathbf{r}'} t^\dagger_{+,\mathbf{r}}\right) t_{0,\mathbf{r}} \\ &- t^\dagger_{0,\mathbf{r}}\left(t^\dagger_{+,\mathbf{r}'} t_{+,\mathbf{r}'} - t^\dagger_{-,\mathbf{r}'} t_{-,\mathbf{r}'}\right) \mp t^\dagger_{0,\mathbf{r}'}\left(t^\dagger_{+,\mathbf{r}} t_{+,\mathbf{r}} - t^\dagger_{-,\mathbf{r}} t_{-,\mathbf{r}}\right) \\ &+ t^\dagger_{0,\mathbf{r}'}\left(t^\dagger_{+,\mathbf{r}} t_{+,\mathbf{r}'} - t^\dagger_{-,\mathbf{r}} t_{-,\mathbf{r}'}\right) \pm t^\dagger_{0,\mathbf{r}}\left(t^\dagger_{+,\mathbf{r}'} t_{+,\mathbf{r}} - t^\dagger_{-,\mathbf{r}'} t_{-,\mathbf{r}}\right) \end{aligned} \tag{C.10b}$$

$$\begin{aligned} T_4(\mathbf{r},\mathbf{r}') = &\left[t^\dagger_{0,\mathbf{r}} t_{0,\mathbf{r}'}\left(t^\dagger_{+,\mathbf{r}'} t_{+,\mathbf{r}} + t^\dagger_{-,\mathbf{r}'} t_{-,\mathbf{r}}\right) + \text{H.c.}\right] \\ &- \left[t^\dagger_{0,\mathbf{r}} t^\dagger_{0,\mathbf{r}'}\left(t_{+,\mathbf{r}} t_{-,\mathbf{r}'} + t_{-,\mathbf{r}} t_{+,\mathbf{r}'}\right) + \text{H.c.}\right] \\ &+ \left(t^\dagger_{+,\mathbf{r}} t_{+,\mathbf{r}} - t^\dagger_{-,\mathbf{r}} t_{-,\mathbf{r}}\right)\left(t^\dagger_{+,\mathbf{r}'} t_{+,\mathbf{r}'} - t^\dagger_{-,\mathbf{r}'} t_{-,\mathbf{r}'}\right) . \end{aligned} \tag{C.10c}$$

Appendix D

Analysis of the effective model

Here we present details of the analysis of the effective Hamiltonians for the asymmetric ladder generated by continuous unitary transformations (CUTs). More details are given in the references [Knetter *et al.*(2003a)], [Knetter(2003)] and [Kirschner(2004)] for the special case of a particle conserving effective Hamiltonian.

The generators $G_{\mathrm{pc}}(\ell)$ and $G_{\mathrm{gs,1p}}(\ell)$ isolate the one-particle subspace from all other subspaces (cf. figure 3.1 and figure 3.5). Therefore, the one-particle eigenvalues can be calculated solely by equation (D.2) without considering states with a higher particle number. In the case of the generator $G_{\mathrm{pc}}(\ell)$ also the two-particle space is isolated. Thus the two-particle eigenvalues can be obtained by equation (D.3) and equation (D.12).

The effective Hamiltonians obtained by the generator $G_{\mathrm{gs}}(\ell)$ still contain interactions between the one-particle subspace and other subspaces (cf. figure 3.3). Consequently, a diagonalization in the one-particle subspace only gives an approximation for the eigenvalues of the effective Hamiltonian, namely an upper bound for the eigenvalues if the ground state energy is sufficiently well described. The results for the eigenvalues can be improved by considering higher particle subspaces as well (see figure D.1).

In this thesis we consider subspaces which consist of states which contain up to three triplons.

The Fourier transformed one-, two- and three-particle states are given by

$$\left|Q,\alpha_0\right\rangle = \frac{1}{\sqrt{\mathcal{N}}}\sum_r \mathrm{e}^{\mathrm{i}Qr}\left|r,\alpha_0\right\rangle \tag{D.1a}$$

$$\left|Q,\alpha_0\right\rangle\left|d_1,\alpha_1\right\rangle = \frac{1}{\sqrt{\mathcal{N}}}\sum_r \mathrm{e}^{\mathrm{i}Q\left(r+\frac{d_1}{2}\right)}\left|r,\alpha_0\right\rangle\left|r+d_1,\alpha_1\right\rangle \tag{D.1b}$$

$$\left|Q,\alpha_0\right\rangle\left|d_1,\alpha_1\right\rangle\left|d_2,\alpha_2\right\rangle = \frac{1}{\sqrt{\mathcal{N}}}\sum_r \mathrm{e}^{\mathrm{i}Q\left(r+\frac{2d_1+d_2}{3}\right)}\left|r,\alpha_0\right\rangle\left|r+d_1,\alpha_1\right\rangle\left|r+d_1+d_2,\alpha_2\right\rangle \tag{D.1c}$$

with $d_1, d_2 > 0$. In any practical calculation the relative distances d_1 and d_2 must be truncated to make the subspace finite. Note that due to the hard-core algebra it is not

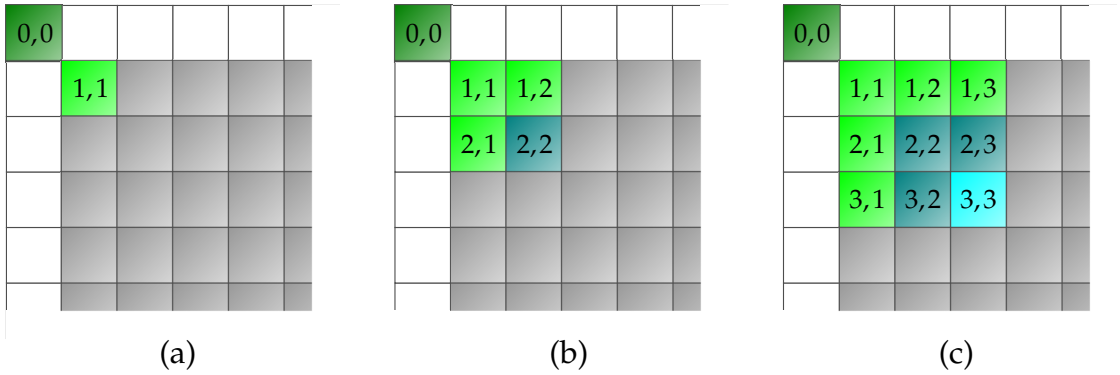

Figure D.1: Considered subspaces to analyze the effective Hamiltonian obtained by the generator $G_{\mathrm{gs}}(\ell)$. The generator $G_{\mathrm{gs}}(\ell)$ only isolates the part H_0^0. Colored blocks illustrate interactions which are included. Grey blocks illustrate neglected interactions. Panel (a) describes an analysis within the one-triplon subspace. Panel (b) describes an analysis within the one- and two-triplon subspace. Panel (c) describes an analysis within the one-, two- and three-triplon subspace, see equations (D.1)

possible that two particles occupy the same rung. Below, the action of the various parts of the effective Hamiltonians are given.

D.1 $H_{\mathrm{eff}}\big|_1^1$

The action of the operator $H_{\mathrm{eff}}\big|_1^1$ on the one-triplon state $\left|Q,\beta_0\right\rangle$ is given by

$$H_{\mathrm{eff}}\big|_1^1 \left|Q,\beta_0\right\rangle = \sum_{l_0,\alpha_0} {}^{\alpha_0}_{\beta_0}\left[c_{H|_1^1}\right]_{l_0} \mathrm{e}^{\mathrm{i}Ql_0} \left|Q,\alpha_0\right\rangle \tag{D.2a}$$

with

$${}^{\alpha_0}_{\beta_0}\left[c_{H|_1^1}\right]_{l_0} := \left\langle r,\alpha_0\right| H_{\mathrm{eff}}\big|_1^1 \left|r+l_0,\beta_0\right\rangle \tag{D.2b}$$

and $l_0 \in \mathbb{Z}$. Note that due to the translational symmetry only the relative distance l_0 between the states $\left|r,\alpha_0\right\rangle$ and $\left|r+l_0,\beta_0\right\rangle$ occurs in the coefficient ${}^{\alpha_0}_{\beta_0}\left[c_{H|_1^1}\right]_{l_0}$. In the special case of a SU(2) symmetric Hamiltonian the coefficients ${}^{\alpha_0}_{\beta_0}\left[c_{H|_1^1}\right]_{l_0}$ obey the relation ${}^{\alpha_0}_{\beta_0}\left[c_{H|_1^1}\right]_{l_0} = \delta_{\alpha_0,\beta_0}\left[c_{H|_1^1}\right]_{l_0}$. The used truncation scheme (cf. section 3.4.3) causes ${}^{\alpha_0}_{\beta_0}\left[c_{H|_1^1}\right]_{l_0} = 0$ for $|l_0| > D_2$. All other coefficients ${}^{\alpha_0,\alpha_1,\ldots,\alpha_{N_c}}_{\beta_0,\beta_1,\ldots,\beta_{N_a}}\left[c_{H|_{N_a}^{N_c}}\right]^{d_1,\ldots,d_{N_c}}_{l_0,l_1,\ldots,l_{N_a}}$ which appear in the following are affected by the truncation scheme in an analogous way.

The action of the operator $H_{\text{eff}}\big|_1^1$ on the two-triplon state $\big|Q,\beta_0\big\rangle\big|l_1,\beta_1\big\rangle$ is given by

$$\begin{aligned} H_{\text{eff}}\big|_1^1 \big|Q,\beta_0\big\rangle\big|l_1,\beta_1\big\rangle = &\sum_{\substack{l_0>-l_1\\ \alpha_0}} {}^{\alpha_0}_{\beta_0}\big[c_{H|_1^1}\big]_{l_0}\, \mathrm{e}^{\mathrm{i}Q\frac{l_0}{2}}\, \big|Q,\alpha_0\big\rangle\big|l_0+l_1,\beta_1\big\rangle \\ &+\sum_{\substack{l_0<-l_1\\ \alpha_0}} {}^{\alpha_0}_{\beta_0}\big[c_{H|_1^1}\big]_{l_0}\, \mathrm{e}^{\mathrm{i}Q\frac{l_0}{2}} \big|Q,\beta_1\big\rangle\big|-(l_0+l_1),\alpha_0\big\rangle \\ &+\sum_{\substack{l_0<l_1\\ \alpha_0}} {}^{\alpha_0}_{\beta_1}\big[c_{H|_1^1}\big]_{l_0}\, \mathrm{e}^{\mathrm{i}Q\frac{l_0}{2}} \big|Q,\beta_0\big\rangle\big|-(l_0-l_1),\alpha_0\big\rangle \\ &+\sum_{\substack{l_0>l_1\\ \alpha_0}} {}^{\alpha_0}_{\beta_1}\big[c_{H|_1^1}\big]_{l_0}\, \mathrm{e}^{\mathrm{i}Q\frac{l_0}{2}} \big|Q,\alpha_0\big\rangle\big|l_0-l_1,\beta_0\big\rangle\,. \end{aligned} \tag{D.3}$$

The action of the operator $H_{\text{eff}}\big|_1^1$ on the three-triplon state $\big|Q,\beta_0\big\rangle\big|l_1,\beta_1\big\rangle\big|l_2,\beta_2\big\rangle$ is given by

$$
\begin{aligned}
H_{\text{eff}}\big|_1^1\,\big|Q,\beta_0\big\rangle\big|l_1,\beta_1\big\rangle\big|l_2,\beta_2\big\rangle = &\sum_{\substack{l_0>-l_1\\ \alpha_0}} {}^{\alpha_0}_{\beta_0}\big[c_{H|_1^1}\big]_{l_0}\, \mathrm{e}^{\mathrm{i}Q\frac{l_0}{3}}\big|Q,\alpha_0\big\rangle\big|l_0+l_1,\beta_1\big\rangle\big|l_2,\beta_2\big\rangle\\
&+\sum_{\substack{-(l_1+l_2)<l_0<-l_1\\ \alpha_0}} {}^{\alpha_0}_{\beta_0}\big[c_{H|_1^1}\big]_{l_0}\, \mathrm{e}^{\mathrm{i}Q\frac{l_0}{3}}\big|Q,\beta_1\big\rangle\big|-(l_0+l_1),\alpha_0\big\rangle\big|l_0+l_1+l_2,\beta_2\big\rangle\\
&+\sum_{\substack{l_0<-(l_1+l_2)\\ \alpha_0}} {}^{\alpha_0}_{\beta_0}\big[c_{H|_1^1}\big]_{l_0}\, \mathrm{e}^{\mathrm{i}Q\frac{l_0}{3}}\big|Q,\beta_1\big\rangle\big|l_2,\beta_2\big\rangle\big|-(l_0+l_1+l_2),\alpha_0\big\rangle\\
&+\sum_{\substack{-l_2<l_0<l_1\\ \alpha_0}} {}^{\alpha_0}_{\beta_1}\big[c_{H|_1^1}\big]_{l_0}\, \mathrm{e}^{\mathrm{i}Q\frac{l_0}{3}}\big|Q,\beta_0\big\rangle\big|-(l_0-l_1),\alpha_0\big\rangle\big|l_0+l_2,\beta_2\big\rangle\\
&+\sum_{\substack{l_0>l_1\\ \alpha_0}} {}^{\alpha_0}_{\beta_1}\big[c_{H|_1^1}\big]_{l_0}\, \mathrm{e}^{\mathrm{i}Q\frac{l_0}{3}}\big|Q,\alpha_0\big\rangle\big|l_0-l_1,\beta_0\big\rangle\big|l_1+l_2,\beta_2\big\rangle\\
&+\sum_{\substack{l_0<-l_2\\ \alpha_0}} {}^{\alpha_0}_{\beta_1}\big[c_{H|_1^1}\big]_{l_0}\, \mathrm{e}^{\mathrm{i}Q\frac{l_0}{3}}\big|Q,\beta_0\big\rangle\big|l_1+l_2,\beta_2\big\rangle\big|-(l_0+l_2),\alpha_0\big\rangle\\
&+\sum_{\substack{l_0<l_2\\ \alpha_0}} {}^{\alpha_0}_{\beta_2}\big[c_{H|_1^1}\big]_{l_0}\, \mathrm{e}^{\mathrm{i}Q\frac{l_0}{3}}\big|Q,\beta_0\big\rangle\big|l_1,\beta_1\big\rangle\big|-(l_0-l_2),\alpha_0\big\rangle\\
&+\sum_{\substack{l_2<l_0<l_1+l_2\\ \alpha_0}} {}^{\alpha_0}_{\beta_2}\big[c_{H|_1^1}\big]_{l_0}\, \mathrm{e}^{\mathrm{i}Q\frac{l_0}{3}}\big|Q,\beta_0\big\rangle\big|-(l_0-l_1-l_2),\alpha_0\big\rangle\big|l_0-l_2,\beta_1\big\rangle\\
&+\sum_{\substack{l_0>l_1+l_2\\ \alpha_0}} {}^{\alpha_0}_{\beta_2}\big[c_{H|_1^1}\big]_{l_0}\, \mathrm{e}^{\mathrm{i}Q\frac{l_0}{3}}\big|Q,\alpha_0\big\rangle\big|l_0-l_1-l_2,\beta\big\rangle\big|l_1,\beta_1\big\rangle
\end{aligned}
\tag{D.4}
$$

D.2 $H_{\text{eff}}\big|_1^2$

The action of the operator $H_{\text{eff}}\big|_1^2$ on the one-triplon state $\big|Q,\beta_0\big\rangle$ is given by

$$
H_{\text{eff}}\big|_1^2\,\big|Q,\beta_0\big\rangle = \sum_{\substack{l_0,d_1\\ \alpha_0,\alpha_1}} {}^{\alpha_0,\alpha_1}_{\beta_0}\big[c_{H|_1^2}\big]^{d_1}_{l_0}\, \mathrm{e}^{\mathrm{i}Q\left(l_0-\frac{d_1}{2}\right)}\big|Q,\alpha_0\big\rangle\big|d_1,\alpha_1\big\rangle \tag{D.5a}
$$

with

$$
{}^{\alpha_0,\alpha_1}_{\beta_0}\big[c_{H|_1^2}\big]^{d_1}_{l_0} := \big\langle r,\alpha_0\big|\big\langle r+d_1,\alpha_1\big|\,H_{\text{eff}}\big|_1^2\,\big|r+l_0,\beta_0\big\rangle\,. \tag{D.6}
$$

The action of the operator $H_{\text{eff}}\big|_1^2$ on the two-triplon state $\big|Q,\beta_0\big\rangle\big|l_1,\beta_1\big\rangle$ is given by

$$
\begin{aligned}
H_{\text{eff}}\big|_1^2\,\big|Q,\beta_0\big\rangle\big|l_1,\beta_1\big\rangle = &\sum_{\substack{l_0>-l_1+d_1,d_1\\ \alpha_0,\alpha_1}} {}^{\alpha_0,\alpha_1}_{\beta_0}\big[c_{H|_1^2}\big]_{l_0}^{d_1}\, \mathrm{e}^{\mathrm{i}Q\left(\frac{4l_0+l_1-2d_1}{6}\right)}\,\big|Q,\alpha_0\big\rangle\big|d_1,\alpha_1\big\rangle\big|l_0+l_1-d_1,\beta_1\big\rangle \\
&+\sum_{\substack{-l_1<l_0<-l_1+d_1,d_1\\ \alpha_0,\alpha_1}} {}^{\alpha_0,\alpha_1}_{\beta_0}\big[c_{H|_1^2}\big]_{l_0}^{d_1}\, \mathrm{e}^{\mathrm{i}Q\left(\frac{4l_0+l_1-2d_1}{6}\right)}\,\big|Q,\alpha_1\big\rangle\big|l_0+l_1,\beta_1\big\rangle\big|-(l_0+l_1)+d_1,\alpha_2\big\rangle \\
&+\sum_{\substack{l_0<-l_1,d_1\\ \alpha_0,\alpha_1}} {}^{\alpha_0,\alpha_1}_{\beta_0}\big[c_{H|_1^2}\big]_{l_0}^{d_1}\, \mathrm{e}^{\mathrm{i}Q\left(\frac{4l_0+l_1-2d_1}{6}\right)}\,\big|Q,\beta_1\big\rangle\big|-(l_0+l_1),\alpha_0\big\rangle\big|d_1,\alpha_1\big\rangle \\
&+\sum_{\substack{l_0<l_1,d_1\\ \alpha_0,\alpha_1}} {}^{\alpha_0,\alpha_1}_{\beta_1}\big[c_{H|_1^2}\big]_{l_0}^{d_1}\, \mathrm{e}^{\mathrm{i}Q\left(\frac{4l_0-l_1-2d_1}{6}\right)}\,\big|Q,\beta_0\big\rangle\big|-l_0+l_1,\alpha_0\big\rangle\big|d_1,\alpha_1\big\rangle \\
&+\sum_{\substack{l_1<l_0<l_1+d_1,d_1\\ \alpha_0,\alpha_1}} {}^{\alpha_0,\alpha_1}_{\beta_1}\big[c_{H|_1^2}\big]_{l_0}^{d_1}\, e^{\mathrm{i}Q\left(\frac{4l_0-l_1-2d_1}{6}\right)}\,\big|Q,\alpha_0\big\rangle\big|l_0-l_1,\beta_0\big\rangle\big|-l_0+l_1+d_1,\alpha_1\big\rangle \\
&+\sum_{\substack{l_0>l_1+d_1,d_1\\ \alpha_0,\alpha_1}} {}^{\alpha_0,\alpha_1}_{\beta_1}\big[c_{H|_1^2}\big]_{l_0}^{d_1}\, \mathrm{e}^{\mathrm{i}Q\left(\frac{4l_0-l_1-2d_1}{6}\right)}\,\big|Q,\alpha_0\big\rangle\big|d_1,\alpha_1\big\rangle\big|l_0-(l_1+d_1),\beta_0\big\rangle
\end{aligned}
\tag{D.7}
$$

D.3 $H_{\mathbf{eff}}\big|_2^1$

The action of the operator $H_{\text{eff}}\big|_2^1$ on the two-triplon state $\big|Q,\beta_0\big\rangle\big|l_1,\beta_1\big\rangle$ is given by

$$
H_{\text{eff}}\big|_2^1\,\big|Q,\beta_0\big\rangle\big|l_1,\beta_1\big\rangle = \sum_{l_0,\alpha_0} {}^{\alpha_0}_{\beta_0,\beta_1}\big[c_{H|_2^1}\big]_{l_0,l_1}\, \mathrm{e}^{\mathrm{i}Q\left(l_0+\frac{l_1}{2}\right)}\,\big|Q,\alpha_0\big\rangle \tag{D.8a}
$$

with

$$
{}^{\alpha_0}_{\beta_0,\beta_1}\big[c_{H|_2^1}\big]_{l_0,l_1} := \big\langle r,\alpha_0\big|\, H_{\text{eff}}\big|_2^1\,\big|r+l_0,\beta_0\big\rangle\big|r+l_0+l_1,\beta_1\big\rangle\,. \tag{D.8b}
$$

The action of the operator $H_{\text{eff}}\big|_2^1$ on the three-triplon state $\big|Q,\beta_0\big\rangle\big|l_1,\beta_1\big\rangle\big|l_2,\beta_2\big\rangle$ is given by

$$\begin{aligned}
H_{\text{eff}}\big|_2^1\,\big|Q,\beta_0\big\rangle\big|l_1,\beta_1\big\rangle\big|l_2,\beta_2\big\rangle = &\sum_{\substack{l_0>-(l_1+l_2)\\ \alpha_0}} {}^{\alpha_0}_{\beta_0,\beta_1}\big[c_{H|_2^1}\big]_{l_0,l_1}\, \mathrm{e}^{\mathrm{i}Q\left(\frac{3l_0+l_1-l_2}{6}\right)}\,\big|Q,\alpha_0\big\rangle\big|l_0+l_1+l_2,\beta_2\big\rangle\\
&+\sum_{\substack{l_0<-(l_1+l_2)\\ \alpha_0}} {}^{\alpha_0}_{\beta_0,\beta_1}\big[c_{H|_2^1}\big]_{l_0,l_1}\, \mathrm{e}^{\mathrm{i}Q\left(\frac{3l_0+l_1-l_2}{6}\right)}\,\big|Q,\beta_2\big\rangle\big|-(l_0+l_1+l_2),\alpha_0\big\rangle\\
&+\sum_{\substack{l_0<l_1\\ \alpha_0}} {}^{\alpha_0}_{\beta_1,\beta_2}\big[c_{H|_2^1}\big]_{l_0,l_2}\, \mathrm{e}^{\mathrm{i}Q\left(\frac{3l_0+l_1+2l_2}{6}\right)}\,\big|Q,\beta_0\big\rangle\big|-l_0+l_1,\alpha_0\big\rangle\\
&+\sum_{\substack{l_0>l_1\\ \alpha_0}} {}^{\alpha_0}_{\beta_1,\beta_2}\big[c_{H|_2^1}\big]_{l_0,l_2}\, \mathrm{e}^{\mathrm{i}Q\left(\frac{3l_0+l_1+2l_2}{6}\right)}\,\big|Q,\alpha_0\big\rangle\big|l_0-l_1,\beta_0\big\rangle\\
&+\sum_{\substack{l_0>-l_1\\ \alpha_0}} {}^{\alpha_0}_{\beta_0,\beta_2}\big[c_{H|_2^1}\big]_{l_0,l_1+l_2}\, \mathrm{e}^{\mathrm{i}Q\left(\frac{3l_0+l_1+2l_2}{6}\right)}\,\big|Q,\alpha_0\big\rangle\big|l_0+l_1,\beta_1\big\rangle\\
&+\sum_{\substack{l_0<-l_1\\ \alpha_0}} {}^{\alpha_0}_{\beta_0,\beta_2}\big[c_{H|_2^1}\big]_{l_0,l_1+l_2}\, \mathrm{e}^{\mathrm{i}Q\left(\frac{3l_0+l_1+2l_2}{6}\right)}\,\big|Q,\beta_1\big\rangle\big|-(l_0+l_1),\alpha_0\big\rangle
\end{aligned} \tag{D.9}$$

D.4 $H_{\text{eff}}\big|_1^3$

The action of the operator $H_{\text{eff}}\big|_1^3$ on the one-triplon state $\big|Q,\beta_0\big\rangle$ is given by

$$H_{\text{eff}}\big|_1^3\,\big|Q,\beta_0\big\rangle = \sum_{\substack{l_0,d_1,d_2\\ \alpha_0,\alpha_1,\alpha_2}} {}^{\alpha_0,\alpha_1,\alpha_2}_{\beta_0}\big[c_{H|_1^3}\big]_{l_0}^{d_1,d_2}\, \mathrm{e}^{\mathrm{i}Q\left(l_0-\frac{2d_1+d_2}{3}\right)}\,\big|Q,\alpha_0\big\rangle\big|d_1,\alpha_1\big\rangle\big|d_2,\alpha_2\big\rangle \tag{D.10a}$$

with

$${}^{\alpha_0,\alpha_1,\alpha_2}_{\beta_0}\big[c_{H|_1^3}\big]_{l_0}^{d_1,d_2} := \big\langle r,\alpha_0\big|\big\langle r+d_1,\alpha_1\big|\big\langle r+d_1+d_2,\alpha_2\big|\,H_{\text{eff}}\big|_1^3\,\big|r+l_0,\beta_0\big\rangle\,. \tag{D.10b}$$

D.5 $H_{\mathbf{eff}}\big|_3^1$

The action of the operator $H_{\text{eff}}\big|_3^1$ on the three-triplon state $\big|Q,\beta_0\big\rangle\big|l_1,\beta_1\big\rangle\big|l_2,\beta_2\big\rangle$ is given by

$$H_{\text{eff}}\big|_3^1\,\big|Q,\beta_0\big\rangle\big|l_1,\beta_1\big\rangle\big|l_2,\beta_2\big\rangle=\sum_{l_0,\alpha_0}\;{}^{\alpha_0}_{\beta_0,\beta_1,\beta_2}\Big[c_{H|_3^1}\Big]_{l_0,l_1,l_2}\,\mathrm{e}^{\mathrm{i}Q\left(l_0+\frac{2l_1+l_2}{3}\right)}\,\big|Q,\alpha_0\big\rangle \tag{D.11a}$$

with

$${}^{\alpha_0}_{\beta_0,\beta_1,\beta_2}\Big[c_{H|_3^1}\Big]_{l_0,l_1,l_2}:=\big\langle r,\alpha_0\big|\,H_{\text{eff}}\big|_3^1\,\big|r+l_0,\beta_0\big\rangle\big|r+l_0+l_1,\beta_1\big\rangle\big|r+l_0+l_1+l_2,\beta_0\big\rangle\,. \tag{D.11b}$$

D.6 $H_{\mathbf{eff}}\big|_2^2$

The action of the operator $H_{\text{eff}}\big|_2^2$ on the two-triplon state $\big|Q,\beta_0\big\rangle\big|l_1,\beta_1\big\rangle$ is given by

$$H_{\text{eff}}\big|_2^2\,\big|Q,\beta_0\big\rangle\big|l_1,\beta_1\big\rangle=\sum_{\substack{l_0,d_1\\ \alpha_0,\alpha_1}}\;{}^{\alpha_0,\alpha_1}_{\beta_0,\beta_1}\Big[c_{H|_2^2}\Big]^{d_1}_{l_0,l_1}\,\mathrm{e}^{\mathrm{i}Q\left(l_0+\frac{l_1-d_1}{2}\right)}\,\big|Q,\alpha_0\big\rangle\big|d_1,\alpha_1\big\rangle \tag{D.12a}$$

with

$${}^{\alpha_0,\alpha_1}_{\beta_0,\beta_1}\Big[c_{H|_2^2}\Big]^{d_1}_{l_0,l_1}:=\big\langle r,\alpha_0\big|\big\langle r+d_1,\alpha_1\big|\,H_{\text{eff}}\big|_2^2\,\big|r+l_0,\beta_0\big\rangle\big|r+l_0+l_1,\beta_1\big\rangle\,. \tag{D.12b}$$

The action of the operator $H_{\text{eff}}\big|_2^2$ on the three-triplon state $\big|Q,\beta_0\big\rangle\big|l_1,\beta_1\big\rangle\big|l_2,\beta_2\big\rangle$ is given by

$$
\begin{aligned}
&H_{\text{eff}}\big|_2^2\,\big|Q,\beta_0\big\rangle\big|l_1,\beta_1\big\rangle\big|l_2,\beta_2\big\rangle \\
&\quad=\sum_{\substack{l_0>-(l_1+l_2)+d_1,d_1\\ \alpha_0,\alpha_1}}^{\substack{\alpha_0,\alpha_1\\ \beta_0,\beta_1}}\Big[c_{H|_2^2}\Big]_{l_0,l_1}^{d_1}\,\mathrm{e}^{\mathrm{i}Q\left(\frac{2l_0+l_1-d_1}{3}\right)}\,\big|Q,\alpha_0\big\rangle\big|d_1,\alpha_1\big\rangle\big|l_0+l_1+l_2-d_1,\beta_2\big\rangle \\
&\quad+\sum_{\substack{-(l_1+l_2)<l_0<-(l_1+l_2)+d_1,d_1\\ \alpha_0,\alpha_1}}^{\substack{\alpha_0,\alpha_1\\ \beta_0,\beta_1}}\Big[c_{H|_2^2}\Big]_{l_0,l_1}^{d_1}\,\mathrm{e}^{\mathrm{i}Q\left(\frac{2l_0+l_1-d_1}{3}\right)}\,\big|Q,\alpha_0\big\rangle\big|l_0+l_1+l_2,\beta_2\big\rangle\big|-(l_0+l_1+l_2)+d_1,\alpha_1\big\rangle \\
&\quad+\sum_{\substack{l_0<-(l_1+l_2)\\ d_1,\alpha_0,\alpha_1}}^{\substack{\alpha_0,\alpha_1\\ \beta_0,\beta_1}}\Big[c_{H|_2^2}\Big]_{l_0,l_1}^{d_1}\,\mathrm{e}^{\mathrm{i}Q\left(\frac{2l_0+l_1-d_1}{3}\right)}\,\big|Q,\beta_2\big\rangle\big|-(l_0+l_1+l_2),\alpha_0\big\rangle\big|d_1,\alpha_1\big\rangle \\
&\quad+\sum_{\substack{-l_1<l_0<d_1,d_1\\ \alpha_0,\alpha_1}}^{\substack{\alpha_0,\alpha_1\\ \beta_0,\beta_2}}\Big[c_{H|_2^2}\Big]_{l_0,l_1+l_2}^{l_1+d_1}\,\mathrm{e}^{\mathrm{i}Q\left(\frac{2l_0+l_2-d_1}{3}\right)}\,\big|Q,\alpha_0\big\rangle\big|l_0+l_1,\beta_1\big\rangle\big|-r+d_1,\alpha_1\big\rangle \\
&\quad+\sum_{\substack{l_0<-l_1,d_1\\ \alpha_0,\alpha_1}}^{\substack{\alpha_0,\alpha_1\\ \beta_0,\beta_2}}\Big[c_{H|_2^2}\Big]_{l_0,l_1+l_2}^{l_1+d_1}\,\mathrm{e}^{\mathrm{i}Q\left(\frac{2l_0+l_2-d_1}{3}\right)}\,\big|Q,\beta_1\big\rangle\big|-(l_0+l_1),\alpha_0\big\rangle\big|l_1+d_1,\alpha_1\big\rangle \\
&\quad+\sum_{\substack{l_0>d_1,d_1\\ \alpha_0,\alpha_1}}^{\substack{\alpha_0,\alpha_1\\ \beta_0,\beta_2}}\Big[c_{H|_2^2}\Big]_{l_0,l_1+l_2}^{l_1+d_1}\,\mathrm{e}^{\mathrm{i}Q\left(\frac{2l_0+l_2-d_1}{3}\right)}\,\big|Q,\alpha_0\big\rangle\big|l_1+d_1,\alpha_1\big\rangle\big|l_0-d_1,\beta_1\big\rangle \\
&\quad+\sum_{\substack{l_0<l_1,d_1\\ \alpha_0,\alpha_1}}^{\substack{\alpha_0,\alpha_1\\ \beta_1,\beta_2}}\Big[c_{H|_2^2}\Big]_{l_0,l_2}^{d_1}\,\mathrm{e}^{\mathrm{i}Q\left(\frac{2l_0+l_2-d_1}{3}\right)}\,\big|Q,\beta_0\big\rangle\big|-l_0+l_1,\alpha_0\big\rangle\big|d_1,\alpha_1\big\rangle \\
&\quad+\sum_{\substack{l_1<l_0<l_1+d_1,d_1\\ \alpha_0,\alpha_1}}^{\substack{\alpha_0,\alpha_1\\ \beta_1,\beta_2}}\Big[c_{H|_2^2}\Big]_{l_0,l_2}^{d_1}\,\mathrm{e}^{\mathrm{i}Q\left(\frac{2l_0+l_2-d_1}{3}\right)}\,\big|Q,\alpha_0\big\rangle\big|l_0-l_1,\beta_0\big\rangle\big|-l_0+l_1+d_1,\alpha_1\big\rangle \\
&\quad+\sum_{\substack{l_0>l_1+d_1,d_1\\ \alpha_0,\alpha_1}}^{\substack{\alpha_0,\alpha_1\\ \beta_1,\beta_2}}\Big[c_{H|_2^2}\Big]_{l_0,l_2}^{d_1}\,\mathrm{e}^{\mathrm{i}Q\left(\frac{2r+l_2-d_1}{3}\right)}\,\big|Q,\alpha_0\big\rangle\big|d_1,\alpha_1\big\rangle\big|l_0-(l_1+d_1),\beta_0\big\rangle
\end{aligned}
\tag{D.13}
$$

D.7 $H_{\text{eff}}\big|_2^3$

The action of the operator $H_{\text{eff}}\big|_2^3$ on the two-triplon state $\big|Q,\beta_0\big\rangle\big|l_1,\beta_1\big\rangle$ is given by

$$
H_{\text{eff}}\big|_2^3\,\big|Q,\beta_0\big\rangle\big|l_1,\beta_1\big\rangle=\sum_{\substack{l_0,d_1,d_2\\ \alpha_0,\alpha_1,\alpha_2}}^{\substack{\alpha_0,\alpha_1,\alpha_2\\ \beta_0,\beta_1}}\Big[c_{H|_2^3}\Big]_{l_0,l_1}^{d_1,d_2}\,\mathrm{e}^{\mathrm{i}Q\left(l_0+\frac{3l_1-4d_1-2d_2}{6}\right)}\,\big|Q,\alpha_0\big\rangle\big|d_1,\alpha_1\big\rangle\big|d_2,\alpha_2\big\rangle \tag{D.14a}
$$

with

$$\begin{matrix}\alpha_0,\alpha_1,\alpha_2\\ \beta_0,\beta_1\end{matrix}\left[c_{H|_2^3}\right]_{l_0,l_1}^{d_1,d_2} := \left\langle r,\alpha_0\right|\left\langle r+d_1,\alpha_1\right|\left\langle r+d_1+d_2,\alpha_2\right| H_{\text{eff}}\big|_2^3 \left|r+l_0,\beta_0\right\rangle\left|r+l_0+l_1,\beta_1\right\rangle . \tag{D.14b}$$

D.8 $H_{\mathbf{eff}}\big|_3^2$

The action of the operator $H_{\text{eff}}\big|_3^2$ on the three-triplon state $\left|Q,\beta_0\right\rangle\left|l_1,\beta_1\right\rangle\left|l_2,\beta_2\right\rangle$ is given by

$$H_{\text{eff}}\big|_3^2 \left|Q,\beta_0\right\rangle\left|l_1,\beta_1\right\rangle\left|l_2,\beta_2\right\rangle := \sum_{\substack{l_0,d_1\\ \alpha_0,\alpha_1}} \begin{matrix}\alpha_0,\alpha_1\\ \beta_0,\beta_1,\beta_2\end{matrix}\left[c_{H|_3^2}\right]_{l_0,l_1,l_2}^{d_1} \mathrm{e}^{\mathrm{i}Q\left(l_0+\frac{4l_1+2l_2-3d_1}{6}\right)}\left|Q,\alpha_0\right\rangle\left|d_1,\alpha_1\right\rangle \tag{D.15a}$$

with

$$\begin{matrix}\alpha_0,\alpha_1\\ \beta_0,\beta_1,\beta_2\end{matrix}\left[c_{H|_3^2}\right]_{l_0,l_1,l_2}^{d_1} := \left\langle r,\alpha_0\right|\left\langle r+d_1,\alpha_1\right| H_{\text{eff}}\big|_3^2 \left|r+l_0,\beta_0\right\rangle\left|r+l_0+l_1,\beta_1\right\rangle\left|r+l_0+l_1+l_2,\beta_2\right\rangle . \tag{D.15b}$$

D.9 $H_{\mathbf{eff}}\big|_3^3$

The action of the operator $H_{\text{eff}}\big|_3^3$ on the three-triplon state $\left|Q,\beta_0\right\rangle\left|l_1,\beta_1\right\rangle\left|l_2,\beta_2\right\rangle$ is given by

$$H_{\text{eff}}\big|_3^3 \left|Q,\beta_0\right\rangle\left|l_1,\beta_1\right\rangle\left|l_2,\beta_2\right\rangle = \sum_{\substack{l_0,d_1,d_2\\ \alpha_0,\alpha_1,\alpha_2}} \begin{matrix}\alpha_0,\alpha_1,\alpha_2\\ \beta_0,\beta_1,\beta_2\end{matrix}\left[c_{H|_3^3}\right]_{l_0,l_1,l_2}^{d_1,d_2} \mathrm{e}^{\mathrm{i}Q\left(l_0+\frac{2(l_1-d_1)+(l_2-d_2)}{3}\right)}\left|Q,\alpha_0\right\rangle\left|d_1,\alpha_1\right\rangle\left|d_2,\alpha_2\right\rangle \tag{D.16a}$$

with

$$\begin{matrix}\alpha_0,\alpha_1,\alpha_2\\ \beta_0,\beta_1,\beta_2\end{matrix}\left[c_{H|_3^3}\right]_{l_0,l_1,l_2}^{d_1,d_2} := \left\langle r,\alpha_0\right|\left\langle r+d_1,\alpha_1\right|\left\langle r+d_1+d_2,\alpha_2\right| H_{\text{eff}}\big|_3^3 \left|r+l_0,\beta_0\right\rangle\left|r+l_0+l_1,\beta_1\right\rangle\left|r+l_0+d_1+d_2,\beta_2\right\rangle . \tag{D.16b}$$

D.10 Spin subspace $S = 1$, $m = 0$

Due to the SU(2) spin symmetry it is possible to reduce the computational effort. The one-, two- and three-triplon states with $S = 1$ and $m = 0$ are listed in table D.1. Since

Table D.1: States of the $S = 1$ and $m = 0$ subspace.

$\big\|Q\big\rangle^{S=1}_{m=0}$	$\big\|z\big\rangle$
$\big\|Q,d_1\big\rangle^{S=1}_{m=0}$	$\frac{\mathrm{i}}{\sqrt{2}}\big(\big\|x,y\big\rangle - \big\|y,x\big\rangle\big)$
$\big\|Q,d_1,d_2,1\big\rangle^{S=1}_{m=0}$	$-\sqrt{\frac{3}{20}}\big(\big\|z,x,x\big\rangle + \big\|z,y,y\big\rangle + \big\|x,z,x\big\rangle + \big\|y,z,y\big\rangle\big)$
	$-\sqrt{\frac{2}{30}}\big(2\big\|z,z,z\big\rangle - \big\|x,x,z\big\rangle - \big\|y,y,z\big\rangle\big)$
$\big\|Q,d_1,d_2,2\big\rangle^{S=1}_{m=0}$	$\frac{1}{2}\big(\big\|z,x,x\big\rangle + \big\|z,y,y\big\rangle - \big\|x,z,x\big\rangle - \big\|y,z,y\big\rangle\big)$
$\big\|Q,d_1,d_2,3\big\rangle^{S=1}_{m=0}$	$\frac{1}{\sqrt{3}}\big(\big\|x,x,z\big\rangle + \big\|y,y,z\big\rangle + \big\|z,z,z\big\rangle\big)$

they are independent of the total momentum Q and the relative distances d_1 and d_2 we omit the dependence on these parameters.

Appendix E

Fourier transformed effective observables

Let $O_{\text{eff}}(r)$ be a local effective observable given as a sum over terms of local creation and annihilation operators. We use the notation defined in equation (3.103). The action of the local effective observable $O_{\text{eff}}(r)$ on the vacuum state $|0\rangle$ is given by

$$O_{\text{eff}}(r)\big|0\big\rangle = \sum_{i\geq 0} O_{\text{eff}}(r)\big|_0^i \,\big|0\big\rangle \tag{E.1a}$$

$$\begin{aligned}
&= \Big[c_{O|_0^0}\Big]\big|0\big\rangle \\
&\quad + \sum_{d_0,\alpha_0}{}^{\alpha_0}\Big[c_{O|_0^1}\Big]^{d_0}\,\big|r+d_0,\alpha_0\big\rangle \\
&\quad + \sum_{\substack{d_0,d_1\\ \alpha_0,\alpha_1}}{}^{\alpha_0\alpha_1}\Big[c_{O|_0^2}\Big]^{d_0,d_1}\big|r+d_0,\alpha_0\big\rangle\big|r+d_0+d_1,\alpha_1\big\rangle \\
&\quad + \sum_{\substack{d_0,d_1,d_2\\ \alpha_0,\alpha_1,\alpha_2}}{}^{\alpha_0\alpha_1\alpha_2}\Big[c_{O|_0^3}\Big]^{d_0,d_1,d_2}\,\big|r+d_0,\alpha_0\big\rangle\big|r+d_0+d_1,\alpha_1\big\rangle\big|r+d_0+d_1+d_2,\alpha_2\big\rangle \\
&\quad + \dots
\end{aligned} \tag{E.1b}$$

with $d_0 \in \mathbb{Z}$ and $d_1, d_2, \dots > 0$. The Fourier transformation of the state $O_{\text{eff}}(r)\,|0\rangle$ is defined as

$$O_{\text{eff}}(Q)\big|0\big\rangle := \frac{1}{\sqrt{N}}\sum_{r=0}^{N} \mathrm{e}^{\mathrm{i}Qr} O_{\text{eff}}(r)\big|0\big\rangle\,. \tag{E.2}$$

Each part $O_{\text{eff}}(r)\big|_0^i$ of $O_{\text{eff}}(r)$ can be investigated separately. The Fourier transformation of the one-particle sector is given by

$$O_{\text{eff}}(Q)\big|_0^1 \big|0\big\rangle = \frac{1}{\sqrt{\mathcal{N}}} \sum_{r=0}^{\mathcal{N}} \mathrm{e}^{\mathrm{i}Qr} \sum_{d_0,\alpha_0} {}^{\alpha_0}\Big[c_{O|_0^1}\Big]^{d_0} \, \big|r+d_0,\alpha_0\big\rangle \tag{E.3a}$$

$$= \sum_{d_0,\alpha_0} {}^{\alpha_0}\Big[c_{O|_0^1}\Big]^{d_0} \, \mathrm{e}^{-\mathrm{i}Qd_0} \big|Q,\alpha_0\big\rangle \tag{E.3b}$$

$$= \sum_{\alpha_0} {}^{\alpha_0}\Big[C_{O|_0^1}(Q)\Big] \big|Q,\alpha_0\big\rangle \tag{E.3c}$$

with

$${}^{\alpha_0}\Big[C_{O|_0^1}(Q)\Big] := \sum_{d_0} {}^{\alpha_0}\Big[c_{O|_0^1}\Big]^{d_0} \, \mathrm{e}^{-\mathrm{i}Qd_0} \, . \tag{E.3d}$$

The two-particle sector is given by

$$O_{\text{eff}}(Q)\big|_0^2 \big|0\big\rangle = \frac{1}{\sqrt{\mathcal{N}}} \sum_{r=0}^{\mathcal{N}} \mathrm{e}^{\mathrm{i}Qr} \sum_{\substack{d_0,d_1 \\ \alpha_0,\alpha_1}} {}^{\alpha_0,\alpha_1}\Big[c_{O|_0^2}\Big]^{d_0,d_1} \, \big|r+d_0,\alpha_0\big\rangle \big|r+d_0+d_1,\alpha_1\big\rangle \tag{E.4a}$$

$$= \frac{1}{\sqrt{\mathcal{N}}} \sum_{r=0}^{\mathcal{N}} \sum_{\substack{d_0,d_1 \\ \alpha_0,\alpha_1}} {}^{\alpha_0,\alpha_1}\Big[c_{O|_0^2}\Big]^{d_0,d_1} \, \mathrm{e}^{\mathrm{i}Q(r-d_0)} \big|r,\alpha_0\big\rangle \big|r+d_1,\alpha_1\big\rangle \tag{E.4b}$$

$$= \sum_{\substack{d_0,d_1 \\ \alpha_0,\alpha_1}} {}^{\alpha_0,\alpha_1}\Big[c_{O|_0^2}\Big]^{d_0,d_1} \, \mathrm{e}^{-\mathrm{i}Q\left(\frac{2d_0+d_1}{2}\right)} \frac{1}{\sqrt{\mathcal{N}}} \sum_{r=0}^{\mathcal{N}} \mathrm{e}^{\mathrm{i}Q\left((r+\frac{d_1}{2}\right)} \big|r,\alpha_0\big\rangle \big|r+d_1,\alpha_1\big\rangle \tag{E.4c}$$

$$= \sum_{\substack{d_0,d_1 \\ \alpha_0,\alpha_1}} {}^{\alpha_0,\alpha_1}\Big[c_{O|_0^2}\Big]^{d_0,d_1} \, \mathrm{e}^{-\mathrm{i}Q\left(\frac{2d_0+d_1}{2}\right)} \big|Q,\alpha_0\big\rangle \big|d_1,\alpha_1\big\rangle \tag{E.4d}$$

$$= \sum_{\substack{d_1 \\ \alpha_0,\alpha_1}} {}^{\alpha_0,\alpha_1}\Big[C_{O|_0^2}(Q)\Big]^{d_1} \, \big|Q,\alpha_0\big\rangle \big|d_1,\alpha_1\big\rangle \tag{E.4e}$$

with

$${}^{\alpha_0,\alpha_1}\Big[C_{O|_0^2}(Q)\Big]^{d_1} := \sum_{d_0} {}^{\alpha_0,\alpha_1}\Big[c_{O|_0^2}\Big]^{d_0,d_1} \, \mathrm{e}^{-\mathrm{i}Q\left(\frac{2d_0+d_1}{2}\right)} \tag{E.4f}$$

and $d_1 > 0$. Finally, the three-particle sector is given by

$$
\begin{aligned}
&O_{\mathrm{eff}}(Q)\big|_0^3\,|0\rangle \\
&= \frac{1}{\sqrt{N}}\sum_{r=0}^{N} \mathrm{e}^{\mathrm{i}Qr} \sum_{\substack{d_0,d_1,d_2\\ \alpha_0,\alpha_1,\alpha_2}} {}^{\alpha_0,\alpha_1,\alpha_2}\Big[c_{O|_0^3}\Big]^{d_0,d_1,d_2} \big|r+d_0,\alpha_0\big\rangle\big|r+d_0+d_1,\alpha_1\big\rangle\big|r+d_0+d_1+d_2,\alpha_2\big\rangle
\end{aligned}
\tag{E.5a}
$$

$$
= \sum_{\substack{d_0,d_1,d_2\\ \alpha_0,\alpha_1,\alpha_2}} {}^{\alpha_0,\alpha_1,\alpha_2}\Big[c_{O|_0^3}\Big]^{d_0,d_1,d_2} \mathrm{e}^{-\mathrm{i}Q\left(\frac{3d+2d_1+d_2}{3}\right)} \big|Q,\alpha_0\big\rangle\big|d_1,\alpha_1\big\rangle\big|d_2,\alpha_2\big\rangle \tag{E.5b}
$$

$$
= \sum_{\substack{d_1,d_2\\ \alpha_0,\alpha_1,\alpha_2}} {}^{\alpha_0,\alpha_1,\alpha_2}\Big[C_{O|_0^3}(Q)\Big]^{d_1,d_2} \big|Q,\alpha_0\big\rangle\big|d_1,\alpha_1\big\rangle\big|d_2,\alpha_2\big\rangle \tag{E.5c}
$$

with

$$
{}^{\alpha_0,\alpha_1,\alpha_2}\Big[C_{O|_0^3}(Q)\Big]^{d_1,d_2} := \sum_{d_0} {}^{\alpha_0,\alpha_1,\alpha_2}\Big[c_{O|_0^3}\Big]^{d_0,d_1,d_2} \mathrm{e}^{-\mathrm{i}Q\left(\frac{3d_0+2d_1+d_2}{3}\right)} \tag{E.5d}
$$

and $d_1, d_2 > 0$.

E.1 Spin subspace $S = 1$, $m = 0$

Let us consider the local observable

$$
O(r) = S_1^z(r) \tag{E.6a}
$$

$$
= \frac{1}{2}\Big[\Big(t_{z,r}^\dagger + t_{z,r}\Big) - \mathrm{i}\Big(t_{x,r}^\dagger t_{y,r} - t_{y,r}^\dagger t_{x,r}\Big)\Big]\,. \tag{E.6b}
$$

Applying $S_1^z(r)$ on an arbitrary state with total spin $S = 0$ and $m = 0$ yields a state with total spin $S = 1$ and $m = 0$. If the continuous unitary transformation (CUT) does not break the SU(2) symmetry during the flow, this property can be used to simplify equations (E.3), (E.4) and (E.5).

The action of the operator $S^z_{1,\mathrm{eff}}(Q)\big|_0^1$ on the vacuum state $|0\rangle$ is given by

$$
S^z_{1,\mathrm{eff}}(Q)\big|_0^1\,|0\rangle = C^{S=1,m=0}_{S_1^z|_0^1}(Q)\big|Q\big\rangle^{S=1}_{m=0} \tag{E.7a}
$$

with

$$
C^{S=1,m=0}_{S_1^z|_0^1}(Q) := \sum_{d_0} {}^{z}\Big[c_{S_1^z|_0^1}\Big]^{d_0} \mathrm{e}^{-\mathrm{i}Qd_0}\,. \tag{E.7b}
$$

Analogously, the action of the operator $S^z_{1,\mathrm{eff}}(Q)\big|_0^2$ on the vacuum state $|0\rangle$ is given by

$$S^z_{1,\mathrm{eff}}(Q)\big|_0^2\,\big|0\big\rangle = \sum_{d_1}\Big[C^{S=1,m=0}_{S^z_1|^2_0}(Q)\Big]^{d_1}\,\big|Q,d_1\big\rangle^{S=1}_{m=0} \tag{E.8a}$$

with

$$\Big[C^{S=1,m=0}_{S^z_1|^2_0}(Q)\Big]^{d_1} := \frac{\mathrm{i}}{\sqrt{2}}\sum_{d_0}\Big(\ {}^{xy}\Big[c_{S^z_1|^2_0}\Big]^{d_0,d_1} - \ {}^{yx}\Big[c_{S^z_1|^2_0}\Big]^{d_0,d_1}\Big)\,\mathrm{e}^{-\mathrm{i}Q\left(\frac{2d_0+d_1}{2}\right)}. \tag{E.8b}$$

The action of $S^z_{1,\mathrm{eff}}(Q)\big|_0^3$ on the vacuum state $|0\rangle$ is more difficult due the fact that in the three-particle space for each Q, d_1 and d_2 three states with $S=1$ and $m=0$ exist. It is given by

$$S^z_{1,\mathrm{eff}}(Q)\big|_0^3\,\big|0\big\rangle = \sum_{d_1,d_2}\sum_{a=1}^{3}\ {}^{a}\Big[C^{S=1,m=0}_{S^z_1|^3_0}(Q)\Big]^{d_1,d_2}\big|Q,d_1,d_2,a\big\rangle^{S=1}_{m=0} \tag{E.9a}$$

with

$$\begin{aligned}{}^{1}\Big[C^{S=1,m=0}_{S^z_1|^3_0}(Q)\Big]^{d_1,d_2} := \frac{1}{\sqrt{60}}\sum_{d_0}\Big(2\ {}^{xxz}\Big[c_{S^z_1|^3_0}\Big]^{d_0,d_1,d_2} + 2\ {}^{yyz}\Big[c_{S^z_1|^3_0}\Big]^{d_0,d_1,d_2}\\ -3\ {}^{zxx}\Big[c_{S^z_1|^3_0}\Big]^{d_0,d_1,d_2} - 3\ {}^{zyy}\Big[c_{S^z_1|^3_0}\Big]^{d_0,d_1,d_2}\\ -3\ {}^{xzx}\Big[c_{S^z_1|^3_0}\Big]^{d_0,d_1,d_2} - 3\ {}^{yzy}\Big[c_{S^z_1|^3_0}\Big]^{d_0,d_1,d_2}\\ -4\ {}^{zzz}\Big[c_{S^z_1|^3_0}\Big]^{d_0,d_1,d_2}\Big)\,\mathrm{e}^{-\mathrm{i}Q\left(\frac{3d_0+2d_1+d_2}{3}\right)}\end{aligned} \tag{E.9b}$$

and

$$\begin{aligned}{}^{2}\Big[C^{S=1,m=0}_{S^z_1|^3_0}(Q)\Big]^{d_1,d_2} := \frac{1}{2}\sum_{d_0}\Big(\ {}^{zxx}\Big[c_{S^z_1|^3_0}\Big]^{d_0,d_1,d_2} + \ {}^{zyy}\Big[c_{S^z_1|^3_0}\Big]^{d_0,d_1,d_2}\\ -\ {}^{xzx}\Big[c_{S^z_1|^3_0}\Big]^{d_0,d_1,d_2} - \ {}^{yzy}\Big[c_{S^z_1|^3_0}\Big]^{d_0,d_1,d_2}\Big)\,\mathrm{e}^{-\mathrm{i}Q\left(\frac{3d+2d_1+d_2}{3}\right)}\end{aligned} \tag{E.9c}$$

and

$$\begin{aligned}{}^{3}\Big[C^{S=1,m=0}_{S^z_1|^3_0}(Q)\Big]^{d_1,d_2} := \frac{1}{\sqrt{3}}\sum_{d_0}\Big(\ {}^{xxz}\Big[c_{S^z_1|^3_0}\Big]^{d_0,d_1,d_2} + \ {}^{yyz}\Big[c_{S^z_1|^3_0}\Big]^{d_0,d_1,d_2}\\ +\ {}^{zzz}\Big[c_{S^z_1|^3_0}\Big]^{d_0,d_1,d_2}\Big)\,\mathrm{e}^{-\mathrm{i}Q\left(\frac{3d_0+2d_1+d_2}{3}\right)}.\end{aligned} \tag{E.9d}$$

E.2 Lattice symmetry

For all discussed ladder models (cf. chapter 4, chapter 5 and chapter 6) the lattice is invariant under a rotation by 180 degrees. This symmetry yields to relations between the coefficients for a spin $\mathbf{S}_1$ acting on leg 1 and the coefficients for a spin $\mathbf{S}_2$ acting on leg 2. These relations are given by

$$^{\alpha_0}\left[c_{S^z_{2|0}}\right]^{d_0} = - \; ^{\alpha_0}\left[c_{S^z_{1|0}}\right]^{-d_0} \tag{E.10a}$$

$$^{\alpha_0,\alpha_1}\left[c_{S^z_{2|0}}\right]^{d_0,d_1} = \; ^{\alpha_1,\alpha_0}\left[c_{S^z_{1|0}}\right]^{-(d_0+d_1),d_1} \tag{E.10b}$$

$$^{\alpha_0,\alpha_1,\alpha_2}\left[c_{S^z_{2|0}}\right]^{d_0,d_1,d_2} = - \; ^{\alpha_2,\alpha_1,\alpha_0}\left[c_{S^z_{1|0}}\right]^{-(d_0+d_1+d_2),d_2,d_1} . \tag{E.10c}$$

Therefore, it is sufficient to consider $\mathbf{S}_1$ only. All quantities for $\mathbf{S}_2$ can be deduced from $\mathbf{S}_1$.

Appendix F

Inelastic neutron scattering theory

Since neutrons possess a magnetic momentum, inelastic neutron scattering (INS) can be used to probe the magnetic structure of matter. A detailed description of INS can be found , for example, in the book "*Theory of thermal neutron scattering*" by Marshall and Lovesey [Marshall & Lovesey(1971)] or in the book "*Introduction to the theory of thermal neutron scattering*" by squires [Squires(1978)].

In this appendix we only quote the relevant formulae to compare theoretical results to data provided by INS measurements. Especially, we focus on the case of the asymmetric spin $S = 1/2$ Heisenberg ladder.

F.1 Dynamical structure factor

For compounds with only one type of magnetic (spin $S = 1/2$) ions the partial differential cross section of INS is proportional to the dynamical structure factor given by

$$S^{\alpha\beta}(\mathbf{Q},\omega) = \frac{1}{2\pi}\int_{-\infty}^{\infty} \mathrm{d}t\, \mathrm{e}^{\mathrm{i}\omega t}\left\langle S^{\alpha}(-\mathbf{Q},t)\, S^{\beta}(\mathbf{Q},0)\right\rangle \tag{F.1}$$

depending on the momentum transfer $\mathbf{Q}$ and on the energy transfer ω. The time dependence of the Fourier transformed spin operators $S^{\alpha}(\mathbf{Q},t)$ with $\alpha \in \{x,y,z\}$ is given by the Heisenberg picture

$$S^{\alpha}(\mathbf{Q},t) = \mathrm{e}^{\mathrm{i}Ht}\, S^{\alpha}(\mathbf{Q})\, \mathrm{e}^{-\mathrm{i}Ht} \tag{F.2}$$

and the Fourier transformation is defined by

$$S^{\alpha}(\mathbf{Q}) = \frac{1}{\sqrt{N}}\frac{1}{\sqrt{N_{\mathrm{b}}}}\sum_{\mathbf{r},\mathbf{b}} \mathrm{e}^{\mathrm{i}\mathbf{Q}(\mathbf{r}+\mathbf{b})}\, S^{\alpha}(\mathbf{r}+\mathbf{b})\ , \tag{F.3}$$

where **r** denotes lattice vectors and **b** denotes basis vectors. The total number of lattice vectors is given by $\mathcal{N}$ and the number of basis vectors per unit cell by $\mathcal{N}_\mathrm{b}$. Note, for $\mathbf{Q} = \mathbf{0}$ the FOURIER transformation $S^\alpha(\mathbf{Q})$ is proportional to the α-component of the total spin

$$S^\alpha(\mathbf{Q}=\mathbf{0}) = \frac{1}{\sqrt{\mathcal{N}}}\frac{1}{\sqrt{\mathcal{N}_\mathrm{b}}}\sum_{\mathbf{r},\mathbf{b}} S^\alpha(\mathbf{r}+\mathbf{b}) \tag{F.4a}$$

$$= \frac{1}{\sqrt{\mathcal{N}}}\frac{1}{\sqrt{\mathcal{N}_\mathrm{b}}} S^\alpha_\mathrm{total}\,. \tag{F.4b}$$

The fluctuation-dissipation theorem [Kubo(1966)]

$$S^{\alpha\beta}(\mathbf{Q},\omega) = -\frac{1}{\pi}\frac{1}{1-e^{-\omega/T}}\mathrm{Im}\,\mathcal{G}^{\alpha\beta}(\mathbf{Q},\omega) \tag{F.5}$$

with the temperature T yields a connection between the dynamical structure factor $S^{\alpha\beta}(\mathbf{Q},\omega)$ and the imaginary part of the GREEN function $\mathcal{G}^{\alpha\beta}(\mathbf{Q},\omega)$ given by

$$\mathcal{G}^{\alpha\beta}(\mathbf{Q},\omega) = \int_{-\infty}^{\infty} \mathrm{d}t\; \mathrm{e}^{\mathrm{i}\omega t}\, \mathcal{G}^{\alpha\beta}(\mathbf{Q},t) \tag{F.6}$$

with

$$\mathcal{G}^{\alpha\beta}(\mathbf{Q},t) = -\mathrm{i}\theta(t)\left\langle\left[S^\alpha(-\mathbf{Q},t), S^\beta(\mathbf{Q},0)\right]\right\rangle\,. \tag{F.7}$$

F.1.1 Sum rule

The sum rule for the dynamical structure factor $S^{\alpha\alpha}(\mathbf{Q},\omega)$ for the above definitions is given by

$$I = \int_{-\pi}^{\pi}\frac{\mathrm{d}^{\mathcal{D}}\mathbf{Q}}{(2\pi)^{\mathcal{D}}}\int_{-\infty}^{\infty}\mathrm{d}\omega\; S^{\alpha\alpha}(\mathbf{Q},\omega) \tag{F.8a}$$

$$= \frac{1}{\mathcal{N}\mathcal{N}_\mathrm{b}}\sum_{\mathbf{r},\mathbf{r}'}\sum_{\mathbf{b},\mathbf{b}'}\delta(\mathbf{r}+\mathbf{b}-\mathbf{r}'-\mathbf{b}')\; S^\alpha(\mathbf{r}+\mathbf{b})S^\alpha(\mathbf{r}'+\mathbf{b}') \tag{F.8b}$$

$$= \frac{1}{\mathcal{N}\mathcal{N}_\mathrm{b}}\sum_{\mathbf{r}}\sum_{\mathbf{b},\mathbf{b}'}\underbrace{S^\alpha(\mathbf{r}+\mathbf{b})S^\alpha(\mathbf{r}+\mathbf{b})}_{S^2} \tag{F.8c}$$

$$= S^2\mathcal{N}_\mathrm{b} \tag{F.8d}$$

with the total spectral weight I.

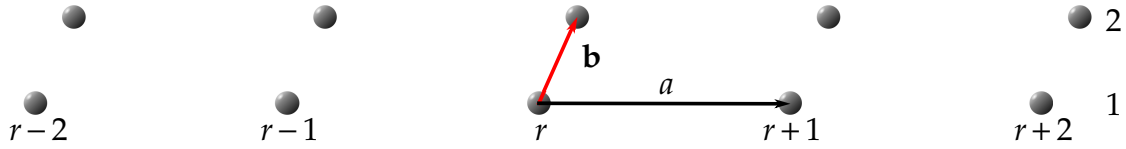

Figure F.1: Schematic representation of a HEISENBERG spin ladder. Circles indicate spins with spin $S = 1/2$. The lattice is one-dimensional. Different rungs are labelled by r and their distance a is typically set to one. Ladder rungs are defined by the vector $\mathbf{b}$. Spins of the lower leg are denoted by $\mathbf{S}_1(r)$ and spins of the upper leg are denoted by $\mathbf{S}_2(r)$.

F.2 Spin ladder

Figure F.1 depicts the configuration of spins in a HEISENBERG spin ladder. Spins of the lower leg are denoted by $\mathbf{S}_1(r)$ and spins of the upper leg are denoted by $\mathbf{S}_2(r)$. Different rungs of this one-dimensional lattice are labelled by r, where the distance a between them is typically set to one. Although the lattice is one-dimensional, in general the basis vector $\mathbf{b}$ defining the ladder rungs has a component perpendicular to the ladder direction. Therefore, we divide the basis vector $\mathbf{b}$ and the momentum $\mathbf{Q}$ in components along the ladder and perpendicular to it, i.e.

$$\mathbf{b} = (b, \mathbf{b}_\perp)^T \tag{F.9}$$

and

$$\mathbf{Q} = (Q, \mathbf{Q}_\perp)^T \ . \tag{F.10}$$

In that case equation (F.3) becomes

$$S^\alpha(Q) = \frac{e^{i\mathbf{Q}\frac{\mathbf{b}}{2}}}{\sqrt{2\mathcal{N}}} \sum_r e^{iQr} \left(e^{-i\mathbf{Q}\frac{\mathbf{b}}{2}} \ S_1^\alpha(r) + e^{i\mathbf{Q}\frac{\mathbf{b}}{2}} \ S_2^\alpha(r) \right) . \tag{F.11}$$

For temperature $T = 0$ the expectation values $\langle . \rangle$ in equation (F.1) and equation (F.7) are given by the ground state expectation value $\langle \mathrm{g} | . | \mathrm{g} \rangle$. After the discussed continuous unitary transformations (CUTs) the ground state is represented by the vacuum state $|0\rangle = U^\dagger |\mathrm{g}\rangle$ and the spin operators are given by $S^\alpha_{\mathrm{eff}}(r) = U^\dagger S^\alpha(r) U$.

F.2.1 Sum rule

In chapter 4, chapter 5 and chapter 6 the dynamical structure factor $S^{zz}(Q,\omega)$ is discussed for the cases $\mathbf{Qb} = 0$ and $\mathbf{Qb} = \pi$. For $\mathbf{Qb} = 0$ equation

$$\int_{-\pi}^{\pi} \frac{\mathrm{d}Q}{2\pi} \left\langle S^{\alpha}(-Q)S^{\alpha}(Q)\right\rangle\Big|_{\mathbf{Qb}=0} = \frac{1}{2\mathcal{N}} \sum_{r} \left\langle \left(S_1^{\alpha}(r) + S_2^{\alpha}(r)\right)^2 \right\rangle \tag{F.12a}$$

holds and for $\mathbf{Qb} = \pi$ equation

$$\int_{-\pi}^{\pi} \frac{\mathrm{d}Q}{2\pi} \left\langle S^{\alpha}(-Q)S^{\alpha}(Q)\right\rangle\Big|_{\mathbf{Qb}=\pi} = \frac{1}{2\mathcal{N}} \sum_{r} \left\langle \left(S_1^{\alpha}(r) - S_2^{\alpha}(r)\right)^2 \right\rangle \tag{F.12b}$$

holds. The integral over the sum of these two contributions yields the total spectral weight

$$\begin{aligned} I &= \int_{-\pi}^{\pi} \frac{\mathrm{d}Q}{2\pi} \left\langle S^{\alpha}(-Q)S^{\alpha}(Q)\right\rangle\Big|_{\mathbf{Qb}=0} + \int_{-\pi}^{\pi} \frac{\mathrm{d}Q}{2\pi} \left\langle S^{\alpha}(-Q)S^{\alpha}(Q)\right\rangle\Big|_{\mathbf{Qb}=\pi} && \text{(F.13a)} \\ &= \frac{1}{\mathcal{N}} \sum_{r} \left\langle \left(S_1^{\alpha}(r)\right)^2 + \left(S_2^{\alpha}(r)\right)^2 \right\rangle && \text{(F.13b)} \\ &= 2S^2 = \frac{1}{2}\,. && \text{(F.13c)} \end{aligned}$$

F.2.2 Spin subspace $S = 1$, $m = 0$

In a SU(2) symmetric system it is sufficient to consider $S^{zz}(\mathbf{Q},\omega)$. The action of the Fourier transformation $S^z_{\mathrm{eff}}(Q)$ of the effective spin operator $S^z_{\mathrm{eff}}(r)$ on the vacuum state $|0\rangle$ is given by

$$\begin{aligned} S^z_{\mathrm{eff}}(Q)\big|0\big\rangle &= \frac{\mathrm{e}^{\mathrm{i}\mathbf{Q}\frac{\mathbf{b}}{2}}}{\sqrt{2\mathcal{N}}} \sum_{r} \mathrm{e}^{\mathrm{i}Qr} \left(\mathrm{e}^{-\mathrm{i}\mathbf{Q}\frac{\mathbf{b}}{2}}\, S^z_{1,\mathrm{eff}}(r) + \mathrm{e}^{\mathrm{i}\mathbf{Q}\frac{\mathbf{b}}{2}}\, S^z_{2,\mathrm{eff}}(r)\right)\big|0\big\rangle && \text{(F.14a)} \\ &= \frac{\mathrm{e}^{\mathrm{i}\mathbf{Q}\frac{\mathbf{b}}{2}}}{\sqrt{2}} \left(\mathrm{e}^{-\mathrm{i}\mathbf{Q}\frac{\mathbf{b}}{2}}\, S^z_{1,\mathrm{eff}}(Q) + \mathrm{e}^{\mathrm{i}\mathbf{Q}\frac{\mathbf{b}}{2}}\, S^z_{2,\mathrm{eff}}(Q)\right)\big|0\big\rangle && \text{(F.14b)} \\ &= \frac{\mathrm{e}^{\mathrm{i}\mathbf{Q}\frac{\mathbf{b}}{2}}}{\sqrt{2}} \sum_{i} \left(\mathrm{e}^{-\mathrm{i}\mathbf{Q}\frac{\mathbf{b}}{2}}\, S^z_{1,\mathrm{eff}}(Q)\Big|_0^i + \mathrm{e}^{\mathrm{i}\mathbf{Q}\frac{\mathbf{b}}{2}}\, S^z_{2,\mathrm{eff}}(Q)\Big|_0^i\right)\big|0\big\rangle\,. && \text{(F.14c)} \end{aligned}$$

The one-particle part is given by

$$\frac{e^{i\mathbf{Q}\frac{\mathbf{b}}{2}}}{\sqrt{2}}\left(e^{-i\mathbf{Q}\frac{\mathbf{b}}{2}}\ S^z_{1,\text{eff}}(Q)\big|_0^1 + e^{i\mathbf{Q}\frac{\mathbf{b}}{2}}\ S^z_{2,\text{eff}}(Q)\big|_0^1\right)\big|0\big\rangle \tag{F.15a}$$

$$= \frac{e^{i\mathbf{Q}\frac{\mathbf{b}}{2}}}{\sqrt{2}}\sum_{d_0}\left({}^{z}\left[c_{S^z_1|^1_0}\right]^{d_0} e^{-iQd_0}\, e^{-i\mathbf{Q}\frac{\mathbf{b}}{2}} + {}^{z}\left[c_{S^z_2|^1_0}\right]^{d_0} e^{-iQd_0}\, e^{i\mathbf{Q}\frac{\mathbf{b}}{2}}\right)\big|Q\big\rangle^{S=1}_{m=0}$$

$$= \frac{e^{i\mathbf{Q}\frac{\mathbf{b}}{2}}}{\sqrt{2}}\sum_{d_0}\ {}^{z}\left[c_{S^z_1|^1_0}\right]^{d_0}\left(e^{-iQd_0}\, e^{-i\mathbf{Q}\frac{\mathbf{b}}{2}} - e^{iQd_0}\, e^{i\mathbf{Q}\frac{\mathbf{b}}{2}}\right)\big|Q\big\rangle^{S=1}_{m=0} \tag{F.15b}$$

$$= -\sqrt{2}ie^{i\mathbf{Q}\frac{\mathbf{b}}{2}}\sum_{d_0}\ {}^{z}\left[c_{S^z_1|^1_0}\right]^{d_0}\sin\left(Qd_0 + \mathbf{Q}\mathbf{b}/2\right)\big|Q\big\rangle^{S=1}_{m=0} \tag{F.15c}$$

$$= C^{S=1,m=0}_{S^z|^1_0}(Q)\big|Q\big\rangle^{S=1}_{m=0} \tag{F.15d}$$

with

$$C^{S=1,m=0}_{S^z|^1_0}(Q) = -\sqrt{2}ie^{i\mathbf{Q}\frac{\mathbf{b}}{2}}\sum_{d_0}\ {}^{z}\left[c_{S^z_1|^1_0}\right]^{d_0}\sin\left(Qd_0 + \mathbf{Q}\mathbf{b}/2\right)\ . \tag{F.16}$$

Analogously, the two-particle part is given by

$$\frac{e^{i\mathbf{Q}\frac{\mathbf{b}}{2}}}{\sqrt{2}}\left(e^{-i\mathbf{Q}\frac{\mathbf{b}}{2}}\ S^z_{1,\text{eff}}(Q)\big|_0^2 + e^{i\mathbf{Q}\frac{\mathbf{b}}{2}}\ S^z_{2,\text{eff}}(Q)\big|_0^2\right)\big|0\big\rangle = \sum_{d_1}\left[C^{S=1,m=0}_{S^z|^2_0}(Q)\right]^{d_1}\big|Q,d_1\big\rangle^{S=1}_{m=0} \tag{F.17}$$

with

$$\left[C^{S=1,m=0}_{S^z|^2_0}(Q)\right]^{d_1} = e^{i\mathbf{Q}\frac{\mathbf{b}}{2}}\sum_{d_0}\left({}^{xy}\left[c_{S^z_1|^2_0}\right]^{d_0,d_1} - {}^{yx}\left[c_{S^z_1|^2_0}\right]^{d_0,d_1}\right)\sin\left(Q\left(2d_0+d_1/2\right) + \mathbf{Q}\mathbf{b}/2\right)\ . \tag{F.18}$$

The three-particle sector is considerably more involved. Nevertheless, we can write

$$\frac{e^{i\mathbf{Q}\frac{\mathbf{b}}{2}}}{\sqrt{2}}\left(e^{-i\mathbf{Q}\frac{\mathbf{b}}{2}}\ S^z_{1,\text{eff}}(Q)\big|_0^3 + e^{i\mathbf{Q}\frac{\mathbf{b}}{2}}\ S^z_{2,\text{eff}}(Q)\big|_0^3\right)\big|0\big\rangle = \sum_{d_1,d_2}\sum_{a=1}^{3}\ {}^{a}\left[C^{S=1,m=0}_{S^z|^3_0}(Q)\right]^{d_1,d_2}\big|Q,d_1,d_2,a\big\rangle^{S=1}_{m=0} \tag{F.19}$$

with

$${}^{a}\left[C^{S=1,m=0}_{S^z|^3_0}(Q)\right]^{d_1,d_2} = \frac{e^{i\mathbf{Q}\frac{\mathbf{b}}{2}}}{\sqrt{2}}\left(e^{-i\mathbf{Q}\frac{\mathbf{b}}{2}}\ {}^{a}\left[C^{S=1,m=0}_{S^z_1|^3_0}(Q)\right]^{d_1,d_2} + e^{i\mathbf{Q}\frac{\mathbf{b}}{2}}\ {}^{a}\left[C^{S=1,m=0}_{S^z_2|^3_0}(Q)\right]^{d_1,d_2}\right)\ . \tag{F.20}$$

For the definition of ${}^{a}\left[C^{S=1,m=0}_{S^z_1|^3_0}(Q)\right]^{d_1,d_2}$ see equation (E.9b), equation (E.9c) and equa-

tion(E.9d). The definition of ${}^{a}\left[C^{S=1,m=0}_{S^z_2|^3_0}(Q)\right]^{d_1,d_2}$ is analogous.

Appendix G

Magnetization

In this appendix details about the description of the ordered regime, also known as Bose-condensed phase, of isopropylammonium trichlorocuprate(II) $(CH_3)_2CHNH_3CuCl_3$ (IPA-$CuCl_3$) in a magnetic field are given. Results are discussed in section 6.3. The calculations are analogous to the calculations performed by Matsumoto *et al.* to describe the field-induced transitions in $TlCuCl_3$ [Matsumoto *et al.*(2004)]. The crucial difference to Matsumoto *et al.* is that we start from an effective model generated by self-similar continuous unitary transformations (sCUTs) instead of the initial spin model. Hence we are able to describe physical situations much further away from the dimer limit.

We start from the bilinear part of the two-dimensional effective model for IPA-$CuCl_3$ in real space in a magnetic field (6.41) given by

$$H^{\text{bilinear}}_{\text{IPA-CuCl}_3,\text{eff}} = H^{\text{bilinear}}_{1\mathcal{D},\text{eff}} + H^{\text{bilinear}}_{\text{int,eff}} + H_h \tag{G.1a}$$

with

$$H^{\text{bilinear}}_{1\mathcal{D},\text{eff}} = J_3 \sum_{r,s} \sum_{m} \sum_{d} \left[c_{H_{1\mathcal{D}}|^1_1}\right]_d \, t^\dagger_{m,r,s} t_{m,r+d,s} \tag{G.1b}$$

$$H^{\text{bilinear}}_{\text{int,eff}} = J_4 \sum_{r,s} \sum_{\delta,\delta'} \sum_{m} \left[c_{S^m_1|^1_0}\right]^\delta \left[c_{S^m_2|^1_0}\right]^{\delta'} \left[t^\dagger_{m,r,s}\left(t^\dagger_{\overline{m},r+1+(\delta'-\delta),s+1} + t_{m,r+1+(\delta'-\delta),s+1}\right) + \text{H.c.}\right] \tag{G.1c}$$

$$H_h = -h \sum_{r,s} \left(t^\dagger_{+,r,s} t_{+,r,s} - t^\dagger_{-,r,s} t_{-,r,s}\right) \tag{G.1d}$$

with the bond operators $t^\dagger_{m,r,s}$ ($t_{m,r,s}$), cf. appendix C, acting on site $\mathbf{r} = (r,s)$ with spin polarization $m \in \{+,-,0\}$ ($\overline{m} = -m$). Following Matsumoto *et al.* [Matsumoto *et al.*(2004)]

we perform a local transformation

$$|\tilde{s}_{\mathbf{r}}\rangle = u\,|s_{\mathbf{r}}\rangle + v\mathrm{e}^{\mathrm{i}\mathbf{Q}_0\mathbf{r}}\left(f\left|t_{+,\mathbf{r}}\right\rangle + g\left|t_{-,\mathbf{r}}\right\rangle\right) \tag{G.2a}$$

$$\left|\tilde{t}_{+,\mathbf{r}}\right\rangle = u\left(f\left|t_{+,\mathbf{r}}\right\rangle + g\left|t_{-,\mathbf{r}}\right\rangle\right) - v\mathrm{e}^{\mathrm{i}\mathbf{Q}_0\mathbf{r}}\,|s_{\mathbf{r}}\rangle \tag{G.2b}$$

$$\left|\tilde{t}_{0,\mathbf{r}}\right\rangle = \left|t_{0,\mathbf{r}}\right\rangle \tag{G.2c}$$

$$\left|\tilde{t}_{-,\mathbf{r}}\right\rangle = f\left|t_{-,\mathbf{r}}\right\rangle - g\left|t_{+,\mathbf{r}}\right\rangle \tag{G.2d}$$

in real space with **r**-independent coefficients

$$u = \cos(\theta) \tag{G.3a}$$

$$v = \sin(\theta) \tag{G.3b}$$

$$f = \cos(\varphi) \tag{G.3c}$$

$$g = \sin(\varphi) \tag{G.3d}$$

and the wave vector $\mathbf{Q}_0 = (\pi, 0)$ of the minimum of the dispersion.

After the transformation (G.2) the vacuum energy E_0 per site is given by

$$E_0/J_3 = \left(\epsilon_+ g^2 + \epsilon_- f^2\right)v^2 + 2u^2v^2\left(\Lambda_{1\mathcal{D}} + \Lambda_{\mathrm{int}}\right) + 4u^2v^2 f g\,\Lambda_{\mathrm{int}} \tag{G.4}$$

with

$$\epsilon_m = \left[c_{H_{1\mathcal{D}}|_1^1}\right]_0 + m\frac{h}{J_3} \tag{G.5a}$$

$$\Lambda_{1\mathcal{D}} := \sum_{d=-D_2}^{D_2}(-1)^d\left[c_{H_{1\mathcal{D}}|_1^1}\right]_d \tag{G.5b}$$

$$\Lambda_{\mathrm{int}} := z\sum_{\delta,\delta'=-D_1^O}^{D_1^O}(-1)^{1+(\delta'-\delta)}\left[c_{S_1^m|_0^1}\right]^{\delta}\left[c_{S_2^m|_0^1}\right]^{\delta'} \tag{G.5c}$$

and $z = J_4/J_3$. Transformation (G.2) also leads to terms linear in $\tilde{t}^\dagger_{-,\mathbf{r}} + \tilde{t}_{-,\mathbf{r}}$ and linear in $\tilde{t}^\dagger_{+,\mathbf{r}} + \tilde{t}_{+,\mathbf{r}}$ whose prefactors c_- and c_+ are proportional to

$$c_- \propto uv\left[\left(\epsilon_+ g^2 + \epsilon_- f^2\right) + 2\left(u^2 - v^2\right)\left(\Lambda_{1\mathcal{D}} + \Lambda_{\mathrm{int}}\right) + 4\left(u^2 - v^2\right)f g\,\Lambda_{\mathrm{int}}\right] \tag{G.6a}$$

$$c_+ \propto\ v\left[\left(\epsilon_+ - \epsilon_-\right)f g + 2u^2\left(f^2 - g^2\right)\Lambda_{\mathrm{int}}\right] \tag{G.6b}$$

Demanding that these two coefficents vanish fixes the angles θ and φ and also optimizes

E_0. A Fourier transformation

$$\tilde{t}^{\dagger}_{\alpha,\mathbf{r}} := \frac{1}{\sqrt{N}}\frac{1}{\sqrt{N}}\sum_{\mathbf{Q}} \mathrm{e}^{\mathrm{i}\mathbf{Q}\mathbf{r}}\, b^{\dagger}_{\alpha,\mathbf{Q}} \tag{G.7a}$$

$$\tilde{t}_{\alpha,\mathbf{r}} := \frac{1}{\sqrt{N}}\frac{1}{\sqrt{N}}\sum_{\mathbf{Q}} \mathrm{e}^{\mathrm{i}\mathbf{Q}\mathbf{r}}\, b_{\alpha,\mathbf{Q}} \tag{G.7b}$$

(G.7c)

of the bilinear part of the rotated Hamiltonian leads to

$$\begin{aligned} H^{\text{bilinear}}_{\text{rotated}} = J_3 \sum_{\mathbf{Q}} \Big[& \epsilon_0(\mathbf{Q})\, b^{\dagger}_{0,\mathbf{Q}} b_{0,\mathbf{Q}} + \frac{\Delta_0(\mathbf{Q})}{2}\left(b^{\dagger}_{0,\mathbf{Q}} b^{\dagger}_{0,-\mathbf{Q}} + b_{0,\mathbf{Q}} b_{0,-\mathbf{Q}}\right) \\ & + \epsilon_+(\mathbf{Q})\, b^{\dagger}_{+,\mathbf{Q}} b_{+,\mathbf{Q}} + \frac{\Delta_+(\mathbf{Q})}{2}\left(b^{\dagger}_{+,\mathbf{Q}} b^{\dagger}_{+,-\mathbf{Q}} + b_{+,\mathbf{Q}} b_{+,-\mathbf{Q}}\right) \\ & + \epsilon_-(\mathbf{Q})\, b^{\dagger}_{-,\mathbf{Q}} b_{-,\mathbf{Q}} + \frac{\Delta_-(\mathbf{Q})}{2}\left(b^{\dagger}_{-,\mathbf{Q}} b^{\dagger}_{-,-\mathbf{Q}} + b_{-,\mathbf{Q}} b_{-,-\mathbf{Q}}\right) \\ & + \epsilon_{\pm}(\mathbf{Q})\left(b^{\dagger}_{+,\mathbf{Q}} b_{-,\mathbf{Q}} + b^{\dagger}_{-,\mathbf{Q}} b_{+,\mathbf{Q}}\right) + \Delta_{\pm}(\mathbf{Q})\left(b^{\dagger}_{+,\mathbf{Q}} b^{\dagger}_{-,-\mathbf{Q}} + b_{+,\mathbf{Q}} b_{-,-\mathbf{Q}}\right)\Big]. \end{aligned} \tag{G.8}$$

The appearing coefficients are given by

$$\begin{aligned} \epsilon_-(\mathbf{Q}) = & \left(u^2 - v^2\right)\left(\epsilon_+ g^2 + \epsilon_- f^2\right) - 8u^2v^2\left(\Lambda_{1D} + \Lambda_{\text{int}}\right) - 16u^2v^2 fg\, \Lambda_{\text{int}} \\ & + \left(u^4 + v^4\right)\Xi(\mathbf{Q}) - 4u^2v^2 fg\, \Lambda(\mathbf{Q}) \end{aligned} \tag{G.9a}$$

$$\epsilon_0(\mathbf{Q}) = \epsilon_0 - v^2\left(\epsilon_+ g^2 + \epsilon_- f^2\right) - 4u^2v^2\left(\Lambda_{1D} + \Lambda_{\text{int}}\right) - 8u^2v^2 fg\, \Lambda_{\text{int}} + u^2\, \Xi(\mathbf{Q}) \tag{G.9b}$$

$$\begin{aligned} \epsilon_+(\mathbf{Q}) = & \epsilon_+ f^2 + \epsilon_- g^2 - v^2\left(\epsilon_+ g^2 + \epsilon_- f^2\right) - 4u^2v^2\left(\Lambda_{1D} + \Lambda_{\text{int}}\right) - 8u^2v^2 fg\, \Lambda_{\text{int}} \\ & + u^2\, \Xi(\mathbf{Q}) \end{aligned} \tag{G.9c}$$

$$\epsilon_{\pm}(\mathbf{Q}) = ufg\left(\epsilon_+ - \epsilon_-\right) - 2uv^2\left(f^2 - g^2\right)\Lambda_{\text{int}} - uv^2\left(f^2 - g^2\right)\Lambda(\mathbf{Q}) \tag{G.9d}$$

$$\Delta_-(\mathbf{Q}) = -2u^2v^2\, \Xi(\mathbf{Q}) + 2\left(u^4 + v^4\right) fg\, \Lambda(\mathbf{Q}) \tag{G.9e}$$

$$\Delta_0(\mathbf{Q}) = u^2\, \Lambda(\mathbf{Q}) \tag{G.9f}$$

$$\Delta_+(\mathbf{Q}) = -2u^2 fg\, \Lambda(\mathbf{Q}) \tag{G.9g}$$

$$\Delta_{\pm}(\mathbf{Q}) = u^3\left(f^2 - g^2\right)\Lambda(\mathbf{Q}) \tag{G.9h}$$

with

$$\Xi(\mathbf{Q}) = 2\sum_{d=1}^{D_2}\left[c_{H_{1\mathcal{D}}|^1_1}\right]_d \cos(Q_x d) + \Lambda(\mathbf{Q}) \tag{G.10a}$$

$$\Lambda(\mathbf{Q}) = 2z \sum_{\delta,\delta'=-D_1^O}^{D_1^O} \left[c_{S_1^m|^1_0}\right]^{\delta}\left[c_{S_2^m|^1_0}\right]^{\delta'} \cos\left(Q_x(1 + \delta' - \delta) + Q_z\right). \tag{G.10b}$$

The Hamiltonian (G.8) can be diagonalized by two separate Bogoliubov transformations. Since the $m = 0$ mode in the Hamiltonian (G.8) does not mix with the two other modes $m = +, -$, the dispersion $\omega_0(\mathbf{Q})$ of the $m = 0$ mode is simply given by

$$\omega_0(\mathbf{Q}) = \sqrt{\epsilon_0^2(\mathbf{Q}) - \Delta_0^2(\mathbf{Q})}\,. \tag{G.11}$$

The remaining part of the Hamiltonian (G.8) can be written as

$$H^{\text{bilinear}}_{\text{rotated},\pm} = \frac{J_3}{2} \sum_{\mathbf{Q}} \left[\beta^\dagger_{\mathbf{Q}} M(\mathbf{Q}) \beta_{\mathbf{Q}} - \left(\epsilon_+(\mathbf{Q}) + \epsilon_-(\mathbf{Q}) \right) \right] \tag{G.12}$$

with

$$\beta_{\mathbf{Q}} = \begin{pmatrix} b_{+,\mathbf{Q}} \\ b_{-,\mathbf{Q}} \\ b^\dagger_{+,-\mathbf{Q}} \\ b^\dagger_{-,-\mathbf{Q}} \end{pmatrix} \tag{G.13}$$

and

$$M(\mathbf{Q}) = \begin{pmatrix} \epsilon_+(\mathbf{Q}) & \epsilon_\pm(\mathbf{Q}) & \Delta_+(\mathbf{Q}) & \Delta_\pm(\mathbf{Q}) \\ \epsilon_\pm(\mathbf{Q}) & \epsilon_-(\mathbf{Q}) & \Delta_\pm(\mathbf{Q}) & \Delta_-(\mathbf{Q}) \\ \Delta_1(\mathbf{Q}) & \Delta_\pm(\mathbf{Q}) & \epsilon_+(\mathbf{Q}) & \epsilon_\pm(\mathbf{Q}) \\ \Delta_\pm(\mathbf{Q}) & \Delta_-(\mathbf{Q}) & \epsilon_\pm(\mathbf{Q}) & \epsilon_-(\mathbf{Q})\,. \end{pmatrix} \tag{G.14}$$

The matrix (G.14) has two positive eigenvalues where we denote the smaller one by $\omega_+(\mathbf{Q})$ and the larger one by $\omega_-(\mathbf{Q})$. By construction the other two eigenvalues are $-\omega_+(\mathbf{Q})$ and $-\omega_-(\mathbf{Q})$. Figure 6.13 in section 6.3 depicts $\omega_-(\mathbf{Q})$, $\omega_0(\mathbf{Q})$ and $\omega_+(\mathbf{Q})$ for $\mathbf{Q} = \mathbf{Q}_0 = (\pi, 0)$.

Bibliography

[Affleck(1991)] I. Affleck (1991). Bose condensation in quasi-one-dimensional antiferromagnets in strong fields. *Physical Review B* **43**(4), 3215–3222. URL http://prb.aps.org/abstract/PRB/v43/i4/p3215_1. 1

[Affleck *et al.*(1987)] I. Affleck, T. Kennedy, E. H. Lieb & H. Tasaki (1987). Rigorous results on valence-bond ground states in antiferromagnets. *Physical Review Letters* **59**(7), 799–802. URL http://prl.aps.org/abstract/PRL/v59/i7/p799_1. 4

[Anderson(1959)] P. W. Anderson (1959). New Approach to the Theory of Superexchange Interactions. *Physical Review* **115**(1), 2–13. URL http://prola.aps.org/abstract/PR/v115/i1/p2_1. 3.1

[Ashcroft & Mermin(1976)] N. W. Ashcroft & N. D. Mermin (1976). *Solid State Physics*. Saunders College Publishing. 1, 3.4.1

[Barnes *et al.*(1993)] T. Barnes, E. Dagotto, J. Riera & E. S. Swanson (1993). Excitation spectrum of Heisenberg spin ladders. *Physical Review B* **47**(6), 3196–3203. URL http://prb.aps.org/abstract/PRB/v47/i6/p3196_1. 4, 4

[Baxter(1982)] R. J. Baxter (1982). *Exactly Solved Models in Statistical Mechanics*. Academic Press. 4

[Bednorz & Müller(1986)] J. G. Bednorz & K. A. Müller (1986). Possible high T_c superconductivity in the Ba–La–Cu–O system. *Zeitschrift für Physik B Condensed Matter* **64**, 189–193. URL http://dx.doi.org/10.1007/BF01303701. 1

[Bethe(1931)] H. Bethe (1931). Zur Theorie der Metalle: I. Eigenwerte und Eigenfunktionen der linearen Atomkette. *Zeitschrift für Physik A Hadrons and Nuclei* **71**(3-4), 205–226. URL http://dx.doi.org/10.1007/BF01341708. 4

[Bibikov(2007)] P. N. Bibikov (2007). Magnon mode truncation in a rung-dimerized asymmetric spin ladder. *Physical Review B* **76**(17), 174431. URL http://prb.aps.org/abstract/PRB/v76/i17/e174431. 1

[Bray *et al.*(1975)] J. W. Bray, H. R. Hart, L. V. Interrante, I. S. Jacobs, J. S. Kasper, G. D. Watkins, S. H. Wee & J. C. Bonner (1975). Observation of a Spin-Peierls Transition in a Heisenberg Antiferromagnetic Linear-Chain System. *Physical Review Letters* **35**(11), 744–747. URL http://prl.aps.org/abstract/PRL/v35/i11/p744_1. 1

[Brehmer *et al.*(1998)] S. Brehmer, A. K. Kolezhuk, H.-J. Mikeska & U. Neugebauer (1998). Elementary excitations in the gapped phase of a frustrated $S = 1/2$ spin ladder: from spinons to the Haldane triplet. *Journal of Physics: Condensed Matter* **10**(5), 1103. URL http://stacks.iop.org/0953-8984/10/i=5/a=017. 4, 4

[Brehmer *et al.*(1999)] S. Brehmer, H.-J. Mikeska, M. Müller, N. Nagaosa & S. Uchida (1999). Effects of biquadratic exchange on the spectrum of elementary excitations in spin ladders. *Physical Review B* **60**(1), 329–334. URL http://prb.aps.org/abstract/PRB/v60/i1/p329_1. 4

[Brehmer *et al.*(1996)] S. Brehmer, H.-J. Mikeska & U. Neugebauer (1996). The phase diagram and hidden order for generalized spin ladders. *Journal of Physics: Condensed Matter* **8**(38), 7161. URL http://stacks.iop.org/0953-8984/8/i=38/a=018. 4, 4

[Bronstein *et al.*(2001)] I. N. Bronstein, K. A. Semendjajew, G. Musiol & H. Mühlig (2001). *Taschenbuch der Mathematik*. Harri Deutsch. 2

[Bühler(2003)] A. Bühler (2003). *High Temperature Series Expansions for Spin- and Spin-Phonon-Systems*. Ph.D. thesis, Technische Universität Dortmund. URL http://t1.physik.tu-dortmund.de/uhrig/phd.html. 6.1

[Bühler *et al.*(2001)] A. Bühler, U. Löw & G. S. Uhrig (2001). Thermodynamic properties of the dimerized and frustrated $S = 1/2$ chain. *Physical Review B* **64**, 024428. URL http://prb.aps.org/abstract/PRB/v64/i2/e024428. 6, 6.4a, 6.1

[Castilla *et al.*(1995)] G. Castilla, S. Chakravarty & V. J. Emery (1995). Quantum Magnetism of $CuGeO_3$. *Physical Review Letters* **75**, 1823–1826. URL http://prl.aps.org/abstract/PRL/v75/i9/p1823_1. 4

[Chernyshev & Zhitomirsky(2009)] A. L. Chernyshev & M. E. Zhitomirsky (2009). Spin waves in a triangular lattice antiferromagnet: Decays, spectrum renormalization, and singularities. *Physical Review B* **79**(14), 144416. URL http://prb.aps.org/abstract/PRB/v79/i14/e144416. 1

[Chitra *et al.*(1995)] R. Chitra, S. Pati, H. R. Krishnamurthy, D. Sen & S. Ramasesha (1995). Density-matrix renormalization-group studies of the spin-1/2 Heisenberg system with dimerization and frustration. *Physical Review B* **52**, 6581–6587. URL http://prb.aps.org/abstract/PRB/v52/i9/p6581_1. 4

[Chubukov(1989)] A. V. Chubukov (1989). A difference in the properties of one-dimensional antiferromagnets with integer and half-integer spins. *Pis'ma v Zhurnal Eksperimental'noi i Teoreticheskoi Fiziki* **49**, 108–110. URL http://www.jetpletters.ac.ru/ps/1113/article_16848.shtml. [JETP Letters **49**, 129 (1989)]. 4, 6.1, C

[Cohen & Feynman(1957)] M. Cohen & R. P. Feynman (1957). Theory of Inelastic Scattering of Cold Neutrons from Liquid Helium. *Physical Review* **107**(1), 13–24. URL http://prola.aps.org/abstract/PR/v107/i1/p13_1. 1

[Czycholl(2004)] G. Czycholl (2004). *Theoretische Festkörperphysik*. Springer. 1, 3.1

[Dagotto & Rice(1996)] E. Dagotto & T. M. Rice (1996). Surprises on the Way from One- to Two-Dimensional Quantum Magnets: The Ladder Materials. *Science* **271**(5249), 618–623. URL http://www.sciencemag.org/content/271/5249/618.abstract. 4

[Damle & Sachdev(1998)] K. Damle & S. Sachdev (1998). Spin dynamics and transport in gapped one-dimensional Heisenberg antiferromagnets at nonzero temperatures. *Physical Review B* **57**(14), 8307–8339. URL http://prb.aps.org/abstract/PRB/v57/i14/p8307_1. 4, 4.1.1, 4.2.2

[Dawson *et al.*(2008)] C. M. Dawson, J. Eisert & T. J. Osborne (2008). Unifying Variational Methods for Simulating Quantum Many-Body Systems. *Physical Review Letters* **100**(13), 130501. URL http://prl.aps.org/abstract/PRL/v100/i13/e130501. 3.2.2, 3.2.3

[des Cloizeaux & Pearson(1962)] J. des Cloizeaux & J. J. Pearson (1962). Spin-Wave Spectrum of the Antiferromagnetic Linear Chain. *Physical Review* **128**(5), 2131–2135. URL http://prola.aps.org/abstract/PR/v128/i5/p2131_1. 4, 4

[Domb & Green(1972)] C. Domb & M. S. Green (1972). *Phase Transitions and Critical Phenomena*, vol. 1-6. Academic Press. 6.1

[Drescher(2009)] N. A. Drescher (2009). *Optimierte Basiswahl und Trunkierungsfehler bei kontinuierlichen unitären Transformationen am Beispiel der dimerisierten Spin-$\frac{1}{2}$-Kette*. Diploma thesis, Technische Universität Dortmund. URL http://t1.physik.tu-dortmund.de/uhrig/diploma.html. 3.4.3

[Drescher *et al.*(2011)] N. A. Drescher, T. Fischer & G. S. Uhrig (2011). Truncation errors in self-similar continuous unitary transformations. *European Physical Journal B* **79**(2), 225–240. URL http://dx.doi.org/10.1140/epjb/e2010-10723-6. 3.4.3

[Duffe(2010)] S. Duffe (2010). *Effective Hamiltonians for Undoped and Hole-Doped Antiferromagnetic Spin-$\frac{1}{2}$ Ladder by Self-Similar Continuous Unitary Transformations in Real Space*. Ph.D. thesis, Technische Universität Dortmund. URL http://t1.physik.tu-dortmund.de/uhrig/phd.html. 6, 3.2.3, 3.5.1, 3.5.1, 3.5.1, 4.1.1

[Duffe & Uhrig(2011)] S. Duffe & G. S. Uhrig (2011). Hole Dispersions for Antiferromagnetic Spin-1/2 Two-Leg Ladders by Self-Similar Continuous Unitary Transformations. *ArXiv e-prints* URL http://adsabs.harvard.edu/abs/2011arXiv1103.0162D. 3.2.3

[Dusuel *et al.*(2010)] S. Dusuel, M. Kamfor, K. P. Schmidt, R. Thomale & J. Vidal (2010). Bound states in two-dimensional spin systems near the Ising limit: A quantum finite-lattice study. *Physical Review B* **81**(6), 064412. URL http://prb.aps.org/abstract/PRB/v81/i6/e064412. 3.2.3

[Dusuel & Uhrig(2004)] S. Dusuel & G. S. Uhrig (2004). The quartic oscillator: a non-perturbative study by continuous unitary transformations. *Journal of Physics A: Mathematical and General* **37**(39), 9275–9294. URL http://stacks.iop.org/0305-4470/37/9275. 3.2.1, 3.2.2, 3.3.1, 4.2, 4.2.1

[Eccleston *et al.*(1996)] R. S. Eccleston, M. Azuma & M. Takano (1996). Neutron-scattering and susceptibility study of spin chains and spin ladders in $(Sr_{0.8}Ca_{0.2})_{14}Cu_{24}O_{41}$. *Physical Review B* **53**(22), R14721–R14724. URL http://prb.aps.org/abstract/PRB/v53/i22/pR14721_1. 4

[Eggert(1996)] S. Eggert (1996). Numerical evidence for multiplicative logarithmic corrections from marginal operators. *Physical Review B* **54**, R9612–R9615. URL http://prb.aps.org/abstract/PRB/v54/i14/pR9612_1. 4

[Essler & Konik(2008)] F. H. L. Essler & R. M. Konik (2008). Finite-temperature lineshapes in gapped quantum spin chains. *Physical Review B* **78**, 100403. URL http://prb.aps.org/abstract/PRB/v78/i10/e100403. 2

[Exius(2010)] D. E. Exius (2010). *Properties of undoped and doped spin-1/2 ladders at finite temperature*
Continuous unitary transformation combined with a mean field approach and inelastic neutron scattering results for the cuprate family. Ph.D. thesis, Technische Universität Dortmund. URL http://t1.physik.tu-dortmund.de/uhrig/phd.html. 6.1

[Exius *et al.*(2010)] I. Exius, K. P. Schmidt, B. Lake, D. A. Tennant & G. S. Uhrig (2010). Vertex corrections in the dynamic structure factor in spin ladders. *Physical Review B* **82**(21), 214410. URL http://prb.aps.org/abstract/PRB/v82/i21/e214410. 6.4

[Faddeev & Takhtajan(1981)] L. D. Faddeev & L. A. Takhtajan (1981). What is the spin of a spin wave? *Physics Letters A* **85**(6-7), 375–377. URL http://www.sciencedirect.com/science/article/pii/0375960181903352. 4, 4

[Fetter & Walecka(1971)] A. L. Fetter & J. D. Walecka (1971). *Quantum Theory of Many-Particle Systems*. McGraw-Hill. 2.3, 3.4.1

[Feynman(1954)] R. P. Feynman (1954). Atomic Theory of the Two-Fluid Model of Liquid Helium. *Physical Review* **94**(2), 262–277. URL http://prola.aps.org/abstract/PR/v94/i2/p262_1. 1

[Feynman & Cohen(1956)] R. P. Feynman & M. Cohen (1956). Energy Spectrum of the Excitations in Liquid Helium. *Physical Review* **102**(5), 1189–1204. URL http://prola.aps.org/abstract/PR/v102/i5/p1189_1. 1

[Fischer *et al.*(2010)] T. Fischer, S. Duffe & G. S. Uhrig (2010). Adapted continuous unitary transformation to treat systems with quasi-particles of finite lifetime. *New Journal of Physics* **12**(3), 033048. URL http://stacks.iop.org/1367-2630/12/i=3/a=033048. 3.2.2, 3.2.3, 3.2.3, 3.3.2, 4.1.1, 4.2.1, 4.2.2

[Fåk & Bossy(1998)] B. Fåk & J. Bossy (1998). Temperature Dependence of $S(Q,E)$ in Liquid ^{4}He Beyond the Roton. *Journal of Low Temperature Physics* **112**, 1–19. URL http://dx.doi.org/10.1023/A:1022299227239. 1

[Gagliano & Balseiro(1987)] E. R. Gagliano & C. A. Balseiro (1987). Dynamical Properties of Quantum Many-Body Systems at Zero Temperature. *Physical Review Letters* **59**, 2999–3002. URL http://prl.aps.org/abstract/PRL/v59/i26/p2999_1. 4.1.2, 4.2.2

[Garlea *et al.*(2007)] V. O. Garlea, A. Zheludev, T. Masuda, H. Manaka, L.-P. Regnault, E. Ressouche, B. Grenier, J.-H. Chung, Y. Qiu, K. Habicht, K. Kiefer & M. Boehm (2007). Excitations from a Bose-Einstein Condensate of Magnons in Coupled Spin Ladders. *Physical Review Letters* **98**(16), 167202. URL http://prl.aps.org/abstract/PRL/v98/i16/e167202. 1, 6, 6, 6.13

[Giamarchi & Tsvelik(1999)] T. Giamarchi & A. M. Tsvelik (1999). Coupled ladders in a magnetic field. *Physical Review B* **59**(17), 11398–11407. URL http://prb.aps.org/abstract/PRB/v59/i17/p11398_1. 1, 6

[Głazek & Wilson(1993)] S. D. Głazek & K. G. Wilson (1993). Renormalization of Hamiltonians. *Physical Review D* **48**(12), 5863–5872. URL http://prd.aps.org/abstract/PRD/v48/i12/p5863_1. 1, 3, 3.1.1

[Głazek & Wilson(1994)] S. D. Głazek & K. G. Wilson (1994). Perturbative renormalization group for Hamiltonians. *Physical Review D* **49**(8), 4214–4218. URL http://prd.aps.org/abstract/PRD/v49/i8/p4214_1. 1, 3, 3.1.1

[Grüninger *et al.*(2002)] M. Grüninger, M. Windt, T. Nunner, C. Knetter, K. P. Schmidt, G. S. Uhrig, T. Kopp, A. Freimuth, U. Ammerahl, B. Büchner & A. Revcolevschi (2002). Magnetic excitations in two-leg spin 1/2 ladders: experiment and theory. *Journal of Physics and Chemistry of Solids* **63**(12), 2167–2173. URL http://www.sciencedirect.com/science/article/pii/S0022369702002512. 4

[Haga & Suga(2002)] N. Haga & S. Suga (2002). Dynamical structure factors of $S = 1/2$ two-leg spin-ladder systems. *Physical Review B* **66**(13), 132415. URL http://prb.aps.org/abstract/PRB/v66/i13/e132415. 4

[Haldane(1982)] F. D. M. Haldane (1982). Spontaneous dimerization in the $S = \frac{1}{2}$ Heisenberg antiferromagnetic chain with competing interactions. *Physical Review B* **25**, 4925–4928. URL http://prb.aps.org/abstract/PRB/v25/i7/p4925_1. Erratum: *Physical Review B* **26**, 5257 (1982). 4

[Haldane(1983)] F. D. M. Haldane (1983). Nonlinear Field Theory of Large-Spin Heisenberg Antiferromagnets: Semiclassically Quantized Solitons of the One-Dimensional Easy-Axis Néel State. *Physical Review Letters* **50**(15), 1153–1156. URL http://prl.aps.org/abstract/PRL/v50/i15/p1153_1. 1, 4, 6

[Hamerla(2009)] S. A. Hamerla (2009). *Systematic derivation of generalized $t-J$ models from Hubbard models in one and two dimensions at and away from half-filling*. Diploma thesis, Technische Universität Dortmund. URL http://t1.physik.tu-dortmund.de/uhrig/diploma.html. 3.2.3, 3.4.1, 3.4.3, 3.15, 7.2

[Hamerla *et al.*(2010)] S. A. Hamerla, S. Duffe & G. S. Uhrig (2010). Derivation of the $t-J$ model for finite doping. *Physical Review B* **82**(23), 235117. URL http://prb.aps.org/abstract/PRB/v82/i23/e235117. 3, 3.1, 3.2.3, 3.4.1, 3.4.3, 7.2

[Hammar *et al.*(1998)] P. R. Hammar, D. H. Reich, C. Broholm & F. Trouw (1998). Spin gap in a quasi-one-dimensional $S = 1/2$ antiferromagnet: Cu_2(1,4-diazacycloheptane)$_2Cl_4$. *Physical Review B* **57**(13), 7846–7853. URL http://prb.aps.org/abstract/PRB/v57/i13/p7846_1. 4

[Harris & Lange(1967)] A. B. Harris & R. V. Lange (1967). Single-Particle Excitations in Narrow Energy Bands. *Physical Review* **157**(2), 295–314. URL http://prola.aps.org/abstract/PR/v157/i2/p295_1. 3.1

[Hase *et al.*(1993)] M. Hase, I. Terasaki & K. Uchinokura (1993). Observation of the spin-Peierls transition in linear Cu^{2+} (spin-1/2) chains in an inorganic compound $CuGeO_3$. *Physical Review Letters* **70**(23), 3651–3654. URL http://prl.aps.org/abstract/PRL/v70/i23/p3651_1. 1

[Heidbrink & Uhrig(2002)] C. P. Heidbrink & G. S. Uhrig (2002). Renormalization by continuous unitary transformations: one-dimensional spinless fermions. *European Physical Journal B* **30**(4), 443–459. URL http://dx.doi.org/10.1140/epjb/e2002-00401-9. 3.2.3, 3.2.3, 4.1.1, 4.2.1

[Hida(1992)] K. Hida (1992). Crossover between the Haldane-gap phase and the dimer phase in the spin-1/2 alternating Heisenberg chain. *Physical Review B* **45**, 2207–2212. URL http://prb.aps.org/abstract/PRB/v45/i5/p2207_1. 6

[Hong *et al.*(2010)] T. Hong, A. Zheludev, H. Manaka & L.-P. Regnault (2010). Evidence of a magnetic Bose glass in $(CH_3)_2CHNH_3Cu(Cl_{0.95}Br_{0.05})_3$ from neutron diffraction. *Physical Review B* **81**(6), 060410. URL http://prb.aps.org/abstract/PRB/v81/i6/e060410. 6

[Hulthén(1938)] L Hulthén (1938). Über das Austauschproblem eines Kristalles. *Arkiv för Matematik, Astronomi och Fysik A* **26**(11), 1–106. 4

[James *et al.*(2008)] A. J. A. James, F. H. L. Essler & R. M. Konik (2008). Finite-temperature dynamical structure factor of alternating Heisenberg chains. *Physical Review B* **78**, 094411. URL http://prb.aps.org/abstract/PRB/v78/i9/e094411. 2

[Johannsen *et al.*(2005)] N. Johannsen, A. Vasiliev, A. Oosawa, H. Tanaka & T. Lorenz (2005). Magnetoelastic Coupling in the Spin-Dimer System $TlCuCl_3$. *Physical Review Letters* **95**(1), 017205. URL http://prl.aps.org/abstract/PRL/v95/i1/e017205. 1, 6.3

[Johnston *et al.*(2000)] D. C. Johnston, M. Troyer, S. Miyahara, D. Lidsky, K. Ueda, M. Azuma, Z. Hiroi, M. Takano, M. Isobe, Y. Ueda, M. A. Korotin, V. I. Anisimov, A. V. Mahajan & L. L. Miller (2000). Magnetic Susceptibilities of Spin-1/2 Antiferromagnetic Heisenberg Ladders and Applications to Ladder Oxide Compounds. *ArXiv Condensed Matter e-prints* URL http://adsabs.harvard.edu/abs/2000cond.mat..1147J. 4

[Jurecka & Brenig(2000)] C. Jurecka & W. Brenig (2000). Optical absorption of spin ladders. *Physical Review B* **61**(21), 14307–14310. URL http://prb.aps.org/abstract/PRB/v61/i21/p14307_1. 4, 4.1.1

[Kehrein(2006)] S. K. Kehrein (2006). *The Flow Equation Approach to Many-Particle Systems*. Springer. 3

[Kehrein & Mielke(1994)] S. K. Kehrein & A. Mielke (1994). Flow equations for the Anderson Hamiltonian. *Journal of Physics A: Mathematical and General* **27**, 4259–4279. URL http://stacks.iop.org/0305-4470/27/i=12/a=030. Corrigendum **27**, 5705 (1994). 3

[Kehrein & Mielke(1996a)] S. K. Kehrein & A. Mielke (1996a). On the spin-boson model with a sub-ohmic bath. *Physics Letters A* **219**(5-6), 313–318. URL http://www.sciencedirect.com/science/article/pii/0375960196004756. 3

[Kehrein & Mielke(1996b)] S. K. Kehrein & A. Mielke (1996b). Theory of the Anderson Impurity Model: The Schrieffer-Wolff Transformation Reexamined. *Annals of Physics* **252**(1), 1–32. URL http://www.sciencedirect.com/science/article/pii/S0003491696901232. 3

[Kehrein & Mielke(1997)] S. K. Kehrein & A. Mielke (1997). Low temperature equilibrium correlation functions in dissipative quantum systems. *Annalen der Physik* **509**(2), 90–135. URL http://dx.doi.org/10.1002/andp.19975090203. 3, 3.2.3

[Kehrein & Mielke(1998)] S. K. Kehrein & A. Mielke (1998). Diagonalization of System plus Environment Hamiltonians. *Journal of Statistical Physics* **90**, 889–898. URL http://dx.doi.org/10.1023/A:1023289323069. 10.1023/A:1023289323069. 3, 3.2.3

[Kehrein *et al.*(1995)] S. K. Kehrein, A. Mielke & P. Neu (1995). Flow equations for the spin-boson problem. *Zeitschrift für Physik B Condensed Matter* **99**, 269–280. URL http://dx.doi.org/10.1007/BF02769942. 3

[Kirschner(2004)] S. Kirschner (2004). *Multi-particle spectral densities*. Diploma thesis, Universität zu Köln. URL http://t1.physik.tu-dortmund.de/uhrig/diploma.html. D

[Knetter(2003)] C. Knetter (2003). *Perturbative Continuous Unitary Transformations: Spectral Properties of Low Dimensional Spin Systems*. Ph.D. thesis, Universität zu Köln. URL http://t1.physik.tu-dortmund.de/uhrig/phd.html. 4.1.1, D

[Knetter *et al.*(2001)] C. Knetter, K. P. Schmidt, M. Grüninger & G. S. Uhrig (2001). Fractional and Integer Excitations in Quantum Antiferromagnetic Spin 1/2 Ladders. *Physical Review Letters* **87**(16), 167204. URL http://prl.aps.org/abstract/PRL/v87/i16/e167204. 4, 4.2.2, 6

[Knetter *et al.*(2003a)] C. Knetter, K. P. Schmidt & G. S. Uhrig (2003a). High order perturbation theory for spectral densities of multi-particle excitations: $S = \frac{1}{2}$ two-leg Heisenberg ladder. *The European Physical Journal B - Condensed Matter and Complex Systems* **36**(4), 525–544. URL http://dx.doi.org/10.1140/epjb/e2004-00008-2. 3, 4, 4.1, 4.1.1, 4.1.2, 4.2, D

[Knetter *et al.*(2003b)] C. Knetter, K. P. Schmidt & G. S. Uhrig (2003b). The structure of operators in effective particle-conserving models. *Journal of Physics A: Mathematical and General* **36**(29), 7889–7907. URL http://stacks.iop.org/0305-4470/36/i=29/a=302. 3.2.3, 3.4, 3.4.1

[Knetter & Uhrig(2000)] C. Knetter & G. S. Uhrig (2000). Perturbation theory by flow equations: dimerized and frustrated $S = 1/2$ chain . *European Physical Journal B* **13**(2), 209–225. URL http://dx.doi.org/10.1007/s100510050026. 1, 3, 3.2.3, 3.2.3, 3.2.3, 3.2.3, 3.4, 1

[Kojima *et al.*(1995)] K. Kojima, A. Keren, G. M. Luke, B. Nachumi, W. D. Wu, Y. J. Uemura, M. Azuma & M. Takano (1995). Magnetic Behavior of the 2-Leg and 3-Leg Spin Ladder Cuprates $Sr_{n-1}Cu_{n+1}O_{2n}$. *Physical Review Letters* **74**(14), 2812–2815. URL http://prl.aps.org/abstract/PRL/v74/i14/p2812_1. 4

[Kolezhuk & Sachdev(2006)] A. Kolezhuk & S. Sachdev (2006). Magnon Decay in Gapped Quantum Spin Systems. *Physical Review Letters* **96**(8), 087203. URL http://prl.aps.org/abstract/PRL/v96/i8/e087203. 1

[Konstantinović *et al.*(2001)] M. J. Konstantinović, J. C. Irwin, M. Isobe & Y. Ueda (2001). Low-energy excitations in NaV_2O_5. *Physical Review B* **65**(1), 012404. URL http://prb.aps.org/abstract/PRB/v65/i1/e012404. 4

[Kotov *et al.*(1999)] V. N. Kotov, O. P. Sushkov & R. Eder (1999). Excitation spectrum of the $S = 1/2$ quantum spin ladder with frustration: Elementary quasiparticles and many-particle bound states. *Physical Review B* **59**(9), 6266–6277. URL http://prb.aps.org/abstract/PRB/v59/i9/p6266_1. 4.1.1

[Krull(2011)] H. Krull (2011). *Verbesserte perturbative kontinuierliche unitäre Transformation mit direkter Auswertung erläutert anhand der Spin $S = 1/2$ antiferromagnetischen Heisenberg-Leiter*. Diploma thesis, Technische Universität Dortmund. URL http://t1.physik.tu-dortmund.de/uhrig/diploma.html. 3, 3.4, 4.1.1, 4.7, 4.1.1

[Kubo(1966)] R. Kubo (1966). The fluctuation-dissipation theorem. *Reports on Progress in Physics* **29**(1), 255–284. URL http://stacks.iop.org/0034-4885/29/i=1/a=306. F.1

[Kumagai *et al.*(1997)] K. Kumagai, S. Tsuji, M. Kato & Y. Koike (1997). NMR Study of Carrier Doping Effects on Spin Gaps in the Spin Ladder $Sr_{14-x}A_xCu_{24}O_{41}$ (A=Ca, Y, and La). *Physical Review Letters* **78**(10), 1992–1995. URL http://prl.aps.org/abstract/PRL/v78/i10/p1992_1. 4

[Landau(1941a)] L. D. Landau (1941a). The Theory of Superfluidity of Helium II. *Journal of Physics USSR* **5**, 71. 1

[Landau(1941b)] L. D. Landau (1941b). Theory of the Superfluidity of Helium II. *Physical Review* **60**(4), 356–358. URL http://prola.aps.org/abstract/PR/v60/i4/p356_1. 1

[Landau(1947)] L. D. Landau (1947). On the Theory of Superfluidity of Helium II. *Journal of Physics USSR* **11**, 91. 1

[Landau(1956)] L. D. Landau (1956). The Theory of a Fermi Liquid. *Journal of Experimental and Theoretical Physics* **30**, 1058. 1, 2.2

[Landau(1958)] L. D. Landau (1958). On the Theory of the Fermi Liquid. *Journal of Experimental and Theoretical Physics* **35**, 97. 1, 2.2

[Landau *et al.*(1980)] L. D. Landau, E. M. Lifshitz & L. P. Pitaevskii (1980). *Statistical Physics, Part 2 (Course of Theoretical Physics, Volume 9)*. Pergamnon Press. 1, 2.2

[Lenz & Wegner(1996)] P. Lenz & F. Wegner (1996). Flow equations for electron-phonon interactions. *Nuclear Physics B* **482**(3), 693–712. URL http://www.sciencedirect.com/science/article/pii/S0550321396005214. 3

[Lorscheid(2007)] N. Lorscheid (2007). *Systematische Ableitung des allgemeinen $t-J$ Modells aus dem Hubbard-Modell abseits halber Füllung*. Diploma thesis, Universität des Saarlandes. URL http://t1.physik.tu-dortmund.de/uhrig/diploma.html. 3.2.3

[Lüscher & Läuchli(2009)] A. Lüscher & A. M. Läuchli (2009). Exact diagonalization study of the antiferromagnetic spin-1/2 Heisenberg model on the square lattice in a magnetic field. *Physical Review B* **79**(19), 195102. URL http://prb.aps.org/abstract/PRB/v79/i19/e195102. 1

[Majumdar & Ghosh(1969a)] C. K. Majumdar & D. K. Ghosh (1969a). On Next-Nearest-Neighbor Interaction in Linear Chain. I. *Journal of Mathematical Physics* **10**(8), 1388–1398. URL http://dx.doi.org/doi/10.1063/1.1664978. 4

[Majumdar & Ghosh(1969b)] C. K. Majumdar & D. K. Ghosh (1969b). On Next-Nearest-Neighbor Interaction in Linear Chain. II. *Journal of Mathematical Physics* **10**(8), 1399–1402. URL http://dx.doi.org/doi/10.1063/1.1664979. 4

[Manaka *et al.*(2008)] H. Manaka, A. V Kolomiets & T. Goto (2008). Disordered states in IPA-Cu($cl_x br_{1-x}$)$_3$ induced by bond randomness. *Physical Review Letters* **101**, 077204. URL http://prl.aps.org/abstract/PRL/v101/i7/e077204. 6.3

[Manaka *et al.*(2007)] H. Manaka, K. Masamoto & S. Maehata (2007). Three-Dimensional Observation of Composite Haldane Spin Chains in IPA-$CuCl_3$ by Electron Spin Resonance Using a Two-Rotation-Axis Goniometer. *Journal of*

the Physical Society of Japan **76**(2), 023002. URL http://jpsj.ipap.jp/link?JPSJ/76/023002/. 6

[Manaka & Yamada(2000)] H. Manaka & I. Yamada (2000). Crossover from $S = 1/2$ to $S = 1$ Haldane state in the ferromagnetic and antiferromagnetic alternating Heisenberg chain system $(CH_3)_2CHNH_3CuCl_3$ observed with EPR at 24 GHz. *Physical Review B* **62**(21), 14279–14286. URL http://prb.aps.org/abstract/PRB/v62/i21/p14279_1. 6, 6.1

[Manaka *et al.*(1997)] H. Manaka, I. Yamada & K. Yamaguchi (1997). Ferromagnetic-Dominant Alternating Heisenberg Chains with Ferromagnetic and Antiferromagnetic Interactions Formed in $(CH_3)_2CHNH_3CuCl_3$. *Journal of the Physical Society of Japan* **66**(3), 564–567. URL http://jpsj.ipap.jp/link?JPSJ/66/564/. 6, 6, 6.1, 6.1, 6.4b, 6.1, 6.3

[Marshall & Lovesey(1971)] W. Marshall & S. W. Lovesey (1971). *Theory of thermal neutron scattering*. Oxford University Press. F

[Masuda *et al.*(2010)] T. Masuda, S. Kitaoka, S. Takamizawa, N. Metoki, K. Kaneko, K. C. Rule, K. Kiefer, H. Manaka & H. Nojiri (2010). Instability of magnons in two-dimensional antiferromagnets at high magnetic fields. *Physical Review B* **81**(10), 100402. URL http://prb.aps.org/abstract/PRB/v81/i10/e100402. 1

[Masuda *et al.*(2006)] T. Masuda, A. Zheludev, H. Manaka, L.-P. Regnault, J.-H. Chung & Y. Qiu (2006). Dynamics of Composite Haldane Spin Chains in IPA-$CuCl_3$. *Physical Review Letters* **96**(4), 047210. URL http://prl.aps.org/abstract/PRL/v96/i4/e047210. 1.1, 1, 1, 6, 6.1, 6, 6.1, 6.1, 6.1, 6.3, 6.2.1, 6.5, 6.2.4, 6.2.4, 6.2.4, 6.2.4, 2, 6.8, 6.11, 6.2.4, 6.12

[Matsuda *et al.*(2000)] M. Matsuda, K. Katsumata, R. S. Eccleston, S. Brehmer & H.-J. Mikeska (2000). Magnetic excitations and exchange interactions in the spin-1/2 two-leg ladder compound $La_6Ca_8Cu_{24}O_{41}$. *Physical Review B* **62**(13), 8903–8908. URL http://prb.aps.org/abstract/PRB/v62/i13/p8903_1. 4

[Matsumoto *et al.*(2002)] M. Matsumoto, B. Normand, T. M. Rice & M. Sigrist (2002). Magnon Dispersion in the Field-Induced Magnetically Ordered Phase of $TlCuCl_3$. *Physical Review Letters* **89**(7), 077203. URL http://prl.aps.org/abstract/PRL/v89/i7/e077203. 1, 6.3, 6.3

[Matsumoto *et al.*(2004)] M. Matsumoto, B. Normand, T. M. Rice & M. Sigrist (2004). Field- and pressure-induced magnetic quantum phase transitions in $TlCuCl_3$. *Physical Review B* **69**(5), 054423. URL http://prb.aps.org/abstract/PRB/v69/i5/e054423. 6.3, 6.3, 1, G, G

[Mielke(1998)] A. Mielke (1998). Flow equations for band-matrices. *The European Physical Journal B - Condensed Matter and Complex Systems* **5**(3), 605–611. URL http://dx.doi.org/10.1007/s100510050485. 3.2.2, 3.2.2, 3.2.3, 3.2.3, 3.2.3, 4.1.1, 4.2.1

[Mills(2007)] D. L. Mills (2007). Comment on "Bose-Einstein Condensation of Magnons in Cs_2CuCl_4". *Physical Review Letters* **98**(3), 039701. URL http://prl.aps.org/abstract/PRL/v98/i3/e039701. 1

[Mori(1965)] H. Mori (1965). A Continued-Fraction Representation of the Time-Correlation Functions. *Progress of Theoretical Physics* **34**(3), 399–416. URL http://ptp.ipap.jp/link?PTP/34/399/. 4.1.2, 4.2.2

[Mourigal *et al.*(2010)] M. Mourigal, M. E. Zhitomirsky & A. L. Chernyshev (2010). Field-induced decay dynamics in square-lattice antiferromagnets. *Physical Review B* **82**(14), 144402. URL http://prb.aps.org/abstract/PRB/v82/i14/e144402. 1

[Müller & Mikeska(2000)] M. Müller & H.-J. Mikeska (2000). On the dynamics of coupled S = 1/2 antiferromagnetic zigzag chains. *Journal of Physics: Condensed Matter* **12**(34), 7633. URL http://stacks.iop.org/0953-8984/12/i=34/a=309. 4

[Náfrádi *et al.*(2011)] B. Náfrádi, T. Keller, H. Manaka, A. Zheludev & B. Keimer (2011). Low-Temperature Dynamics of Magnons in a Spin-1/2 Ladder Compound. *Physical Review Letters* **106**(17), 177202. URL http://prl.aps.org/abstract/PRL/v106/i17/e177202. 6.4, 6.4

[Nikuni *et al.*(2000)] T. Nikuni, M. Oshikawa, A. Oosawa & H. Tanaka (2000). Bose-Einstein Condensation of Dilute Magnons in $TlCuCl_3$. *Physical Review Letters* **84**(25), 5868–5871. URL http://prl.aps.org/abstract/PRL/v84/i25/p5868_1. 1

[Normand & Rüegg(2011)] B. Normand & Ch. Rüegg (2011). Complete bond-operator theory of the two-chain spin ladder. *Physical Review B* **83**, 054415. URL http://prb.aps.org/abstract/PRB/v83/i5/e054415. 6.3, 6.4, 6.4

[Notbohm *et al.*(2007)] S. Notbohm, P. Ribeiro, B. Lake, D. A. Tennant, K. P. Schmidt, G. S. Uhrig, C. Hess, R. Klingeler, G. Behr, B. Büchner, M. Reehuis, R. I. Bewley, C. D. Frost, P. Manuel & R. S. Eccleston (2007). One- and Two-Triplon Spectra of a Cuprate Ladder. *Physical Review Letters* **98**(2), 027403. URL http://prl.aps.org/abstract/PRL/v98/i2/e027403. 4, 4.1.2

[Nozières & Pines(1999)] P. Nozières & D. Pines (1999). *The Theory of Quantum Liquids*. Perseus Books. 2.2

[Okamoto & Nomura(1992)] K. Okamoto & K. Nomura (1992). Fluid-dimer critical point in $S = 1/2$ antiferromagnetic Heisenberg chain with next nearest neighbor

interactions. *Physics Letters A* **169**(6), 433–437. URL http://www.sciencedirect.com/science/article/pii/0375960192908235. 4

[Palevsky *et al.*(1957)] H. Palevsky, K. Otnes, K. E. Larsson, R. Pauli & R. Stedman (1957). Excitation of Rotons in Helium II by Cold Neutrons. *Physical Review* **108**(5), 1346–1347. URL http://prola.aps.org/abstract/PR/v108/i5/p1346_1. 1

[Peierls(1955)] R. Peierls (1955). *Quantum Theory of Solids*. Clarendon Press. 1

[Pettifor & Weaire(1985)] D. G. Pettifor & D. L. Weaire (1985). *The Recursion Method and its Applications* , vol. 58 of *Springer Series in Solid State Sciences*. D. G. Pettifor and D. L. Weaire. 4.1.2, 4.1.2, 4.2.2, A.1, A.2

[Pitaevskii(1959)] L. P. Pitaevskii (1959). Properties of the spectrum of elementary excitations near the disintegration threshold of the excitations. *Soviet Physics JETP* **9**(4), 830–837. 1

[Press *et al.*(2002)] W. H. Press, S. A. Teukolsky, W. T. Vetterling & B. P. Flannery (2002). *Numerical Recipes in* C++. Cambridge University Press. 3.5.2

[Ragwitz & Wegner(1999)] M. Ragwitz & F. Wegner (1999). Flow equations for electron-phonon interactions: phonon damping. *The European Physical Journal B - Condensed Matter and Complex Systems* **8**, 9–17. URL http://dx.doi.org/10.1007/s100510050663. 3

[Reischl(2006)] A. Reischl (2006). *Derivation of Effective Models using Self-Similar Continuous Unitary Transformations in Real Space*. Ph.D. thesis, Universität zu Köln. URL http://t1.physik.tu-dortmund.de/uhrig/phd.html. 3.2.3, 3.2.3, 3.3.1, 3.3.2, 3.4, 3.4.1, 3.4.3, 3.4.3, 3.4.3, 3.5.1, 3.5.1, 4, 4.1.1, 4.1.1, 4.2, 4.2.1

[Reischl *et al.*(2004)] A. Reischl, E. Müller-Hartmann & G. S. Uhrig (2004). Systematic mapping of the Hubbard model to the generalized $t-J$ model. *Physical Review B* **70**(24), 245124. URL http://prb.aps.org/abstract/PRB/v70/i24/e245124. 3, 3.1, 3.2.3, 3.2.3, 3.3.2, 3.4.1, 3.4.3, 4.2.1

[Renard *et al.*(1987)] J. P. Renard, M. Verdaguer, L. P. Regnault, W. A. C. Erkelens, J. Rossat-Mignod & W. G. Stirling (1987). Presumption for a Quantum Energy Gap in the Quasi-One-Dimensional $S = 1$ Heisenberg Antiferromagnet $Ni(C_2H_8N_2)_2NO_2(ClO_4)$. *Europhysics Letters* **3**(8), 945. URL http://stacks.iop.org/0295-5075/3/i=8/a=013. 1, 4

[Roberts *et al.*(1981)] S. A. Roberts, D. R. Bloomquist, R. D. Willett & H. W. Dodgen (1981). Thermochromic phase transitions in copper(II) halide salts. 1. Crystal structure and magnetic resonance studies of isopropylammonium

trichlorocuprate(II). *Journal of the American Chemical Society* **103**(10), 2603–2610. URL http://pubs.acs.org/doi/abs/10.1021/ja00400a020. 6, 6

[Rüegg *et al.*(2003)] C. Rüegg, N. Cavadini, A. Furrer, H.-U. Güdel, K. Krämer, H. Mutka, A. Wildes, K. Habicht & P. Vorderwisch (2003). Bose-Einstein condensation of the triplet states in the magnetic insulator $TlCuCl_3$. *Nature* **423**, 62–65. URL http://dx.doi.org/10.1038/nature01617. 1

[Rüegg *et al.*(2005)] C. Rüegg, B. Normand, M. Matsumoto, C. Niedermayer, A. Furrer, K. W. Krämer, H.-U. Güdel, P. Bourges, Y. Sidis & H. Mutka (2005). Quantum statistics of interacting dimer spin systems. *Physical Review Letters* **95**, 267201. URL http://prl.aps.org/abstract/PRL/v95/i26/e267201. 6.4, 6.4

[Sachdev(1999)] S. Sachdev (1999). *Quantum Phase Transitions*. Cambridge University Press. 3.4.3

[Sachdev & Bhatt(1990)] S. Sachdev & R. N. Bhatt (1990). Bond-operator representation of quantum spins: Mean-field theory of frustrated quantum Heisenberg antiferromagnets. *Physical Review B* **41**(13), 9323–9329. URL http://prb.aps.org/abstract/PRB/v41/i13/p9323_1. 4, 6.1, 6.4, C

[Schmidiger *et al.*(2011)] D. Schmidiger, S. Muehlbauer, S. N. Gvasaliya, T. Yankova & A. Zheludev (2011). Long-lived magnons throughout the Brillouin zone of the strong-leg spin ladder $(C_7H_{10}N)_2CuBr_4$. *condmat/1105.4832* URL http://arxiv.org/abs/1105.4832. 4

[Schmidt(2004)] K. P. Schmidt (2004). *Spectral Properties of Quasi One-dimensional Quantum Antiferromagnets Perturbative Continuous Unitary Transformations*. Ph.D. thesis, Universität zu Köln. URL http://t1.physik.tu-dortmund.de/uhrig/phd.html. 4.1.1, 4.7, 4.1.2, 4.8, 4.1.2, 4.1.2, 4.2

[Schmidt(2008)] K. P. Schmidt (2008). *Festkörpertheorie II*. Lecture notes. 3.1

[Schmidt *et al.*(2001)] K. P. Schmidt, C. Knetter & G. S. Uhrig (2001). Raman response in antiferromagnetic two-leg $S = 1/2$ Heisenberg ladders. *Europhysics Letters* **56**(6), 877–883. URL http://stacks.iop.org/0295-5075/56/i=6/a=877. 4

[Schmidt *et al.*(2004)] K. P. Schmidt, C. Knetter & G. S. Uhrig (2004). Spectral properties of the dimerized and frustrated $S = 1/2$ chain. *Physical Review B* **69**(10), 104417. URL http://prb.aps.org/abstract/PRB/v69/i10/e104417. 4

[Schmidt & Uhrig(2003)] K. P. Schmidt & G. S. Uhrig (2003). Excitations in One-Dimensional $S = 1/2$ Quantum Antiferromagnets. *Physical Review Letters* **90**(22), 227204. URL http://prl.aps.org/abstract/PRL/v90/i22/e227204. 2, 4, 4.1, 6

[Schmidt & Uhrig(2005)] K. P. Schmidt & G. S. Uhrig (2005). Spectral Properties of Magnetic Excitations in Cuprate Two-Leg Ladder Systems. *Modern Physics Letters B* **19**, 1179–1205. URL http://www.worldscinet.com/mplb/19/1924/S0217984905009237.html. 3.2.3, 4, 4, 4.1.2, 4.8, 4.1.2, 6

[Schmidt & Uhrig(2006)] K. P. Schmidt & G. S. Uhrig (2006). Hard-core magnons in the $S = 1/2$ Heisenberg model on the square lattice. *Physical Review B* **73**(17), 172407. URL http://link.aps.org/abstract/PRB/v73/e172407. 3

[Schwenk *et al.*(1996)] H. Schwenk, M. Sieling, D. König, W. Palme, S. A. Zvyagin, B. Lüthi & R. S. Eccleston (1996). Magnetic resonances and magnetization in the spin ladder compound $(VO)_2P_2O_7$. *Solid State Communications* **100**(6), 381–384. URL http://www.sciencedirect.com/science/article/pii/0038109896000002. 4

[Sénéchal(1993)] D. Sénéchal (1993). Haldane gap in the quasi-one-dimensional nonlinear σ model. *Physical Review B* **48**(21), 15880–15885. URL http://prb.aps.org/showrefs/PRB/v48/i21/p15880_1. 6.4

[Shastry & Sutherland(1981)] B. S. Shastry & B. Sutherland (1981). Excitation Spectrum of a Dimerized Next-Neighbor Antiferromagnetic Chain. *Physical Review Letters* **47**, 964–967. URL http://prl.aps.org/abstract/PRL/v47/i13/p964_1. 4

[Shelton *et al.*(1996)] D. G. Shelton, A. A. Nersesyan & A. M. Tsvelik (1996). Antiferromagnetic spin ladders: Crossover between spin S=1/2 and S=1 chains. *Physical Review B* **53**, 8521–8532. URL http://prb.aps.org/abstract/PRB/v53/i13/p8521_1. 4.1.2

[Shiramura *et al.*(1997)] W. Shiramura, K.-I. Takatsu, H. Tanaka, K. Kamishima, M. Takahashi, H. Mitamura & T. Goto (1997). High-Field Magnetization Processes of Double Spin Chain Systems $KCuCl_3$ and $TlCuCl_3$. *Journal of the Physical Society of Japan* **66**(7), 1900–1903. URL http://jpsj.ipap.jp/link?JPSJ/66/1900/. 1

[Sirker *et al.*(2005)] J. Sirker, A. Weisse & O. P. Sushkov (2005). The Field-Induced Magnetic Ordering Transition in $TlCuCl_3$. *Journal of the Physical Society of Japan* **74S**(Supplement), 129–134. URL http://jpsj.ipap.jp/link?JPSJS/74S/129/. 1

[Smith *et al.*(1977)] A. J. Smith, R. A. Cowley, A. D. B. Woods, Stirling W. G. & P. Martel (1977). Roton-roton interactions and excitations in superfluid helium at large wavevectors. *Journal of Physics C: Solid State Physics* **10**(4), 543–553. URL http://stacks.iop.org/0022-3719/10/i=4/a=011. 1

[Sommer *et al.*(2001)] T. Sommer, M. Vojta & K. W. Becker (2001). Magnetic properties and spin waves of bilayer magnets in a uniform field. *The European Physical Journal B* **23**(3), 329–339. URL http://dx.doi.org/10.1007/s100510170052. 6.3, 6.3

[Squires(1978)] G. L. Squires (1978). *Introduction to the theory of thermal neutron scattering*. Cambridge University Press. F

[Stein(1997)] J. Stein (1997). Flow equations and the strong-coupling expansion for the Hubbard model. *Journal of Statistical Physics* **88**, 487–511. URL http://dx.doi.org/10.1007/BF02508481. 3, 3.2.3

[Stein(1998)] J. Stein (1998). Flow equations and extended Bogoliubov transformation for the Heisenberg antiferromagnet near the classical limit. *The European Physical Journal B - Condensed Matter and Complex Systems* **5**, 193–201. URL http://dx.doi.org/10.1007/s100510050434. 3.2.3

[Stone *et al.*(2001)] M. B. Stone, I. Zaliznyak, D. H. Reich & C. L. Broholm (2001). Frustration-induced two-dimensional quantum disordered phase in piperazinium hexachlorodicuprate. *Physical Review B* **64**(14), 144405. URL http://prb.aps.org/abstract/PRB/v64/i14/e144405. 1.2

[Stone *et al.*(2006)] M. B. Stone, I. A. Zaliznyak, T. Hong, C. L. Broholm & D. H. Reich (2006). Quasiparticle breakdown in a quantum spin liquid. *Nature* **400**, 187–190. URL http://dx.doi.org/10.1038/nature04593. 1, 1.2, 1

[Sugai & Suzuki(1999)] S. Sugai & M. Suzuki (1999). Magnetic Raman Scattering in Two-Leg Spin Ladder $Sr_{14-x-y}Ca_xY_yCu_{24}O_{41}$. *physica status solidi (b)* **215**(1), 653–659. URL http://dx.doi.org/10.1002/(SICI)1521-3951(199909)215:1<653::AID-PSSB653>3.0.CO;2-C. 4

[Sushkov & Kotov(1998)] O. P. Sushkov & V. N. Kotov (1998). Bound States of Magnons in the $S = 1/2$ Quantum Spin Ladder. *Physical Review Letters* **81**(9), 1941–1944. URL http://prl.aps.org/abstract/PRL/v81/i9/p1941_1. 4, 4.1.1, 4.2, 4.2.2

[Syljuåsen(2008)] O. F. Syljuåsen (2008). Numerical evidence for unstable magnons at high fields in the Heisenberg antiferromagneton the square lattice. *Physical Review B* **78**(18), 180413. URL http://prb.aps.org/abstract/PRB/v78/i18/e180413. 1

[Syromyatnikov(2009)] A. V. Syromyatnikov (2009). Collective excitations in a two-dimensional antiferromagnet in a strong magnetic field. *Physical Review B* **79**(5), 054413. URL http://prb.aps.org/abstract/PRB/v79/i5/e054413. 1

[Takahashi(1977)] M. Takahashi (1977). Half-filled Hubbard model at low temperature. *Journal of Physics C: Solid State Physics* **10**(8), 1289. URL http://stacks.iop.org/0022-3719/10/i=8/a=031. 3.1

[Tranquada *et al.*(1995)] J. M. Tranquada, B. J. Sternlieb, J. D. Axe, Y. Nakamura & S. Uchida (1995). Evidence for stripe correlations of spins and holes in copper

oxide superconductors. *Nature* **375**, 561–563. URL http://dx.doi.org/10.1038/375561a0. 4

[Trebst *et al.*(2000)] S. Trebst, H. Monien, C. J. Hamer, Z. Weihong & R. R. P. Singh (2000). Strong-Coupling Expansions for Multiparticle Excitations: Continuum and Bound States. *Physical Review Letters* **85**(20), 4373–4376. URL http://prl.aps.org/abstract/PRL/v85/i20/p4373_1. 4.1.1, 4.2, 4.2.2

[Troyer *et al.*(1994)] M. Troyer, H. Tsunetsugu & D. Würtz (1994). Thermodynamics and spin gap of the Heisenberg ladder calculated by the look-ahead Lanczos algorithm. *Physical Review B* **50**(18), 13515–13527. URL http://prb.aps.org/abstract/PRB/v50/i18/p13515_1. 3.4.1, 6.1, 6.4, 6.4

[Uehara *et al.*(1996)] M. Uehara, T. Nagata, J. Akimitsu, H. Takahashi, N. Môri & K. Kinoshita (1996). Superconductivity in the Ladder Material $Sr_{0.4}Ca_{13.6}Cu_{24}O_{41.84}$. *Journal of the Physical Society of Japan* **65**(9), 2764–2767. URL http://jpsj.ipap.jp/link?JPSJ/65/2764/. 4

[Uhrig(2005)] G. S. Uhrig (2005). *Correlated Fermionic Systems: Fermi Liquid and Luttinger Liquid*. URL http://t1.physik.tu-dortmund.de/uhrig/liquids_ss2004.html. Lecture notes. 2.2

[Uhrig & Normand(1998)] G. S. Uhrig & B. Normand (1998). Magnetic properties of $(VO)_2P_2O_7$ from frustrated interchain coupling. *Physical Review B* **58**(22), R14705–R14708. URL http://prb.aps.org/abstract/PRB/v58/i22/pR14705_1. 1, 3, 3.2.3, 4.1.1, 4.2.2

[Uhrig *et al.*(2004)] G. S. Uhrig, K. P. Schmidt & M. Grüninger (2004). Unifying Magnons and Triplons in Stripe-Ordered Cuprate Superconductors. *Physical Review Letters* **93**, 267003. URL http://prl.aps.org/abstract/PRL/v93/i26/e267003. 4, 6.1

[Uhrig *et al.*(2005a)] G. S. Uhrig, K. P. Schmidt & M. Grüninger (2005a). Magnetic Excitations in Bilayer High-Temperature Superconductors with Stripe Correlations. *Journal of the Physical Society of Japan* **74S**(Supplement), 86–97. URL http://jpsj.ipap.jp/link?JPSJS/74S/86/. 6.1

[Uhrig *et al.*(2005b)] G. S. Uhrig, K. P. Schmidt & M. Grüninger (2005b). Magnetic excitations in the stripe phase of high-T_c superconductors. *Journal of Magnetism and Magnetic Materials* **290–291**(Part 1), 330–333. URL http://www.sciencedirect.com/science/article/pii/S0304885304014702. 4

[Uhrig & Schulz(1996)] G. S. Uhrig & H. J. Schulz (1996). Magnetic excitation spectrum of dimerized antiferromagnetic chains. *Physical Review B* **54**(14), R9624–R9627. URL http://prb.aps.org/abstract/PRB/v54/i14/pR9624_1. Erratum: *Physical Review B* **58**(5), 2900 (1998). 4.1.1, 4.2.2, 6

[Vidal *et al.*(2009)] J. Vidal, S. Dusuel & K. P. Schmidt (2009). Low-energy effective theory of the toric code model in a parallel magnetic field. *Physical Review B* **79**(3), 033109. URL http://prb.aps.org/abstract/PRB/v79/i3/e033109. 3

[Viswanath & Müller(1994)] V. S. Viswanath & G. Müller (1994). *The Recursion Method; Application to Many-Body Dynamics*, vol. m23 of *Lecture Notes in Physics*. Springer. 2.4, 4.1.2, 4.2.2, A, A.1

[Vojta & Ulbricht(2004)] M. Vojta & T. Ulbricht (2004). Magnetic Excitations in a Bond-Centered Stripe Phase: Spin Waves Far from the Semiclassical Limit. *Physical Review Letters* **93**(12), 127002. URL http://prl.aps.org/abstract/PRL/v93/i12/e127002. 4

[Wegner(1994)] F. Wegner (1994). Flow-equations for Hamiltonians. *Annalen der Physik* **506**(2), 77–91. URL http://dx.doi.org/10.1002/andp.19945060203. 1, 3, 3.1.1, 3.2.1, 3.2.1, 3.4

[Wegner(2006)] F. Wegner (2006). Flow equations and normal ordering: a survey. *Journal of Physics A: Mathematical and General* **39**(25), 8221. URL http://stacks.iop.org/0305-4470/39/i=25/a=S29. 3.2.1

[White(1996)] S. R. White (1996). Equivalence of the antiferromagnetic Heisenberg ladder to a single $S = 1$ chain. *Physical Review B* **53**, 52–55. URL http://prb.aps.org/abstract/PRB/v53/i1/p52_1. 4

[Yang & Yang(1966a)] C. N. Yang & C. P. Yang (1966a). One-Dimensional Chain of Anisotropic Spin-Spin Interactions. I. Proof of Bethe's Hypothesis for Ground State in a Finite System. *Physical Review* **150**(1), 321–327. URL http://prola.aps.org/abstract/PR/v150/i1/p321_1. 4

[Yang & Yang(1966b)] C. N. Yang & C. P. Yang (1966b). One-Dimensional Chain of Anisotropic Spin-Spin Interactions. II. Properties of the Ground-State Energy Per Lattice Site for an Infinite System. *Physical Review* **150**(1), 327–339. URL http://prola.aps.org/showrefs/PR/v150/i1/p327_1. 4

[Yang *et al.*(2010)] H.-Y. Yang, A. M. Läuchli, F. Mila & K. P. Schmidt (2010). Effective Spin Model for the Spin-Liquid Phase of the Hubbard Model on the Triangular Lattice. *Physical Review Letters* **105**, 267204. URL http://prl.aps.org/abstract/PRL/v105/i26/e267204. 3

[Yang & Schmidt(2011)] H.-Y. Yang & K. P. Schmidt (2011). Effective models for gapped phases of strongly correlated quantum lattice models. *Europhysics Letters* **94**(1), 17004. URL http://stacks.iop.org/0295-5075/94/i=1/a=17004. 3

[Zaliznyak *et al.*(2001)] I. A. Zaliznyak, S.-H. Lee & S. V. Petrov (2001). Continuum in the Spin-Excitation Spectrum of a Haldane Chain Observed by Neutron Scattering in $CsNiCl_3$. *Physical Review Letters* **87**, 017202. URL http://prl.aps.org/abstract/PRL/v87/i1/e017202. 5, 7.2

[Zhang & Rice(1988)] F. C. Zhang & T. M. Rice (1988). Effective Hamiltonian for the superconducting Cu oxides. *Physical Review B* **37**(7), 3759–3761. URL http://prb.aps.org/abstract/PRB/v37/i7/p3759_1. 1

[Zheludev *et al.*(2007)] A. Zheludev, V. O. Garlea, T. Masuda, H. Manaka, L.-P. Regnault, E. Ressouche, B. Grenier, J.-H. Chung, Y. Qiu, K. Habicht, K. Kiefer & M. Boehm (2007). Dynamics of quantum spin liquid and spin solid phases in IPA-$CuCl_3$ under an applied magnetic field studied with neutron scattering. *Physical Review B* **76**(5), 054450. URL http://prb.aps.org/abstract/PRB/v76/i5/e054450. 1, 6, 6.13

[Zheludev *et al.*(2008)] A. Zheludev, V. O. Garlea, L.-P. Regnault, H. Manaka, A. Tsvelik & J.-H. Chung (2008). Extended Universal Finite-T Renormalization of Excitations in a Class of One-Dimensional Quantum Magnets. *Physical Review Letters* **100**(15), 157204. URL http://prl.aps.org/abstract/PRL/v100/i15/e157204. 6.4

[Zheng *et al.*(2006a)] W. Zheng, J. O. Fjærestad, R. R. P. Singh, R. H. McKenzie & R. Coldea (2006a). Anomalous Excitation Spectra of Frustrated Quantum Antiferromagnets. *Physical Review Letters* **96**(5), 057201. URL http://prl.aps.org/abstract/PRL/v96/i5/e057201. 1

[Zheng *et al.*(2006b)] W. Zheng, J. O. Fjærestad, R. R. P. Singh, R. H. McKenzie & R. Coldea (2006b). Excitation spectra of the spin-1/2 triangular-lattice Heisenberg antiferromagnet. *Physical Review B* **74**(22), 224420. URL http://prb.aps.org/abstract/PRB/v74/i22/e224420. 1

[Zheng *et al.*(2001)] W. Zheng, C. J. Hamer, R. R. P. Singh, S. Trebst & H. Monien (2001). Linked cluster series expansions for two-particle bound states. *Physical Review B* **63**(14), 144410. URL http://prb.aps.org/abstract/PRB/v63/i14/e144410. 4, 4.1.1

[Zhitomirsky(2006)] M. E. Zhitomirsky (2006). Decay of quasiparticles in quantum spin liquids. *Physical Review B* **73**, 100404(R). URL http://prb.aps.org/abstract/PRB/v73/i10/e100404. 1, 2, 2.1, 2.1

[Zhitomirsky & Chernyshev(1999)] M. E. Zhitomirsky & A. L. Chernyshev (1999). Instability of Antiferromagnetic Magnons in Strong Fields. *Physical Review Letters* **82**(22), 4536–4539. URL http://prl.aps.org/abstract/PRL/v82/i22/p4536_1. 1

[Zwanzig(1961)] R. Zwanzig (1961). Statistical Mechanics of Irreversibility. In: *Lectures in Theoretical Physics, Volume III* (W. E. Brittin, B. W. Downs & J.Downs, eds.). Interscience, pp. 106–141. 4.1.2, 4.2.2

Teilpublikationen

- T. Fischer, S. Duffe & G. S. Uhrig (2010).
  Adapted continuous unitary transformation to treat systems with quasi-particles of finite lifetime.
  New Journal of Physics **12**(3), 033048, **arXiv**:0911.5007v2

- T. Fischer, S. Duffe & G. S. Uhrig (2011).
  Microscopic model for Bose-Einstein condensation and quasiparticle decay.
  Europhysics Letters **96**(4), 47001, **arXiv**:1009.3375v3

Danksagung

An dieser Stelle möchte ich mich herzlich bei all denen bedanken, die zum Gelingen dieser Arbeit beigetragen haben.

Besonderer Dank gebührt Prof. Dr. Götz S. Uhrig für die Vergabe des interessanten Themas und der hervorragenden Betreuung der vorliegenden Arbeit. Die vielen Ratschläge und anregenden Diskussionen in stets freundschaftlicher Atmosphäre bildeten die Grundlage für das Gelingen dieser Arbeit.

Des Weiteren möchte ich mich bei Prof. Dr. Oleg P. Sushkov für seine große Gastfreundschaft und die Betreuung während meines Aufenthaltes an der University of New South Wales bedanken.

Prof. Dr. Frithjof B. Anders und Prof. Dr. Bruce Normand danke ich für die Begutachtung meiner Arbeit. Bei Dr. Carsten Raas möchte ich mich für die geduldige Unterstützung in Softwarefragen jeglicher Art bedanken. Dr. Kai P. Schmidt danke ich für viele hilfreiche Diskussionen. Bei Dr. Sebastian Duffe und Nils Drescher bedanke ich mich für die ausgezeichnete Zusammenarbeit. Zusätzlich möchte ich mich bei Nils Drescher und Simone Hamerla für die Durchsicht der vorliegenden Arbeit bedanken. Vielen Dank an alle Mitarbeiter der Lehrstühle T1 und T2 für das sehr angenehme Arbeitsumfeld.

Nicht zuletzt danke ich meiner Familie für die Unterstützung in jeglicher Hinsicht.